Propagation of ultrasounds in random multi-scale media and effecitve speed of sound estimation

Quentin Goepfert

INSTITUT POLYTECHNIQUE DE PARIS

NNT : 2024IPPAE016

Thèse de doctorat

ENSTA

IP PARIS

Propagation of ultrasounds in random multi-scale media and effective speed of sound estimation

Thèse de doctorat de l'Institut Polytechnique de Paris
préparée à l'École nationale supérieure de techniques avancées

École doctorale n°574 École doctorale de mathématiques Hadamard (EDMH)
Spécialité de doctorat : Mathématiques appliquées

Thèse présentée et soutenue à Palaiseau, le 20/09/2024, par

QUENTIN GOEPFERT

Composition du Jury :

Sonia Fliss Professeure, ENSTA Paris (POEMS)	Présidente
Guillaume Bal Professeur, University of Chicago (Departments of Statistics and Mathematics)	Rapporteur
Shari Moskow Professor, Drexel University (Department of Mathematics)	Rapportrice
Alexandre Aubry Directeur de recherche, ESPCI Paris, (Institut Langevin)	Examinateur
Liliana Borcea Professeure, Columbia University (Department of Applied Physics and Applied Mathematics)	Examinatrice
Mitia Duerinckx Research associate, Université Libre de Bruxelles (Département de Mathémathiques)	Examinateur
Josselin Garnier Professeur, École polytechnique (CMAP)	Directeur de thèse
Laure Giovangigli Enseignante-chercheuse, ENSTA Paris (POEMS)	Co-encadrante de thèse
Pierre Millien Chargé de recherche, ESPCI Paris, (Institut Langevin)	Co-encadrant de thèse

Remerciements

Mes premiers remerciements vont à ma direction de thèse : **Josselin Garnier, Laure Giovangigli** et **Pierre Millien**. Vous avez tous les trois été des sources d'encouragement et d'inspiration tout au long de ces trois années. Vos précieuses remarques m'ont permis de grandir, tant sur le plan scientifique que personnel. Vous avez toujours pris le temps de m'accompagner, presque chaque semaine, et je vous en suis infiniment reconnaissant.
Josselin, je sais à quel point ton emploi du temps est chargé, mais tu as maintenu ce rythme hebdomadaire de suivi qui m'a été très bénéfique. En particulier, tu as toujours été disponible lorsque je me trouvais face à un obstacle. Ta capacité à expliquer des phénomènes physiques complexes à travers des mathématiques de haut niveau m'a toujours fasciné.
Pierre, à chaque rencontre, que ce soit à l'Institut Langevin ou à l'ENSTA, nos échanges ont toujours été riches. Nous avons souvent abordé des sujets dépassant le cadre professionnel, explorant des disciplines variées, parfois non scientifiques, mais aussi des discussions plus personnelles, centrées sur le bien-être. La thèse peut parfois être frustrante, et nos conversations ont toujours été un soulagement précieux.
Laure, tu as été présente au quotidien. J'ai pu te solliciter de nombreuses fois, que ce soit pour des questions scientifiques, administratives, ou même personnelles. Tu as toujours pris le temps de me répondre avec honnêteté et bienveillance. Je suis certain que ta bonne humeur est appréciée par l'ensemble des doctorants de l'UMA !

Je tiens également à remercier les rapporteurs **Guillaume Bal** et **Shari Moskow**, qui ont accepté de lire mon manuscrit en plein mois d'août. Merci d'avoir pris ce temps précieux et pour vos retours qui ont permis d'améliorer encore mon travail.
Ma gratitude va aussi aux membres du jury, **Alexandre Aubry, Liliana Borcea, Mitia Duerinckx** et **Sonia Fliss**, qui ont accepté d'examiner cette thèse. Je suis honoré d'avoir un jury composé de tant d'experts avec qui j'ai déjà eu l'occasion d'échanger. J'attends avec impatience vos remarques et questions.

Merci à l'ensemble des membres de l'Institut Langevin et CMAP avec qui j'ai eu l'occasion d'échanger. Un remerciement particulier à **Jessie** qui fut ma camarade de master et avec qui on a toujours beaucoup de choses à échanger.
Un remerciement à **Flavien Bureau** qui a pris de son temps pour m'expliquer et me réexpliquer certains des résultats physiques qu'il a obtenu et qui ont été étudiés dans cette thèse.

Un grand merci également aux membres de l'UMA. J'ai eu la chance d'être accueilli dans une structure où règnent entraide et collaboration. Vive les Psaume ! J'ai d'abord rencontré plusieurs d'entre vous en tant qu'étudiant, lorsque vous étiez mes professeurs. Vous avez nourri ma passion pour les mathématiques, et en particulier pour les EDPs, ces équations qui régissent les phénomènes physiques du monde. J'ai énormément appris grâce à vous, et je vous en suis profondément reconnaissant.

Je tiens à remercier la direction et le personnel administratif de l'UMA, du CMAP, de l'institut Langevin et de l'école doctorale. Vous êtes souvent trop peu mentionnés, mais sans vous, rien ne fonctionnerait. Un remerciement spécial à **Corinne**, l'assistante de l'UMA. Tu es une personne exceptionnelle. Tu veilles au bien-être des doctorants avec un dévouement sans faille. Je me souviens encore comme tu t'es battue pour que mon inscription à l'école doctorale soit validée à temps. On ne t'appelle pas la "maman de l'UMA" pour rien !

Merci aussi à **Nicolas**. Tu as été indispensable pour l'ensemble des doctorants de POEMS, toujours disponible pour installer un logiciel, aider sur du code ou développer de nouvelles fonctionnalités. Tu es même prêt à répondre en plein week-end ! Que la force soit toujours avec toi !

À mes anciens camarades, **Damien, Mahran, Meryem, Akram, Othmane, Jean-François, Amandine, Clara, Alice, Cristian, Alejandro, Amond, Etienne, Anh, Laura...** Merci à tous. Vous avez été extraordinaires. Merci en particulier à **Damien** et **Mahran**, qui m'ont accueilli au sein des doctorants de l'UMA. Mes débuts ont été mémorables, comme ce moment gênant partagé avec **Clara**, lorsque nous attendions les mêmes personnes à quelques mètres de distance, sans oser nous parler !
Un merci tout spécial à mes co-bureau : **Meryem, Akram, Amandine, Cédric**, ainsi qu'au duo inséparable **Alice** et **Laura**. Vous avez toujours supporté mes incessantes questions et mon inévitable jambe agitée. Merci à **Raphaël**, alias Terrine pour les intimes. Nous avons beaucoup appris ensemble, bien que rarement sur des sujets scientifiques. Nous avons appris qu'Hans Zimmer a fait partie de *The Buggles* et qu'Olivia Newton-John est la petite fille de Max Born. Nous avons aussi partagé des débats passionnés sur *Syd Matters, Daft Punk, Beach House* et bien d'autres.
Je remercie aussi les doctorants avec qui j'ai partagé la fameuse pause-café, initiée par **Paul**. Merci à **Sarah, Antonin, Timothée, Natalia, Adrien, Mario, Yassine, En, Farah, Aurelien, ...**
Un merci tout particulier à **Morgane, Fabien(g)** et **Thibaut**, avec qui j'ai savouré des moments gourmands autour de mets raffinés, comme le fameux foie gras de papy Pourre, toujours sublimé par les rosés les plus délicats choisis par **Thibaut** et accompagné des délicieux fromages fondants dévorés par **Morgane**.

À mes amis, **Adrien, Alexandre, Anatole, Axel, Cécile, Gabriel, Iliana, Madeleine,**

Maël, Marie, Maxence, Paul, Virginie et bien sûr **Théo**. Vous avez été une source inépuisable de motivation. Peu importe où vous vous trouvez, je sais que je peux toujours compter sur vous pour me remonter le moral.

Je tiens à exprimer ma profonde reconnaissance à ma grande famille, les **Goepfert**, les **Dubosclard**, les **Harivel** et les **Boisgontier**.
Merci **papy** et merci **mamie**.
Merci **Fabrice**, pour m'avoir accompagné toutes ces années, et à chaque retrouvaille, c'est toujours un grand plaisir.
Merci **maman**, pour ton soutien constant.
À **Julia**, ma soeur, avec qui j'ai grandi en écoutant *The Magic Key* et *Ananau*. Merci d'être toujours là pour moi. Ton grand frère est très fier de toi.
Enfin, **Elise**, tu partages ma vie, mes joies et mes peines. Tu as été d'un soutien inestimable durant cette thèse, relisant des chapitres, me remontant le moral, et t'intéressant à un sujet qui n'était pourtant pas le tien. Pour tout cela, et bien plus encore, merci.

GENERAL INTRODUCTION

CHAPTER 1

General introduction - French

Les premiers examens d'échographie remontent au début des années 1930 [1]. Depuis lors, l'échographie s'est imposée comme un examen des plus courants [2]. Comparée à d'autres méthodes, l'échographie présente de nombreux avantages. En effet, les appareils et, plus largement, la technique d'imagerie dans sa globalité, est peu coûteuse et non irradiante. De plus, les appareils sont portatifs et deviennent maintenant même compatibles avec les téléphones portables [3].
Parmi les nombreuses applications des ultrasons (utilisés dans les échographies), on retrouve, entre autres, le contrôle du développement du fœtus, l'imagerie du cœur, celle des cellules sanguines, l'imagerie de l'œil, de la thyroïde, du cerveau, de la poitrine, des organes abdominaux, de la peau et des muscles [4]. Les images ne sont plus seulement en 2D, mais désormais en 3D, voire en 4D, correspondant à des films d'images 3D [5].
Les images sont formées en excitant un transducteur piézoélectrique, qui émet une onde ultrasonore. Cette onde se diffuse dans le milieu et génère des échos. Ces échos rétrodiffusés sont ensuite mesurés et enregistrés par le transducteur piézoélectrique. La connaissance de la vitesse du son dans le milieu que l'on cherche à imager nous permet, grâce à un algorithme simple, en ajoutant des délais appropriés à chacun des signaux, de retrouver les zones échogènes du milieu étudié. Cet algorithme, appelé *delay-and-sum algorithm*, est aussi connu sous le nom de migration de Kirchhoff lorsqu'il est calculé à partir de données fréquentielles [6]. L'examen d'imagerie par ultrasons peut également être interprété comme un examen de retournement temporel [7], où les échos mesurés sont numériquement rétropropagés dans un milieu fictif où les ondes se propagent à la vitesse c_s.
Grâce aux nombreux progrès dans l'ingénierie des capteurs et l'évolution de la puissance de calcul, la résolution des images ne cesse de s'améliorer et des techniques d'échographie quantitative ont vu le jour. Ces techniques ne visent plus seulement à afficher une image du milieu, mais aussi à obtenir des informations quantitatives sur celui-ci, telles que l'atténuation ou la vitesse du son à l'intérieur du milieu [8, 9, 10]. En particulier, une estimation de la vitesse du son dans le milieu peut être utilisée comme biomarqueur pour diagnostiquer la stéatose hépatique ou les cancers du sein [11, 12, 13, 14, 15, 16]. De plus, la précision de l'estimation de la vitesse du son détermine la fidélité de la reconstruction tomographique. En effet, lorsque la vitesse de

rétropropagation ne correspond pas à la vitesse réelle du son dans le milieu, l'image apparaît floue et déformée. Pour quantifier la vitesse du son à l'intérieur du milieu, la communauté scientifique travaillant sur l'imagerie a développé plusieurs techniques, décrites en détail dans [8, 9, 10].
Alexandre Aubry et ses collaborateurs ont développé une nouvelle méthode inspirée de l'optique adaptative [17]. Physiquement, le processus d'imagerie consiste à focaliser une onde en un point x à l'intérieur du milieu pour créer un réflecteur virtuel et capter les échos de ce réflecteur. Cependant, en raison du décalage entre la vitesse de rétropropagation du son c_s et la vitesse réelle du son dans le milieu c_0, l'onde n'est pas réellement focalisée en x, mais la profondeur de focalisation varie. Pour tenir compte de cet effet, l'idée d'Aubry est de focaliser une onde à la profondeur $c_s t$ pour un temps donné $t > 0$. En maximisant l'amplitude de l'écho renvoyé à partir de la profondeur $c_s t$, tout en modifiant la vitesse de rétropropagation du son c_s, on peut retrouver la vitesse du son c_0. Le point $c_s t$ sert alors de *guide star* (étoile guide) virtuelle, sur lequel nous focalisons l'onde pour réviser la vitesse de rétropropagation de l'algorithme et retrouver la véritable vitesse de propagation des ondes à l'intérieur du milieu c_0.
La modélisation mathématique de ces techniques et, plus généralement, des expériences biologiques par ultrasons est une tâche complexe. À première vue, les tissus peuvent être modélisés comme des milieux homogènes, auquel cas seules les interfaces devraient être imagées. Cependant, l'image est en fait un motif de *speckle* (chatoiement). Il est communément admis que les échos rétrodiffusés par les tissus proviennent des nombreux diffuseurs à l'intérieur de ces tissus, ce qui donne lieu à ce motif de chatoiement sur l'image, car ces nombreux diffuseurs ne sont pas résolus. En effet, leur taille typique est bien inférieure à la résolution du système d'imagerie ultrasonore (qui caractérise les détails distinguables sur l'image). De plus, nous n'avons pas accès à la distribution spatiale de ces diffuseurs. Les tissus peuvent donc être modélisés comme des milieux aléatoires multi-échelles. Ainsi, dans la continuité des récents travaux d'Alexandre Aubry, on cherche ici à établir un cadre mathématique et numérique pour mieux modéliser les tissus biologiques et comprendre les limites et les potentialités des nouvelles méthodes d'imagerie. Pour ce faire, un nouveau modèle sera introduit pour décrire la propagation des ultrasons dans les tissus mous : un modèle composite, multi-échelle et aléatoire.

Dans la première partie I du manuscrit, nous dressons un aperçu de l'état actuel de l'imagerie ultrasonore. Cette étude nous motive à dériver un nouveau modèle qui est celui établi dans la section 3.3.1. Nous introduisons donc un modèle aléatoire multi-échelle qui sera étudié tout au long du manuscrit.
Dans la partie II, nous étudions la rétrodiffusion des milieux aléatoires multi-échelles. Plus précisément, nous étudions le champ diffusé par un milieu composite aléatoire se trouvant dans l'espace libre dans le but d'obtenir une forme simple du champ rétrodiffusé (qui correspond aux mesures ultrasonores). Mathématiquement, nous étudions l'équation de Helmholtz sous forme de divergence avec des coefficients aléatoires fortement oscillants. Nous réalisons une étude asymptotique en utilisant des techniques

quantitatives d'homogénéisation stochastique et dérivons un développement d'ordre élevé dans le Théorème 39.
Dans une troisième partie, nous utilisons ce développement asymptotique pour mathématiquement justifier l'utilisation des estimateurs de la vitesse effective du son c_0, à l'intérieur des tissus biologiques introduits par Alexandre Aubry. Dans ce cadre, nous étudions la migration de Kirchhoff. Plus précisément, nous étudions la dépendance de la fonctionnelle d'imagerie par rapport à la vitesse de rétropropagation c_s dans le régime paraxial et ce, pour deux situations. Dans un premier temps, nous étudions le cas simple de l'imagerie d'une cible isolée et petite (par rapport à la longueur d'onde) dans un milieu homogène. Nous cherchons alors à récupérer la vitesse de propagation à l'intérieur de ce milieu homogène. Dans un second temps, nous considérons l'imagerie d'un milieu composite aléatoire correspondant au milieu introduit dans la partie I avec l'aide du développement asymptotique que l'on a obtenu après l'analyse faite dans la partie II.

Contenu détaillé du manuscrit

Le manuscrit est organisé comme suit.

Dans la partie I, nous abordons le contexte scientifique de cette thèse. Dans le chapitre 3, nous passons en revue un bref historique des techniques d'imagerie par ultrasons. Grâce aux améliorations apportées aux dispositifs d'imagerie et à la compréhension théorique de la diffusion des ondes, les limites des techniques d'imagerie par ultrasons peuvent être quantifiées et surmontées. L'objectif des systèmes d'imagerie par ultrasons est maintenant d'obtenir des estimations quantitatives des paramètres physiques des tissus à partir des mesures ultrasonores. Ceci est expliqué dans la section 3.2. Néanmoins, pour obtenir une telle estimation quantitative, il est nécessaire d'avoir un modèle quantitatif qui relie les propriétés physiques du milieu aux mesures. Les mesures sont modélisées par un champ diffusé qui correspond à la solution d'une équation de Helmholtz sous forme divergence avec des propriétés acoustiques (coefficients) variables. La dérivation d'estimateurs quantitatifs nécessite alors de comprendre mathématiquement les propriétés de la solution d'une telle équation. Comme mentionné ci-dessus, la propagation des ultrasons dans les tissus biologiques correspond mathématiquement à un problème multi-échelle par sa nature. Il existe plusieurs modèles pour la diffusion de tels milieux, qui sont examinés dans la section section:ScatteredFieldApprox. Ces modèles, bien que raisonnables pour la modélisation des tissus biologiques, ne tiennent pas compte des effets de la microstructure sur les propriétés macroscopiques des tissus. C'est ce qui explique le développement du nouveau modèle présenté à la section 3.3.1. On décidera de modéliser la position de chacune des hétérogénéités à l'intérieur du milieu par un processus aléatoire.

Pour étudier ce modèle, nous décidons d'utiliser des techniques d'homogénéisation stochastique. En effet, comme expliqué dans le chapitre 4, la discipline mathématique de l'homogénéisation est développée pour étudier les problèmes multi-échelles et comprendre leurs propriétés macroscopiques. Ainsi, sous des hypothèses de stationnarité et d'ergodicité qui sont discutées dans la section 4.3 sur le processus qui sert à décrire les propriétés physiques aléatoires du milieu, il est possible d'approximer la diffusion par le milieu multi-échelle aléatoire complexe par un milieu aux propriétés homogènes.
Le but de l'homogénéisation quantitative est alors de quantifier l'erreur entre la solution calculée avec les propriétés effectives obtenues et la solution calculée dans le milieu initial. Le domaine de l'homogénéisation quantitative stochastique a connu des avancées importantes dans les années 2010 que nous présentons dans la section 4.4. Nous utilisons ces résultats récents pour mener à bien l'étude de notre problème multi-échelle aléatoire. Malheureusement, le problème de diffusion obtenu en appliquant l'homogénéisation stochastique habituelle à notre modèle n'est pas satisfaisant. En effet, en remplaçant le milieu multi-échelle aléatoire par un milieu homogène plus simple, nous perdons la nature aléatoire du champ diffusé, et l'image résultante ne ressemble pas au motif de *speckle* des images traditionnelles. C'est pourquoi nous développons un développement d'homogénéisation d'ordre élevé dans la partie II. Plus précisément, nous allons au-delà de la solution effective, homogénéisée donnée par la théorie de l'homogénéisation et construisons également un terme correctif. Ce terme correctif contiendra les effets de micro-échelle que nous recherchons. Nous quantifions également l'erreur entre la solution initiale et l'approximation construite. Par conséquent, nous établissons d'abord l'expansion asymptotique l'expansion asymptotique quantitative à deux échelles dans la Proposition 37 qui est suivie par le développement d'ordre supérieur du Théorème 39. En outre, pour illustrer ces deux résultats, nous réalisons des expériences numériques au chapitre 8. Les résultats numériques obtenues sont conformes aux résultats théorique prédit par la Proposition 36 et par le développement d'ordre supérieur du Théorème 39.

La forme simple du champ rétrodiffusé obtenue dans le Théorème 39 est alors notre modèle de base pour l'analyse des estimateurs de la vitesse effective (homogénéisée) du son introduits par Alexandre Aubry. Nous effectuons une analyse asymptotique de la migration de Kirchhoff dans la partie III. Avant de travailler sur un milieu complexe qui imitent les propriétés des tissus, nous commençons par une analyse asymptotique simple de la migration de Kirchhoff d'un réflecteur-point dispersé dans un milieu homogène. En particulier, nous étudions la dépendance de la fonctionnelle d'imagerie par rapport la vitesse de rétropropagation du son utilisé dans cet algorithme d'imagerie et ce, dans le régime paraxial. Ce régime est décrit dans le chapitre 10. Nous montrons dans le Théorème 54 que le position du point de l'image au centre de la tache focale dépend de la vitesse de rétropropagation du son, et que l'amplitude affichée sur l'image diminue lorsque l'erreur dans la vitesse de rétropropagation du son augmente. Par conséquent, en recherchant le maximum global de l'amplitude de

la fonction d'imagerie, nous pouvons récupérer la vitesse du son du milieu homogène environnant.
Cependant, dans les tissus biologiques, il n'y a pas de cible isolée que l'on peut utiliser pour indentifier un maximum d'amplitude correspondant à l'image d'une cible en particulier. Ainsi, le maximum d'amplitude sur l'image peut rarement être utilisé comme critère pour quantifier la vitesse effective du son. Tout de même, dans le chapitre 12, nous poursuivons l'analyse de la migration de Kirchhoff avec l'expression du champ diffusé obtenue dans le théorème 39. Nous prouvons que dans le régime paraxial, l'imagerie à une profondeur z avec une vitesse de rétropropagation c est similaire à la création d'un réflecteur virtuel à la position $z\frac{c_0}{c}$ avec c_0 étant la vitesse effective du son. En particulier, cela justifie l'idée d'Aubry de focaliser à ct pour un temps t donné. En effet, en procédant ainsi, on arrive à toujours focaliser notre onde à la position $c_0 t$, position qui ne dépend pas de c et qui est notre *guide star* (étoile guide) virtuelle. La maximisation de l'amplitude peut alors être utilisée pour retrouver la vitesse effective du son. En outre, grâce aux propriétés d'ergodicité que nous supposons sur la distribution aléatoire des diffuseurs, nous montrons qu'un moyennage spatial permet de récupérer les propriétés statistiques pour un seul ensemble de mesures *c.-à-d.* une seule réalisation du milieu aléatoire que l'on cherche à imager. L'étude du chapitre 12 correspond à l'analyse mathématique des estimateurs introduits par Alexandre Aubry et son équipe [17]. Les résultats du chapitre 12 justifient donc mathématiquement les nombreux résultats des expériences menées par Alexandre Aubry et son équipe [17]. Dans le chapitre 13, nous réalisons des expériences numériques et retrouvons la vitesse effective du son dans les milieux simulés. Ces simulations numériques reproduisent l'expérience des ultrasons réalisée expérimentalement dans [17]. Les courbes affichées dans le chapitre 13 sont assez similaires aux courbes affichées dans [17, chapitre 6] qui sont calculées à partir de données expérimentales. Le modèle asymptotique que nous construisons dans cette thèse semble donc être en parfait accord avec les expériences pratiques d'échographie.

Contributions principales dans la thèse

Dans la partie II, nous établissons et prouvons un développement d'homogénéisation quantitative pour un problème de transmission de l'équation de Helmholtz. Plus précisément, nous prouvons un développement asymptotique du champ diffusé par un domaine bourné avec une micro-structure fortement oscillante, caractérisée par des coefficients constants par morceaux, domaine lui-même intégré dans l'espace libre. Nous prouvons non seulement une convergence d'ordre 1 en norme L^2 de la solution vers la solution homogénéisée et une convergence d'ordre $1/2$ en norme H^1 pour le développement à deux échelles, mais aussi une convergence d'ordre $(d+1)/2$ en norme L^2 en introduisant un nouveau terme de correction que nous construisons et étudions.

Le domaine, étant borné, rompt l'hypothèse traditionnelle de stationnarité utilisé pour l'homogénéisation stochastique. Cela introduit ce que l'on appelle une *couche limite* qui doit être quantifié pour obtenir le taux de convergence quantitatif de la Proposition 37 et de la Proposition 36. Son étude est difficile car les correcteurs de frontière satisfont un problème oscillant similaire au problème du champ initial, avec des termes sources fortement oscillants à l'interface entre l'espace libre et le milieu borné.
Nous représentons ensuite le terme d'erreur par une représentation intégrale qui peut être interprétée comme une représentation de Lippmann-Schwinger du champ diffusé. Le *commutateur d'homogénéisation stochastique* [18, 19] apparaît dans l'équation. Cette quantité a été introduite à l'origine pour étudier les fluctuations du développement à deux échelles. En utilisant des outils mathématiques similaires à ceux de [18, 19] (*e.g.* calcul de Malliavin, inégalité de Poincaré dans l'espace des probabilités), nous sommes capables d'améliorer le développpment à deux échelles dont l'erreur est d'ordre 1 dans la norme L^2 au développement d'ordre supérieur dont l'erreur est d'ordre $(d+1)/2$, comme démontré dans le chapitre 7.
Dans la partie III, nous nous concentrons ensuite sur l'analyse asymptotique de la migration de Kirchhoff dans le régime paraxial. Il s'agit d'un problème à trois échelles où la taille des hétérogénéités est petite devant la longueur d'onde, elle-même petite devant la taille du milieu. Le but de notre étude est de mettre en évidence les différences entre l'image affichée avec la vraie vitesse du milieu et celle affichée avec une autre vitesse de rétropropagation. En effet, le maximum d'amplitude sur l'image diminue. Nous retrouvons la forme typique de l'amplitude décroissante, qui est une fonction pic dont la largeur est théoriquement caractérisée.
Nous considérons ensuite le milieu aléatoire multi-échelle avec le développement asymptotique du Théorème 39. Nous montrons que la fonction d'imagerie en un point donné x est équivalente à la création d'un petit réflecteur virtuel. Nous explicitons la dépendance de la position du réflecteur virtuel par rapport à la vitesse de rétro-propagation. De plus, nous montrons que sur une distance de l'ordre de la longueur d'onde, la fonction d'imagerie est asymptotiquement un processus stationnaire et ergodique. Cela signifie que les moyennes locales de la fonction d'imagerie permettent de retrouver des propriétés statistiques. La moyenne spatiale locale de l'amplitude de l'image correspond à l'estimateur *incohérent* introduit par Alexandre Aubry [17] et nos résultats théoriques sont en accord avec les observations expérimentales. Alexandre Aubry a également introduit un estimateur *cohérent*. Cet estimateur est obtenu en considérant le premier vecteur singulier droit dans la décomposition de la matrice K où $K_{i,j}(x)$ est la fonction d'imagerie en un point x_i « proche » de x (à l'échelle de la longueur d'onde) pour la vitesse de rétropropagation c_j. De manière équivalente, cela correspond au premier vecteur propre de K^*K, K^* étant l'adjoint de K. Nous montrons que sa diagonale est en fait l'estimateur incohérent et nous justifions que son premier vecteur propre peut être utilisé pour retrouver la vitesse du son. Chaque résultat théorique est accompagné d'illustrations numériques. En particulier, nous simulons le problème multi-échelle du problème correspondant au tissus biologiques. Les solutions numériques sont ensuite utilisées pour calculer les estimateurs *incohérent*

et *cohérent*. Les graphiques des estimateurs sont comparés à la forme asymptotique théorique. Non seulement les illustrations numériques montrent une grande concordance avec les résultats théoriques, mais elles sont également très similaires aux estimateurs expérimentaux obtenu expérimentalement dans [17, chapitre 6].

CHAPTER 2

General introduction

The first ultrasound medical exams can be traced back to the end of the 1930s [1]. Since then, ultrasounds have managed to become one of the most known and common medical exams [2]. Ultrasounds present several advantages. The method is cheap, non-ionizing, the devices are now portable and even compatible with cell-phones [3].
Ultrasounds are notably used to monitor the growth and development of the fetus, image the heart, blood vessels, eyes, thyroid, brain, breast, abdominal organs, skin, and muscles [4]. The images can now be displayed not only in 2D but also in 3D and even in 4D, which corresponds to 3D movies [5].
The images are formed by exciting a piezoelectric transducer that emits ultrasound waves which are backscattered by the medium of interest. The ultrasound echoes are then recorded by the ultrasound transducer. The knowledge of the speed of sound inside the medium to be imaged allows, by using a delay-and-sum algorithm to reconstruct the position of echogenic structures. The delay-and-sum algorithm is also known as the Kirchhoff migration when computed in the frequency domain [6]. The ultrasound exam can also be seen as a time reversal experiment [7] where the measured echoes are numerically backpropagated at a given speed c_s.
With the progress in the engineering of sensors and the computational power, the resolution of the images keeps improving and quantitative ultrasound techniques have emerged. These techniques aim at obtaining quantitative information about the medium to image, such as the attenuation of the speed of sound inside the medium [8, 9, 10]. In particular, an estimation of the speed of sound inside the medium can be used as a biomarker to diagnose steatosis of the liver, or breast cancers [11, 12, 13, 14, 15, 16]. Furthermore, the accuracy of the speed of sound estimation drives the fidelity of the tomographic reconstruction. Indeed, when the backpropagation speed does not match the true speed of sound inside the medium, the image is blurred and distorted. To quantify the speed of sound in a medium, the imaging community has developed several types of techniques that are addressed in [8, 9, 10]. Alexandre Aubry and his collaborators developed a new method inspired from adaptative optics [17]. Physically, the imaging process consists in focusing a wave at a point x inside the medium to create a virtual reflector and listening the echoes from this reflector. However, due to the mismatch between the backpropagation speed of sound c_s and the actual speed of sound inside the medium c_0, the wave is not actually focused at

x but the depth of focusing changes. To take into account this effect, the idea of Aubry is then to focus a wave at depth $c_s t$ for a given time $t > 0$. By maximizing the returned echo amplitude from the depth $c_s t$ while changing the backpropation speed of sound c_s, we can recover the speed of sound c_0. The point $c_s t$ then acts as the virtual guide star at which we focus to revise the backpropagation speed of sound of the algorithm.
The mathematical modeling of these techniques and more generally of biological ultrasound experiments is a hard task. At first sight, the tissues can be modeled by homogeneous media but then only the interfaces are imaged. However, the image is in fact a speckle pattern. It is commonly accepted that the echoes backscattered by the tissue originate from the numerous scatterers inside this tissue which results in this speckle pattern on the image. The scatterers are unresolved. Indeed, their typical size if way below the resolution of the ultrasound imaging system (which characterizes the distinguishable details on the image). Furthermore, we do not have access to the spatial distribution of these scatterers. The tissues can then be modeled by random multi-scale media. In the context of Aubry's work, we aim to provide a mathematical and numerical framework for modeling and analyzing the modern quantitative ultrasound methods. We introduce a new model for the acoustic properties of soft tissues: a multi-scale random composite media.

In the first Part I of the manuscript, we give a brief overview of the current state of ultrasound imaging. This motivates us to derive a new model that is established in Section 3.3.1 and that will be studied throughout the entire manuscript. In Part II, we study the backscattering of random multi-scale media. More precisely, we study the backscattering of a random composite medium embedded in the free space with the aim to obtain a simple form of the backscattered field. Mathematically, we study the divergence form Helmholtz equation with highly oscillating random coefficients. We perform an asymptotic study by using quantitative stochastic homogenization techniques and derive a high-order expansion in Theorem 39.
In a third Part III, we use this asymptotic to justify the estimators of the effective speed of sound inside the biological tissue introduced by Aubry. We study the Kirchhoff migration with respect to the backpropagation speed in the paraxial regime for two situations. First, the simple case of imaging an isolated small target (with respect to the wavelength) in a homogeneous medium with the aim to recover the propagation speed inside the latter. Second, we study the imaging of random composite medium introduced in Part I with the asymptotic expansion derived in Part II.

Detailed content of the manuscript

The manuscript is organized as follows.

In Part I, we address the scientific context of this thesis. In Chapter 3, we review a brief history of the ultrasound imaging techniques. With the improvements both in the imaging devices and in the theoretical comprehension of the wave scattering, the limi-

tations of the ultrasound imaging techniques can be quantified and overcome. The goal is now to obtain quantitative estimations of the physical parameters of the tissues from the ultrasound measurements. This is explained in Section 3.2. Nevertheless, to obtain any quantitative estimation, it is required to have a quantitative model which links the properties of the medium and the measurements. The measurements are modeled by the scattered field solution of a divergence form Helmholtz equation with varying acoustic properties. The derivation of quantitative estimators then requires to mathematically understand the properties of the scattering solution. As mentioned above, the propagation of ultrasounds in biological tissues is a multi-scale problem by nature. Mathematically, it exists several models for the scattering of media which are discussed in Section 3.3.3. These models, although reasonable for modeling biological tissues, do not capture the effects of the micro-structure on the macroscopic properties of the tissues. This explains the development of the new model introduced in Section 3.3.1. We decide to model the position of the unresolved heterogeneities by a random process.
To study this model, we decide to use stochastic homogenization techniques. Indeed, as explained in Chapter 4, the mathematical discipline of homogenization is being develop to study multi-scale problems and understand their macroscopic properties. Under ergodic and stationary hypotheses discussed in Section 4.3 on the random physical properties of the medium, it is possible to approximate the scattering by the complex random multi-scale medium by a medium with homogeneous properties.
The aim of quantitative homogenization is then to quantify the error between the solution computed with the effective properties and the solution computed in the initial medium. The field of stochastic quantitative homogenization has known important breakthroughs in the 2010s that we present in Section 4.4. We use these recent results to carry out the study our random multi-scale problem. Unfortunately, the scattering problem obtained by applying the usual stochastic homogenization to our model is not satisfying. Indeed, by replacing the random multi-scale medium by a simpler homogeneous one, we lose the random nature of the scattered field, and the resulting image does not look like the speckle pattern of traditional images. That is why, we develop a high-order homogenization expansion of Part II. More precisely, we go beyond the effective solution given by the homogenization theory and also build a corrective term. This corrective term will contain the micro-scale effects that we seek for. We also quantify the error between the initial solution and the built approximation. Therefore, we first establish the quantitative two-scale asymptotic expansion in Proposition 37 which is followed by the higher-order expansion of Theorem 39. Furthermore, to illustrate these two results, we perform numerical experiments in Chapter 8. The displayed results are in accordance with the results of Proposition 36 and with the higher-order expansion of Theorem 39.
The simple form of the backscattered field obtained in Theorem 39 is then our ground model for the analysis of the estimators of the effective (homogenized) speed of sound introduced by Aubry. We perform an asymptotic analysis of the Kirchhoff migration in Part III. Before working on complex tissue mimicking medium, we start with a simple asymptotic analysis for the Kirchhoff migration of a point-like scattered in a homoge-

neous medium. In particular, we study the dependency on the backpropagation speed of sound of the algorithm in the paraxial regime. This regime is described in Chapter 10. We show in Theorem 54 that the point on the image at the center of the focal spot depends on the backpropagation speed of sound, and that the displayed amplitude on the image decreases with the error in the backpropagation speed of sound. Therefore, by looking for the overall maximum of amplitude of the imaging function, we can recover the speed of sound of the background medium. In biological tissue, there is no isolated target to focus on and the maximum of amplitude on the image can rarely be used as a criteria to quantify the effective speed of sound. In Chapter 12, we pursue the analysis of the Kirchhoff migration with the expression of the scattered field obtained in Theorem 39. We prove that in the paraxial regime, imaging at a depth z with backpropagation speed c is similar to creating a virtual reflector at $z\frac{c_0}{c}$ with c_0 being the effective speed of sound. In particular, this justifies the idea of Aubry to focus at ct for a given t. Indeed, by doing so, one always focuses at $c_0 t$ which does not depend on c and is our virtual guide star. The maximization of the amplitude can then be used to recover the effective speed of sound. Furthermore by the ergodicity properties that we assume on the random distribution of the scatterers, we show that a spatial averaging allows to recover statistical properties for only one set of measurements *i.e.* one realization of the random medium. The study of Chapter 12 corresponds to the mathematical analysis of the estimators introduced by Alexandre Aubry and his team [17]. The results of Chapter 12 thus mathematically justify the many results of the experiments carried out by Alexandre Aubry and his team [17]. In Chapter 13, we perform numerical experiments and recover the effective speed of sound of simulated media. These numerical simulations mimic the ultrasound experiment done in [17]. The displayed curves of Chapter 13 are quite similar to the curves displayed in [17, Chapter 6] which are computed from experimental data. The asymptotic model that we build in this thesis thus appears to be in great agreement with practical ultrasound experiments.

Main contributions

In Part II, we establish and prove a quantitative homogenization expansion for a transmission problem for the Helmholtz equation. More precisely, we prove an asymptotic expansion of the scattering solution of a bounded domain with highly oscillating micro-structure characterized by piecewise constant coefficients embedded in the free space. We not only prove an order 1 L^2-convergence of the solution towards the homogenized solution and an order $1/2$, H^1-convergence for the two-scale problem, but also an order $(d+1)/2$, L^2-convergence by introducing a new correction term that we build.
The boundness of the domain causes the traditional stationarity assumption of stochastic homogenization to break at the edge of the domain. This introduces so-called *boundary layers* which must be quantified to obtain the quantitative rate of convergence of Proposition 37 and Proposition 36. Its study is challenging as the boundary correc-

tors satisfies a oscillating problem similar to the initial problem, with highly oscillating source terms at the interface between the free space and the bounded medium.
We then represent the error term with an integral representation which can be interpreted as a Lippmann-Schwinger representation of the scattered field. The so-called *commutator* of stochastic homogenization [18, 19] appears in the equation. This quantity is originally introduced to study the fluctuations of the two-scale expansion. By using similar mathematical tools as those of [18, 19] (*e.g.* Malliavin's calculus, Poincaré inequalities in the probability space...), we are able to upgrade the two-scale expansion whose error is of order 1 in the L^2-norm to the higher expansion whose error is of order $(d+1)/2$, as proven in Chapter 7.
In the Part III, we then focus on the asymptotic analysis of the Kirchhoff migration in the paraxial regime. This is a three scale problem where the size of the heterogeneities is small in front of the wavelength, itself small in front of size of the medium. The goal of our study is to highlight the differences between the image displayed with the true speed of the medium and the one displayed with another backpropagation speed. In fact, the maximum of amplitude on the image decreases. We recover the typical shape of the decaying amplitude, which is a peak function whose width is theoretically characterized.
We then consider the random multi-scale medium with the asymptotic expansion of Theorem 39. We show that the imaging function at a given point x is equivalent to the creation of a small virtual reflector. We explicit the dependency on backpropagation speed of the position of the virtual reflector. Furthermore, we show that at the order of the wavelength, the imaging function is asymptotically a stationary and ergodic process. This means that local averages of the imaging function allows to recover statistical properties. The local spatial average of the image amplitude corresponds to the *incoherent* estimator introduced by Alexandre Aubry [17] and our theoretical results are in accordance with the experimental observations. Alexandre Aubry also introduced a *coherent* estimator. This estimator is obtained by considering the first right singular vector in the decomposition of the matrix K where $K_{i,j}(x)$ is the imaging function at a point x_i "close" to x (at the scale of the wavelength) for the backpropagation sped c_j. Equivalently, this corresponds to the first eigenvector of K^*K with K^* the adjoint of K. We show that its diagonal is actually the incoherent estimator and we justify that its first eigenvector can be used to recover the speed of sound. Each theoretical result is accompanied with numerical illustrations. In particular, we simulate the multi-scale problem of the tissue mimicking problem. The numerical solutions are then used to compute the *incoherent* and *coherent* estimators. The plots of the estimators are compared with the theoretical asymptotic form. Not only do our numerical illustrations show great agreement with our theoretical results, but they are also quite similar to the experimental estimators of [17, Chapter 6].

Contents

PART I

SCIENTIFIC CONTEXT

CHAPTER 3

Medical ultrasound imaging

3.1 A brief history

3.1.1 Before medical imaging

The beginning of the studies on the use of ultrasounds for imaging is closely related to the discovery of the piezoelectric effect. Piezoelectricity is the reversible property exhibited by certain materials whereby they accumulate electric charges in response to mechanical stress. The piezoelectric effect was first observed by the Curie brothers, Pierre and Jacques, in 1880 [20]. The first significant application of piezoelectricity can be traced back to the First World War [21]. The French physicist Paul Langevin [22] and his colleagues developed the first sonar system of the history, to detect German submarines. A transducer comprising a thin quartz crystal (a piezoelectric material) is carefully glued between two steel plates, thereby emitting a sound wave that propagates in the ocean. The wave is scattered by the submarines and the resulting echoes are measured by a hydrophone, which is a piezoelectric transducer that converts pressure waves into an electric signal. By measuring the time required for the echo to be recorded, it is possible to calculate the distance to the submarines [23].
During the interwar decades, experimentalists conducted research into the physical, chemical and biological effects of the exposure to high-intensity ultrasonic waves. In 1918, Langevin realized that he could kill a fish placed under the beam of an ultrasonic wave, and that a painful sensation could be felt when plunging the hand in this region. It was concluded in the late 1930s that high-intensity ultrasounds could be used in the therapy of cancers [24]. The German physicist Reimar Pohlman rejected this idea and investigated instead the use of ultrasounds at low intensity to stimulate healing [25]. The first clinical trials for ultrasound therapy were carried out in Berlin in 1938 (see Figure 3.1).

As well as for therapy, numerous attempts were made to utilize ultrasounds for medical diagnosis. However, it was not until the end of the 1950s that ultrasounds were established as a revolutionary diagnostic tool for medical imaging. We refer to the review [24, 26] and the references within for a comprehensive picture of the history of ultrasounds for medical imaging.

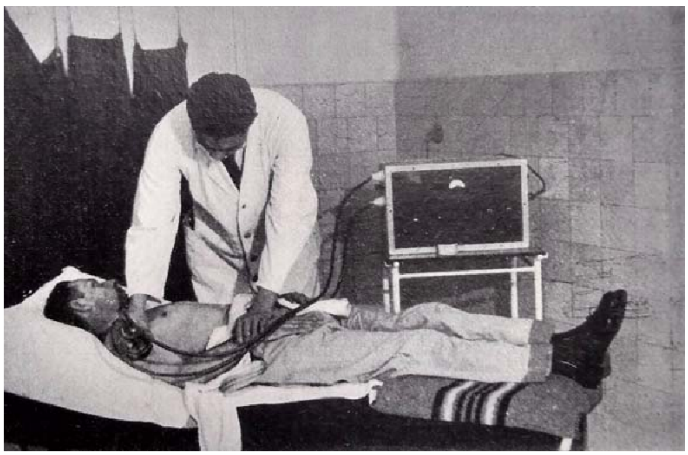

Figure 3.1: First clinical ultrasound therapy at Martin Luther Hospital in Berlin (1938). Figure reproduced from [1]

3.1.2 A-mode and M-mode scanners

In the 1960s, ultrasounds were widely used to compute images which were produced by simple instruments called A-scanners. An A-scanner consists in a single transducer that insonifies the medium with a short ultrasound pulse, and then switches to echo mode to listen to the echo [27]. The raw recorded signal corresponds to an amplitude $A(t)$ recorded over time t and is then transformed into a $1D$ image of the amplitude displayed over position x, via the simple relation $x = ct$, where c is the propagation speed inside the medium. However, the desire to display $2D$ (or $3D$) images and the presence of heterogeneities throughout biological tissues rapidly led to the rejection of the use of A-scans for ultrasound imaging, in favor of B-scans (see Section 3.1.3). A-scanners can still be used for motion imaging, designated as M-mode. The origin of M-mode can be traced back to the 1950s and is credited to Carl Helmuth Hertz and Inge Edler [28]. During an exam to assess mitral stenosis (a disease of the heart) by using A-scans, they remarked that from one acquisition to another, the position of the membrane of the heart on the image changed in accordance with the motion of the heart, allowing to image this motion. This marked the birth of echocardiography. As the ultrasound wave propagates in the tissues at approximately the speed of sound in water (1540 m.s^{-1}), "slower" movements such as the motion of the heart or the blood flow can be detected and imaged (see Figure 3.2).

3.1.3 B-mode scanners

The rapid evolution of transducers and signal processing technologies led to the improvement of A-scanners to B-scanners in the 1970s. Although the A-scans consist in plotting the recording amplitude of signal over depth, the B-scans consist in using

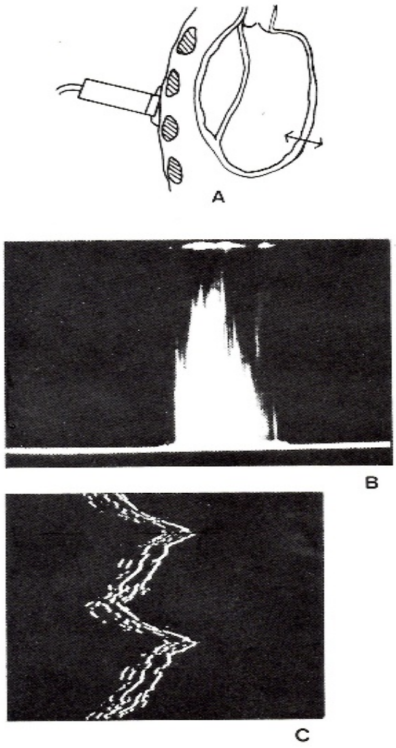

Figure 3.2: Principle of M-scanning. (a) Transducer directed at moving structure of interest and held fixed, (b) echoes may be observed on an A-scan display but this does not give a record of motion, (c) echo dots sweep up the screen to provide a trace of position versus time. Figure reproduced from [27]

several A-scanners to produce a $1D$-swept image *i.e.* a $2D$ image. In practice, to enhance the signal-to-noise ratio, to compute the local reflectivity, that is the variation of acoustic properties at x, the A-scanners are combined to produce a wave that focuses on x at $t = t_0$. This can be done by knowing the speed of sound c inside the medium. The backscattered signals are measured by the ultrasound transducers and are summed with the right delays [29]. More precisely, the signal originated from x will be heard at $t(z) = t_0 + \frac{|z-x|}{c}$ for the transducer at z. The image $I(x)$ at x is then computed with

$$I(x) := \sum_{k=0}^{N} u_k \left(t_0 + \frac{|z_k - x|}{c} \right)$$

where N is the number of transducers, u_k is the signal recorded by the k-th transducer and z_k is the position of the k-th transducer. Thanks to the fast propagation of the ultrasound waves in water, it is possible with this technique to image the medium in real time with 20 to 100 images per seconds [29].
Further tests have also shown that the air at the interface between transducer and tissues must be excluded for the waves to propagate (and not to be absorbed by the air). This explains the continued usage of oil or gel [27].

3.2 Ultrasound imaging nowadays

Since the discovery of the piezoelectric effect by the Curie brothers, ultrasounds are now among the most used techniques in medical imaging. The advancements in both the ultrasound transducers manufacturing and the signal processing techniques have enabled the computation of 3D or even 4D ultrasound images (movies) [30].

3.2.1 Clinical use of ultrasound imaging

From January 2023 to January 2024, more than 20% of the imaging exams in England were ultrasound exams [2]. They present the advantage of being non-invasive, non-ionising, real time and cheap exams [31].

When thinking of ultrasound imaging, obstetrics application is the first thing that comes to mind. But sonography (also named ultrasonography) is used to image many other organs as well. Ultrasounds can be used for [32]:

- Obstetric ultrasound - to view the fetus in the womb.
- Abdominal ultrasound - to image the organs of the abdomen. It is also used to detect and monitor breast cancer [33].
- Vascular ultrasound - to view the blood vessels, which is know as Doppler ultrasonography.

- Echocardiography - to view the heart (it also includes the fetal heart).
- Pelvic sonogram - to view the organs of the pelvic region.
- Neurosonography - to view the brain (it also includes the fetal brain).
- Ophthalmology - A-scans provide the length of the eye, while B-scans produce a cross-sectional view of the eye and the orbit [34].
- Dermatology - to measure the skin thickness.

We also mention that ultrasounds can be used to clean teeth in dental hygiene or to remove cysts or tumors by focalizing heat on them, and have many other therapeutic applications which are not detailed here but can be found in [31, 32].
For superficial organs such as muscles, tendons, the breasts and the neonatal brain, the transducers emit waves at 7 to 18 MHz [32]. However, as the absorption of the waves is linked to the emission frequency, for deeper organs such as the liver or the kidney, the frequency is reduced to 1 to 6 MHz. Note that the frequency typically drives the axial and lateral resolutions [32].

3.2.2 Plane wave and matrix imaging

The huge improvements of ultrasound metrology have led to the development of new generation of ultrasound probes. With the newer devices, one has a series of N independent programmable transducers. One or several transducers can insonify the medium with a pulse. All (or a part of) the transducers switch to the echo mode to listen to the echoes. Each of them then measures a time series corresponding to the wavefield backscattered by the medium. The physical effects behind the scattering of biological tissues can be modeled by the linear law of acoustics [35]. The linearity of the phenomenon can be exploited, and in particular the data can be recombined in post-processing. Indeed, the signals are not analogically monitored anymore, but the signal from each transducer is now numerically stored and can be post-processed after the data acquisition. This allows more flexibility in the signal processing and in particular, to consider more complex speed of sound maps $c(x)$ in the computation of the image.

Ultrafast ultrasound imaging

For historical reasons, the ultrasound images are computed by a sum-and-delay algorithm applied to the signal recorded by a set of ultrasound transducers, which have previously sent a short pulse that focalizes at each and every point of the medium. This corresponds to the pulse-echo mode. However, as the physical phenomena at stake are mainly linear, in the end of the 1980s, it was envisaged to utilize the linearity, and insonify the medium all at once. The signals recorded by each transducer are then

numerically and linearly recombined to generate the response of a focalized wave. This idea comes from optics and is comprehensively described in [36] to which we refer for more details on ultrafast imaging.
The medium can be insonified with *e.g.* plane waves:

$$p^i_\theta(\omega, x) = \exp\left(i\frac{\omega}{c}\theta \cdot x\right)$$

for $\theta \in \mathbb{S}^{d-1}$ a direction on the sphere, and $x \in \mathbb{R}^d$ and c is the speed of sound inside water.
The whole medium is insonified at once with a series of N_θ plane waves $(p^i_{\theta_j}(\omega, \cdot))_{j=1...N_\theta}$ (see Figure 3.4). For a given plane wave θ_j, the response $S_{j,k}$ is measured by all N transducers, placed at x_k, $k = 1...N$. This response is designated as the scattering matrix. The matrix S encodes all the properties of the medium and is called the transmission matrix when the scattered field is measured by transducers positioned on the other side of the medium, or the reflection matrix when it is measured by the transducers that insonified the medium (this is typically the configuration of imaging). By using unfocused (plane) waves, it is now possible to produce 350 images per second, when it was only possible to produce 25 images per second with focused waves [36].
Note that spherical waves can also be used instead of plane waves, but plane waves are preferred due to the signal-to noise-ratio. Indeed, while spherical waves are emitted with one transducer, several transducers need to emit all at once to produce a plane wave. Then, more energy is sent into the medium and the signal-to-noise ratio is enhanced.

Time-reversal and DORT

Historically, this matrix approach was developped in the 1990s via the iterative time-reversal procedure [7] which consists in iteratively reemitting "in reverse" the time measurements. When the medium is composed of a single scatterer, it was shown that the process converges towards the wavefront that perfectly focuses on that scatterer when it is reemitted in the medium [37]. A further analysis of the scattering matrix has shown that for a medium with M isolated scatterers (with different contrasts), the matrix S is of rank M and has M singular values when all the scatterers behave like monopoles. The i-th singular vector is the wavefront that focuses on the i-th brightest scatterer. This is the basis of the DORT method (French acronym for *Décomposition de l'opérateur de retournement temporel*, which stands for decomposition of the time reversal operator) which was introduced during the Ph.D. of Claire Prada [37, 38, 39].
These works by Mathias Fink and Claire Prada inspired many works in aberration correction [40, 41, 42, 43], target detection in a heterogeneous medium [44], flaw detection in non-destructive testing and many more.

Matrix imaging

As previously stated, the medium is now insonified in its entirety with unfocused plane (or spherical) waves and the acquired data are stored numerically. As an input data set, one then has access to the numerical matrix $R(t) \in \mathbb{R}^{M\times N}$, where $R_{j,k}(t)$ is the time series of the j-th emitted plane wave, measured by the k-th transducer (see Figure 3.3). This acquisition operation is known as the full matrix capture (FMC) [45]. The matrix $R(t)$ can then be numerically post-processed. Intuitively, even if no focalized wave sent at x, it would be possible to recover the local reflectivity at x with a linear combination of the (unfocalized) plane waves. This idea drives the concept of matrix imaging and ultrafast imaging [36]. By knowing the speed of sound $c > 0$ within the medium, it is possible to transform the time series into an image of the local reflectivity. If a plane wave is sent at angle θ_i and measured at x_j by the j-th transducer, the echo measured at t and the echoes coming from the point y can be measured at

$$t = \frac{\theta_i \cdot y + |y - x_j|}{c}.$$

By summing over all the time series, meaning over all the M emission waves and the received echoes by the N transducers, the ultrasound image is computed. The image $\mathcal{I}$ at a point y is then defined by

$$\mathcal{I}(y) := \sum_{i=1}^{M}\sum_{j=1}^{N} R_{i,j}\left(\frac{\theta_i \cdot y + |y - x_j|}{c}\right). \tag{3.1}$$

Usually, c is taken to be constant at the speed of sound in water, but as the matrix R is numerically stored it is possible to adjust the speed of sound in the imaging algorithm or even consider more complex backpropagation speed of sound maps.
By a Fourier transform, the imaging process can be rewritten as

$$\mathcal{I}(y) := \int_{\mathcal{B}} \Psi(y,\omega)^T \overline{\hat{R}(\omega)} \Phi(y,\omega) d\omega, \tag{3.2}$$

where $\Phi(\cdot,\omega) \in \mathbb{C}^N$ is the vector

$$\Phi_j(y,\omega) := \exp\left(i\omega\frac{|x_j - y|}{c}\right),$$

$\Psi(\cdot,\omega) \in \mathbb{C}^{N_\theta}$ is the vector

$$\Psi_j(y,\omega) := \exp\left(i\frac{\omega}{c}\theta \cdot y\right),$$

Ψ^T is the transpose of Ψ, and $\hat{R}$ is the Fourier transform of R. The properties of the matrix have been extensively studied by the research group of Alexandre Aubry [46, 47, 48] and the group of Claire Prada [49, 50, 51] at Institut Langevin.

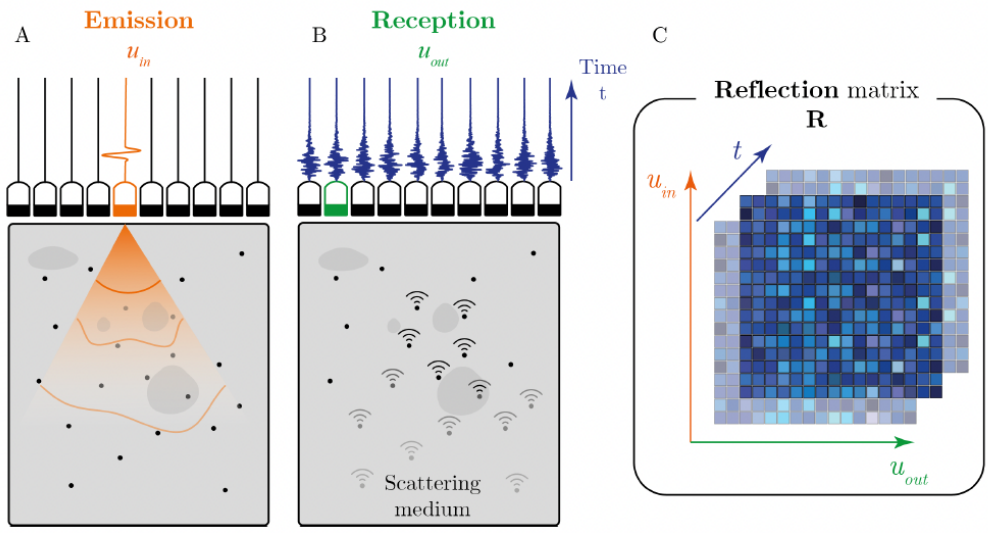

Figure 3.3: The reflection matrix acquired in ultrafast ultrasound imaging. The impulse responses are recorded between each emitter at the input and each receiver at the output, both located on the same side of the medium. All this wealth of information is stored in the so-called reflection matrix, denoted R. Figure reproduced from [17]

3.2.3 A priori assumptions

Ultrasound images are displayed as structural representations of the medium under investigation. However, in order to accurately represent the medium, the processes of propagation and of scattering of the ultrasound wave must fulfill several key hypotheses which are described here. When one of the several assumption breaks, so-called aberrations can arise on the image. Furthermore, due to physical limitations such as *e.g.* the finite bandwidth and finite size of the transducer, it is not possible to distinguish on the image the presence of two close scatterers. The measurement of "how close" they must be to be distinguished is called the resolution of the image and can also be characterized.

Known propagation speed

The image at x corresponds to the local reflectivity of the medium at x. This image is computed from time measurements. One must translate the acquired time signal into a map of the reflectivity of the medium. In particular, one needs to know the speed of sound within the medium. However, in clinical situations the speed of sound can range from 1400 m.s^{-1} in fat tissues up to 1650 m.s^{-1} in the skin or muscles [52]. Images are usually computed by assuming the speed of sound in water (1540 m.s^{-1}). Errors on the speed of sound have some effects which are the topic of Section 3.2.5.

Single scattering

Even if the speed of sound c is actually known, one assesses that the strength of the echoes measured at time $t > 0$ can be matched to the reflectivity of the medium at the position x on the image via the space-map correspondence induced by the speed of sound map. However, this correspondence is valid only when the medium is in the single scattering regime. Indeed, when multiple scattering is no more negligible, the echoes measured at time t can no longer be associated with the isochrone curves of the speed of sound map. Intuitively, the number of possible paths increases when $|x|$ grows, which also explains why the images deteriorate at greater depth. In [53], Alexandre Aubry and Arnaud Derode established that the ratio of multiple scattering over the single scattering effect in *in-vivo* breast imaging reaches 50% at 50 μs. Quantifying multiple scattering is a challenging task and is discussed in Section 3.3.3.

Motionless media and frame rate limitations

The images are computed by assuming that the medium is immobile from the start to the end of the data acquisition. This assumption is even more crucial with the newer techniques of matrix imaging (see Section 3.2.2), as the data of several incident waves are combined together.

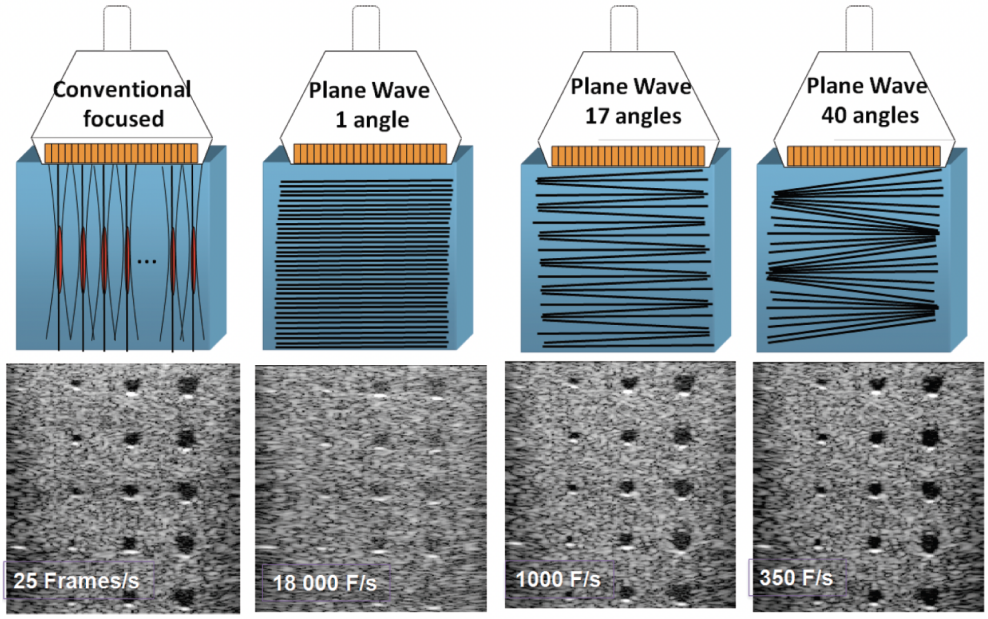

Figure 3.4: Conventional focused and ultrafast ultrasound imaging sequences for a typical medical imaging setup (4-cm deep region of interest): (a) conventional focused imaging (128 focused beams and 4 focal depths leading to 25 fps), (b) plane-wave imaging (18 000 fps), (c) plane-wave compounding with 17 angles (1000 fps), and (d) plane-wave compounding with 40 angles (350 fps). Figure reproduced from [36]

Ultrasound imaging is a real-time imaging method. However, the insonification process is not instantaneous. Indeed, to image at depth $z > 0$, one must wait for the echoes originated from z to return to the transducer array *i.e.* to wait for $T = 2\frac{z}{c}$ s. Therefore, if one wants to image of N pixels, it takes a total of NT s, which limits the frame rate of the imaging system to $f_r = \frac{1}{NT}$ Hz. Typically, $N = 300$, $z = 10$ cm and $f_r = 25$ Hz [29]. With the techniques of ultrasfast imaging, it takes only a few waves to illuminate the entire medium and image the latter. The frame rate goes up to 1000 Hz [36] (see Figure 3.4).

Image resolution:

The resolution of an imaging system intuitively corresponds to "how detailed" the image is. It is characterized by the point spread function (PSF). The point spread function is the image of a point-like object. This image is a spot called the focal spot (see Figure 3.5). The knowledge of the typical size of the focal spot allows to characterize the expected details on the image, and the minimal distance needed between two reflectors to distinguish one from the other. The typical expected resolution, when the

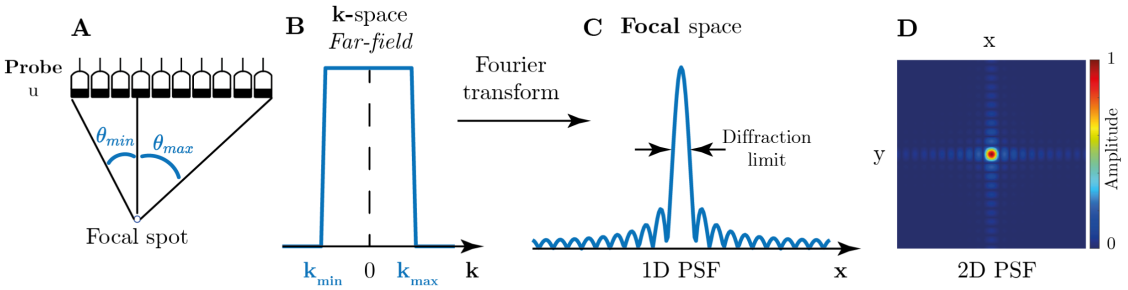

Figure 3.5: Numerical aperture and Point Spread Function (PSF). (A) The aperture of an imaging system defines the maximum angle of insonification that reaches the targeted focal point. (B) Flat aperture function in k-space. This space can be considered as a plane wave basis or a far-field basis. (C) The Fourier transform of the aperture function defines the Point Spread Function of the system, which determines the transverse resolution of the imaging system. In other words, it defines the limit of the system for distinguishing two points. (D) Point Spread function in 3D imaging. Figure reproduced from [17].

aforementioned hypotheses are satisfied, is [54, 55]:

- $\Delta z = \frac{c}{2B}$ where B is the bandwidth of the transducer, in the axial direction. B corresponds to the inverse of the typical time duration of the incident emitted signal.
- The transverse resolution depends on many parameters, and especially on the depth z at which the image is computed. Typically, one can expect a transverse resolution of $\Delta x(z) = \frac{zc}{af_0}$ where a is the size of the array and f_0 the central frequency of the transducer [55]. The most common method of defining the transverse resolution is the Rayleigh criterion, *i.e.* the full Width at half maximum of the point spread function in the transverse direction.

Note that this resolution corresponds to the expected resolution when c is the actual speed of sound inside the medium. When it exists a mismatch between the backpropagation speed and the actual speed c, the size and shape of the focal spot are altered. This phenomenon is mathematically investigated in Chapter 11.

3.2.4 Other ultrasounds based imaging methods

Ultrasounds are a powerful tool to image deep organs thanks to their penetration depth. However, as the acoustic properties of soft tissues are close to those of water (see Table 3.1), the images are not very contrasted. For example imaging blood vessels

Tissue/Material	Speed of sound (m.s^{-1})	Density
Breast	1510	1020
Healthy liver	1575–1600	1050
Diseased liver	1525	$\lesssim 1050$

Table 3.1: Ultrasound properties of various human tissues and materials. Values are extracted from [52, 57]

or distinguish certain types of malign carcinoma from kysts can be difficult. On the other hand, other physical parameters like absorption of shear modulus can vary significantly. For example, a palpable nodule has a shear modulus ranging from 10^5 to 10^7 Pa while a the glandular tissue of breast has a shear modulus ranging from 10^3 to 10^4 Pa [56]. Using multi-physics coupling such as for instance the thermo-elastic effect, hybrid techniques have been developed to image quantities related to those parameters. Before using sophisticated multi-waves physics, a first idea to increase the range of clinical applications is to assess the movement inside the tissues to estimate blood flow. The most common ultrasounds based movement imaging technique is the Doppler exam.

Imaging movement

Doppler effect: When the source of the sound wave is moving relative to an observer, the frequency of the wave changes. This is known as the Doppler effect.
This effect can be witnessed in the frequency shift of the field sccatered by moving scatterers relative to the incident field. Measuring the frequency shift enables then to measure the speed of the blood inside the cells with the aim to image the blood cells. However, due to the low sensitivity of ultrasounds, it was not possible to follow in real-time the blood flow in small capillaries with the conventional techniques. This is now possible thanks to the ultrasfast imaging techniques [58] (see Figure 3.6). We refer to [58] for more information about functional imaging using the Doppler effect.

Ultrasound elastography: Diseased tissues and healthy tissues show similar acoustic response [56], but the stiffness of the diseased tissue varies, which explains why physicians process to palpation. Elastography typically consists in reproducing this exam and obtaining quantitative information about the stiffness *i.e.* the Young's modulus E of the tissue. Furthermore, as palpation only gives insight about the superficial stiffness of the tissues, elastography can also give information about the stiffness of deep organs [59]. Typically two methods exists:

- **Quasi-static method:** a constant stress σ is applied to the tissues. This generate a displacement and a strain ϵ. The measurement of the strain is done by cross-correlating the B-mode images before, and during the application of the stress. The Young's modulus E can then estimated by Hooke's law: $\sigma = E\epsilon$. This requires to have a precise knowledge of the applied stress which is not the case in

practice [60]. But this still gives qualitative information about the local stiffness. When the stress is applied as an external force from the operator, this only gives information about the superficial organs such as the breast or the thyroid [59] but it is more challenging to assess elasticity of deeper organs such as the liver [61]. To compensate for these issues, the internal physiologic motion such as cardiovascular, respiratory motion can be used as the stress, while the ultrasound probe is held steady. This allows to access to the strain of deeper organs [60].

- **Dynamic method:** when applying a time-varying mechanical force (which can be a transient force or an oscillatory force at fixed frequency), not only a compression wave is generated (which is used for the B-mode images) but a shear-wave also propagates. However, due to attenuation, only the low frequency shear-waves (10-2000 Hz) propagate [60]. By imaging the medium using ultrasounds (ultrasonic pressure waves) whose speed of propagation is several orders of magnitude larger than the one of shear-waves, it is possible to follow the propagation of the shear-waves. The speed of the shear waves V_s is related with the shear modulus of the medium μ via the relation $\mu = \rho V_s$ (with ρ the density which is usually assumed to be the one of water). Tissues are almost incompressible which allows to compute the Young's modulus via the relation $E = 3\mu$ [60].

We refer to the two reviews [60, 62] for more technical details and for more information about the clinical applications ultrasound elastography.

Photoacoustic imaging

Other physical effects such as the photoacoustic can also be used to obtain an enhanced contrast on the ultrasound images (see Figure 3.6).
Electromagnetic waves are sent within the tissues of interest. These waves are absorbed by soft tissues, heating them. Due to the thermo-elastic effect, a compression wave is emitted - this is the photoacoustic effect. The emitted acoustic wave is measured by the ultrasound transducers. By tracking down the sources of the signal, its is possible to image the electromagnetic absorption properties of the tissues [63]. In particular, the light-absorption of hemoglobin is way higher than the surrounding proteins, and thus photoacoustic techniques allows to image the blood vessels. It is also possible to use exogenous contrast agents to enhance the quality of the image [64]. We refer to the two reviews [63, 64] for more details about photoacoustic imaging.

Ultrasound localized microscopy (ULM)

Another way of increasing contrast to image blood vessels is to use microbubbles contrast agent [65, 66]. Indeed, gas microbubbles in a liquid exhibit resonances in the ultrasound range, known as Minnaert resonances. They then behave like a highly contrasted point-like scatterer for ultrasound waves.
Inspired by the methods developed in optics to localize single emitters with a precision order of magnitudes below the usual Rayleigh criterion such as PALM-STORM

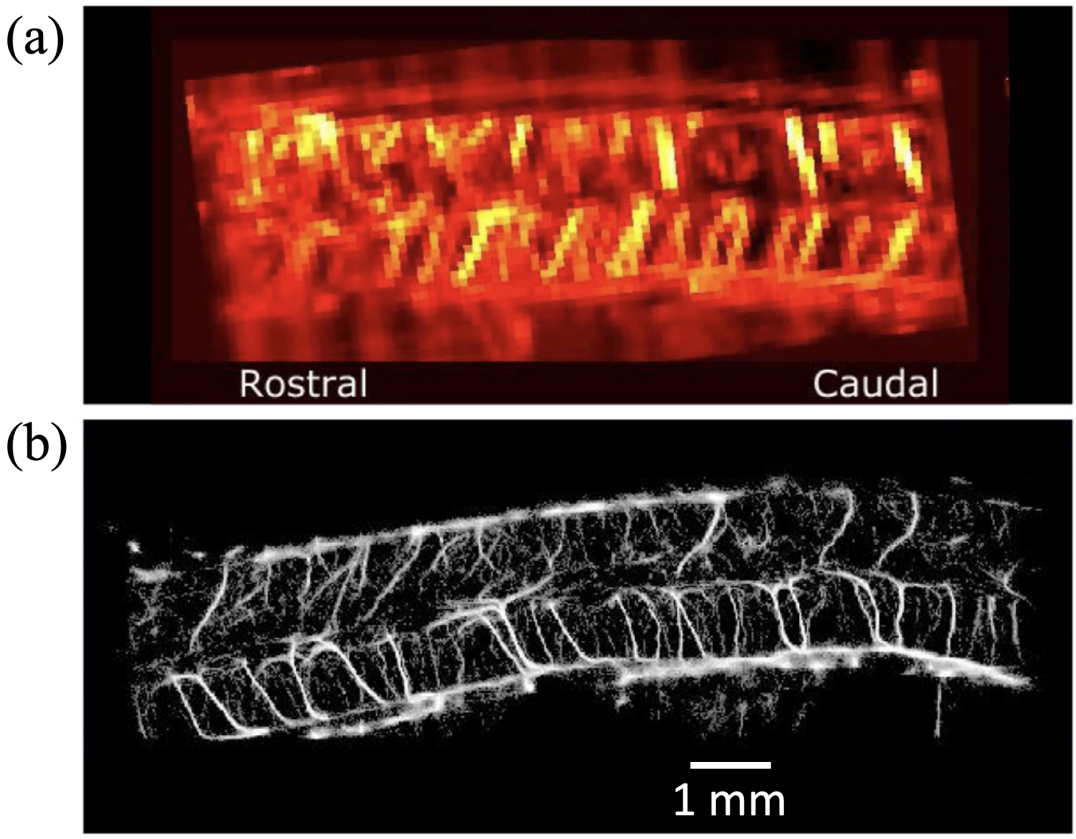

Figure 3.6: Amplitude image using Ultrafast Doppler Imaging of the intact spine of a rat (a) and Ultrasound Localization Microscopy (b) in the same animal. Scale bar 1 mm for both images. Figure reproduced from [72]

[67, 68, 69], Olivier Couture and his team developed a technique called ultrasound localized microscopy (ULM) [70]. By localizing each microbubbles at the center of the point spread function over time, Olivier Couture is able to produce super-resolved images of blood vessels (see Figure 3.6). Moreover, by tracking the motion of each bubble, it is also possible to map the blood motion flow with a similar resolution.
This constitutes a major breakthrough in imaging as it is now possible to image the blood vessels with resolution close to those of optics, but with the penetration depth of the ultrasounds. These techniques are now being applied pre-clinically and clinically for the imaging of the microvasculature of the brain, kidney, skin, tumors and lymph nodes [71].
We refer to [71, 72, 66] for more information about ultrasound localized microscopy and also mention the work of Siepmann Monica and her team [73] whose tremendous results are obtained in parallel of those of Olivier Couture and his.

3.2.5 Quantitative ultrasound and speed of sound mapping

The stupendous results of the functional imaging could only be achieved thanks to joint improvements in the transducers manufacturing, the data management and the scattering theory. The digitalization of acquisition data has also opened the doors to quantitative ultrasound (QUS) imaging techniques.

Quantitative ultrasound

The goal is no longer only to obtain a high fidelity structural image, but is also to obtain quantitative assessments of the properties of the tissues [8] (see Figure 3.7). Quantitative ultrasound is a field that has been active for more than 50 years [8] and was originally described as Ultrasound tissue characterization [74]. This vast topic is covered in [75] and we also refer to the reviews [10] and [8].
For soft tissues, three parameters are often investigated: the speed of sound, the attenuation coefficient and the backscattering coefficient of the tissue [8].

Speed of sound estimation

The variation of speed of sound within the tissues can be used as a biomarker changing in accordance with the pathological state of the tissue [76] and can thus be used for the diagnosis *e.g.* of hepatic steatosis [77, 78, 79]. Furthermore, we recall that classical imaging algorithm rely on the assumption that the speed of sound throughout the medium is constant and known. Local variations induce aberrations and mislocalization on the image. Moreover an error on the backpropagationspeed of sound in the algorithm affects the quality of focusing in the medium therefore deteriorating the signal-to-noise ratio. The estimation of the speed of sound was originally developed to improve images quality [80, 81, 82, 83].
Among the techniques that have been developed for the speed of sound assessment, one can consider the *focusing methods* which consist in adjusting the speed of sound to maximize a *quality indicator* of the image. The *quality indicator* of the image can be evaluated or estimated by parameters such as the lateral resolution, the echo amplitude [10] or the coherence factor [77, 79]. The coherence factor C_f (see *e.g.* [84]) is defined as the ratio of the square of the coherent sum (which is the image) to the incoherent sum (summing the amplitude of the measured signal). For plane wave imaging it was introduced in [85] and can is then expressed as

$$C_f(y) = \frac{\left| \sum_{i=1}^{M} \sum_{j=1}^{N} R_{i,j}\left(\frac{\theta_i \cdot y + |y - x_j|}{c} \right) \right|^2}{MN \sum_{i=1}^{M} \sum_{j=1}^{N} \left| R_{i,j}\left(\frac{\theta_i \cdot y + |y - x_j|}{c} \right) \right|^2}. \tag{3.3}$$

This coefficient ranges from 0 to 1. When the backpropagation speed of sound does not match the speed of sound of the medium, it induces phase error on the backpropa-

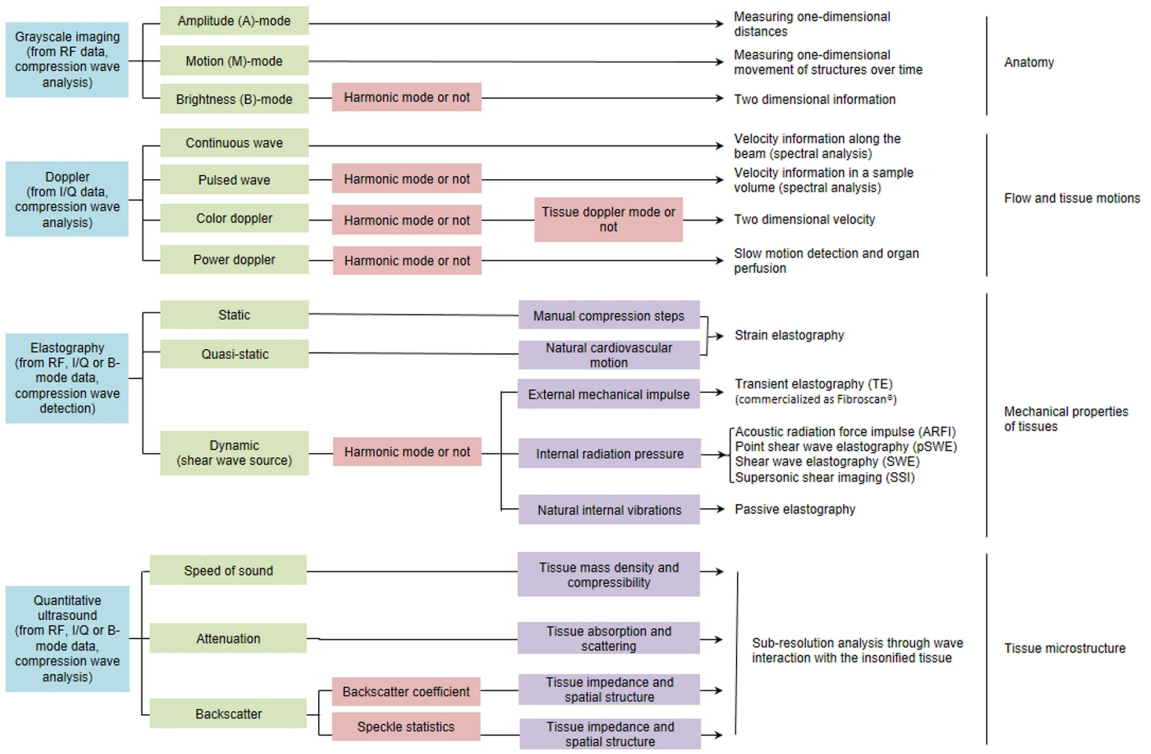

Figure 3.7: Classification of ultrasound techniques. From top to bottom, grayscale imaging modes provide information on organ anatomy. Doppler techniques assess flow and tissue motions (direction, velocity, and backscatter in power Doppler mode). Elastography methods provide information on mechanical properties of tissues. Quantitative ultrasound (QUS) detects sub-resolution acoustic properties to provide information on tissue microstructure. RF refers to radiofrequency data, I/Q to in-phase and quadrature data, whereas compression and shear waves refer to elastic waves used in ultrasound imaging. Figure reproduced from [8]

gated signals and the numerator decreases. The incoherent sum in the denominator is less sensitive to these changes and can thus normalize the coherence factor.
Other focusing methods consists in maximizing the strong reflectors brightness (see the reviews [8, 9, 10]). When there is a strongly contrasted reflector, the idea is to maximize the echo amplitude returned from the this reflector. Finally, the speed of sound can be recovered by deconvoluting the image with a given data set of point spread functions build upon several backpropgation speed of sound [86, 87]. The speed of sound is estimated by minimizing the amplitude of the coefficients of autocorrelation of the deconvoluted image.
Recently, the group of Alexandre Aubry also developed a new method [88, 47, 17] that we briefly describe here. In a confocal imaging setting the ultrasound images are formed by focusing a wave at x in the medium (so-called focusing in emission) and backpropagating the echoes at the point x (so-called focusing in reflection). The change of paradigm in Aubry's work is to decouple those two focusing points. He introduced the reflection point spread function RPSF which consists for a given x at a given depth to focus a wave at $x - \Delta x$ for Δx at the same depth and to listen to echoes returned from $x + \Delta x$ and then summing over all $0 \leq \Delta x \leq \Delta x_{\max}$. Using the matrix imaging notations, it reads:

$$\mathrm{RPSF}(x, \Delta x_{\max}) := \int_{B(0,\Delta x_{\max})} \int_{\mathcal{B}} \Psi(x - \Delta x, \omega)^T \overline{\hat{R}(\omega)} \Phi(x + \Delta x, \omega) d\omega d\Delta x. \qquad (3.4)$$

The function $\mathrm{RPSF}(x, \cdot)$ is a peak function whose width is narrower when single scattering dominates and when the backpropagation speed of sound matches the one of the medium. From this observation, they introduce a new focusing criterium

$$F(x) := \frac{\mathrm{FWHM}(x)}{\mathrm{FWHM}_0(x)},$$

where $\mathrm{FWHM}(x)$ is the full width at half maximum of $\mathrm{RPSF}(x, \cdot)$ and where $\mathrm{FWHM}_0(x)$ corresponds to the theoretical diffraction limit:

$$\mathrm{FWHM}_0(x) := \frac{\omega_0}{2c \sin\left(\arctan\left(\frac{a}{2z(x)}\right)\right)},$$

where ω_0 is the central frequency, a the size of the transducer array and $z(x)$ corresponds to the depth of x. This focusing criterion appears to be more sensitive than the coherence factor [46, 48]. As pointed out in [17], note that these methods are designed to give a estimator of the integrated (or averaged) speed of sound at a given depth and not the actual local speed of the sound at this depth.
Another category of methods is called *compounding methods*. When the backpropagation speed matches the true speed of sound of the medium, the images computed by using different incident steering angles are almost identical. However, an error in the speed of sound induces spatial errors on the images and the difference between the

images depends both on the steering angle and on the error on the backpropagation speed. Therefore, by cross-correlating the images for several steering angles, the discrepancies of speed of sound can be identified, as the images are different. It is then possible to optimize the backpropagation map of the speed of sound by solving an inverse problem as described in [89]. This is the concept of the computed ultrasound tomography in echo mode (CUTE) method [89].
Some other techniques rely on the measurement of the transmitted field [13] which limits their applicability to the breasts, because other body parts contain bones and air that obstruct ultrasound propagation, and it also limits their portability as the devices are much larger.
Lastly, with the improvements in data science, new methods based on neural networks have emerged [90]. Nevertheless, these methods require a large training data set. Numerical simulations to enlarge the data set remain costly. Furthermore, the reconstructed speed of sound map relies heavily on the numerical modelization of the tissues and how accurate it describes the actual tissues.

Reflectivity of the medium

A difficult task it to quantify the relation between the image amplitude at a given point and the local variations of the acoustic properties around this point. In the imaging community, it is accepted that the image amplitude is related to the local acoustic reflectivity of the medium. However, its definition depends on the physical model for soft tissue. Several model for the reflectivity exist as a function of the bulk modulus κ and the density ρ. Though, remark that in the context of ultrasound imaging, as the measurements are done in reflection, it is quite difficult to distinguish the effect of a varying density to those of a varying bulk modulus. Indeed, the resulting scattered field by a small obstacle with contrast in ρ (which acts as a dipole) or with contrast in κ (which acts as a monopole) is notably similar in the direction of the incident wave as shown on Figure 3.8. That is why as a first approximation, due to the reflection setup only variations in the speed of sound $c = \sqrt{\frac{\kappa}{\rho}}$ are considered. Note that the picture would be different if we had access to data in every directions, or at least if to a wider range of incident angle.

By assuming that the single scattering regime holds, in [91], the reflectivity is then defined as $\gamma = \frac{\kappa-\kappa_0}{\kappa_0} - \frac{\rho-\rho_0}{\rho_0}$ and it is mentioned that *for the case of soft tissues imaging, it is often assumed that* $\frac{\kappa-\kappa_0}{\kappa_0}$ *predominates over* $\frac{\rho-\rho_0}{\rho_0}$ *in which case,* $\gamma \approx \frac{\kappa-\kappa_0}{\kappa_0}$. However, to derive this formula, multiple scattering is neglected, furthermore the polarization tensors (see [92]) are also neglected.
Alexandre Aubry and his collaborators introduce a new model where the reflectivity of the medium is the realization of a δ-correlated random process [46]. That is, the reflectivity γ is a zero-mean process that verifies:

$$\mathrm{Cov}(\gamma(x), \gamma(y)) = \sigma^2 \delta(x-y)$$

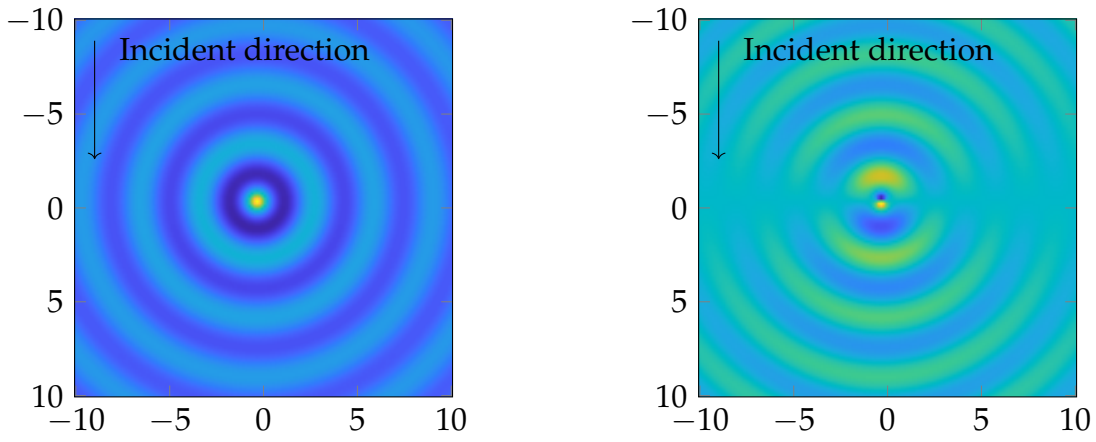

(a) Contrast in κ

(b) Contrast in ρ

Figure 3.8: Real part of the scattered field by an inclusion with either contrast in κ or in ρ for a plane incident wave originating from the top.

with δ the Dirac distribution and $\sigma^2 > 0$ is the variance of the reflectivity. The idea is that the echogenic sources in biological tissues have a characteristic size which is one or two order smaller of magnitude below the wavelength. In this multi-scale context, it is natural to consider that the reflectivity is a random process with fast (with respect to the wavelength) decorrelation properties. The displayed image corresponds then to spatial local averages of the reflectivity.
To quantify the echogenic property, several usual scattering approximation can be used. These scattering approximations as well as the model that we use in quantitative reconstructions are presented in the next Section 3.3.

3.3 Wave propagation in random media

We assume that the ultrasound sensors measure the pressure field p. Therefore we focus on the equation verified by p and want to understand the properties of p.
The pressure field p satisfies a divergence form wave equation with heterogeneous density ρ and heterogeneous bulk modulus κ inside the domain $D \subset \mathbb{R}^d$ [35, Chapter 3.3.3]. D is the tissue to image. We assume it to be a bounded subset of $\mathbb{R}^d$ with a regular boundary ∂D. The density ρ and heterogeneous bulk modulus κ could depend both on space and time. The time-dependency can be neglected as the ultrasound experiment is of the order of the μs while the properties of the medium vary on a longer time scale. Note that this is a fundamental assumption for the matrix imaging formalism to work.
Mathematically speaking, for a given end time T of acquisition, the problem is now to

find the pressure field $p \in L^\infty([0,T]; H^1_{loc}(\mathbb{R}^d))$ and $\partial_t p \in L^\infty([0,T]; L^2_{loc}(\mathbb{R}^d))$ solution of [93, Section 2.1]:

$$\begin{cases} -\nabla \cdot \left(\frac{1}{\rho}\nabla p\right) + \frac{1}{\kappa}\frac{\partial^2}{\partial t^2} p = F & \text{in } [0,T]\times\mathbb{R}^d, \\ p(0,x) = p_0(x) & \text{in } \mathbb{R}^d, \\ \partial_t p(0,x) = p_1(x) & \text{in } \mathbb{R}^d, \end{cases} \tag{3.5}$$

where $0 < \rho_- < \rho \in L^\infty(\mathbb{R}^d)$ and $0 < \kappa_- < \kappa \in L^\infty(\mathbb{R}^d)$. The functions $p_0, p_1 \in H^1_{loc}(\mathbb{R}^d)$ are given initial conditions and $F \in L^\infty([0,T]; H^{-1}(\mathbb{R}^d))$ is the source term which models the transducer impulse. The function F is a short time pulse and is compactly supported in space. In fact F is supported on the transducer array $\mathcal{A}$.
The ultrasound acquisition then consists on the illumination of the medium with a series of M impulses $\{F_i\}_{i=1\dots M}$ sent by the transducers array and the total field is then measured by the transducer array. Outside of the domain to image D, $\rho = \rho_0$ and $\kappa = \kappa_0$ where ρ_0 and κ_0 are positive constants.
Equivalently, we can look for the scattered field $u^s \in H^1_{loc}(\mathbb{R}^d)$, solution of the Helmholtz equation:

$$\begin{cases} -\nabla \cdot \left(\frac{1}{\rho}\nabla(u^s + u^i)\right) - \frac{\omega^2}{\kappa}(u^s + u^i) = 0 & \text{in } \mathbb{R}^d, \\ \lim\limits_{|x|\to\infty} |x|^{\frac{d-1}{2}} \left(\frac{1}{\rho_0}\frac{\partial}{\partial|x|} u^s - i\frac{\omega}{\kappa_0} u^s\right)(x) = 0 \end{cases} \tag{3.6}$$

where $\omega \in \mathcal{B}$ is the frequency and $\mathcal{B}$ is the bandwidth of the ultrasound sensors. $u^i \in H^1_{loc}(\mathbb{R}^d)$ is the incident field, solution of:

$$-\nabla \cdot \left(\frac{1}{\rho_0}\nabla u^i\right) - \frac{\omega^2}{\kappa_0} u^i = f \text{ in } \mathbb{R}^d, \tag{3.7}$$

with $f \in H^{-1}(\mathbb{R}^d)$ the Fourier transform in time of the source term F.
The incident field are usually taken to be plane waves in the direction $\theta \in \mathbb{S}^{d-1}$, defined for $x \in \mathbb{R}^d$ by:

$$u^i_\theta(x) := \exp\left(i\omega\sqrt{\frac{\rho_0}{\kappa_0}}\theta \cdot x\right), \tag{3.8}$$

or incident spherical waves in x_e, defined for $x \in \mathbb{R}^d \setminus \{x_e\}$ by:

$$u^i_{x_e}(x) := \begin{cases} \frac{i}{4}\,\mathrm{H}^1_0\left(\omega\sqrt{\frac{\rho_0}{\kappa_0}}|x - x_e|\right) & \text{if } d = 2, \\ \frac{\exp\left(i\omega\sqrt{\frac{\rho_0}{\kappa_0}}|x - x_e|\right)}{4\pi|x - x_e|} & \text{if } d = 3, \end{cases} \tag{3.9}$$

where $H_0^{(1)}$ is the Hankel function of the first kind [94].
Note that the coefficient $\frac{1}{\rho}$ could be replaced by a uniformly elliptic matrix.

Biological tissues are complex media with a complicated microstructure and variations of parameters at different scales. The goal is to accurately model the spatial distribution of ρ and κ so that the resulting scattered field can effectively reproduce the type of signal recorded by medical ultrasound transducers. In practice, soft tissues have acoustic properties that are close to those of water (compressibility and density). Nevertheless, if a tissue were to be modeled by a water-like homogeneous medium, the echogenic properties of the tissue will not be captured by the model. It is accepted that the small micro-scale biological structures (cell nucleus, mitochondria...) are the sources of the backscattered field. In the next Subsection 3.3.1, we detail the model for the coefficients.

3.3.1 A model for soft tissues

The backscattered field is due to the numerous unresolved scatterers inside the medium. We thus assume that the tissue under study is a homogeneous medium (with the compressibility and the density of the water) in which lies small contrasted scatterers of typical size ε, small in front of the size of the medium and of the wavelength. As we cannot access the spatial distribution of those small scatterers, we model the distribution process as a random process. We consider the typical setting of Figure 3.9. We will use stochastic homogenization techniques to describe the scattered field and this is the topic of Part II. We present here the model that we use throughout the entire thesis.

We consider a bounded acoustic medium $D \subset \mathbb{R}^d$, $d \in [\![1,3]\!]$ with a $\mathcal{C}^4$- boundary ∂D and we study the scattering of either time-harmonic plane wave u^i_θ of (3.8) with wave number k and direction $\theta \in \mathbb{S}^{d-1}$ or spherical incident waves $u^i_{x_e}$ of (3.9) with wave number k and emitted at the point $x_e \in \mathbb{R}^d \setminus \overline{D}$. We assume that a set S^ε of randomly distributed inclusions of characteristic size $\varepsilon > 0$ lies inside the medium D. ε is small compared to the wavelength of the incoming field $2\pi k^{-1}$.

The outer medium $\mathbb{R}^d \setminus \overline{D}$, the background $D \setminus \overline{S^\varepsilon}$ and the scatterers S^ε are assumed to be homogeneous with respective parameters (Id, n_0), (a_M, n_M) and (a_S, n_S). The medium parameters are then given by

$$\begin{cases} a_\varepsilon := Id\,\mathbb{1}_{\mathbb{R}^d\setminus\overline{D}} + a_M\mathbb{1}_{D\setminus\bar{S}^\varepsilon} + a_S\mathbb{1}_{S^\varepsilon}, \\ n_\varepsilon := n_0\mathbb{1}_{\mathbb{R}^d\setminus\overline{D}} + n_M\mathbb{1}_{D\setminus\bar{S}^\varepsilon} + n_S\mathbb{1}_{S^\varepsilon}, \end{cases} \tag{3.10}$$

where a_M and a_S are positive definite matrices of $\mathcal{M}_d(\mathbb{R})$ and n_0, n_M, n_S are positive. The total field u_ε is then the unique solution almost sure in $H^1_{loc}(\mathbb{R}^d)$ of the following problem:

$$\begin{cases} -\nabla\cdot(a_\varepsilon(x)\nabla u_\varepsilon(x)) - k^2 n_\varepsilon(x)u_\varepsilon(x) = 0 & \text{for } x \in \mathbb{R}^d, \\ \lim\limits_{|x|\to+\infty} |x|^{\frac{d-1}{2}}\left(\dfrac{\partial(u_\varepsilon - u^i)}{\partial|x|}(x) - ik\,(u_\varepsilon - u^i)(x)\right) = 0. \end{cases} \tag{3.11}$$

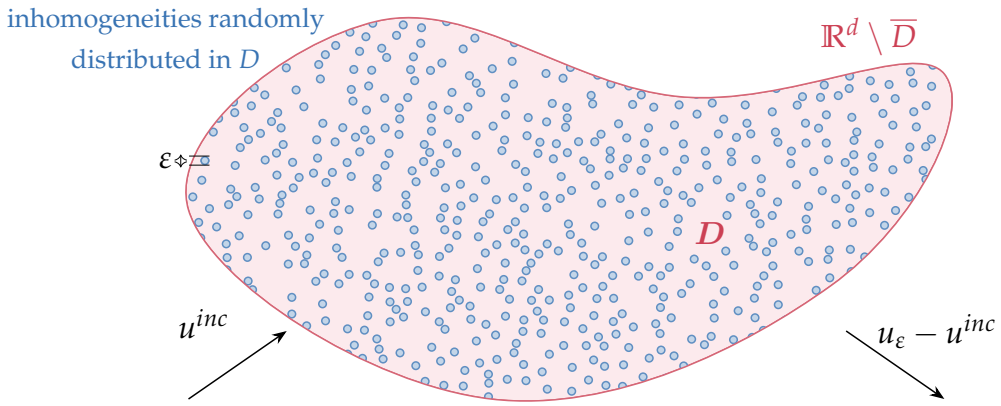

Figure 3.9: Scattering by an (multi-scale) obstacle in the stochastic homogenization regime

To link with the previous equation (3.11), u_ε still denotes the pressure. a_ε and n_ε relate to the inverse of the mass density and the bulk modulus of the inner and outer media [35, Chapter 3.3]. We choose identical parameters for all scatterers. The study can easily be extended to independent and identically distributed parameters as long as the assumptions of uniform ellipticity for a_ε and uniform boundness from below and above for n_ε are satisfied. We specify in the following section the different assumptions that we make on the random distribution of scatterers.

Description of the distribution of scatterers

Let $(x_i)_{i\in\mathbb{N}}$ be the point process in $\mathbb{R}^d$ corresponding to the centers of the scatterers. A scatterer s_i, $i \in \mathbb{N}$ centered at x_i consists in an open connected Lipschitz domain $\mathcal{Q}$ of radius $r := \max_{x,y\in\mathcal{Q}} |x-y|$. We denote by $S := \bigcup_{i\in\mathbb{N}} s_i$ the set of scatterers of radius $r = 1$ in $\mathbb{R}^d$. Let $(\Omega, \mathcal{F}, \mathbb{P})$ be a probability space. We make the following assumptions on $(x_i)_{i\in\mathbb{N}}$:

- $(x_i)_{i\in\mathbb{N}}$ is stationary, *i.e.* its distribution law is invariant by translation and ergodic;

- the scatterers lie at a distance at least $\delta > 0$ from one another, *i.e.* there exists $\delta > 0$ such that

$$\forall i \neq j,\ dist(s_i, s_j) > \delta \quad \text{a.s.}$$

Stationarity and ergodicity are described in details in Section 4.3. We introduce the parameters

$$\begin{cases} a := a_M \mathbb{1}_{\mathbb{R}^d \setminus \overline{S}} + a_S \mathbb{1}_S, \\ n := n_M \mathbb{1}_{\mathbb{R}^d \setminus \overline{S}} + n_S \mathbb{1}_S. \end{cases} \tag{3.12}$$

For $\varepsilon > 0$, we define

$$\mathcal{N}_\varepsilon := \{i \in \mathbb{N} \mid \varepsilon x_i \in D\}.$$

$\mathcal{N}_\varepsilon$ corresponds to the collection of scatterers of size ε that lie in D. We subsequently denote

$$S^\varepsilon := \bigcup_{i \in \mathcal{N}_\varepsilon} \varepsilon s_i \cap D. \tag{3.13}$$

Note that we have then

$$\forall x \in D,\ a_\varepsilon(x) = a\left(\frac{x}{\varepsilon}\right) \text{ and } n_\varepsilon(x) = n\left(\frac{x}{\varepsilon}\right).$$

In this thesis, we chose a Matèrn point process. However, any point process that satisfies a quantitative ergodic assumption could be used (see Section 4.4).

3.3.2 Wave propagation in random multi-scale media

A random multi-scale framework appears to be well-suited for the analysis of the wave propagation in biological tissues. Experiments and theoretical results [95, Chapter 5] suggest that 3 characteristic lengths determine the behavior of the wavefield. These are the correlation length inside the medium l, the wavelength λ and the size of the medium L. The correlation length is the typical size at which the acoustic properties of the medium varies. It characterizes the typical size of the heterogeneities within the medium. Moreover, the contrast $\sigma := \left\| \frac{1}{\kappa} - \frac{1}{\kappa_0} \right\|_{L^\infty(D)}$ of the medium's properties also affects the wavefield. We can distinguish three interesting regimes depending on the respective scaling of each parameter as shown in [95, Chapter 5].

Effective regime

The effective regime corresponds to the regime where

$$l \ll \lambda \sim L \qquad \sigma \sim 1 \text{ or } \sigma \ll 1.$$

Physically, this corresponds to the regimes where the heterogeneities are smaller than the wavelength. Even if the heterogeneities are small, the contrast is of order 1, at the limit when the size of the heterogeneities goes to zero, the scattered field cannot be approximated by the scattered field of the background medium. In fact, the scattered field is close to the field scattered by a homogeneous medium whose parameters $\rho^\star$ and $\kappa^\star$ are effective parameters which are usually different of ρ_0 and κ_0. As the size

of the medium is of the order of the wavelength, the propagation distances are not sufficient for the randomness to dominate the wavefield. That is why, as the scale of the wavelength, the wavefield "sees" an effective, homogeneous medium and the wave propagation can be accurately described with effective properties. This regime corresponds for example to the regime of homogenization [96]. The homogenization process is detailed in Chapter 4.

Weakly heterogeneous regime

When the size of the heterogeneities is of the order of the wavelength (and the medium larger), the picture is different. If the contrast were to be of order 1, the phase of wavefield would be totally random and few "local" information about the scattering process would be retrievable, as the imaging function relies on phases alignment. Because the fluctuations are of small amplitude $\sigma \ll 1$, the wavefield must propagate over large propagation distances to experience a significant scattering by the medium. This corresponds to the weakly heterogeneous regime (see [95, Chapter 18] for more details) where

$$l \sim \lambda \ll L \qquad \sigma \ll 1.$$

This regime has been studied for time-reversal imaging. In this case, the goal is to identify the position of sources [97, 55] or of reflectors [98, 55]. To that aim, in [99], the time-reversal invariance is used to refocus on targets inside a scattering medium. It is observed that the multiple scattering actually enhances the resolution of the time-reversal imaging in comparison with the case of targets lying in an homogeneous medium. This is mathematically studied in [97].
In this weakly scattering regime, the problem can even sometimes simplify to a random travel time problem under more hypotheses described in example in [100]. Indeed in this regime, the phase of the scattered field is primarily affected [100], and not the amplitude. The goal is then to recover the correct phase or equivalently the correct travel time, so that the position of the sources of reflector can be recovered.
In [100], two methods compared. The coherent interferometric imaging method introduced in [101, 102, 103] which consists in a backpropagation of the cross correlation of the signals is opposed to the Kirchhoff migration. The coherent interferometric is more robust to noise, but loses resolution in comparison to the Kirchhoff migration.
In the book [55], an extensive mathematical analysis of the passive imaging methods is done. The passive imaging methods were introduced by Campillo [104] consists in recording the "ambient noise". The recorded "ambient noise" is in fact the scattering response of the medium under investigation to randomly positioned sources. One can think of the measurement done by a seismometer which are produced by the movements inside the Earth's crust. The distribution of the sources is typically a white noise, and by auto-correlating the signal it is possible to recover deterministic information about the medium to image, such as the position of a reflector. Note that the Kirchhoff migration corresponds to (3.2), where the vector $\Phi(\omega)$ is taken to be the Green function of the Helmholtz equation at wave number $\frac{\omega}{c}$.

Strongly heterogeneous regime

The strongly heterogeneous regime corresponds to the regime where the fluctuations of the medium are strong, but the heterogeneities are small in front of every other characteristic length *i.e.*

$$l \ll \lambda \ll L \qquad \sigma \sim 1.$$

In this regime, the fluctuations of the medium dominate, both the amplitude and the phase of the wavefield are impacted. A source or a reflector is then more challenging to identify in comparison the weakly scattering regime, but it corresponds to regimes encountered in practice. In exploration seismology, the wavelength is of the order of 100 m, the probed depths are of the order of 10 km, while the correlation length can be estimated of the order of 1 m [95]. In medical ultrasound imaging, similar observations can be made: $\lambda \approx 0.1 - 1$ mm; $L \approx 10$ cm; and $l \approx 1$ μm [17]. This regime is considered in [95] for the study of layered media and imaging techniques have been proposed in [105, 106].

In this thesis, we consider the backscattering of strongly heterogeneous media under a new prism, by using stochastic homogenization techniques to describe the backscattered field. As the typical size of the medium is large compared to the wavelength, the traditional effective model fails. However, this difficulty is surpassed by establishing a higher order expansion which is described in Part II.

3.3.3 Scattered field approximations

We aspire to quantitatively estimate the speed of sound inside the biological tissues. The first theoretical step is to quantitatively link the acoustic properties of the medium to the backscattered field. This is often done by the Born approximation as we describe in this section.
One can always write that the total field $u = u^s + u^i$ is the unique solution in $H^1(D)$ of the Lippman-Schwinger equation [107, Chapter 8.2]:

Lemma 1: Lippman-Schwinger equation

For any $x \in D$,

$$u(x) = u^i(x) + \int_D \left(\frac{1}{\rho_0} - \frac{1}{\rho}\right) \nabla u(y) \cdot \nabla G(x,y) + \omega^2 \left(\frac{1}{\kappa} - \frac{1}{\kappa_0}\right) u(y) G(x,y) dy, \quad (3.14)$$

where for any $y \in \mathbb{R}^d$, the Green function $x \mapsto G(x,y)$ is the solution in $\mathcal{D}'(\mathbb{R}^d)$ of:

$$\begin{cases} -\nabla \cdot \left(\frac{1}{\rho_0} \nabla G(x,y)\right) - \frac{\omega^2}{\kappa_0} G(x,y) = \delta(x-y) \quad \text{in } \mathbb{R}^d \setminus \{y\}, \\ \lim_{|x|\to\infty} |x|^{\frac{d-1}{2}} \left(\frac{\partial}{\partial |x|} G - i\omega \sqrt{\frac{\rho_0}{\kappa_0}} G\right)(x,y) = 0. \end{cases} \quad (3.15)$$

We have explicit forms for $G(x,y)$ in dimensions 2 and 3 [108, Lemma 2.21]:

$$G(x,y) = \begin{cases} \rho_0 \frac{i}{4} \mathrm{H}_0^{(1)}(k|x-y|) & \text{for } d = 2, \\ \rho_0 \frac{\exp(ik|x-y|}{4\pi|x-y|} & \text{for } d = 3, \end{cases} \quad (3.16)$$

where $k := \omega \sqrt{\frac{\rho_0}{\kappa_0}}$ is the wavenumber and $\mathrm{H}_0^{(1)}$ is the Hankel function of the first kind [94].
The equation (3.15) is an implicit equation that can be rewritten for $x \in D$ as

$$u(x) = u^i(x) + \mathcal{L}[u](x),$$

where $\mathcal{L} : H^1(D) \to H^1(D)$ is the Lippmann-Schwinger operator:

$$\mathcal{L}[u](x) := \int_D \left(\frac{1}{\rho_0} - \frac{1}{\rho}\right) \nabla u(y) \cdot \nabla G(x,y) + \omega^2 \left(\frac{1}{\kappa} - \frac{1}{\kappa_0}\right) u(y) G(x,y) dy$$

and

$$(I - \mathcal{L})[u] = [u^i],$$

where I is the identity function of $L^2(D)$. The knowledge of $u(x)$ for $x \in D$ allows to compute u everywhere. Without any assumption on ρ and κ, it is quite hard to obtain any further information. However, when the contrasts $(\frac{1}{\rho_0} - \frac{1}{\rho})$ and $(\frac{1}{\kappa} - \frac{1}{\kappa_0})$ are "small" in a certain norm, simple forms of the scattered field can be computed.

Born approximation

When the medium is weakly scattering and in particular when the contrasts are of small amplitude *i.e.* $\left\|\frac{1}{\rho}-\frac{1}{\rho_0}\right\|_{L^\infty(D)} \ll 1$ and $\left\|\frac{1}{\kappa}-\frac{1}{\kappa_0}\right\|_{L^\infty(D)} \ll 1$, it is clear that $\|\mathcal{L}\| := \sup_{v\in H^1(D), v\neq 0} \frac{\|\mathcal{L}[v]\|_{H^1(D)}}{\|v\|_{H^1(D)}} < 1$. The Neumann series converges and

$$u = \sum_{j=0}^{\infty} \mathcal{L}^j[u^i].$$

By truncation of this series, one can approximate u by

$$u = (I+\mathcal{L})[u^i] + \mathcal{O}(\|\mathcal{L}\|^2).$$

This is known as the first order Born approximation [54]. The solution u can then be written as:

$$u(x) = u^i(x) + \int_D \left(\frac{1}{\rho_0}-\frac{1}{\rho}\right) \nabla u^i(y)\cdot\nabla G(x,y) + \omega^2\left(\frac{1}{\kappa}-\frac{1}{\kappa_0}\right) u^i(y)G(x,y)dy + \mathcal{O}(\|\mathcal{L}\|^2). \quad (3.17)$$

This form is much simpler, it allows to fastly compute the scattered field and links the properties of κ and ρ to those of u via a simple integral relation. The Born approximation can be enhanced by considering n terms of the series:

$$u = \sum_{j=0}^{n} \mathcal{L}^j[u^i] + \mathcal{O}(\|\mathcal{L}\|^{n+1}).$$

The Born approximation is also called the single scattering approximation as it corresponds to the field that is scattered only once by the medium. The term of the series beyond the first one then corresponds to the multiple scattering.
The ultrasound imaging process relies on single scattering approximations *i.e.* on the Born approximation. The quantification of the multiple scattering effects is actually not an easy task. It has been done in the series of work [109, 53, 88, 46, 47, 48, 110] by Derode and Aubry and their collaborators where they consider the matrix formalism for imaging. We also refer to [111] for the scattering of heterogeneous obstacles. The Born series has been extensively studied by Shari Moswkow and John Schotland and their coauthors [112, 113]. More precisely, they investigated both the convergence of the Born series for $\rho = \rho_0$ both theoretically and numerically [114, 113], and for $\kappa = \kappa_0$ in [115]. These studies are carried out in view to obtain convergence conditions on the inverse Born series (see [115]), which consists in recovering the function $\frac{1}{\kappa}-\frac{1}{\kappa_0}$ from the measurements of u^s.

Foldy-Lax model

When the supports $\mathrm{supp}(\frac{1}{\rho}-\frac{1}{\rho_0})$ and $\mathrm{supp}(\frac{1}{\kappa}-\frac{1}{\kappa_0})$ are small, another model can be used, the so-called Foldy-Lax model or coupled dipole approximation [116].
More precisely, assume that the medium is composed of a set of N heterogeneneities $S := \{S_j\}_{j=1...N}$ where S_j is centered in z_j, with variable properties $\rho_j > 0$, $\kappa_j > 0$ embedded in a homogeneous domain D *i.e*

$$\rho(x) = \begin{cases} \rho_0 & \text{if } x \in D \setminus \overline{S} \\ \rho_j & \text{if } x \in S_j \end{cases} \text{ and } \kappa(x) = \begin{cases} \kappa_0 & \text{if } x \in D \setminus \overline{S} \\ \kappa_j & \text{if } x \in S_j, \end{cases}$$

and that each inhomogeneneity is small in front of the wavelength.
In this case, the Lippmann-Schwinger equation (3.15) rewrites for all $x \notin S$:

$$u(x) \approx u^i(x) + \sum_{j=1}^{N} \tau_j \left(\frac{1}{\rho_j} - \frac{1}{\rho_0}\right) \nabla u(z_j) \cdot \nabla G(x - z_j) + \omega^2 \left(\frac{1}{\kappa_j} - \frac{1}{\kappa_0}\right) u(z_j) G(x - z_j), \quad (3.18)$$

where each $\tau_j \in \mathcal{M}_d(\mathbb{R})$ is the polarization tensor of S_j (see [92] for more details) which depends only on the shape of the j-th inhomogeneity.
To compute $u(x)$ for all x, it is necessary to know $u(z_j)$. The Foldy-Lax model of the coupled dipole approximation consists in approximating $u(z_j)$ by:

$$u(z_j) = u^i(z_j) + \sum_{k=1,k\neq j}^{N} \tau_k \left(\frac{1}{\rho_k} - \frac{1}{\rho_0}\right) \nabla u(z_k) \cdot \nabla G(z_j - z_k) + \omega^2 \left(\frac{1}{\kappa_k} - \frac{1}{\kappa_0}\right) u(z_k) G(z_j - z_k), \quad (3.19)$$

and for $l = 1...d$, $\partial_l u(z_j)$ by:

$$\partial_l u(z_j) = \partial_l u^i(z_j) + \sum_{k=1,k\neq j}^{N} \tau_k \left(\frac{1}{\rho_k} - \frac{1}{\rho_0}\right) \nabla u(z_k) \cdot \nabla \partial_l G(z_j - z_k) + \omega^2 \left(\frac{1}{\kappa_k} - \frac{1}{\kappa_0}\right) u(z_k) \partial_l G(z_j - z_k). \quad (3.20)$$

This model has been studied in [117] when ρ is constant (equal to ρ_0) and in [118] when κ is constant (equal to κ_0). As pointed out in [117], when the density of scatterers increases, the system may not always be invertible. Furthermore, the system becomes quite large and costly to solve.
Still, this method allows to transfer the resolution of a large problem posed on the

unknown $u \in H^1(D)$ to a smaller linear system of size $(d+1)N \times (d+1)N$ to identify each coefficients $u(z_j)$ and $\nabla u(z_j)$.
Also note that by taking $u(z_j) = u^i(z_j)$ and $\nabla u(z_j) = \nabla u^i(z_j)$, a similar expression to the Born approximation is recovered, modified by the polarization tensors.

Homogenization regime

The Born approximation holds when the L^∞ norm of the contrast is small. The coupled dipole approximation holds when the support of the contrast is small. Another way of defining a "small" contrast is trough weak norms. Typically, when the contrasts oscillate very fast, the homogenization theory (see [96] for periodic media and [119] for random media) allows to approximate the scattered field as the solution u_0 in a homogeneous medium with homogenized density and bulk modulus. This is described in details in Chapter 4. However, this approximation only holds when the size of the medium is of the order of the wavelength.

Biological tissues modeling

The three previous approximations usually do not hold in biological tissues. The contrast is small, but the multiple scattering cannot be neglected (and increases with depth [53]). The support of the contrast is not small, as the biological tissues are typically composed of numerous unresolved scatterers. Classical homogenization could allow to characterize the backscattered field but the wave typically propagates on many wavelengths, which heavily deteriorates the homogenization error.
Fortunately, the theory of homogenization allows to expand the solution in a series of corrective terms. Even if the approximation $u \approx u_0$ does not hold in large domains of the order of hundred of wavelength, we construct a corrective term u_1, which depends on the realization of the medium, such that

$$u \approx u_0 + u_1$$

holds in large domains. We see the strongly heterogeneous regime as a homogenization process in a large domain. For these reasons, we decide to use stochastic homogenization techniques to describe the pressure field u, with the goal of first defining the reflectivity, and then constructing an estimator of the effective speed of sound.

CHAPTER 4

Homogenization for linear elliptic equations

The definition of a "homogeneous material" depends on the scale of observation. When observed under a microscope, so-called homogeneous materials reveal their heterogeneities. For theoretical and computational reasons, these irregularities are not always taken into account, and their properties are replaced with those of a homogeneous material.
This process, which is possible when the spatial variations of the source excitement occur at a scale much larger than the spatial variations of the properties of the material under study, is called homogenization.
The objective of homogenization is to comprehend and describe the macroscopic behavior of the material via the internal microscale structure.
The study of the homogenization process involves two (or more) scales: the observable scale, designated as the macroscopic scale, at which we aim to calculate the effective (or homogenized) properties, and one (or more) underresolved scales designed as the microscopic scales.
From a numerical point of view, homogenization often presents a significant advantage. Once the effective properties are known, it is possible to compute mechanical responses at the macroscopic scale reducing the computational costs significantly.
The mathematical discipline of homogenization aims to understand this mechanism and make it rigorous. This discipline dates back to the 1970s when the first results were obtained (see [96]).

4.1 G and H convergence

Mathematically, the homogenization discipline started in the 1970s with the following problem. First for a bounded compact domain D of $\mathbb{R}^d$ and $0 < \alpha < \beta$, let us define the set of coefficients:

$$E(\alpha, \beta, D) := \{a \ : \ D \to \mathcal{M}_d(\mathbb{R}) \mid a \text{ is measurable and is elliptic in the sense of (4.1)}\},$$

where ellipticity is defined as follows: $a : D \to \mathcal{M}_d(\mathbb{R})$ is elliptic if there exists $0 < \alpha < \beta < \infty$ such that for all $x \in D$ and for all $\xi \in \mathbb{R}^d$,

$$\alpha|\xi|^2 \leq |a(x)\xi \cdot \xi| \text{ and } |a(x)\xi| \leq \beta|\xi|. \tag{4.1}$$

Consider a small parameter $\varepsilon > 0$. Given $a_\varepsilon \in E(\alpha, \beta, D)$, the goal is to understand the convergence as $\varepsilon \to 0$ of the unique solution $u_\varepsilon \in H_0^1(D)$ of

$$\begin{cases} -\nabla \cdot (a_\varepsilon \nabla u_\varepsilon) = f & \text{in } D, \\ u_\varepsilon = 0 & \text{on } \partial D, \end{cases} \tag{4.2}$$

for a given source term $f \in H^{-1}(D)$. *In what sense does u_ε converge? Under what conditions? Towards which limit?* At the end of the 70's, Ennio De Giorgi and Spagnolo gave a first answer for symmetric operators *i.e.* for the sequence $a_\varepsilon \in E_{\text{sym}}(\alpha, \beta, D) := \{a \in \mathbb{E}(\alpha, \beta, D), a \text{ is symmetric}\}$ [120, 121, 122] via the G-convergence (the G stands for Green as it corresponds to the convergence of the Green kernel). The theory is soon extended to coefficients that are not symmetric. This is the H-convergence (where the H stands for homogenization).

Definition 2: H-convergence

As $\varepsilon \to 0$, $a_\varepsilon \in E(\alpha, \beta, D)$ H-converges to $a^\star \in E(\alpha', \beta', D)$ if and only if

1. $u_\varepsilon \xrightarrow{H_0^1(D)} u_0$
2. $a_\varepsilon \nabla u_\varepsilon \xrightarrow{L^2(D)} a^\star \nabla u_0$.

u_0 is the unique solution in $H_0^1(D)$ of

$$\begin{cases} -\nabla(a^\star \nabla u_0) = f & \text{in } D, \\ u_0 = 0 & \text{on } \partial D, \end{cases} \tag{4.3}$$

and we write $a_\varepsilon \xrightarrow{H} a^\star$.

The above definition of H-convergence makes sense as a consequence of the following Theorem:

Theorem 3: Compactness theorem

For any $a_\varepsilon \in E_{\text{sym}}(\alpha, \beta, D)$, it exists a subsequence (still indexed by ε) and a homogenized limit $a^\star \in E_{\text{sym}}(\alpha, \beta, D)$, such that

$$a_\varepsilon \xrightarrow{H} a^\star$$

Remark 4.1.1. *The previous Theorem 3 also holds for $a_\varepsilon \in E(\alpha, \beta, D)$, but the limit $a^\star$ belongs to $E(\alpha, \frac{\beta^2}{\alpha}, D)$.*

We present here a few properties of the H-convergence.

Proposition 4: Properties of the H-convergence

The H-limit of a_ε, if it exists,

1. is unique,
2. verifies (4.1) with ellipticity constant $0 < \alpha < \beta$ (or $0 < \alpha < \frac{\beta^2}{\alpha}$ if a_ε is not symmetric),
3. is independent of the source term f,
4. is independent of the boundary condition on ∂D,
5. is local, in the sense that if a_ε coincides with b_ε on $D' \subset D$, then $a^\star = b^\star$ on D'.

Given the previous theorem and the properties of the H-convergence, the homogenization problem seems to be solved at first sight - the solution converges towards the solution in a homogeneous medium with the properties described by $a^\star$. However, this does not explain how to compute the limiting operator. $a^\star$ exists, but we have no idea how to compute it. Two regimes in which the limiting operator can be computed have been identified. Suppose that $a \in E(\alpha, \beta, \mathbb{R}^d)$ is either

- Y-periodic, where $Y = (0,1)^d$ is the unit cell
- or the realization of a *stationary and ergodic* random field.

In the regimes where for $x \in D$,

$$a_\varepsilon(x) = a(\frac{x}{\varepsilon}),$$

it is possible to have a closed form for $a^\star$. These two regimes will be presented in the next sections.

4.2 Periodic setting

Let $a \in E(\alpha, \beta, \mathbb{R}^d)$ be Y-periodic where $Y = (0,1)^d$ is the unit cell. Define for all $x \in D$,

$$a_\varepsilon(x) = a(\frac{x}{\varepsilon}).$$

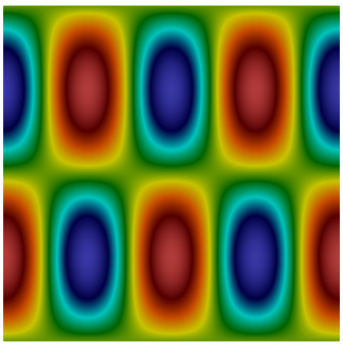

(a) Reference periodic coefficient $a(x) = 2 + \cos(4\pi x_1)\sin(2\pi x_2)$ in Y

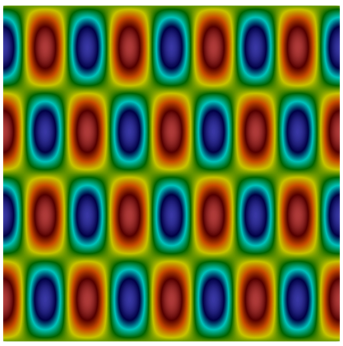

(b) $a_\varepsilon(x) := a(\frac{x}{\varepsilon})$ for $\varepsilon = 1/2$

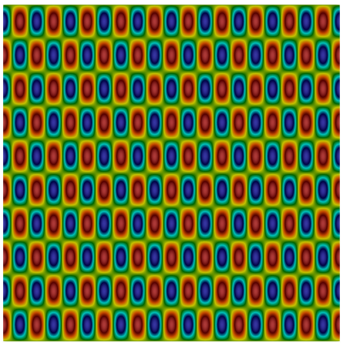

(c) $a_\varepsilon(x)$ for $\varepsilon = 1/5$

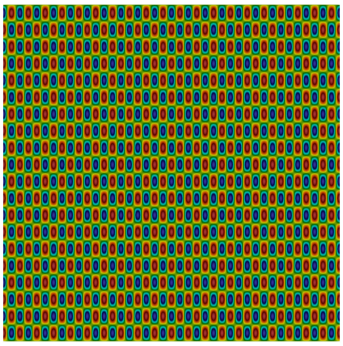

(d) $a_\varepsilon(x)$ for $\varepsilon = 1/10$

Figure 4.1: a_ε for several values of ε

Let $u_\varepsilon \in H_0^1(D)$ be the unique solution of

$$\begin{cases} -\nabla \cdot (a_\varepsilon \nabla u_\varepsilon) = f & \text{in } D, \\ u_\varepsilon = 0 & \text{on } \partial D. \end{cases} \tag{4.4}$$

By the above Theorem 3, u_ε converges weakly in $H_0^1(D)$ towards u_0 the solution in $H_0^1(D)$ of (4.3). When the coefficient a_ε is periodic, the homogenized coefficient $a^\star$ can be computed. A formula for $a^\star$ can be derived by a formal two-scale expansion on the solution u_ε that is described in the following Section 4.2.1. The rigorous proof of the expansion will be presented in Section 4.2.4 (see also [96, 123, 124]).

4.2.1 Formal expansion

In the following sections, we denote by $y := \frac{x}{\varepsilon}$ the microscopic scale while x is the macroscopic scale. We formally assume that the solution can be expanded for all $x \in D$

as:

$$u_\varepsilon(x) = u_0(x,y) + \varepsilon u_1(x,y) + \varepsilon^2 u_2(x,y) + ...,$$

where all functions u_i, $i \geq 0$ are periodic with respect to their second variable. By the chain rule:

$$\nabla u_i(x, \frac{x}{\varepsilon}) = (\nabla_x + \frac{1}{\varepsilon}\nabla_y) u_i(x, \frac{x}{\varepsilon}).$$

We then insert this Ansatz into the main equation (4.4) and identify the different powers of ε. This leads to a cascade of equations. In particular, the first three equations are as follows for $x \in D$ and $y \in Y$,

$$(\varepsilon^{-2}) \quad -\nabla_y \cdot a(y)\nabla_y u_0(x,y) = 0, \tag{4.5}$$

$$(\varepsilon^{-1}) \quad -\nabla_x \cdot a(y)\nabla_y u_0(x,y) - \nabla_y \cdot a(y)(\nabla_x u_0(x,y) + \nabla_y u_1(x,y)) = 0, \tag{4.6}$$

$$(\varepsilon^{0}) \quad -\nabla_x \cdot a(y)(\nabla_x u_0(x,y) + \nabla_y u_1(x,y)) \tag{4.7}$$

$$-\nabla_y \cdot a(y)(\nabla_x u_1(x,y) + \nabla_y u_2(x,y)) = f(x). \tag{4.8}$$

The study of the cascade of equations requires the study of the existence and uniqueness of the periodic solution v of the following problem posed in Y:

$$-\nabla \cdot (a\nabla v) = F. \tag{4.9}$$

with $F \in L^2(Y)$. This problem has a unique solution (up to an additive constant solution) in $H^1_{\text{per}}(Y) := \{v \in H^1_{loc}(\mathbb{R}^d),\ v \text{ is } Y\text{-periodic}\}$ if and only if

$$\int_Y F = 0 \tag{4.10}$$

For a given and fixed $x \in D$, (4.5) has then a unique solution up to an additive constant solution in $H^1_{\text{per}}(Y)$. This implies that u_0 is independent of the slow scale y and we simply write

$$u_0(x, \frac{x}{\varepsilon}) = u_0(x).$$

This means that the homogenized solution will not oscillate on the microscopic scale, which is what we hoped for. Note that only the volume equations are written. The boundary conditions are a major issue that we will discuss in Section 4.4.3.

4.2.2 Correctors

Since u_0 is independent of y, by linearity

$$u_1(x,y) = \sum_{i=1}^{d} \partial_i u_0(x) \phi_i(y) \tag{4.11}$$

where for $1 \leq i \leq d$, ϕ_i is the unique solution (up to an additive constant) in $H^1_{\text{per}}(Y)$ of

$$-\nabla_y \cdot (a(y)e_i + \nabla\phi_i(y)) = 0. \tag{4.12}$$

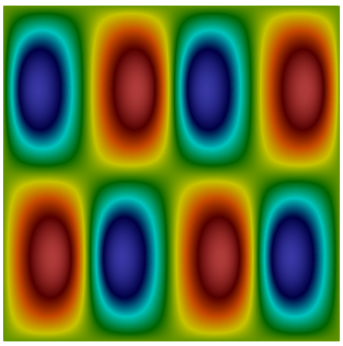

(a) ϕ_1

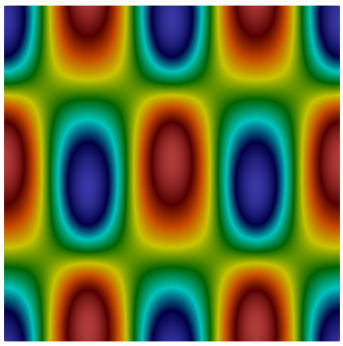

(b) ϕ_2

Figure 4.2: Correctors of periodic homogenization associated with $a(x) = 2 + \cos(4\pi x_1)\sin(2\pi x_2)$ in the two directions

ϕ_i is called the corrector or the cell-problem solution and is a fundamental quantity in homogenization. We recall that by periodicity, $\int_Y \nabla_y \cdot (a(y)e_i)dy = 0$, which ensures the well-posedness of (4.12). Simulations of the correctors are plotted on Figure 4.2 for a coefficient as chosen on Figure 4.1.

Remark 4.2.1. *Usually the constant is fixed by a* 0*-mean value condition on* Y *i.e.*

$$\int_Y \phi = 0.$$

4.2.3 Effective tensor

The last equation (4.8) gives the homogenized equation. For a given $x \in D$, a solution $u_2(x,\cdot)$ of (4.8) exists if and only if (4.10) is satisfied *i.e.*

$$\int_Y \nabla_x \cdot a(y)\nabla_x u_0(x) + \nabla_y \cdot a(y)\nabla_x u_1(x,y) + \nabla_x \cdot a(y)\nabla_y u_1(x,y) + f(x)dy = 0. \quad (4.13)$$

We recall that for periodic functions g,

$$\int_Y \nabla g(y)dy = 0.$$

The condition (4.13) of the well-posedness of $y \mapsto u_2(x,y)$ can thus be rewritten for $x \in D$ as:

$$-\nabla \cdot a^\star \nabla u_0(x) = f(x), \quad (4.14)$$

where for $1 \leq i \leq d$,

$$a^\star e_i := \int_Y a(y)(e_i + \nabla\phi_i(y))dy. \quad (4.15)$$

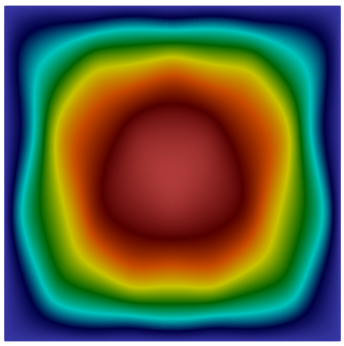

(a) u_ε with $\varepsilon = 1/2$ and $f = 1$

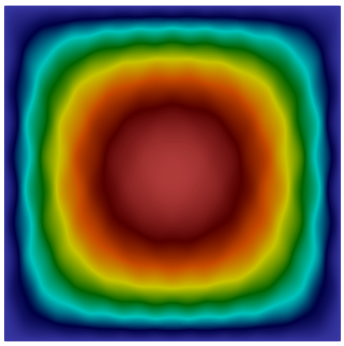

(b) $u_\varepsilon(x)$ with $\varepsilon = 1/5$ and $f = 1$

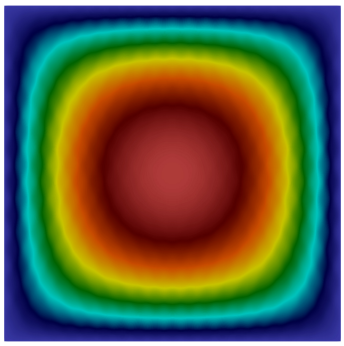

(c) u_ε with $\varepsilon = 1/10$ and $f = 1$

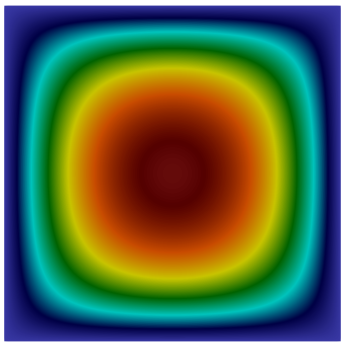

(d) Homogenized solution u_0

Figure 4.3: Illustration of the homogenization process - Solutions u_ε of (4.4) for several values of ε (with a given in Figure 4.2) and limiting solution u_0.

This is the homogenized equation. So far, we have derived a formal equation for u_0. The numerical simulations of Figure 4.3 seems to validate the convergence of u_ε towards u_0 in the particular case of a periodic coefficient chosen as in Figure 4.1. In fact, the formal expansion can be justified and is the topic of the next Section 4.2.4.

4.2.4 Energy method via oscillating test functions

The justification of the convergence between u_ε and u_0 is more complex. The idea is to study the convergence of the variational formulation:

$$\int_D a_\varepsilon \nabla u_\varepsilon \cdot \nabla v = \int_D f v \tag{4.16}$$

for $v \in H^1(D)$. By weak compactness, up to a subsequence, $a_\varepsilon \nabla u_\varepsilon$ converges weakly in $L^2(D)$ towards some $F^\star$. By uniqueness of u_0, it remains to show that $F^\star = a^\star \nabla u_0$ to obtain the convergence of u_ε to u_0. This is done by the method of the *oscillating*

test function introduced by Tartar and Murat (see [125, 126]). The idea is to choose ε-dependent test functions v that converge weakly in $H_0^1(D)$ allowing to characterize $F^\star$. However, proceeding like this requires to deal with the limit of the product of two weakly converging functions. Two methods are usually used to deal with this limit: *the two-scale convergence* [127] (Allaire) and *the compensated compactness* [125, 126] (Tartar and Murat). We recall here the two key theorems to obtain the $H_0^1(D)$-weak convergence of u_ε towards u_0.

Two-scale convergence

For periodic functions, Gregoire Allaire introduced in [127] the notion of two-scale convergence that we recall here.

Theorem 5: Two-scale convergence ([127, Theorem 0.1])

Let v_ε be a bounded sequence in $L^2(D)$. There exists a subsequence (still denoted v_ε) and a function $v_0 \in L^2(D \times Y)$ such that

$$\lim_{\varepsilon \to 0} \int_D v_\varepsilon(x) \psi(x, \frac{x}{\varepsilon}) dx = \int_D \int_Y v_0(x,y) \psi(x,y) dx\, dy \tag{4.17}$$

for any smooth ψ periodic in Y. v_ε is said to two-scale converge to $v_0(x,y)$.

Compensated compactness

Another technique is to use the famous *div-curl* Lemma.

Lemma 6: *div-curl* Lemma

Let $u_n \xrightarrow{L^2(D)} u$ and $v_n \xrightarrow{L^2(D)} v$. Further assume $\nabla \cdot u_n$ and $\nabla \times v_n$ compact in $H^{-1}(D)$, then

$$u_n v_n \xrightarrow{\mathcal{D}'(D)} uv.$$

Using one of these two methods, it can be shown that:

Theorem 7: Periodic homogenization theorem

The unique solution u_ε in $H_0^1(D)$ of:

$$\begin{cases} -\nabla \cdot a_\varepsilon \nabla u_\varepsilon = f & \text{in } D, \\ u_\varepsilon = 0 & \text{on } \partial D \end{cases}$$

converges weakly in $H_0^1(D)$ towards u_0 the solution in $H_0^1(D)$ of:

$$\begin{cases} -\nabla \cdot a^\star \nabla u_0 = f & \text{in } D, \\ u_0 = 0 & \text{on } \partial D \end{cases}$$

and $a^\star$ is defined by (4.15).

We will not go deeper into the details of the proof which can be found in [96] for the method of compensated compactness or in [127], where the two-scale convergence is used.
Note that the homogenized matrix $a^\star$ is independent of f, and can be computed by solving d corrector problems posed on a unit cell. The numerical computation of u only involves macroscopic quantities, and can be done on the macroscopic scale. Consequently, the limiting quantities are much cheaper to compute than the solution u_ε at a given small ε.
The error $\|u_\varepsilon - u\|_{L^2(D)}$ can be quantified by looking at the equation verified by this error term. This is discussed in Section 4.4. To gain in precision and upgrade the convergence to a strong H^1 convergence, one can consider the enriched expansion

$$w_\varepsilon(x) = u(x) + \varepsilon u_1(x, \frac{x}{\varepsilon}).$$

It can be shown, when $u_0 \in H^2(D)$ *i.e.* for D regular enough, that $u_\varepsilon - w_\varepsilon \xrightarrow[\varepsilon \to 0]{H^1(D)} 0$ (see *e.g* [96, 127] for more details). This justifies the formal expansion of Section 4.2.1. Quantitative error estimates can also be obtained (see Section 4.4) but boundary effects must be taken in account (see [128, 129]). This phenomenon is discussed in Section 4.4.3.

4.3 Random setting

For the homogenization process to happen, some sort of disorder averaging must take place. In the periodic setting, this was done by an averaging over the periodicity cell. In random media, an ensemble average is done. In the late 1970s, it was found by Papanicolaou and Varadhan [130] and by Kozlov [131] that a stationary coefficient a_ε with ergodic properties is the perfect framework for homogenization in random media.

The medium is characterized by the coefficient field a_ε modeled as a random process on a probability space $(\Omega, \mathcal{F}, \mathbb{P})$. We assume that for $x \in D$, $\omega \in \Omega$ and $\varepsilon > 0$,

$$a_\varepsilon(x, \omega) := a(\frac{x}{\varepsilon}, \omega).$$

where a is uniformly elliptic *i.e.* there exists $0 < \alpha < \beta$ such that for almost every $\omega \in \Omega$, for all $x \in D$ and for all $\xi \in \mathbb{R}^d$,

$$\alpha|\xi|^2 \leq |a(x, \omega)\xi \cdot \xi| \text{ and } |a(x, \omega)\xi| \leq \beta|\xi|. \tag{4.18}$$

In particular, α, β are independent of the realization ω. Furthermore, a is supposed to be stationary and ergodic. These definitions are recalled here.

Definition 8: Stationarity

Let $(\tau_x)_{x\in\mathbb{R}^d}$ be an action of the group $(\mathbb{R}^d, +)$ on $(\Omega, \mathcal{F})$ that preserves $\mathbb{P}$, *i.e.* we equip $(\Omega, \mathcal{F})$ with $(\tau_x)_{x\in\mathbb{R}^d}$ that verifies:

- the map $\tau : \begin{cases} \mathbb{R}^d \times \Omega & \to & \Omega \\ (x, \omega) & \mapsto & \tau_x\omega \end{cases}$ is measurable,
- $\forall x, y \in \mathbb{R}^d$, $\tau_{x+y} = \tau_x \circ \tau_y$,
- for all $x \in \mathbb{R}^d$, τ_x preserves $\mathbb{P}$, *i.e.*

$$\forall A \in \mathcal{F},\ \mathbb{P}(\tau_x A) = \mathbb{P}(A).$$

A process $f : (\mathbb{R}^d \times \Omega) \mapsto \mathbb{R}^p$ is said to be stationary for the action τ if for all $x, y \in \mathbb{R}^d$, and $\omega \in \Omega$

$$f(x + y, \omega) = f(x, \tau_y\omega).$$

Definition 9: Ergodicity

Let $(\tau_x)_{x\in\mathbb{R}^d}$ be an action of the group $(\mathbb{R}^d, +)$ on $(\Omega, \mathcal{F})$ that preserves $\mathbb{P}$. The action τ is said to be ergodic if for any τ-invariant event has probability 0 or 1, that is,

$$\forall A \in \mathcal{F},\ (\forall x \in \mathbb{R}^d,\ \tau_x^{-1}A = A) \implies (\mathbb{P}(A) \in \{0, 1\}). \tag{4.19}$$

Remark 4.3.1. *The action $(\tau_x)_x$ can also be defined on the group $(\mathbb{Z}^d, +)$. This is the case for conductivity models, for example.*

Intuitively, the stationary assumption ensures a spatial independence of the law of the coefficient. In particular, the expectation of a stationary coefficient is independent of the x-variable. Thus, the homogenized coefficient will also be independent of the

x-variable. Ergodicity is better understood via the ergodic Theorem below, which is a consequence of Birkhoff's ergodic Theorem. More information about ergodic theorems can be found in [132, 133].

Theorem 10: Ergodic theorem

Let $f \in L^1(\Omega, L^1_{loc}(\mathbb{R}^d))$ be a stationary process for the action τ. Assume that τ is ergodic. Then, almost surely and in $L^1(\Omega)$, for all $x \in \mathbb{R}^d$,

$$\frac{1}{|B_R|}\int_{B_R} f(x+y)dy \xrightarrow[R\to\infty]{} \mathbb{E}[f] \tag{4.20}$$

where B_R is the ball of radius $R > 0$ centered in the origin.

Ergodicity is a property that encodes the decorrelation of the process on large domains. In particular, statistical average can be recovered with spatial averages. In a sense, the ergodic theorem can be seen as a law of large numbers, extending the case of identically distributed independent (i.i.d.) random variables. As a consequence of the previous Theorem 10, we have the following lemma:

Lemma 11: Ergodic theorem in $L^2_{loc}(\mathbb{R}^d)$

Let $f \in L^1(\Omega, L^2_{loc}(\mathbb{R}^d))$ be a stationary process for the action τ. Assume that τ is ergodic. Then, almost surely and in $L^1(\Omega)$, for all $x \in \mathbb{R}^d$ and,

$$f(\frac{\cdot}{\varepsilon}) \xrightarrow[\varepsilon\to 0]{L^2_{loc}(\mathbb{R}^d)} \mathbb{E}[f]. \tag{4.21}$$

The weak convergence of $f(\frac{\cdot}{\varepsilon})$ also holds in $L^p_{loc}(\mathbb{R}^d)$ for any $1 < p < \infty$.

Remark 4.3.2. *The periodic framework can be seen as a special case of the stationary and ergodic framework. A Y-periodic coefficient b is stationary for the translation on $\mathbb{Z}^d$, and*

$$\frac{1}{|YR|}\int_{RY} b(x+y)dy = \frac{1}{|Y|}\int_Y b(y)dy$$

for $R \in \mathbb{N}^*$, which corresponds to the ergodic theorem.

Three typical examples of processes satisfying the stationary and ergodic assumptions are presented and illustrated here (see Figure 4.4). First, one can consider an identically distributed independent Bernoulli distribution on each cell of the checkerboard. The coefficient a for the checkerboard is given by

$$a(x) = \begin{cases} a_0 & \text{if } x \text{ is inside a black cells,} \\ a_1 & \text{if } x \text{ is inside a white cells,} \end{cases} \tag{4.22}$$

where $0 < a_0, a_1$. The construction of the coefficient can be easily complexified by choosing another law for each cell, or by correlating the value of the cells with their neighbors.

Secondly, the coefficient a can also be constructed via a homogeneous Poisson point process. We first recall here the definition of a homogeneous Poisson point process.

Definition 12: Homogeneous Poisson point process

X is a Poisson point process on $K \subset \mathbb{R}^d$ with intensity λ if:

- The number of points $N(K)$ sampled with X that falls inside of K are Poisson distributed with mean λ, where a random variable N follows the Poisson distribution if
$$\forall n \in \mathbb{N},\ \mathbb{P}(N = n) = \frac{\lambda^n}{n!}\exp(-n).$$
- For k disjoint bounded Borel sets $A_1, ...A_k$ of K, the random variables $N(A_1), ..., N(A_k)$ are independent.

Typically, an homogeneous Poisson point process is sampled by drawing first the number of points N that lie inside the domain $K \subset \mathbb{R}^d$ from a Poisson distribution with parameter λ and then by uniformly placing them inside K. This gives a set $S := \{x_i\}_{i=1...N}$ of points where x_i is the i-th point.

We then construct $S_0 := \{x \in \mathbb{R}^d \,|\text{dist}(x, S) \leq 1\}$ which corresponds to the union of the balls of radius 1 centered in S. The coefficient a is then defined as:

$$a(x) = \begin{cases} a_0 & \text{if } x \in S_0, \\ a_1 & \text{if } x \notin S_0. \end{cases} \tag{4.23}$$

Once more, the process can be complexified by considering balls of random radii or by considering different values for a in each ball.
In this thesis we will consider a Matèrn point process (see [134, Section 6.5.2]) which is constructed from a Poisson point process and is also stationary and ergodic. It is a thinning of the previous Poisson point process whenever two points are too close from one another. We describe here the thinning process which can also be found in [134].
We are given a intensity λ and a minimal distance r_0. Consider a Poisson point process with intensity λ which engenders the N points $S = \{x_i\}_{i=1....N}$ in a domain $K \subset \mathbb{R}^d$. Assign randomly a score $m_i \in [0, 1]$ to each of the N balls. Then the point x_i is retained if and only if $x_i \notin B(x_j, r_0)$ for all $j \neq i$ such that $m_j < m_i$. This condition is fulfilled whenever no point with a lower score is in the neighborhood of x_i. We end up with a set of $M \leq N$ points and the corresponding balls $S_M \subseteq S_0$ that lie at a distance of r_0 from one another.
This construction corresponds to a (type II) Matèrn point process. It can be shown [134,

Chapter 6.5.2] that the probability to retain the point x_i with score $m(x_i)$ is:

$$r(m(x_i)) = \exp(-\lambda V_d(r_0) m(x_i)),$$

where $V_d(r_0)$ is the volume of the ball of radius r_0 in dimension d. The final intensity of the process is then

$$\lambda_M := p\lambda$$

where p is the Palm retention probability,

$$p := \int_0^1 r(t)dt = \frac{1 - \exp(-\lambda V_d(r_0))}{\lambda V_d(r_0)}.$$

The coefficient a is then defined by:

$$a(x) = \begin{cases} a_0 & \text{if } x \in S_M, \\ a_1 & \text{if } x \notin S_M. \end{cases} \tag{4.24}$$

The process can also be complexified by considering a random minimal distance assigned to each on the point $x \in S$ or by considering different values for a in each ball. We illustrate the three processes on Figure 4.4.

4.3.1 Formal expansion

For a given $\varpi \in \Omega$, we are looking for the solution $u_\varepsilon \in H_0^1(D)$ of:

$$\begin{cases} -\nabla \cdot a_\varepsilon(x) \nabla u_\varepsilon(x) = f(x) & \text{in } D, \\ u_\varepsilon = 0 & \text{on } \partial D. \end{cases} \tag{4.25}$$

As in the periodic framework, we define the microscopic scale $y = \frac{x}{\varepsilon}$ for $x \in D$. We assume the formal expansion:

$$u_\varepsilon(x) = u_0(x, y) + \varepsilon u_1(x, y) + \varepsilon^2 u_2(x, y) + ...,$$

where the functions u_i, $i \geq 0$ are assumed to be stationary processes for the action τ with respect to their second variable. The formal expansion will allow to find the equation on the homogenized solution u_0. However, we insist on the fact that this is only formal. In fact, the terms u_i, $i \geq 0$ are not always stationary as we explain in the next Section 4.3.2. We also emphasize that the microscopic variable y lives in the whole space $\mathbb{R}^d$ and that the study cannot be restrained to a bounded domain. This makes a great difference with the periodic homogenization both in the theoretical and the numerical studies of the homogenization process.

The cascade of equations (4.5), (4.6) and (4.8) remains unchanged. However, it is necessary to find the right functional framework to look for the solutions of (4.5) and for the corrector to conclude on the existence and uniqueness of u_0 and the corrector and the independence of u_0 on the microscopic scale $y \in \mathbb{R}^d$.

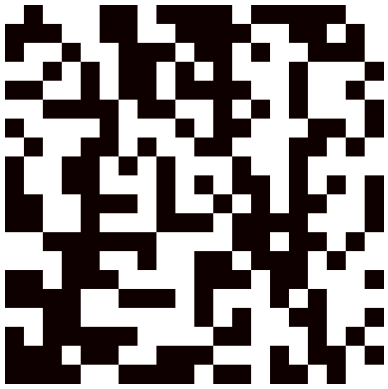

(a) Coefficient a constructed from a random checkerboard on the grid $[-L, L]^2$ with $L = 10$

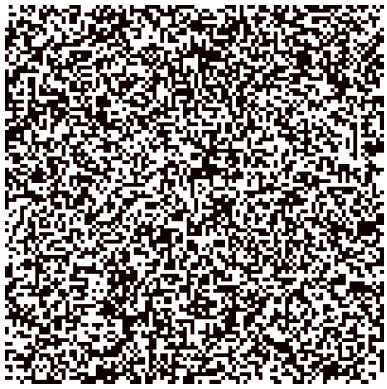

(b) Coefficient a constructed from a random checkerboard on the grid $[-L, L]^2$ with $L = 50$

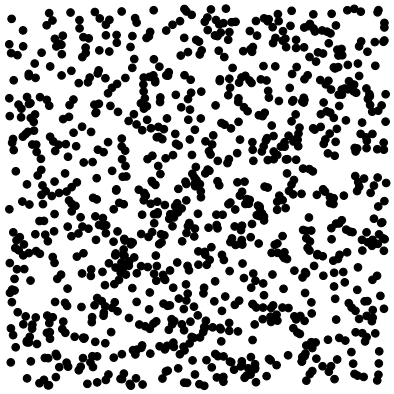

(c) Coefficient a constructed from a Poisson point process on the grid $[-L, L]^2$ with $L = 50$ and $\lambda = 1000$

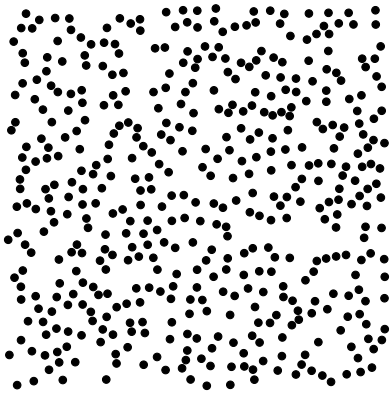

(d) Coefficient a constructed from a Matèrn process on the grid $[-L, L]^2$ with $L = 50$ and $\lambda = 1000$

Figure 4.4: Example of coefficients constructed from a random checkerboard, a Poisson point process and a Matèrn process.

4.3.2 Correctors

Let us assume for now that u_0 is independent of the microscopic scale y and we write $u_0(x,y) = u_0(x)$. This assumption will be justified at the end of this section.
By linearity, u_1 is then defined as

$$u_1(x,y) = \sum_{i=1}^{d} \partial_i u_0 \phi_i(y)$$

where for $1 \leq i \leq d$, ϕ_i is solution of:

$$-\nabla_y \cdot (a(\cdot)e_i + \nabla\phi_i(\cdot)) = 0 \text{ in } \mathbb{R}^d \tag{4.26}$$

The existence and uniqueness (up to a random constant) of $(\phi_i)_{i=1...d}$ can be proved via several methods. The existence can be proven via a Weyl's decomposition [124, Section 7.2]. We define

$$\mathcal{V}_{\text{pot}}(\Omega) := \{f \in L^2(\Omega) \mid \mathbb{E}[f] = 0,\ f \text{ is potential in the sense of (4.27)}\ \},$$

where a potential process f satisfies for all $i,j = 1...d$, $g \in \mathcal{C}_c^\infty(\mathbb{R}^d)$ and *a.e.* $\omega \in \Omega$,

$$\int_{\mathbb{R}^d} \left(\tilde{f}_i \frac{\partial g}{\partial x_j} - \tilde{f}_j \frac{\partial g}{\partial x_i} \right) = 0, \tag{4.27}$$

where $\tilde{f}(\cdot) := f(\tau_\cdot(\omega))$. Note that $\tilde{f} \in L^2_{loc}(\mathbb{R}^d)^d$ admits an almost sure representation of the form

$$\tilde{f} = \nabla\phi$$

for a $\phi \in H^1_{loc}(\mathbb{R}^d)$. The idea is then to prove the existence of the solution $\Psi_i \in \mathcal{V}_{\text{pot}}(\Omega)$ (a closed subset of $L^2(\Omega)$) of:

$$\mathbb{E}[\nabla \cdot a(\Psi_i + e_i)] = 0,$$

and use the representation

$$\tilde{\Psi}_i = \nabla\phi_i$$

to define the corrector ϕ_i.
The existence of the corrector can also be proven by a regularization approach (see [119] or [135]). The idea is to consider a large parameter $T > 0$ and consider the regularized corrector $\phi_{i,T}$ unique solution in $\mathcal{H} := \{\text{a.s. } v \in H^1_{loc}(\mathbb{R}^d) |\ v \text{ stationary, } \mathbb{E}[|v|^2 + |\nabla v|^2] < \infty\}$ of:

$$-\nabla \cdot a\nabla\phi_{i,T} + \frac{1}{T}\phi_{i,T} = \nabla \cdot ae_i. \tag{4.28}$$

The corrector ϕ_i is then constructed as the unique function (up to a random constant) in $H^1_{loc}(\mathbb{R}^d)$ such that

$$\nabla\phi_{i,T} \xrightarrow[T\to\infty]{\mathcal{L}} \nabla\phi_i,$$

where $\mathcal{L} := \{\text{a.s. } v \in L^2_{loc}(\mathbb{R}^d),\ v \text{ stationary},\ \mathbb{E}[|v|^2] < \infty\}$.
For a given $i = 1...d$, the uniqueness is proven by showing that ϕ_i has sublinear growth and adding an anchoring condition. The sublinear growth is proven via the following:

Lemma 13: Sublinearity

Let $u \in L^1(\Omega, H^1_{loc}(\mathbb{R}^d)$ be a process such that ∇u is stationary and $\mathbb{E}[\nabla u] = 0$. Then u has a sublinear growth in the sense that almost surely,

$$\limsup_{R\to\infty} \frac{1}{R^2}\Big(\frac{1}{|B_R|}\int_{B_R} |u|^2\Big) = 0. \tag{4.29}$$

The sublinear growth is a "condition at infinity" which eliminates any linear (or superlinear) solution to (4.26), so that the corrector can be defined up to an additive constant. In the periodic framework, the sublinear growth is ensured by the Poincaré inequality on the periodic cell Y.
We recall here the proper definition of the corrector $(\phi_i)_{i=1...d}$ given in [136, Lemma 1].

Theorem 14: Existence of the corrector [136, Lemma 1]

There exists a unique process $(\phi_i)_{i=1...d}$ (up to a random constant) such that

1. almost surely $(\phi_i)_{i=1...d} \in H^1_{loc}(\mathbb{R}^d)$ is solution in $\mathcal{D}'(\mathbb{R}^d)$ of:

$$-\nabla_y \cdot (a(\cdot)e_i + \nabla\phi_i(\cdot)) = 0 \text{ in } \mathbb{R}^d. \tag{4.30}$$

2. $\nabla\phi_i$ is stationary, has bounded second moments $\mathbb{E}[|\nabla\phi|^2] < \infty$ and has vanishing expectation.

Huge differences with the corrector of periodic homogenization can be pointed out. First of all, the corrector is no longer bounded in L^∞. In particular, this has consequences on the derivation of quantitative results (see Section 4.4 for more details). Secondly, it is shown (see *e.g.* [119]) that no stationary corrector ϕ_i (and thus u_1) can be constructed if $d < 3$, but recall that the gradient of the corrector $\nabla\phi_i$ is stationary. Building on this, Yu Gu shows in [137] that the corrector of order n can be constructed as stationary when $d \geq 2n+1$ and its gradient is stationary when $d \geq 2n-1$ which severely restricts the order of the two-scale expansion, as the corrector u_2 can only be constructed when $d \geq 3$. This is a major difference with periodic homogenization where the correctors exist at every order (as long as the regularity on the coefficients allows their well-definition).
Following the proof of the well-definition of the corrector, it can be shown that the equation (4.5) has a unique solution (up to an additive constant) which justifies that u_0 is independent of the fast scale, and the definition of u_1.

4.3.3 Effective tensor

Still formally, for a fixed $x \in D$, to guarantee the potential existence of a solution $u_2(x,\cdot)$ to (4.8), the source term must satisfy a 0-expectation condition. This leads to

$$-\nabla_x \cdot a^\star \nabla u_0(x) - \mathbb{E}[\nabla_y \cdot a(y)\nabla_x u_1(x,y)] = f(x), \tag{4.31}$$

where the homogenized matrix $a^\star$ reads for $1 \leq i \leq d$:

$$a^\star e_i := \mathbb{E}[a(e_i + \nabla \phi_i)]. \tag{4.32}$$

As we assumed that $u_1(x,\cdot)$ is stationary,

$$\mathbb{E}[\nabla_y \cdot a(y)\nabla_x u_1(x,y)] = 0,$$

where we used that for g stationary, $\mathbb{E}[\nabla \cdot g] = 0$. u_0 is then the unique solution in $H_0^1(D)$ of:

$$\begin{cases} -\nabla \cdot (a^\star \nabla u_0(x)) = f(x) & \text{in } D, \\ u_0 = 0 & \text{on } \partial D, \end{cases} \tag{4.33}$$

The rigorous convergence $u_\varepsilon \xrightarrow{H_0^1(D)} u_0$ is proven for example in [124]. The proof relies on the arguments of Tartar, developed in the periodic setting. The chosen oscillating test functions and their limit are obtained by adjusting some of the arguments of the periodic setting and in particular, using the sublinearity and Birkhoff's ergodic theorem.
As in the periodic case, the computation of $a^\star$ requires the computation of the correctors ϕ_i. However, in the random regime, ϕ_i is the solution in an infinite domain. An artifical boundary condition must be added to compute the corrector. Numerical experiments [138, 139] have shown that the best approximations are obtained with a periodic boundary condition posed on a sufficiently large box [140, 141]. For a defined in (4.22), we simulate and plot on Figure 4.5 the correctors computed with periodic conditions on a large box and illustrate the homogenization process on Figure 4.6

4.4 Towards quantitative homogenization

So far, we only discussed the qualitative convergence of u_ε towards u_0. However, by the Rellich theorem, there exists a subsequence such that $u_\varepsilon \xrightarrow{L^2(D)} u_0$. This naturally raises the question of quantifying the error $\|u_\varepsilon - u_0\|_{L^2(D)}$. By the formal two scale expansion, one expects that

$$\|u_\varepsilon - u_0\|_{L^2(D)} = O(\varepsilon). \tag{4.34}$$

This can be made rigorous but the proof is complex even in the periodic case and requires first to estimate the two-scale error $\|u_\varepsilon - u_0 - \varepsilon u_1\|_{H^1(D)}$ (see [96, 127, 119] for

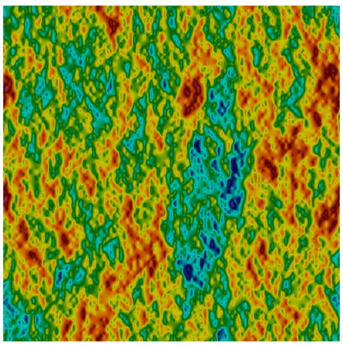

(a) ϕ_1 for a defined by (4.22) in the x_1 direction

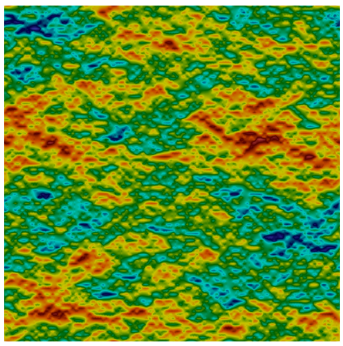

(b) ϕ_2 for a defined by (4.22) in the x_2 direction

Figure 4.5: Correctors of stochastic homogenization for a defined by (4.22) via a random checkerboard with periodic boundary conditions computed on the grid $[-L, L]^2$ with $L = 100$.

more details). We recall that $u_1(x, \frac{x}{\varepsilon}) = \sum_{i=1}^{d} \partial_i u_0(x) \phi_i(\frac{x}{\varepsilon})$. The H^1-regularity of u_1 is achieved by considering a domain D and a source term f sufficiently regular so that $u_0 \in H^2(D)$. We justify in the following sections the result (4.34).

4.4.1 Error estimates

We start with the study of the problem verified by

$$z_\varepsilon(\cdot) := u_\varepsilon(\cdot) - u_0(\cdot) - \varepsilon u_1(\cdot, \frac{\cdot}{\varepsilon}). \tag{4.35}$$

To do so, we consider the flux corrector σ. The flux corrector is a classical quantity in periodic homogenization (see *e.g.* [124]) and was introduced for stochastic homogenization in [142]. We recall here its definition in the stochastic homogenization framework.

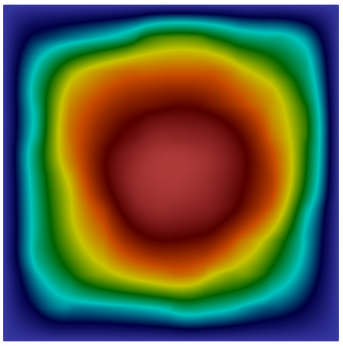

(a) u_ε with $\varepsilon = 1/5$ and $f = 1$

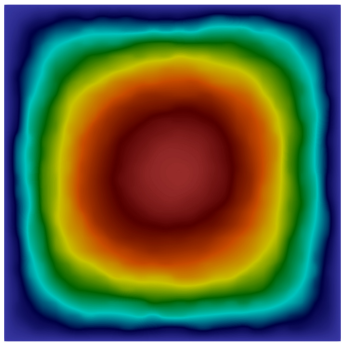

(b) u_ε with $\varepsilon = 1/10$ and $f = 1$

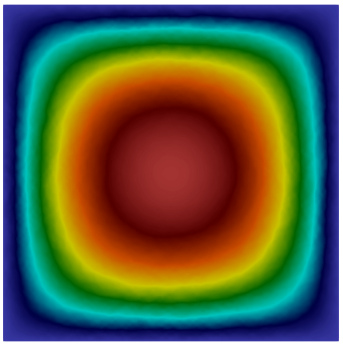

(c) u_ε with $\varepsilon = 1/100$ and $f = 1$

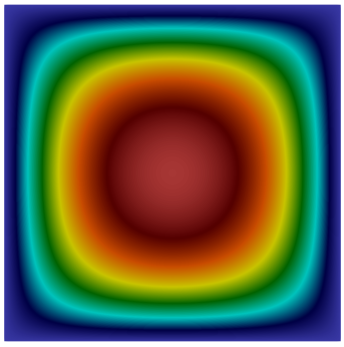

(d) Homogenized solution u_0

Figure 4.6: Illustration of the homogenization process - Solutions u_ε of (4.25) for several values of ε (with a defined by (4.22)) and limiting solution u_0.

Theorem 15: Existence of the flux corrector [136, Lemma 1]

Let $\sigma := (\sigma_{i,jm})_{i,j,m\in[\![1,d]\!]}$ be the unique tensor field such that for all $i,j,m \in [\![1,d]\!]$, a.s. $\sigma_{i,jm} \in H^1_{loc}(\mathbb{R}^d)$ is the solution in $\mathcal{D}'(\mathbb{R}^d)$ of:

$$-\Delta\sigma_{i,jm}(y) = \partial_j q_{im}(y) - \partial_m q_{ij}(y), \tag{4.36}$$

with

$$q_i := a(e_i + \nabla\phi_i) - a^{hom}e_i, \tag{4.37}$$

and is anchored with the condition:

$$\frac{1}{|Y|}\int_Y \sigma_{i,jm} = 0. \tag{4.38}$$

Furthermore, σ_i is skew-symmetric and verifies a.s.

$$\nabla\cdot\sigma_i = q_i, \tag{4.39}$$

where for $i,j \in [\![1,d]\!]$,

$$(\nabla\cdot\sigma_i)_j := \sum_{m=1}^{d}\partial_m\sigma_{i,jm}. \tag{4.40}$$

Furthermore, $\nabla\sigma_{i,jm}$ is stationary, has finite second moments and vanishing expectation.

The two scale error z_ε then satisfies in $\mathcal{D}'(D)$,

$$\begin{aligned} -\nabla\cdot a_\varepsilon\nabla z_\varepsilon &= -\sum_{i=1}^{d}\nabla\cdot(a_\varepsilon e_i - a^\star(e_i+\nabla\phi_i)\partial_i u_0 + \nabla\cdot a_\varepsilon\phi_i\nabla(\partial_i u_0) \\ &= \varepsilon\sum_{i=1}^{d}\nabla\cdot((a_\varepsilon\phi_i - \sigma_i)\nabla(\partial_i u_0)). \end{aligned} \tag{4.41}$$

We are willingly avoiding the question of the boundary condition as it poses severe problems in the quantitative estimations.
In the periodic setting, the estimation of the two-scale error amounts to the estimation of $\left\|\phi(\frac{\cdot}{\varepsilon})\right\|_{L^2(D)}$ and $\left\|\sigma(\frac{\cdot}{\varepsilon})\right\|_{L^2(D)}$. Thanks to the periodicity, the corrector and the flux corrector are uniformly bounded in $L^\infty(D)$ which allows to conclude that in view of (4.41) the bulk z_ε is typically of order ε.
In the stochastic setting, the previous arguments do not apply and the analysis is more delicate. The ergodic assumption is a purely qualitative description of the decorrelation of a. Though, the estimation of $\left\|\phi(\frac{\cdot}{\varepsilon})\right\|_{L^2(D)}$ depends on the correlation of the process a. Therefore, without any further quantitative ergodic assumptions on the stationary process a, the norm of these two correctors cannot be estimated. In the following

Section 4.4.2, we present different quantitative stochastic homogenization assumptions and the associated corrector bounds.

4.4.2 Quantitative ergodicity assumptions

We recall that the correlation function of a is defined for $x \in \mathbb{R}^d$ by

$$\mathcal{C}_a(x) = \mathrm{Cov}[a(\cdot), a(\cdot + x)].$$

Intuitively, quantifying the decorrelation properties of a amounts to describe "how fast" $\mathcal{C}_a$ decreases. A first common assumption is to consider a strongly linear mixing hypothesis for a.

Linear mixing assumption

Two typical linear mixing assumptions can be made for a - finite range dependence or α-mixing. These two assumptions are presented here.
First, for all Borel subsets $\mathcal{U} \subset \mathbb{R}^d$, we define $\mathcal{F}_\mathcal{U}$ as the σ-algebra generated by $a(x)$ for $x \in \mathcal{U}$. One simple assumption to quantify the decorrelation of a is a finite range of dependence:

Definition 16: Finite range of dependence

The process a is said to be of l-range of dependence if there exists $l > 0$ such that for all $\mathcal{U}, \mathcal{V} \subset \mathbb{R}^d$, we have:

$$\mathrm{dist}(\mathcal{U}, \mathcal{V}) \geq l \implies \mathcal{F}_\mathcal{U} \text{ and } \mathcal{F}_\mathcal{V} \text{ are independent.} \tag{4.42}$$

In this case, the covariance function $\mathcal{C}_a$ has a compact support. The random checkerboard with i.i.d. cells typically satisfies the a 1-range of dependence, as the color of two cells of the board are totally independent.
This assumption is used in [143, 144] and in the book [119] by Scott Armstrong, Tuomo Kuusi, and Jean-Christope Mourrat to show quantitative results on the correctors and on the two-scale expansion. Both teams have independently proven optimal results in this setting.
To describe the correlation properties of some complex processes that exhibit correlation at any finite distance, one can use a α-mixing hypothesis.

Definition 17: α-mixing hypothesis

The process a is said to be α-mixing if there exists $C > 0$ and $\alpha > 0$ such that for all $\mathcal{U}, \mathcal{V} \subset \mathbb{R}^d$, $A \in \mathcal{F}_\mathcal{U}$ and $B \in \mathcal{F}_\mathcal{V}$, we have

$$|\mathbb{P}(A \cap B) - \mathbb{P}(A)\mathbb{P}(B)| \leq C(1 + \mathrm{dist}(\mathcal{U}, \mathcal{V}))^{-\alpha} \tag{4.43}$$

The covariance function $C_a(x)$ is then assumed to decrease like $\frac{1}{(1+x)^\alpha}$. Several behaviors can be observed whether $\alpha > d$ or $d \leq \alpha$. Indeed, in the case where $\alpha > d$, the covariance function is integrable. The quantification of the limiting distribution of $u_\varepsilon - u_0$ in a one-dimensional problem was studied for both integrable (short-range correlation) in [145] and non-integrable (long-range correlation) covariance functions in [146].
There exists other mixing assumptions (β-mixing, γ-mixing) described in [133] to which we refer for more information about mixing-conditions.

Non-linear mixing assumption - multiscale variance inequality

The corrector depends non-linearly on the coefficient a. The previous α-mixing assumption does not allow to link the properties of the correctors ϕ_i, $i = 1..d$ to those of a and to obtain bounds for $\left\|\phi_i(\frac{\cdot}{\varepsilon})\right\|_{L^2(D}$. For correlated processes a, we then rely on functional inequalities that bound the variance of any $F(a)$ in terms of its functional derivative with respect to a. We first define the functional derivative $\partial^{\text{fct}}_{a,B(x)}$ which designates either:

- $\partial^{\text{fct}}_{a,B(x)}F(a) := \int_{B(x)} |\frac{\partial F(a)}{\partial a}|$ with $\frac{\partial F(a)}{\partial a}$ the Malliavin derivative of F (see [147] for more information on the Malliavin calculus) when the field a is a Gaussian field with integrable covariance.

or

- $\partial^{\text{fct}}_{a,B(x)} := \partial^{\text{osc}}_{a,B(x)}$, the oscillatory derivative:

$$\partial^{osc}_{a,B(x)}F(a) := \text{sup ess}\left\{F(a')|a'_{|_{\mathbb{R}^d\setminus B(x)}} = a_{|_{\mathbb{R}^d\setminus B(x)}}\right\} - \text{inf ess}\left\{F(a')|a'_{|_{\mathbb{R}^d\setminus B(x)}} = a_{|_{\mathbb{R}^d\setminus B(x)}}\right\}.$$

Here, $B(x)$ denotes the unit ball centered at x. The simplest functional inequality is the following Poincaré or spectral gap inequality:

Definition 18: Poincaré inequality

We say that a verifies a Poincaré inequality if there exists $C > 0$ such that for all $\sigma(a)$-measurable square integrable random variable $F(a)$,

$$\text{Var}[F(a)] \leq C\mathbb{E}\left[\int_{\mathbb{R}^d}\left|\partial^{\text{fct}}_{a,B(x)}F(a)\right|^2 dx\right]. \tag{4.44}$$

Another common functional inequality is the following logarithmic Sobolev inequality which reads as:

Definition 19: Logarithmic Sobolev inequality

We say that a verifies a logarithmic Sobolev inequality if there exists $C > 0$ such that for all $\sigma(a)$-measurable square integrable random variable $F(a)$,

$$\begin{aligned} \mathrm{Ent}[F(a)^2] &:= \mathbb{E}\left[F(a)^2 \log\left(\frac{F(a)^2}{\mathbb{E}[F(a)]^2}\right)\right] \\ &\leq C\mathbb{E}\left[\int_{\mathbb{R}^d} \left|\partial^{\mathrm{fct}}_{a,B(x)} F(a)\right|^2 dx\right]. \end{aligned} \tag{4.45}$$

The idea behind the functional inequalities is to see how fast the random variable $F(a)$ oscillates with respect to the randomness. That is, for two realizations a and a' that are "close" in the sense they only differ locally around x, to understand how "close" $F(a)$ and $F(a')$ are. If they are close, then F is not very sensitive to a at x, and $|\partial^{\mathrm{fct}}_{a,B(x)} F(a)|$ is small. The mathematical theory behind the Malliavin's calculus requires more advanced probabilistic tools which are not presented here, but we refer to the books [148, 147]. Unfortunately, this formalism is only applicable under strong hypothesis on the structure of a (Gaussian with integrable covariance for the Malliavin's derivative, product measure for the oscillatory derivative). That is why in [149], Antoine Gloria and Mitia Duerinckx introduce *multiscale functional inequalities*, which are weighted versions of the standard functional inequalities, but hold in a more general setting (see [149, 150] for more details). Furthermore, in [150], the link between α-mixing properties and spectral-gap inequalities is proven.
In this thesis, we consider a Matèrn point process to model the distribution of the heterogeneities. We recall the weighted multiscale variance inequality (see [149, Section 3]) verified by this process. Note that other common hardcore point processes such as random parking also verify Hypothesis 20.

Hypothesis 20: Mixing hypothesis

There exists a non-increasing integrable weight function $\pi : \mathbb{R}^+ \to \mathbb{R}^+$ such that a verifies for all $\sigma(a)$-measurable square integrable random variable $F(a)$,

$$\mathrm{Var}\left[F(a)\right] \leq \mathbb{E}\left[\int_1^{+\infty} \int_{\mathbb{R}^d} \left(\partial^{osc}_{a,B_\ell(x)} F(a)\right)^2 \mathrm{d}x \ell^{-d} \pi(\ell - 1) \mathrm{d}\ell\right], \tag{4.46}$$

where $B_\ell(x)$ is the ball with radius $\ell \geq 0$ and center $x \in \mathbb{R}^d$ and the oscillation $\partial^{osc}_{a,B_\ell(x)}F(a)$ of $F(a)$ with respect to S on $B_\ell(x)$ is defined by:

$$\partial^{osc}_{a,B_\ell(x)}F(a) := \text{sup ess}\left\{F(a')|a'_{|_{\mathbb{R}^d\setminus B_\ell(x)}} = a_{|_{\mathbb{R}^d\setminus B_\ell(x)}}\right\} - \text{inf ess}\left\{F(a')|a'_{|_{\mathbb{R}^d\setminus B_\ell(x)}} = a_{|_{\mathbb{R}^d\setminus B_\ell(x)}}\right\}.$$

Remark 4.4.1. *In view of [150, Proposition 1.3], if a verifies Hypothesis 20 then the covariance function of $\mathcal{C}_a(x)$ satisfies*

$$\forall x \in \mathbb{R}^d,\ |\mathcal{C}_a(x)| \leq C\int_{\max(\frac{1}{2}(|x|-2),0)}^{\infty}\pi(\ell)\mathrm{d}\ell, \tag{4.47}$$

for some $C > 0$.

Proposition 21: [Matèrn process [149, Proposition 3.3]]

The Matèrn point process verifies (4.46) with the weight function π:

$$\pi(l) = Ce^{-\frac{1}{C}l} \tag{4.48}$$

for some $C > 0$.

Antoine Gloria, Felix Otto and their collaborators also obtained quantitative results on the corrector first in a discrete setting in [151, 152], by using a discrete version of the spectral gap inequality of Definition 18. The results are then extended in the continuum setting with the spectral gap inequality of Definition 18 [135] and for the weighted multiscale functional inequalities [142].

Corrector bounds

Using quantitative ergodic assumptions, the L^2-norm of the corrector can be estimated. In particular, we recall here the result obtained in [142, Theorem 4] regarding coefficients that satisfies Hypothesis 20 with a weight π with super-algebraic decay. We will rely on these results in Part II to derive quantitative homogenization estimates for our problem.
We define for any integrable function f and any domain D the notation $⨍_D f$ as

$$⨍_D f := \frac{1}{|D|}\int_D f.$$

Proposition 22: Corrector bounds [142, Theorem 4]

Assume that a verifies the mixing Hypothesis 20 with weight π with super-algebraic decay.

(a) ($\mathbb{P}-a.s.$ corrector bound):
There exists an a.s. finite (non-stationary) random field $x \mapsto \mathcal{C}(x)$ such that for all $x \in \mathbb{R}^d$,

$$\left(\fint_{\square_x} |\phi|^2 + |\sigma|^2\right)^{\frac{1}{2}} \leq \mathcal{C}(x)\mu_d(|x|), \tag{4.49}$$

where for all $y \in \mathbb{R}^+$,

$$\mu_d(y) = \begin{cases} \sqrt{y} & \text{if } d = 1, \\ |\log(2+y)|^{\frac{1}{2}} & \text{if } d = 2, \\ 1 & \text{if } d = 3. \end{cases} \tag{4.50}$$

and $\square_x$ denotes the unit square centered at x

$$\square_x := [-\frac{1}{2} + x, \frac{1}{2} + x]^d. \tag{4.51}$$

(b) (Corrector bound in average):
Furthermore, for all $y \in \mathbb{R}^d$, $\mathcal{C}(y)$ satisfies the following stochastic integrability

$$\mathbb{E}[\exp(\frac{1}{C}\mathcal{C}(y)^\gamma)] \leq 2 \tag{4.52}$$

for some constant $C > 0$ depending on d, α, β and exponent $\gamma > 0$ depending on d and the exponential decay rate of π.

(c) (Mean-value property):
There exists a stationary $\frac{1}{8}$-Lipschitz continuous random field $r_* > 1$ (the so-called minimal radius) satisfying (4.52) such that for all $\ell \geq 1$

$$\int_{B_\ell(x)} |\nabla\phi|^2 \lesssim (\ell + r_*(x))^d. \tag{4.53}$$

Remark 4.4.2. *When a is shows finite range dependence (4.49) also holds [119]. When $\pi(\ell) \sim \frac{1}{(1+\ell)^\alpha}$, the bounds depends on the exponent α and on the dimension d (see [142, Theorem 2].*

Fluctuations

In the random setting, it is also interesting to quantify the fluctuations of the solution around its limiting process. Typically, fluctuations can be characterized either by the

stronger norm,

$$F_s = \mathrm{Var}[\|u_\varepsilon - u_0\|_{L^2(D)}],$$

or the weaker norm

$$F_w(g) = \mathrm{Var}\left[\int_D (u_\varepsilon(x) - u_0(x))g(x)dx\right],$$

for $g \in \mathcal{C}_c^\infty(D)$. One can also be interested in the fluctuations of the gradient or the flux in a weak norm, as u_ε converges weakly towards u_0 in $H_0^1(D)$ and the flux converges weakly in $L^2(D)$. The quantification of F_s has already been presented in Section 4.4.2. The problem of the quantification of $F_w(g)$ is presented and treated in the series of work [18, 19, 153]. As expected, the results depend on the quantitative ergodic assumptions on a. The authors identify in [18] a quantity the so-called *homogenization commutator* which allows to recover both the fluctuations of the gradient and the flux. This quantity is the vector field Ξ defined for $i = [\![1, N]\!]$ as:

$$\Xi_i := (a - a^\star)(\nabla\phi + e_i). \tag{4.54}$$

In particular, it is shown in [19] that for all $g \in \mathcal{C}_c^\infty(\mathbb{R}^d)^d$.

$$\mathrm{Var}\left[\varepsilon^{-\frac{d}{2}}\int_{\mathbb{R}^d}(a_\varepsilon - a^\star)\nabla u_\varepsilon \cdot g - \sum_{i=1}^d \Xi_i(\frac{\cdot}{\varepsilon})\partial_i u_0 \cdot g\right]^{\frac{1}{2}} \leq C\varepsilon\mu_d(\frac{1}{\varepsilon}), \tag{4.55}$$

for some $C > 0$. We will be using this result in Part II to derive a high-order homogenization result for our problem. Note that in [19], results are also obtained for Gaussian processes a with non-integrable covariance. The characterization of the fluctuations can also be used to establish the equivalent of a central limit theorem for $u_\varepsilon - u_0$ which is done in [146] in a 1-dimensional case. In [146] for a α-mixing process a (for $\alpha < 1$), the limiting distribution of $\frac{u_\varepsilon - u_0}{\varepsilon^{\frac{\alpha}{2}}}$ is obtained by studying the fluctuations of $\frac{1}{a} - \frac{1}{a^\star}$. We also mention the works by Bal and his coauthors [154, 155], where the fluctuations of $\frac{u_\varepsilon - u_0}{\varepsilon}$ are characterized when u_ε is the solution of a linear [154] and semilinear [155] elliptic equation perturbed by a random potential. In [156], the scaling limit of the commutator is studied for both weakly and strongly correlated Gaussian coefficients.

Error estimates on the two-scale error in the bulk

We present here quantitative results on the two-scale error in the bulk both for the periodic and stochastic settings.

It holds in the **periodic homogenization** framework that

Theorem 23: [128, Theorem 2.3]

Assume that $u_0 \in W^{3,\infty}(D)$ for any subset $K \subset\subset D$ compactly embedded in D, there exists a constant C, depending on K but not on ε, such that

$$\left\| u_\varepsilon(\cdot) - u_0(\cdot) - \varepsilon u_1(\cdot, \frac{\cdot}{\varepsilon}) \right\|_{H^1(K)} \lesssim C\varepsilon. \tag{4.56}$$

In the **stochastic homogenization** framework, consider that $D = \mathbb{R}^d$ and that f has a compact support. In this setting, it is proven under finite range dependency that:

Theorem 24: [119, Theorem 6.3]

Assume that $u_0 \in W^{2,\infty}(D)$, it holds

$$\mathbb{E}\left[\left\| \nabla \cdot a_\varepsilon(\cdot) \nabla (u_\varepsilon(\cdot) - u_0(\cdot) - \varepsilon u_1(\cdot, \frac{\cdot}{\varepsilon})) \right\|^2_{H^{-1}(D)} \right]^{\frac{1}{2}} \lesssim \varepsilon \mu_d(\frac{1}{\varepsilon}) \left\| u_0 \right\|_{W^{2,\infty}(D)}. \tag{4.57}$$

Remark 4.4.3. *When u_0 is only in $W^{1+\alpha,p}(D)$ for $\alpha > 0$ and $p > 2$, error estimates can still be obtained but the two-scale error is deteriorated (see [119, Chapter 6.2]).*

Remark 4.4.4. *The result of Theorem 24 also holds when a is a correlated field that satisfies a (weighted) spectral gap inequality [142, 157].*

We expect z_ε to converge in $H^1(D)$. However, in the bounded domain D, z_ε does not satisfy a homogeneous Dirichlet boundary condition.
To compensate for this mismatch, a boundary layer corrector must be added. This deteriorates the two-scale error and this is the topic of the next Section 4.4.3.

4.4.3 Boundary layers

It can be shown [128] that $\|z_\varepsilon\|_{H^1(D)} = O(\varepsilon^{\frac{1}{2}})$:

Proposition 25: Two-scale error with Dirichlet boundary condition (periodic homogenization) [128]

Under the previous regularity assumptions on u_0, the two-scale error for periodic homogenization with Dirichlet boundary conditions satisfies:

$$\left\| u_\varepsilon(\cdot) - u_0(\cdot) - \varepsilon u_1(\cdot, \frac{\cdot}{\varepsilon}) \right\|_{H^1(D)} \lesssim \varepsilon^{1/2} \left\| u_0 \right\|_{W^{2,\infty}(D)}. \tag{4.58}$$

and

Proposition 26: Two-scale error with Dirichlet boundary (stochastic homogenization) [119, Chapter 6.3]

Under finite range assumptions on a and the previous $W^{2,\infty}(D)$ regularity assumption on u_0, the two-scale error for stochastic homogenization with Dirichlet boundary conditions satisfies:

$$\mathbb{E}\left[\left\|u_\varepsilon(\cdot) - u_0(\cdot) - \varepsilon u_1(\cdot, \frac{\cdot}{\varepsilon})\right\|_{H^1(D)}^2\right]^{\frac{1}{2}} \lesssim \varepsilon^{1/2}\mu_d(\frac{1}{\varepsilon})^{1/2}\left\|u_0\right\|_{W^{2,\infty}(D)}. \tag{4.59}$$

The convergence in $\mathcal{O}(\varepsilon^{\frac{1}{2}})$ rather than $\mathcal{O}(\varepsilon)$ is due to so-called *boundary layer tail* (see [128]). Note that this phenomenon also occurs for Neumann or Robin boundary conditions.
To estimate the H^1-norm of the two-scale error $\|z_\varepsilon\|_{H^1(D)}$, a boundary layer corrector θ_ε is added to z_ε to study a simpler problem with homogeneous boundary condition. It was introduced for periodic homogenization by Allaire in [128] to study the two-scale error for the problem (4.4). This boundary layer corrector θ_ε is then defined as the unique solution in $H^1(D)$ of:

$$\begin{cases} -\nabla\cdot(a_\varepsilon(\cdot)\nabla\theta_\varepsilon(\cdot)) = 0 & \text{in } D, \\ \theta_\varepsilon(\cdot) = u_1(\cdot, \frac{\cdot}{\varepsilon}) & \text{on } \partial D. \end{cases} \tag{4.60}$$

It is shown ([128] for periodic homogenization

$$\left\|u_\varepsilon(\cdot) - u_0(\cdot) - \varepsilon\left(u_1(\cdot, \frac{\cdot}{\varepsilon}) - \theta_\varepsilon(\cdot)\right)\right\|_{H^1(D)} \lesssim \varepsilon\left\|u_0\right\|_{W^{2,\infty}(D)}. \tag{4.61}$$

Furthermore,

$$\left\|\theta_\varepsilon\right\|_{H^1(D)} \lesssim \varepsilon^{-1/2}\left\|u_0\right\|_{W^{2,\infty}(D)}, \tag{4.62}$$

which allows to recover (4.58).

Remark 4.4.5. *It was shown in [158] for Dirichlet boundary conditions and [159] for Neumann boundary conditions that the regularity required on u_0 is in fact only $H^2(D)$.*

For stochastic homogenization and a with finite range dependence [119, Chapter 6.3], it holds that

$$\mathbb{E}\left[\left\|u_\varepsilon(\cdot) - u_0(\cdot) - \varepsilon\left(u_1(\cdot, \frac{\cdot}{\varepsilon}) - \theta_\varepsilon(\cdot)\right)\right\|_{H^1(D)}^2\right]^{\frac{1}{2}} \lesssim \varepsilon\mu_d(\frac{1}{\varepsilon})\left\|u_0\right\|_{W^{2,\infty}(D)}. \tag{4.63}$$

Furthermore,

$$\mathbb{E}\left[\left\|u_\varepsilon(\cdot) - u_0(\cdot) - \varepsilon\left(u_1(\cdot, \frac{\cdot}{\varepsilon}) - \theta_\varepsilon(\cdot)\right)\right\|_{H^1(D)}^2\right]^{\frac{1}{2}} \lesssim \varepsilon\mu_d(\frac{1}{\varepsilon})^{1/2}\left\|u_0\right\|_{W^{2,\infty}(D)}, \tag{4.64}$$

which allows to recover (4.59).
From a numerical point of view, this boundary layer is a real disaster. To obtain an error in ε, it is necessary to compute θ_ε which solves an oscillating equation with oscillating boundary conditions. This problem is as costly as the initial problem. This explains why there is active research on approximations of the boundary layer corrector.
In the periodic homogenization setting, (4.62) has been established in [128]. The boundary layer must then be taken into account to build higher-order correctors, that approximates $u_\varepsilon \in H^1(D)$. In particular, it requires to deeply understand the homogenization of the boundary layer corrector problem, which strongly depends on the boundary of the domain. The first results were obtain for polygonal domain with rational slopes [160, 128]. For such problems, the homogenization process depends on the chosen subsequence ε as discussed in [160]. Indeed, in the latter [160], it was noticed by Santosa and Vogelius that the boundary corrector can have several limits. The phenomenon was then proven by Moskow and Vogelius and in [158] and they furthermore characterized the possible limits of the boundary correctors. In [161], Gérard-Varet and Masmoudi consider the case of polygonal domain with irrational slopes under a diophantine condition on the normals. The diophantine approximation measures how well an irrational number can be approximated by a rational one. The expected convergence of $\mathcal{O}(\varepsilon)$ in the interior of D is recovered. They extend their result in [162] to the case of uniformly convex domain, although they obtain a deteriorated convergence rate. Finally, in [163], the convergence for any irrational slope is considered and it is shown that in the very general case, the homogenization convergence of the boundary layer corrector is arbitrarily slow.
The behavior of the limit of the eigenvalues of the homogenization problem (4.4) has been studied in [158] for Dirichlet boundary conditions and [159] for Neumann boundary conditions. The behavior of these eigenvalues also depends on the interaction of the micro-structure at the boundary of the domain. In the stochastic homogenization framework, homogenization results with boundaries have also been obtained for Dirichlet or Neumann condition [119] (up to a factor $\mu_d(\frac{1}{\varepsilon})$). Moreover in [164], quantitative results for the two-scale expansion for the case of the interface problem between two heterogeneous media problem are obtained and in [165] quantitative decay estimates for the boundary layer corrector in stochastic homogenization in the case of a half-space boundary has been obtained.
The boundary corrector has also been studied for wave propagation phenomena. In particular, in [129], the construction of high order effective boundary conditions is proposed for the Helmholtz equation in the case of a periodic domain with Dirichlet and Neumann boundary conditions and the conditions are efficiently numerically implemented.
In this thesis, we consider the scattering by a random domain with highly oscillating acoustic properties, *i.e.* the solution of (3.11) where the coefficients a_ε and n_ε are given by (3.12). A similar problem but in the periodic setting was studied in the series of work [166, 167, 168] by Shari Moskow and Fioralba Cakoni, in which they consider a transmission problem in a highly oscillating periodic medium. More precisely, they the

study the unique solution $u_\varepsilon \in H^1(D) \times H^1_{loc}(\mathbb{R}^d \setminus \overline{D})$ of:

$$\begin{cases} -\nabla \cdot \left(a_\varepsilon(x)\nabla u_\varepsilon^+(x)\right) - k^2 n_\varepsilon(x) u_\varepsilon^+(x) = 0 & \text{for } x \in D, \\ -\Delta u_\varepsilon(x)^- - k^2 u_\varepsilon^-(x) = 0 & \text{for } x \in \mathbb{R}^d \setminus \overline{D}, \\ a_\varepsilon \nabla u_\varepsilon^+ \cdot \nu - \nabla u_\varepsilon^- \cdot \nu = f & \text{on } \partial D, \\ u_\varepsilon^+ - u_\varepsilon^- = g & \text{on } \partial D, \\ \lim\limits_{|x|\to+\infty} |x|^{\frac{d-1}{2}} \left(\dfrac{\partial(u_\varepsilon - u^i)}{\partial |x|}(x) - ik\,(u_\varepsilon^- - u^i)(x) \right) = 0 \end{cases} \tag{4.65}$$

where a_ε and n_ε are periodic coefficients satisfying the assumptions of Section 4.2. The superscript $+$ and $-$ designate the solution in the interior of the exterior of D respectively. $f \in H^{-\frac{1}{2}}(\partial D)$ and $g \in H^{\frac{1}{2}}(\partial D)$ are the sources terms. u_ε converge weakly in $H^1(D) \times H^1_{loc}(\mathbb{R}^d \setminus \overline{D})$ towards u_0 which is unique the solution of:

$$\begin{cases} -\nabla \cdot \left(a^\star(x)\nabla^+ u_0(x)\right) - k^2 n^\star(x) u_0^+(x) = 0 & \text{for } x \in D, \\ -\Delta u_0^-(x) - k^2 u_0^-(x) = 0 & \text{for } x \in \mathbb{R}^d \setminus \overline{D}, \\ a^\star \nabla u_0^+ \cdot \nu - \nabla u_0^- \cdot \nu = f & \text{on } \partial D, \\ u_0^+ - u_0^- = g & \text{on } \partial D, \\ \lim\limits_{|x|\to+\infty} |x|^{\frac{d-1}{2}} \left(\dfrac{\partial(u_0 - u^i)}{\partial |x|}(x) - ik\,(u_0^- - u^i)(x) \right) = 0 \end{cases} \tag{4.66}$$

with $n^\star = \int_Y n(y)dy$ and $a^\star$ is defined in (4.15). To study the two-scale error, they first prove (under regularity assumptions on u_0) a two-scale expansion with a boundary layer corrector which reads as:

$$\|u_\varepsilon - u_0 - \varepsilon u_{1,\varepsilon} - \varepsilon\theta_\varepsilon\|_{H^1(D)} \leq C\varepsilon \|u_0\|_{W^{2,\infty}(D)}, \tag{4.67}$$

where $u_{1,\varepsilon}(x) := \sum_{i=1}^{d} \phi_i(x)\partial_i u_0(x)$ with ϕ the corrector of (4.12) and $\theta_\varepsilon \in H^1(D) \times H^1(\mathbb{R}^d \setminus \overline{D})$ is the boundary corrector which satisfies a problem similar to (4.65), but with oscillating boundary data f and g. The problem then amounts to the study of θ_ε in order to derive quantitative results on the two-scale error. They also derive an order 2 asymptotic expansion and study the problem for polygonal domains so that they can obtain an asymptotic $\theta^\star$ of θ_ε. In this thesis, we prove a similar result to (4.67) in the random setting and we quantify the two-scale error on the scattered field in $\mathbb{R}^d \setminus \overline{D}$. To that aim, an approach similar to the one of [167] is considered but with several differences. Indeed, the mathematical tools that are involved are different in the context of stochastic homogenization, as the corrector presents several dissimilarities that were discussed in Section 4.3.2.

We also mention the work of [169]. A transmission problem between a homogeneous half space and a periodic half space is also addressed but the techniques involved are different, a so-called *matched asymptotic expansion* is used.

The study of the homogenization of (3.11) is the topic of the following Part II.

PART II

SCATTERED WAVEFIELD IN THE STOCHASTIC HOMOGENIZATION REGIME

CHAPTER 5

Introduction

Abstract

In the context of providing a mathematical framework for the propagation of ultrasound waves in a random multiscale medium, we consider the scattering of classical waves (modeled by a divergence form scalar Helmholtz equation) by a bounded object with a random composite micro-structure embedded in an unbounded homogeneous background medium. Using *quantitative* stochastic homogenization techniques, we provide asymptotic expansions of the scattered field in the background medium with respect to a scaling parameter describing the spatial random oscillations of the micro-structure. Introducing a boundary layer corrector to compensate for the breakdown of stationarity assumptions at the boundary of the scattering medium, we prove quantitative L^2- and H^1- error estimates for the asymptotic first-order expansion. The theoretical results are supported by numerical experiments.

Keywords: Helmholtz equation, quantitative stochastic homogenization, transmission problem, boundary layer

French abstract

Afin de fournir un cadre mathématique pour l'étude de la propagation d'ondes ultrasonores dans un milieu aléatoire à plusieurs échelles, nous considérons, classiquement, la diffusion d'ondes (modélisées par une équation de Helmholtz scalaire de forme divergente) par un objet limité avec une micro-structure composite aléatoire incorporée dans un milieu de fond homogène non limité. En utilisant des techniques d'homogénéisation stochastique *quantitative*, nous fournissons des développements asymptotiques du champ diffusé dans le milieu environnant par rapport à un paramètre d'échelle décrivant les oscillations spatiales aléatoires de la micro-structure. En introduisant un correcteur de couche limite pour compenser la rupture des hypothèses de stationnarité à la limite du milieu diffusant, nous prouvons des estimations quantitatives de l'erreur en norme L^2- et H^1- pour le développement asymptotique jusqu'au premier ordre. Les résultats théoriques sont étayés par des expériences

numériques.

Mots-clés: équation de Helmholtz, homogénéisation stochastique quantitative, problème de transmission, couche limite

Introduction

The emergence of quantitative medical imaging techniques that can map the numerical value of a physical parameter in a biological tissue constitutes a major shift of paradigm for the theory of inverse problems. Imaging modalities are now expected not only to produce images that are anatomically accurate (structural images) but also stably and quantitatively reconstruct parameters of interest that can help discriminate pathological states.

Medical ultrasound imaging is a powerful, safe, portable and cheap imaging modality that is used in countless physical exams. Ultrasonic pulses (in the MHz range) are transmitted into the region of interest and the images are obtained by numerically backpropagating the echoes generated by the tissues and recorded on a receiver array. Each tissue and its pathological state will be characterized by a distinct type of speckle on the image.

The technique relies on the fact that most soft tissues have a mass density and compressibility close to those of water (and ultrasonic waves travel in these tissues almost as in water) yet have echogenic properties that can be explained by the presence of acoustic heterogeneities of characteristic size much smaller than the wavelength, see [170].

The quantification of these echogenic properties (known in the literature as *backscattering coefficient estimation* [171]) relied until now on the introduction of an *ultrasonic reflectivity* [91] and approximations of the scattered field derived under a set of restrictive hypotheses that do not hold in many practical situations (usually assumptions of the low scatterer concentration, single scattering regime, strictly homogeneous mass density in the medium, uniformity of the excitation beam ... [75]). Recently, using a formal approach based on a separation of scale in the scattering process, Aubry & al. have recently obtained spectacular results in quantitative speed of sound imaging on experimental data [46].

In this Part II, we aim at providing a mathematical framework for the propagation of ultrasound waves in random multiscale media. Using the tools of *stochastic homogenization*, we provide a mathematical model for the acoustic properties of a soft tissue as well as *quantitative* asymptotic expansions of the scattered field with respect to the scale of the acoustic heterogeneities in the medium.

5.1 Main contribution

We are interested in the scattering of classical waves by a bounded object with a random composite micro-structure embedded in an unbounded homogeneous background medium. The problem considered is modeled by a divergence form scalar Helmholtz equation with discontinuous rapidly oscillating (at some scale ε much smaller than the wavelength) stochastic coefficients.

Building on the methods developed in [136, 142] we establish a first-order (with respect to the parameter ε) asymptotic expansion of the scattered field inside the object (proposition 28). Introducing a boundary layer corrector to enforce transmission conditions at the boundary of the object we prove L^2- and H^1-norm convergence rates (Proposition 35). Using the Lippman-Schwinger equation and results on fluctuations of the commutator [19], we derive a quantitative first-order expansion of the scattered wave outside the object. We also present numerical illustrations of the solution of the multiscale problem as well as the correctors, and the first-order expansion of the solution. Numerical convergence rates are computed to support the theoretical claims.

The Part II is organized as follows:

- In Chapter 5.2 we present the model for the propagation medium and the stochastic framework required to prove stochastic homogenization results.

- Chapter 6 is devoted to proving L^2- *and* H^1- *quantitative estimates* of the error between the solution of the original problem and the first-order two-scale expansion (Proposition 36).

- Using the expansions of the solution and its gradient inside the composite medium established in the previous Chapter 6 in conjonction with (7.2), the Lippman-Schwinger equation satisfied by the scattered field, we derive in Chapter 7 an explicit integral representation formula for an H^1- approximation of the scattered field outside the composite medium of order $(d+1)/2$ (Theorem 39), where d is the dimension. This theorem along with Corollary 40 is the main result of the Part II. It makes it possible to relate the small-scale fluctuations of the composite medium and the scattered wavefield that can be measured outside the medium. This paves the way towards the resolution of quantitative inverse problems that aim at characterizing the statistics of the composite medium from the statistics of the scattered field.

- In Chapter 8, we show numerical results on the original problem, the effective coefficients and the homogenized problem, as well as the different correctors. We compute the different norm errors between the solution of the original problem and its various approximations to confirm the claims of Proposition 37 and Theorem 39.

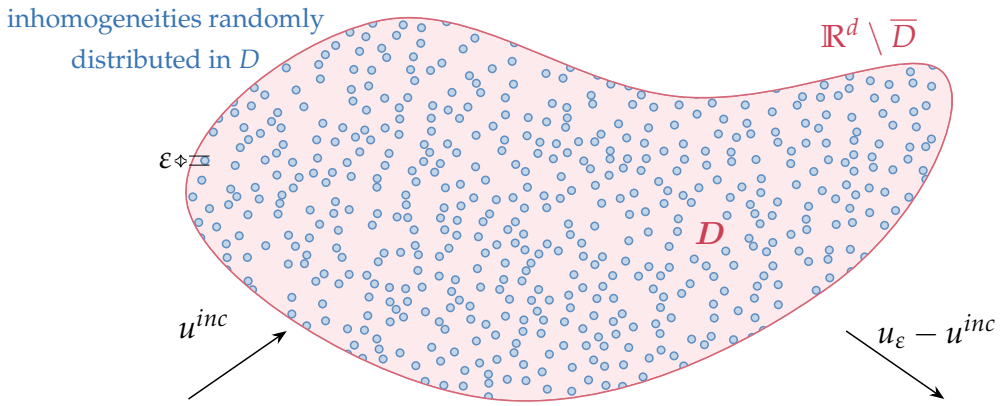

Figure 5.1: Scattering by an obstacle in the stochastic homogenization regime

5.2 Presentation of the model

We quickly recall the model that was presented in Section 3.3.1. We consider here a bounded acoustic medium $D \subset \mathbb{R}^d$, $d \in [\![1,3]\!]$ with a $\mathcal{C}^4$- boundary ∂D and we study the scattering of a time-harmonic plane wave

$$u^i(x) := \exp(ik\theta \cdot x) \quad \text{for } x \in \mathbb{R}^d \tag{5.1}$$

with wave number k and direction $\theta \in \mathbb{S}^{d-1}$. We assume that a set S^ε of randomly distributed inclusions of characteristic size $\varepsilon > 0$ lies inside the medium D. ε is small compared to the wavelength of the incoming field $2\pi k^{-1}$.

The outer medium $\mathbb{R}^d \setminus \overline{D}$, the background $D \setminus \overline{S^\varepsilon}$ and the scatterers S^ε are assumed to be homogeneous. The medium parameters are then given (3.10). The total field u_ε is then the unique solution almost sure in $H^1_{loc}(\mathbb{R}^d)$ of the following problem:

$$\begin{cases} -\nabla \cdot (a_\varepsilon(x)\nabla u_\varepsilon(x)) - k^2 n_\varepsilon(x) u_\varepsilon(x) = 0 & \text{for } x \in \mathbb{R}^d, \\ \lim\limits_{|x|\to+\infty} |x|^{\frac{d-1}{2}} \left(\dfrac{\partial(u_\varepsilon - u^i)}{\partial |x|}(x) - ik\,(u_\varepsilon - u^i)(x) \right) = 0. \end{cases} \tag{5.2}$$

We will derive an asymptotic expansion of $u_\varepsilon(x)$ with respect to ε for $x \in \mathbb{R}^d \setminus \overline{D}$ using quantitative stochastic homogenization techniques. The random distribution of the scatterers satisfies the assumptions of Section 3.3.1. In particular, we recall that a_ε and n_ε are stationary ergodic process and that we have,

$$\forall x \in D,\ a_\varepsilon(x) = a\left(\frac{x}{\varepsilon}\right) \text{ and } n_\varepsilon(x) = n\left(\frac{x}{\varepsilon}\right).$$

for the coefficient a and n defined in (3.12). In Figure 8.1b, we illustrate an example of a realization of a_ε in D, sampled by a Matèrn point process.

The stationary assumption has been defined in Definition 8. As it is customary in stochastic homogenization, stationarity and ergodicity are defined through an action $(\tau_x)_{x\in\mathbb{R}^d}$ of the group $(\mathbb{R}^d,+)$ on $(\Omega,\mathcal{F})$.
We thus equip $(\Omega,\mathcal{F})$ with $(\tau_x)_{x\in\mathbb{R}^d}$ that verifies:

- the map $\tau : \left\{ \begin{array}{ccc} \mathbb{R}^d\times\Omega & \to & \Omega \\ (x,\omega) & \mapsto & \tau_x\omega \end{array} \right.$ is measurable,
- $\forall x,y\in\mathbb{R}^d, \tau_{x+y}=\tau_x\circ\tau_y$,
- For all $x\in\mathbb{R}^d$, τ_x preserves $\mathbb{P}$, *i.e.*

$$\forall A\in\mathcal{F},\ \mathbb{P}(\tau_x A)=\mathbb{P}(A).$$

The stationarity has been defined in Definition 8. Moreover, we assume that the action $(\tau_x)_{x\in\mathbb{R}^d}$ is ergodic in the sense of Definition 9.
We can now write in terms of τ the stationary and ergodic assumption on $\{x_i^\omega\}_{i\in\mathbb{N}}$ the centers of the scatterers for the realization $\omega\in\Omega$.

$$\forall\omega\in\Omega,\ \forall y\in\mathbb{R}^d,\ \{x_i^\omega+y\}_{i\in\mathbb{N}}=\left\{x_i^{\tau_y\omega}\right\}_{i\in\mathbb{N}}. \tag{5.3}$$

These two assumptions are the minimal and classical assumptions on the distribution of scatterers $(x_i)_{i\in\mathbb{N}}$ that we require for qualitative stochastic homogenization. In the rest of Part II, the dependency on randomness $\omega\in\Omega$ is not mentioned explicitly.

We also assume that the process $(x_i)_{i\in\mathbb{N}}$ or equivalently S verifies a quantitative mixing condition. We choose to express this condition as a multiscale variance inequality as introduced in [149] and as discussed in Chapter 4. S verifies the Hypothesis 20 that we rewrite here in the form of Hypothesis 27.

Hypothesis 27: Mixing hypothesis

There exists a non-increasing weight function $\pi:\mathbb{R}^+\to\mathbb{R}^+$ with exponential decay such that S verifies for all $\sigma(S)$-measurable square integrable random variable $F(S)$,

$$\mathrm{Var}\left[F(S)\right]\leq\mathbb{E}\left[\int_1^{+\infty}\int_{\mathbb{R}^d}\left(\partial^{osc}_{S,B_\ell(x)}F(S)\right)^2\mathrm{d}x\ell^{-d}\pi(\ell-1)\mathrm{d}\ell\right], \tag{5.4}$$

where $B_\ell(x)$ is the ball with radius $\ell\geq 0$ and center $x\in\mathbb{R}^d$ and the oscillation $\partial^{osc}_{S,B_\ell(x)}F(S)$ of $F(S)$ with respect to S on $B_\ell(x)$ is defined by:

$$\begin{aligned}\partial^{osc}_{S,B_\ell(x)}F(S):=&\sup\mathrm{ess}\left\{F(S')|S'\cap(\mathbb{R}^d\setminus B_\ell(x))=S\cap(\mathbb{R}^d\setminus B_\ell(x))\right\}\\&-\inf\mathrm{ess}\left\{F(S')|S'\cap(\mathbb{R}^d\setminus B_\ell(x))=S\cap(\mathbb{R}^d\setminus B_\ell(x))\right\}.\end{aligned}$$

Remark 5.2.1. *We recall that the Hypothesis 27 implies that the covariance function of S : $C_S(x) := Cov(S(0), S(x))$ satisfies [150, Proposition 1.3]*

$$\forall x \in \mathbb{R}^d,\ |C_S(x)| \lesssim \int_{\max(\frac{1}{2}(|x|-2),0)}^{\infty} \pi(\ell)\mathrm{d}\ell. \tag{5.5}$$

where the notation $\lesssim$ stands for "inferior up to a multiplicative constant dependent only on the dimension and possibly other controlled quantities" and will be used throughout the Part II. For a Matèrn process, we recall that C_S has an exponential decay [150, Proposition 1.3].

CHAPTER 6

Two-scale asymptotic expansion of the field

6.1 Homogenized problem

We restrict our domain of study to B_R the ball of radius $R > 0$ centered at 0, via the Dirichlet-to-Neumann operator $\Lambda : H^{\frac{1}{2}}(\partial B_R) \to H^{-\frac{1}{2}}(\partial B_R)$. This operator takes a Dirichlet data $g \in H^{\frac{1}{2}}(B_R)$ and maps it to the Neumann trace of u on ∂B_R *i.e.* $\Lambda g = \nabla u \cdot \nu \in H^{-\frac{1}{2}}(\partial B_R)$ where u is the outgoing the solution of

$$-\Delta u - k^2 n_0 u = 0 \text{ in } \mathbb{R}^d \setminus \overline{B_R}, \text{ satisfying } u|_{\partial B_R} = g.$$

Λ is continuous, self-adjoint and non-positive and its expansion in terms of Hankel functions can be found for example in [172], [173, Section 2.6.3] and [174].
We thus consider u_ε the almost sure unique solution in $H^1(B_R)$ to

$$\begin{cases} -\nabla \cdot (a_\varepsilon \nabla u_\varepsilon) - k^2 n_\varepsilon u_\varepsilon = 0 & \text{in } B_R, \\ \nabla (u_\varepsilon - u^i) \cdot \nu = \Lambda (u_\varepsilon - u^i) & \text{on } \partial B_R. \end{cases} \tag{6.1}$$

The well-posedness of (6.1) for non-smooth coefficients is a difficult problem in $3d$. We refer to [175] for the proof in the L^∞ case. However, the proof relies on Fredholm theory and unique continuation principle and therefore does not yield a uniform explicit control with respect to ε and ω. To obtain this type of uniform control that will be necessary for the homogenization process, we have to add some additional assumptions on the coefficients. For kR sufficiently small or $\Im k > 0$ the sesquilinear form associated to (6.1) can be proved to be coercive and the uniform bound in ε and ω of u_ε can be achieved [176]. We also point out that some other methods were developed in [176] and [177] to obtain uniform control of the solution, but they do not apply to our specific problem. Here, we assume that the sesquilinear form associated to (6.1) is coercive so that Proposition 43 holds. The following homogenization theorem follows directly.

Proposition 28: Qualitative homogenization theorem

Almost surely the unique solution $u_\varepsilon \in H^1(B_R)$ of (6.1) converges weakly in $H^1(B_R)$ towards u_0, the unique solution in $H^1(B_R)$ of the following problem

$$\begin{cases} -\Delta u_0 - k^2 n_0 u_0 = 0 & \text{in } B_R \setminus \overline{D}, \\ -\nabla \cdot (a^\star \nabla u_0) - k^2 n^\star u_0 = 0 & \text{in } D, \\ u_0^- - u_0^+ = 0 & \text{on } \partial D, \\ \nabla u_0^- \cdot \nu - a^\star \nabla u_0^+ \cdot \nu = 0 & \text{on } \partial D, \\ \nabla (u_0 - u^i) \cdot \nu = \Lambda (u_0 - u^i) & \text{on } \partial B_R, \end{cases} \tag{6.2}$$

where the superscripts $^-$ and $^+$ denote the traces outside and inside D.
The homogenized coefficients $a^\star \in \mathcal{M}_d(\mathbb{R})$ and $n^{hom} \in (0, +\infty)$ are defined as follows

$$\begin{cases} a^\star_{i,j} = \mathbb{E}[e_j \cdot a(e_i + \nabla \phi_i)], \\ n^\star = \mathbb{E}[n], \end{cases} \tag{6.3}$$

and for $i \in [\![1, d]\!]$ the corrector ϕ_i is defined in the Theorem 14.

Once the uniform bound on u_ε is established, the proof of Proposition 28 follows from the classical steps of stochastic homogenization using Tartar's method [178] of oscillating test functions. For the sake of completeness, we detail it in Appendix B. $a^\star$ is definite positive ensuring the well-posedness of the homogenized problem (6.2).

6.2 Two-scale expansion error and boundary layer

The qualitative homogenization theory implies that almost surely u_ε converges to u_0 strongly in $L^2(B_R)$ and weakly in $H^1(B_R)$. As mentioned in Chapter 4, in order to upgrade this result to strong convergence in $H^1(B_R)$ and get a quantitative rate of convergence, one needs to consider the contribution of the first-order corrector $u_{1,\varepsilon} \in H^1(B_R \setminus \overline{D}) \times H^1(D)$ whose definition is recalled here.

Definition 29: First order corrector

Let $u_{1,\varepsilon} \in H^1(B_R \setminus \overline{D}) \times H^1(D)$ be the first-order corrector defined by:

$$u_{1,\varepsilon}(x) := \mathbb{1}_D(x) \sum_{i=1}^{d} \phi_i\left(\frac{x}{\varepsilon}\right) \partial_i u_0(x) \quad \text{for } x \in B_R. \tag{6.4}$$

This definition of $u_{1,\varepsilon}$ corresponds to the usual definition inside D. Since there is no micro-structure outside of D, we extend it to $u_{1,\varepsilon} = 0$ in $B_R \setminus \overline{D}$.
Since $u^i \in \mathcal{C}^\infty(\mathbb{R}^d)$ and ∂D is $\mathcal{C}^4$, $u_{0|_D}$ is in $H^2(D)$ (see Appendix A, Propo-

sition 44). Therefore, $u_{1,\varepsilon|_D}$ is indeed in $H^1(D)$. Similarly, we introduce $w_\varepsilon \in H^1(B_R \setminus \overline{D}) \times H^1(D)$, the two-scale expansion defined as follows :

Definition 30: Two-scale expansion

$$w_\varepsilon(x) := u_0(x) + \varepsilon u_{1,\varepsilon}(x) \quad \text{for } x \in B_R. \tag{6.5}$$

6.3 Two-scale error - boundary corrector

We want to quantify the error $Z_\varepsilon := u_\varepsilon - w_\varepsilon$ between the solution of (6.1) and its two-scale expansion (6.5) in $H^1(B_R \setminus \overline{D}) \times H^1(D)$.
In a bounded Lipschitz domain U, it has been shown [119, Chapter 6] in dimension 3 that for the Poisson equation, both with Dirichlet and Neumann boundary conditions, the following holds

$$\mathbb{E}[\|\nabla u_\varepsilon - \nabla w_\varepsilon\|^2_{L^2(U)}]^{\frac{1}{2}} \lesssim \varepsilon^{1/2} \|u_0\|_{W^{2,\infty}(U)}.$$

The order $1/2$ of the error is due to the fact that $u_{1,\varepsilon}$ and thus w_ε do not satisfy the Dirichlet or Neumann boundary conditions on ∂U. To obtain an error of order ε, one needs to take into account what happens at the boundary and add the correct boundary corrector [119]. We establish a similar result for the Helmholtz transmission problem. Let us define two extended correctors which appear naturally while deriving the problem verified by Z_ε.

Definition 31: Extended corrector

Let $\beta := (\beta_i)_{i\in[\![1,d]\!]}$ be the unique vector field and let $\sigma := (\sigma_{i,jm})_{i,j,m\in[\![1,d]\!]}$ be the unique tensor field such that for all $i, j, m \in [\![1, d]\!]$,

(a) Almost surely $\beta_i \in H^1_{loc}(\mathbb{R}^d)$ and $\sigma_{i,jm} \in H^1_{loc}(\mathbb{R}^d)$ are the solutions in $\mathcal{D}'(\mathbb{R}^d)$ of:

$$\begin{cases} -\Delta\beta_i(y) = \partial_i(n(y) - n^\star), \\ -\Delta\sigma_{i,jm}(y) = \partial_j q_{im}(y) - \partial_m q_{ij}(y), \end{cases} \tag{6.6}$$

with

$$q_i := a(e_i + \nabla\phi_i) - a^\star e_i$$

and are anchored with the condition:

$$⨍_{\square_0} \sigma_{i,jm} = ⨍_{\square_0} \beta_i = 0. \tag{6.7}$$

Furthermore, σ_i is skew-symmetric and verifies almost surely

$$\nabla \cdot \sigma_i = q_i \tag{6.8}$$

where for $i, j \in [\![1, d]\!]$,

$$(\nabla \cdot \sigma_i)_j := \sum_{m=1}^{d} \partial_m \sigma_{i,jm} \tag{6.9}$$

and β verifies almost surely

$$\nabla \cdot \beta = n - n^\star. \tag{6.10}$$

(b) $\nabla\beta_i$ and $\nabla\sigma_{i,jm}$ are stationary, have finite second moments and vanishing expectation.

σ is the classical extended corrector in stochastic homogenization of the operator $-\nabla \cdot a\nabla$ and can be found for example in [136, Lemma 1]. The well-posedness of β is proven in the exact same manner.

We can now write the problem verified by Z_ε.

Lemma 32: Two-scale error

$Z_\varepsilon := u_\varepsilon - w_\varepsilon$ is almost surely the unique solution in $H^1(B_R \setminus \overline{D}) \times H^1(D)$ of:

$$\begin{cases} -\Delta Z_\varepsilon - k^2 n_0 Z_\varepsilon = 0 & \text{in } B_R \setminus \bar{D}, \\ -\nabla \cdot a_\varepsilon \nabla Z_\varepsilon - k^2 n_\varepsilon Z_\varepsilon = \nabla \cdot F_\varepsilon + k^2 G_\varepsilon & \text{in } D, \\ Z_\varepsilon^- - Z_\varepsilon^+ = \varepsilon u_{1,\varepsilon} & \text{on } \partial D, \\ \nabla Z_\varepsilon^- \cdot \nu - a_\varepsilon \nabla Z_\varepsilon^+ \cdot \nu & \\ \qquad = F_\varepsilon \cdot \nu + \varepsilon \sum_{i=1}^{d} \left(\nabla \cdot (\sigma_i^\varepsilon \partial_i u_0)^+\right) \cdot \nu - k^2 \varepsilon (\beta^\varepsilon u_0)^+ \cdot \nu & \text{on } \partial D, \\ \nabla Z_\varepsilon \cdot \nu = \Lambda(Z_\varepsilon) & \text{on } \partial B_R, \end{cases} \tag{6.11}$$

where $F_\varepsilon \in H^1(D)$, $G_\varepsilon \in H^1(D)$ are defined as follows

$$F_\varepsilon := \varepsilon \sum_{i=1}^{d} (a_\varepsilon \phi_i^\varepsilon - \sigma_i^\varepsilon) \nabla(\partial_i u_0) + \varepsilon k^2 \beta^\varepsilon u_0, \tag{6.12}$$

$$G_\varepsilon := \varepsilon \sum_{i=1}^{d} (n_\varepsilon \phi_i^\varepsilon - \beta_i^\varepsilon) \partial_i u_0. \tag{6.13}$$

Here, ϕ^ε denotes $\phi^\varepsilon(\cdot) := \phi(\frac{\cdot}{\varepsilon})$. β_i^ε and σ_i^ε are defined similarly from β_i and σ_i and for the rest of the Part II. Note that we have then

$$\nabla\phi^\varepsilon(\cdot) = \frac{1}{\varepsilon}(\nabla\phi)(\frac{\cdot}{\varepsilon}).$$

Proof. Let us first derive the problem satisfied by Z_ε before proving well-posedness. In $B_R \setminus \overline{D}$ and on ∂B_R, u_ε and w_ε verify the same equation and so does Z_ε. Using the equation (6.1) for u_ε and equation (6.2) for u_0, we have moreover

$$\begin{aligned}
&-\nabla\cdot(a_\varepsilon\nabla Z_\varepsilon) - k^2 n_\varepsilon Z_\varepsilon \\
&\quad = -\nabla\cdot(a^\star\nabla u_0) - k^2 n^\star u_0 + \nabla\cdot(a_\varepsilon(\nabla u_0 + \varepsilon\nabla u_{1,\varepsilon})) + k^2 n_\varepsilon(u_0 + \varepsilon u_{1,\varepsilon}) \quad \text{in } D.
\end{aligned} \tag{6.14}$$

By the definition of the extended corrector of Definition 31,

$$\begin{aligned}
&-k^2 n^\star u_0 + k^2 n_\varepsilon(u_0 + \varepsilon u_{1,\varepsilon}) \\
&\qquad = k^2(n_\varepsilon - n^\star)u_0 + \varepsilon k^2 n_\varepsilon \sum_{i=1}^d \phi_i^\varepsilon \partial_i u_0 \\
&\qquad = k^2(\nabla\cdot\beta)(\tfrac{\cdot}{\varepsilon})u_0 + \varepsilon k^2 n_\varepsilon \sum_{i=1}^d \phi_i^\varepsilon \partial_i u_0 \\
&\qquad = k^2\varepsilon\nabla\cdot(\beta^\varepsilon u_0) + \varepsilon k^2 \sum_{i=1}^d -\beta_i^\varepsilon\partial_i u_0 + n_\varepsilon\phi_i^\varepsilon\partial_i u_0 \\
&\qquad = k^2 G_\varepsilon + \varepsilon k^2 \nabla\cdot(\beta^\varepsilon u_0).
\end{aligned} \tag{6.15}$$

By the skew-symmetry of σ_i, $i \in [\![1,d]\!]$, for all $x \in D$,

$$\begin{aligned}
\nabla\cdot\left(\sum_{i=1}^d (\nabla\cdot\sigma_i)(\frac{x}{\varepsilon})\partial_i u_0(x)\right) &= \nabla\cdot(\varepsilon\sum_{i=1}^d(\nabla\cdot\sigma_i^\varepsilon(x))\partial_i u_0(x)) \\
&= \varepsilon\sum_{i,j,m=1}^d \partial_j((\partial_m\sigma_{i,jm}^\varepsilon(x))\partial_i u_0(x)) \\
&= \varepsilon\sum_{i,j,m=1}^d \partial_{jm}(\sigma_{i,jm}^\varepsilon(x)\partial_i u_0(x)) - \partial_j(\sigma_{i,jm}^\varepsilon(x)(\partial_{im}u_0(x))) \\
&= -\varepsilon\sum_{i,j,m=1}^d \partial_j(\sigma_{i,jm}^\varepsilon(x)(\partial_{im}u_0(x))) \\
&= -\varepsilon\nabla\cdot\left(\sum_{i=1}^d \sigma_i^\varepsilon(x)\nabla\partial_i u_0(x)\right).
\end{aligned} \tag{6.16}$$

Therefore, we obtain

$$\begin{aligned}
&-\nabla\cdot(a^\star\nabla u_0)+\nabla\cdot(a_\varepsilon(\nabla u_0+\varepsilon\nabla u_{1,\varepsilon}))\\
&\quad=\sum_{i=1}^{d}\nabla\cdot\left(\left((a(e_i+\nabla\phi_i)-a^\star e_i\right)(\tfrac{\cdot}{\varepsilon})\partial_i u_0\right)+\varepsilon\nabla\cdot(a_\varepsilon\phi_i^\varepsilon\nabla(\partial_i u_0))\\
&\quad=\sum_{i=1}^{d}\nabla\cdot\left((\nabla\cdot\sigma_i)(\tfrac{\cdot}{\varepsilon})\partial_i u_0\right)+\varepsilon\nabla\cdot(a_\varepsilon\phi_i^\varepsilon\nabla(\partial_i u_0))\\
&\quad=\nabla\cdot\left(\varepsilon\sum_{i=1}^{d}((a_\varepsilon\phi_i^\varepsilon-\sigma_i^\varepsilon)\nabla\partial_i u_0)\right)\\
&\quad=\nabla\cdot F_\varepsilon-\varepsilon k^2\nabla\cdot(\beta^\varepsilon u_0).
\end{aligned}\tag{6.17}$$

By combining (6.15) and (6.17), we obtain the error satisfied inside D.
Using the jump conditions of u_ε and u_0 across ∂D, one gets:

$$Z_\varepsilon^- - Z_\varepsilon^+ = \varepsilon u_{1,\varepsilon},\tag{6.18}$$

and the flux jump:

$$\begin{aligned}
&\nabla Z_\varepsilon^-\cdot\nu-a_\varepsilon\nabla Z_\varepsilon^+\cdot\nu\\
&\quad=\sum_{i=1}^{d}((a_\varepsilon(e_i+\nabla\phi_i^\varepsilon)-a^\star e_i)\partial_i u_0)^+\cdot\nu+\varepsilon(a_\varepsilon\phi_i^\varepsilon\nabla(\partial_i u_0))^+\cdot\nu\\
&\quad=\sum_{i=1}^{d}(\varepsilon(\nabla\cdot\sigma_i^\varepsilon)\partial_i u_0)^+\cdot\nu+\varepsilon(a_\varepsilon\phi_i^\varepsilon\nabla\partial_i u_0)^+\cdot\nu\\
&\quad=\varepsilon\sum_{i=1}^{d}((a_\varepsilon\phi_i^\varepsilon-\sigma_i^\varepsilon)\nabla(\partial_i u_0))^+\cdot\nu+\nabla\cdot(\sigma_i^\varepsilon\partial_i u_0)^+\cdot\nu\\
&\quad=F_\varepsilon\cdot\nu+\varepsilon\sum_{i=1}^{d}\nabla\cdot(\sigma_i^\varepsilon\partial_i u_0)^+\cdot\nu-k^2\varepsilon(\beta^\varepsilon u_0)^+\cdot\nu.
\end{aligned}\tag{6.19}$$

The well-posedness of (6.11) is a direct consequence of Proposition 43. Since almost surely for $i,j,k\in[\![1,d]\!]$, ϕ_i, β_i, $\sigma_{i,jk}\in H^1_{loc}(\mathbb{R}^d)$ then ϕ_i, β_i, $\sigma_{i,jk}\in H^1(D)$. Moreover, $u_0\in H^2(D)$ and $u_{1,\varepsilon}\in H^1(D)$. Therefore, F_ε, $G_\varepsilon\in H^1(D)$, $u_{1,\varepsilon|\partial D}\in H^{\frac{1}{2}}(\partial D)$ and $F_\varepsilon\cdot\nu+\varepsilon\sum_{i=1}^{d}\nabla\cdot(\sigma_i^\varepsilon\partial_i u_0)^+\cdot\nu-k^2\varepsilon(\beta^\varepsilon u_0)^+\cdot\nu\in H^{-\frac{1}{2}}(\partial D)$, and we can apply Proposition 43. □

As it is customary in homogenization in the presence of boundary (see e.g. [160, 128]), we introduce the boundary corrector v_ε also called boundary layer, that ensures that $Z_\varepsilon-v_\varepsilon$ verifies the transmission conditions on ∂D.

Definition 33: Boundary corrector

Let v_ε be the almost sure unique solution in $H^1(B_R \setminus \overline{D}) \times H^1(D)$ of

$$\begin{cases} -\Delta v_\varepsilon - k^2 n_0 v_\varepsilon = 0 & \text{in } B_R \setminus \overline{D}, \\ -\nabla \cdot a_\varepsilon \nabla v_\varepsilon - k^2 n_\varepsilon v_\varepsilon = 0 & \text{in } D, \\ v_\varepsilon^- - v_\varepsilon^+ = \varepsilon u_{1,\varepsilon} & \text{on } \partial D, \\ \nabla v_\varepsilon^- \cdot \nu - a_\varepsilon \nabla v_\varepsilon^+ \cdot \nu = \varepsilon \sum_{i=1}^{d} \left(\nabla \cdot (\sigma_i^\varepsilon \partial_i u_0)^+\right) \cdot \nu - k^2 \varepsilon (\beta^\varepsilon u_0)^+ \cdot \nu & \text{on } \partial D, \\ \nabla v_\varepsilon \cdot \nu = \Lambda(v_\varepsilon) & \text{on } \partial B_R. \end{cases} \tag{6.20}$$

The well-posedness is once again a consequence of Proposition 43.

Remark 6.3.1. *The definition of this corrector is very similar to the boundary layer introduced in [166] which deals with the periodic case.*
However, all the analysis done in [166] cannot be applied here as it uses the $L^\infty(\mathbb{R}^d)$-boundedness of the corrector which does not hold here.

Proposition 34: Two-scale error with the boundary layer

Almost surely $Z_\varepsilon - v_\varepsilon$ is the unique solution in $H^1(B_R)$ of

$$\begin{cases} -\nabla \cdot a_\varepsilon \nabla (Z_\varepsilon - v_\varepsilon) - k^2 n_\varepsilon (Z_\varepsilon - v_\varepsilon) = \nabla \cdot F_\varepsilon + k^2 G_\varepsilon & \text{in } B_R, \\ \nabla (Z_\varepsilon - v_\varepsilon) \cdot \nu = \Lambda (Z_\varepsilon - v_\varepsilon) & \text{on } \partial B_R. \end{cases} \tag{6.21}$$

Moreover, $Z_\varepsilon - v_\varepsilon$ verifies almost surely

$$\|Z_\varepsilon - v_\varepsilon\|_{H^1(B_R)} \lesssim \|F_\varepsilon\|_{L^2(D)} + \|G_\varepsilon\|_{L^2(D)}. \tag{6.22}$$

Once again, we apply the Proposition 43 for the well-posedness of (6.21).
In order to quantify the convergence of u_ε towards $u_0 + \varepsilon u_{1,\varepsilon} + v_\varepsilon$, we are now left with estimating the right hand side of (6.22). This is easily done with the almost sure corrector estimates established in [142, Theorem 2] for coefficients verifying the mixing Hypothesis 20 as we show in the next section.

6.4 Convergence rate of the two-scale expansion

In this section we estimate the convergence of the two-scale expansion error with and without the boundary layer v_ε both in H^1- and L^2-norms.

As mentioned above, the proof relies on the corrector bounds established in [142, Theorem 4] for correlated fields satisfying the Hypothesis 20. We recalled these results in Chapter 4 in Proposition 22. We also mention that by construction β also verifies the results of Proposition 22.

For any bounded domain $B \subset \mathbb{R}^d$, we consider the covering of B with squares of size ε and define $P_\varepsilon(B)$ as the set of centers of those squares, *i.e.*

$$P_\varepsilon(B) := \{x \in \mathbb{Z}^d, \varepsilon\square_x \cap B \neq \emptyset\}. \tag{6.23}$$

We prove the following estimate for the two-scale expansion error with the boundary layer in $H^1(B_R)$.

Proposition 35: H^1- convergence of the two-scale expansion with the boundary corrector

Let $u_\varepsilon \in H^1(B_R)$ be the almost sure solution of (6.1) and $u_0 \in H^1(B_R)$ such that $u_{0|_D} \in W^{2,\infty}(D)$ be the solution of (6.2). Let $u_{1,\varepsilon}$ be the corrector defined by (6.4) and v_ε be the boundary corrector solution of (6.20).
Then almost surely

$$\|u_\varepsilon - u_0 - \varepsilon u_{1,\varepsilon} - v_\varepsilon\|_{H^1(B_R)} \lesssim \varepsilon\mu_d(\frac{1}{\varepsilon})\chi_\varepsilon \|u_0\|_{W^{2,\infty}(D)}, \tag{6.24}$$

where μ_d is defined in Proposition 22 and χ_ε is the random variable defined as:

$$\chi_\varepsilon := \left(\varepsilon^d \sum_{z\in P_\varepsilon(D)} \mathcal{C}(z)^2\right)^{\frac{1}{2}}, \tag{6.25}$$

with $\mathcal{C}$ also defined in Proposition 22. In particular, χ_ε satisfies the stochastic integrability (4.52) and it holds

$$\mathbb{E}\left[\|u_\varepsilon - u_0 - \varepsilon u_{1,\varepsilon} - v_\varepsilon\|^2_{H^1(B_R)}\right]^{\frac{1}{2}} \lesssim \varepsilon\mu_d(\frac{1}{\varepsilon}) \|u_0\|_{W^{2,\infty}(D)}. \tag{6.26}$$

Remark 6.4.1. *This result is an equivalent of the result obtained in [119, Chapter 6], both for Dirichlet and Neumann boundary conditions on ∂D. The proof of Proposition 35 follows similar steps as the proofs in [119], that dealt with the case $u_{0|_D} \in W^{2,\infty}(D)$.*
In Appendix C, Proposition 48, we extend the result of the proposition to the case where $u_{0|_D} \in W^{1+\alpha,p}(D)$ for $\alpha \in (0,1]$ and $p \in (2,\infty]$. It will be needed in the proof of Proposition 37. However, for the sake of simplicity, we choose to display here the proof in the more regular setting as it relies on the same ideas but requires less technicity.
Note that $u_{0|_D}$ is indeed in $W^{2,\infty}(D)$. By Proposition 44, since D has a $\mathcal{C}^4$- boundary, and $u^i \in \mathcal{C}^\infty(B_R)$, $u_{0|_D}$ is in $H^4(D)$. By [179, Corollary 9.15], one has the embedding

$H^4(D) = W^{4,2}(D) \hookrightarrow \mathcal{C}^2(\overline{D})$. Note that this embedding is true for $d \leq 3$ which is the framework that we consider here.

Proof. By (6.22), one only needs to show that almost surely

$$\|F_\varepsilon\|_{L^2(D)} + \|G_\varepsilon\|_{L^2(D)} \lesssim \varepsilon \mu_d(\frac{1}{\varepsilon}) \chi_\varepsilon \|u_0\|_{W^{2,\infty}(D)}.$$

The definition of F_ε by (6.12) and G_ε by (6.13) implies that almost surely

$$\|F_\varepsilon\|_{L^2(D)} + \|G_\varepsilon\|_{L^2(D)} \lesssim \varepsilon \left(\|\phi^\varepsilon\|_{L^2(D)} + \|\sigma^\varepsilon\|_{L^2(D)} + \|\beta^\varepsilon\|_{L^2(D)} \right) \|u_0\|_{W^{2,\infty}(D)}. \quad (6.27)$$

It then suffices to bound almost surely the norm of each corrector on the right hand side by $\mu_d(\frac{1}{\varepsilon})$ (up to a constant) to obtain the desired estimate.
We prove the bound for $\|\phi^\varepsilon\|_{L^2(D)}$. The two other estimates for $\|\beta^\varepsilon\|_{L^2(D)}$ and $\|\sigma^\varepsilon\|_{L^2(D)}$ are established in a similar manner.
We pave D with squares of size ε, change of variable and use the almost sure corrector bounds (4.49) to obtain

$$\begin{aligned}
\|\phi^\varepsilon\|^2_{L^2(D)} &\lesssim \sum_{z \in P_\varepsilon(D)} \|\phi^\varepsilon\|^2_{L^2(\varepsilon \square_z)} \\
&= \sum_{z \in P_\varepsilon(D)} \int_{\varepsilon \square_z} |\phi(\frac{\cdot}{\varepsilon})|^2 \\
&\lesssim \varepsilon^d \sum_{z \in P_\varepsilon(D)} \fint_{\square_z} |\phi|^2 \\
&\lesssim \mu_d(\frac{1}{\varepsilon})^2 \left(\varepsilon^d \sum_{z \in P_\varepsilon(D)} \mathcal{C}(z)^2 \right) \\
&\lesssim \mu_d(\frac{1}{\varepsilon})^2 \chi_\varepsilon^2.
\end{aligned} \quad (6.28)$$

By [119, Lemma A4], χ_ε satisfies (4.52) which concludes our proof. □

The boundary corrector v_ε, defined by (6.20) solves an almost sure comparable problem as the one verified by u_ε in D, with an oscillatory boundary data on ∂D. The resulting complexity drives us to derive convergence rates of the two-scale expansion error without v_ε. We start with the estimate in the H^1-norm.

Proposition 36: H^1- convergence rate of the two-scale expansion

Let $u_\varepsilon \in H^1(B_R)$ be the solution of (6.1), $u_0 \in H^1(B_R)$ such that $u_{0|_D} \in W^{2,\infty}(D)$ be the solution of (6.2) and $u_{1,\varepsilon}$ be defined by (6.4).
Then, it holds almost surely

$$\|u_\varepsilon - u_0\|_{H^1(B_R\setminus\overline{D})} + \|u_\varepsilon - u_0 - \varepsilon u_{1,\varepsilon}\|_{H^1(D)} \lesssim \varepsilon^{\frac{1}{2}}\mu_d(\frac{1}{\varepsilon})^{\frac{1}{2}}\widehat{\chi}_\varepsilon \|u_0\|_{W^{2,\infty}(D)}, \quad (6.29)$$

where $\widehat{\chi}_\varepsilon$ is a random variable that satisfies the stochastic integrability (4.52). In particular

$$\mathbb{E}\left[\|u_\varepsilon - u_0\|^2_{H^1(B_R\setminus\overline{D})}\right]^{\frac{1}{2}} + \mathbb{E}\left[\|u_\varepsilon - u_0 - \varepsilon u_{1,\varepsilon}\|^2_{H^1(D)}\right]^{\frac{1}{2}} \lesssim \varepsilon^{\frac{1}{2}}\mu_d(\frac{1}{\varepsilon})^{\frac{1}{2}} \|u_0\|_{W^{2,\infty}(D)}. \quad (6.30)$$

In the rest of the article $\widehat{\chi}_\varepsilon$ denotes a random variable satisfying the stochastic integrability (4.52). Its expression in the specific estimate (6.29) is made explicit in the proof.

Proof. Thanks to Proposition 35, we only need to estimate the norm of v_ε in $H^1(B_R \setminus \overline{D}) \times H^1(D)$, and the conclusion follows by the triangle inequality.
We lift the trace jump of v_ε across ∂D by considering $\tilde{v}_\varepsilon := v_\varepsilon - \varepsilon\eta_\varepsilon u_{1,\varepsilon}$ where η_ε is a smooth cutoff satisfying for all $x \in B_R$

$$0 \le \eta_\varepsilon(x) \le 1, \ \ \eta_\varepsilon = 0 \ \text{ in } D_{2\varepsilon\mu_d(\frac{1}{\varepsilon})}, \ \ \eta_\varepsilon = 1 \text{ in } B_R \setminus \overline{D_{\varepsilon\mu_d(\frac{1}{\varepsilon})}}, \ \ |\nabla\eta_\varepsilon(x)| \lesssim \frac{1}{\varepsilon\mu_d(\frac{1}{\varepsilon})},$$

where $D_r = \{x \in B_R \,|\, dist(x, \partial D) > r\}$ for $r > 0$.
By Proposition 43, since $\eta_\varepsilon u_{1,\varepsilon} \in H^1(D)$, $\tilde{v}_\varepsilon$ is almost sure the unique solution in $H^1(B_R)$ to

$$\begin{cases} -\Delta\tilde{v}_\varepsilon - k^2 n_0 \tilde{v}_\varepsilon = 0 & \text{in } B_R \setminus \overline{D}, \\ -\nabla\cdot a_\varepsilon\nabla\tilde{v}_\varepsilon - k^2 n_\varepsilon\tilde{v}_\varepsilon = \varepsilon\nabla\cdot a_\varepsilon\nabla(\eta_\varepsilon u_{1,\varepsilon}) + \varepsilon k^2 n_\varepsilon(\eta_\varepsilon u_{1,\varepsilon}) & \text{in } D, \\ \nabla\tilde{v}_\varepsilon^- \cdot \nu - a_\varepsilon\nabla\tilde{v}_\varepsilon^+ \cdot \nu = a_\varepsilon\nabla(\eta_\varepsilon u_{1,\varepsilon})\cdot\nu & \\ \quad + \varepsilon\sum_{i=1}^d \left(\nabla\cdot(\sigma_i^\varepsilon\partial_i u_0)^+\right)\cdot\nu - k^2\varepsilon(\beta^\varepsilon u_0)^+\cdot\nu & \text{on } \partial D, \\ \nabla\tilde{v}_\varepsilon\cdot\nu = \Lambda(\tilde{v}_\varepsilon) & \text{on } \partial B_R. \end{cases} \quad (6.31)$$

On the boundary it holds that

$$\sum_{i=1}^d \nabla\cdot(\sigma_i^\varepsilon\partial_i u_0)^+)\cdot\nu - k^2\varepsilon(\beta^\varepsilon u_0)^+\cdot\nu = \sum_{i=1}^d \nabla\cdot(\sigma_i^\varepsilon\partial_i u_0\eta_\varepsilon)^+)\cdot\nu - k^2\varepsilon(\beta^\varepsilon u_0\eta_\varepsilon)^+\cdot\nu. \quad (6.32)$$

Furthermore, for all $i \in [\![1, d]\!]$,

$$\nabla \cdot (\nabla \cdot (\sigma_i^\varepsilon \partial_i u_0 \eta_\varepsilon)) = \sum_{j,m=1}^{d} \partial_{jm}(\sigma_{i,jm}^\varepsilon \partial_i u_0 \eta_\varepsilon)) = 0.$$

Thus, $\tilde{v}_\varepsilon$ verifies for all $w \in H^1(B_R)$

$$\begin{aligned}
&\int_{B_R} a_\varepsilon \nabla \tilde{v}_\varepsilon \cdot \nabla \overline{w} - k^2 n_\varepsilon \tilde{v}_\varepsilon \overline{w} - \langle \Lambda(\tilde{v}_\varepsilon), w \rangle_{H^{-\frac{1}{2}}(\partial B_R), H^{\frac{1}{2}}(\partial B_R)} \\
&\quad = \int_D -\varepsilon a_\varepsilon \nabla(\eta_\varepsilon u_{1,\varepsilon}) \cdot \nabla \overline{w} + \varepsilon k^2 n_\varepsilon (\eta_\varepsilon u_{1,\varepsilon}) \overline{w} - \varepsilon \sum_{i=1}^{d} \nabla \cdot (\sigma_i^\varepsilon \partial_i u_0 \eta_\varepsilon) \cdot \nabla \overline{w} \\
&\qquad - k^2 \varepsilon \nabla \cdot (\beta^\varepsilon u_0 \eta_\varepsilon) \overline{w} + k^2 \varepsilon \beta^\varepsilon u_0 \eta_\varepsilon \cdot \nabla \overline{w},
\end{aligned} \tag{6.33}$$

where $\overline{w}$ denotes the conjugate of w and $\langle \cdot, \cdot \rangle_{H^{-\frac{1}{2}}(\partial B_R), H^{\frac{1}{2}}(\partial B_R)}$ denotes the duality product $H^{-\frac{1}{2}}(\partial B_R), H^{\frac{1}{2}}(\partial B_R)$. By the coercivity of the sesquilinear form, we then obtain

$$\begin{aligned}
\|\tilde{v}_\varepsilon\|_{H^1(B_R)} \lesssim \varepsilon \|\eta_\varepsilon u_{1,\varepsilon}\|_{H^1(D)} + \varepsilon \left\| \sum_{i=1}^{d} \nabla \cdot (\sigma_i^\varepsilon \partial_i u_0 \eta_\varepsilon) \right\|_{L^2(D)} \\
+ \varepsilon \|\nabla \cdot (\beta^\varepsilon u_0 \eta_\varepsilon)\|_{L^2(D)} + \varepsilon \|\beta^\varepsilon u_0 \eta_\varepsilon\|_{L^2(D)}.
\end{aligned} \tag{6.34}$$

Let $\mathcal{S}_{\eta_\varepsilon} := \operatorname{supp}(\eta_\varepsilon)$ denote the support of η_ε. By definition of $\tilde{v}_\varepsilon$, it holds

$$\begin{aligned}
&\|v_\varepsilon\|_{H^1(B_R \setminus \overline{D})} + \|v_\varepsilon\|_{H^1(D)} \\
&\quad \lesssim \varepsilon \|\eta_\varepsilon u_{1,\varepsilon}\|_{H^1(D)} + \varepsilon \left\| \sum_{i=1}^{d} \nabla \cdot (\sigma_i^\varepsilon \partial_i u_0 \eta_\varepsilon) \right\|_{L^2(D)} + \varepsilon \|\nabla \cdot (\beta^\varepsilon u_0 \eta_\varepsilon)\|_{L^2(D)} + \varepsilon \|\beta^\varepsilon u_0 \eta_\varepsilon\|_{L^2(D)} \\
&\quad \lesssim \Bigg(\varepsilon \|\nabla \phi^\varepsilon\|_{L^2(\mathcal{S}_{\eta_\varepsilon})} + \varepsilon \|\phi^\varepsilon\|_{L^2(\mathcal{S}_{\eta_\varepsilon})} + \frac{1}{\mu_d(\frac{1}{\varepsilon})} \|\phi^\varepsilon\|_{L^2(\mathcal{S}_{\eta_\varepsilon})} \\
&\qquad + \varepsilon \|\nabla \sigma^\varepsilon\|_{L^2(\mathcal{S}_{\eta_\varepsilon})} + \varepsilon \|\sigma^\varepsilon\|_{L^2(\mathcal{S}_{\eta_\varepsilon})} + \frac{1}{\mu_d(\frac{1}{\varepsilon})} \|\sigma^\varepsilon\|_{L^2(\mathcal{S}_{\eta_\varepsilon})} \\
&\qquad + \varepsilon \|\nabla \beta^\varepsilon\|_{L^2(\mathcal{S}_{\eta_\varepsilon})} + \varepsilon \|\beta^\varepsilon\|_{L^2(\mathcal{S}_{\eta_\varepsilon})} + \frac{1}{\mu_d(\frac{1}{\varepsilon})} \|\beta^\varepsilon\|_{L^2(\mathcal{S}_{\eta_\varepsilon})} \Bigg) \|u_0\|_{W^{2,\infty}(D)}.
\end{aligned} \tag{6.35}$$

We prove the bounds on the corrector ϕ, the two other estimates are established in a

similar manner. Let $\widetilde{\chi_\varepsilon^1}$ and $\widetilde{\chi_\varepsilon^2}$ be the random variables defined by

$$\begin{cases} \widetilde{\chi_\varepsilon^1} := \left(\dfrac{\varepsilon^d}{\varepsilon \mu_d(\frac{1}{\varepsilon})} \displaystyle\sum_{z \in P_\varepsilon(\mathcal{S}_{\eta_\varepsilon})} \mathcal{C}(z)^2 \right)^{\frac{1}{2}}, \\ \widetilde{\chi_\varepsilon^2} := \left(\dfrac{\varepsilon^d}{\varepsilon \mu_d(\frac{1}{\varepsilon})} \displaystyle\sum_{z \in P_\varepsilon(\mathcal{S}_{\eta_\varepsilon})} (1 + r_*(z))^{2d} \right)^{\frac{1}{2}}. \end{cases} \tag{6.36}$$

These two random variables satisfy the stochastic integrability (4.52) since the prefactor $\frac{\varepsilon^d}{\varepsilon \mu_d(\frac{1}{\varepsilon})} \approx \frac{1}{|P_\varepsilon(\mathcal{S}_{\eta_\varepsilon})|}$ is the appropriate renormalization.
By following the proof of Proposition 35, it holds almost surely

$$\varepsilon \left\| \phi^\varepsilon \right\|_{L^2(\mathcal{S}_{\eta_\varepsilon})} \lesssim \varepsilon^{\frac{3}{2}} \mu_d(\frac{1}{\varepsilon})^{\frac{3}{2}} \widetilde{\chi_\varepsilon^1}. \tag{6.37}$$

It remains to estimate $\varepsilon \left\| \nabla \phi^\varepsilon \right\|_{L^2(\mathcal{S}_{\eta_\varepsilon})}$. Using the mean value property of Proposition 22, we get almost surely

$$\varepsilon \left\| \nabla \phi^\varepsilon \right\|_{L^2(\mathcal{S}_{\eta_\varepsilon})} \lesssim \varepsilon^{\frac{1}{2}} \mu_d(\frac{1}{\varepsilon})^{\frac{1}{2}} \widetilde{\chi_\varepsilon^2}. \tag{6.38}$$

By combining (6.37) and (6.38), we obtain

$$\begin{aligned} &\varepsilon \left\| \nabla \phi^\varepsilon \right\|_{L^2(\mathcal{S}_{\eta_\varepsilon})} + \varepsilon \left\| \phi^\varepsilon \right\|_{L^2(\mathcal{S}_{\eta_\varepsilon})} + \frac{1}{\mu_d(\frac{1}{\varepsilon})} \left\| \phi^\varepsilon \right\|_{L^2(\mathcal{S}_{\eta_\varepsilon})} \\ &\qquad \lesssim \varepsilon^{\frac{1}{2}} \mu_d(\frac{1}{\varepsilon})^{\frac{1}{2}} \widetilde{\chi_\varepsilon^2} + \varepsilon^{\frac{3}{2}} \mu_d(\frac{1}{\varepsilon})^{\frac{3}{2}} \widetilde{\chi_\varepsilon^1} + \varepsilon^{\frac{1}{2}} \mu_d(\frac{1}{\varepsilon})^{\frac{1}{2}} \widetilde{\chi_\varepsilon^1} \\ &\qquad \lesssim \varepsilon^{\frac{1}{2}} \mu_d(\frac{1}{\varepsilon})^{\frac{1}{2}} \widetilde{\chi_\varepsilon^3}, \end{aligned} \tag{6.39}$$

where we define $\widetilde{\chi_\varepsilon^3}$ as

$$\widetilde{\chi_\varepsilon^3} := \widetilde{\chi_\varepsilon^2} + (\varepsilon \mu_d(\frac{1}{\varepsilon}) + 1) \widetilde{\chi_\varepsilon^1}. \tag{6.40}$$

As $\widetilde{\chi_\varepsilon^1}$ and $\widetilde{\chi_\varepsilon^2}$ satisfy the stochastic integrability (4.52) , $\widetilde{\chi_\varepsilon^3}$ also satisfies (4.52).
This gives us the following estimate for v_ε in $H^1(B_R \setminus \overline{D}) \times H^1(D)$,

$$\left\| v_\varepsilon \right\|_{H^1(B_R \setminus \overline{D})} + \left\| v_\varepsilon \right\|_{H^1(D)} \lesssim \varepsilon^{\frac{1}{2}} \mu_d(\frac{1}{\varepsilon})^{\frac{1}{2}} \widetilde{\chi_\varepsilon^3} \left\| u_0 \right\|_{W^{2,\infty}(D)}. \tag{6.41}$$

Therefore, we conclude by the triangle inequality

$$\begin{aligned} &\left\| u_\varepsilon - u_0 \right\|_{H^1(B_R \setminus \overline{D})} + \left\| u_\varepsilon - u_0 - \varepsilon u_{1,\varepsilon} \right\|_{H^1(D)} \\ &\qquad \lesssim \left\| u_\varepsilon - u_0 - \varepsilon u_{1,\varepsilon} - v_\varepsilon \right\|_{H^1(B_R)} + \left\| v_\varepsilon \right\|_{H^1(D)} + \left\| v_\varepsilon \right\|_{H^1(B_R \setminus \overline{D})} \\ &\qquad \lesssim \varepsilon^{\frac{1}{2}} \mu_d(\frac{1}{\varepsilon})^{\frac{1}{2}} \left(\varepsilon^{\frac{1}{2}} \mu_d(\frac{1}{\varepsilon})^{\frac{1}{2}} \chi_\varepsilon + \widetilde{\chi_\varepsilon^3} \right) \left\| u_0 \right\|_{W^{2,\infty}(D)} \\ &\qquad \lesssim \varepsilon^{\frac{1}{2}} \mu_d(\frac{1}{\varepsilon})^{\frac{1}{2}} \widehat{\chi_\varepsilon} \left\| u_0 \right\|_{W^{2,\infty}(D)}, \end{aligned} \tag{6.42}$$

where the random variable $\widehat{\chi}_\varepsilon$ defined as

$$\widehat{\chi}_\varepsilon := \varepsilon^{\frac{1}{2}} \mu_d(\frac{1}{\varepsilon})^{\frac{1}{2}} \chi_\varepsilon + \widetilde{\chi_\varepsilon^2} + (\varepsilon \mu_d(\frac{1}{\varepsilon}) + 1)\widetilde{\chi_\varepsilon^1}, \tag{6.43}$$

satisfies the stochastic integrability (4.52). □

We expect the homogenization error $u_\varepsilon - u_0$ to be of order $O(\varepsilon)$ in $L^2(B_R)$ as u_0 verifies the proper transmission conditions on ∂D. This is the subject of the next proposition.

Proposition 37: L^2- rate of convergence of the homogenization error

Let $u_\varepsilon \in H^1(B_R)$ be the almost sure solution of (6.1) and $u_0 \in H^1(B_R)$ such that $u_{0|_D} \in W^{2,\infty}(D)$ be the solution of (6.2).
Then, it holds almost surely

$$\|u_\varepsilon - u_0\|_{L^2(B_R)} \lesssim \varepsilon \mu_d(\frac{1}{\varepsilon}) \widehat{\chi}_\varepsilon \|u_0\|_{W^{2,\infty}(D)}, \tag{6.44}$$

where $\widehat{\chi}_\varepsilon$ is a random variable satisfying the stochastic integrability (4.52). In particular

$$\mathbb{E}\left[\|u_\varepsilon - u_0\|^2_{L^2(B_R)}\right]^{\frac{1}{2}} \lesssim \varepsilon \mu_d(\frac{1}{\varepsilon}) \|u_0\|_{W^{2,\infty}(D)}. \tag{6.45}$$

Remark 6.4.2. *A similar result has been shown in the periodic case in [166]. Though, we cannot adapt the proof, since it uses the L^∞-bound of the corrector, that does not hold in the stochastic setting. In [119, Theorem 6.14], the result is shown for Poisson equation in the Dirichlet case. Our proof is an adaptation of the latter result.*

Proof. To prove (6.44), we use Proposition 35 and the bounds on the correctors, which imply that almost surely

$$\begin{aligned}
\|u_\varepsilon - u_0\|_{L^2(B_R)} &\lesssim \|u_\varepsilon - u_0 - \varepsilon u_{1,\varepsilon} - v_\varepsilon\|_{L^2(B_R)} + \varepsilon \|u_{1,\varepsilon}\|_{L^2(D)} + \|v_\varepsilon\|_{L^2(B_R)} \\
&\lesssim \varepsilon \mu_d(\frac{1}{\varepsilon}) \chi_\varepsilon \|u_0\|_{W^{2,\infty}(D)} + \varepsilon \|\phi^\varepsilon\|_{L^2(D)} \|u_0\|_{W^{2,\infty}(D)} + \|v_\varepsilon\|_{L^2(B_R)} \\
&\lesssim \varepsilon \mu_d(\frac{1}{\varepsilon}) \chi_\varepsilon \|u_0\|_{W^{2,\infty}(D)} + \|v_\varepsilon\|_{L^2(B_R)}.
\end{aligned} \tag{6.46}$$

It remains to estimate the L^2-norm of the boundary corrector, which we do by using a duality argument as in [166].
Let $h \in L^2(B_R)$. We wish to estimate

$$\left| \int_{B_R} v_\varepsilon \overline{h} \right|.$$

To do so, we introduce the auxiliary function $W_\varepsilon \in H^1(B_R)$ solution of

$$\begin{cases} -\nabla \cdot a_\varepsilon^* \nabla W_\varepsilon - k^2 n_\varepsilon W_\varepsilon = \overline{h} & \text{in } B_R, \\ \nabla W_\varepsilon \cdot \nu = \Lambda(W_\varepsilon) & \text{on } \partial B_R. \end{cases} \tag{6.47}$$

Here a_ε^* denote the transpose of a_ε.
We write the variational formulation verified by W_ε in $H^1(B_R)$ and choose $\overline{\tilde{v}_\varepsilon}$ as a test function. Recall that $\tilde{v}_\varepsilon := v_\varepsilon - \varepsilon \eta_\varepsilon u_{1,\varepsilon}$ is the unique solution in $H^1(B_R)$ to (6.31). We obtain

$$\int_{B_R} \tilde{v}_\varepsilon \overline{h} = \int_{B_R} a_\varepsilon^* \nabla W_\varepsilon \cdot \nabla \tilde{v}_\varepsilon - k^2 n_\varepsilon W_\varepsilon \tilde{v}_\varepsilon - \left\langle \Lambda(\tilde{v}_\varepsilon), \overline{W_\varepsilon} \right\rangle_{H^{-\frac{1}{2}}(\partial B_R), H^{\frac{1}{2}}(\partial B_R)}. \tag{6.48}$$

We choose in the variational formulation of $\tilde{v}_\varepsilon$ (6.33), $\overline{W_\varepsilon}$ as a test function and subtract the two expressions to obtain

$$\begin{aligned} \int_{B_R} \tilde{v}_\varepsilon \overline{h} = \int_D -\varepsilon a_\varepsilon \nabla(\eta_\varepsilon u_{1,\varepsilon}) \cdot \nabla W_\varepsilon + \varepsilon k^2 n_\varepsilon (\eta_\varepsilon u_{1,\varepsilon}) W_\varepsilon - \varepsilon \left(\sum_{i=1}^d \nabla \cdot (\sigma_i^\varepsilon \partial_i u_0 \eta_\varepsilon) \right) \cdot \nabla W_\varepsilon \\ - k^2 \varepsilon \nabla \cdot (\beta^\varepsilon u_0 \eta_\varepsilon) W_\varepsilon + k^2 \varepsilon \beta^\varepsilon u_0 \eta_\varepsilon \cdot \nabla W_\varepsilon. \end{aligned} \tag{6.49}$$

We use the estimate (6.39) and get

$$\begin{aligned} \left| \int_{B_R} v_\varepsilon \overline{h} \right| &\lesssim \varepsilon \left| \int_D \eta_\varepsilon u_{1,\varepsilon} \overline{h} \right| + \varepsilon^{\frac{1}{2}} \mu_d(\tfrac{1}{\varepsilon})^{\frac{1}{2}} \widetilde{\chi_\varepsilon^3} \, \|W_\varepsilon\|_{H^1(\mathcal{S}_\varepsilon)} \, \|u_0\|_{W^{2,\infty}(D)} \\ &\lesssim \varepsilon^{\frac{3}{2}} \mu_d(\tfrac{1}{\varepsilon})^{\frac{3}{2}} \widetilde{\chi_\varepsilon^1} \, \|h\|_{L^2(D)} + \varepsilon^{\frac{1}{2}} \mu_d(\tfrac{1}{\varepsilon})^{\frac{1}{2}} \widetilde{\chi_\varepsilon^3} \, \|W_\varepsilon\|_{H^1(\mathcal{S}_\varepsilon)} \, \|u_0\|_{W^{2,\infty}(D)}. \end{aligned} \tag{6.50}$$

It remains to show that

$$\|W_\varepsilon\|_{H^1(\mathcal{S}_{\eta_\varepsilon})} \lesssim \varepsilon^{\frac{1}{2}} \mu_d(\tfrac{1}{\varepsilon})^{\frac{1}{2}} \widetilde{\chi_\varepsilon^4} \, \|h\|_{L^2(B_R)},$$

for a random variable $\widetilde{\chi_\varepsilon^4}$ satisfying the correct stochastic integrability. Following [166], we apply homogenization results to W_ε to obtain the desired estimate.
We thus introduce $W_0 \in H^2(B_R \setminus \overline{D}) \times H^2(D)$ solution of

$$\begin{cases} -\Delta W_0 - k^2 n_0 W_0 = \overline{h} & \text{in } B_R \setminus \overline{D}, \\ -\nabla \cdot a^\star \nabla W_0 - k^2 n^\star W_0 = \overline{h} & \text{in } D, \\ \nabla W_0^- \cdot \nu - a^\star \nabla W_0^+ \cdot \nu = 0 & \text{on } \partial D, \\ \nabla W_0 \cdot \nu = \Lambda(W_0) & \text{on } \partial B_R. \end{cases} \tag{6.51}$$

The regularity of W_0 comes from Proposition 44. Moreover the following estimate holds

$$\|W_0\|_{H^2(D)} \lesssim \|h\|_{L^2(B_R)}. \tag{6.52}$$

However, we have no guarantee that $W_{0|_D}$ is in $W^{2,\infty}(D)$, since h is only in $L^2(B_R)$. Therefore we cannot apply the result of Proposition 36. Note that even if we could, this would yield a control with the $W^{2,\infty}(D)$ norm of W_0, that we cannot directly link to $\|h\|_{L^2(B_R)}$. Instead, Proposition 47 gives a $W^{\frac{3}{2},2+s}(D)$-control, for $s>0$, of the two-scale expansion error.
By the fractional Sobolev embedding (cf. [180, Theorem 7.58]), there exists an exponent $s(d)>0$ such that we have the embedding:

$$W^{2,2}(D) \hookrightarrow W^{\frac{3}{2},2+s}(D).$$

In particular, this yields

$$\|W_0\|_{W^{\frac{3}{2},2+s}(D)} \lesssim \|W_0\|_{H^2(D)} \lesssim \|h\|_{L^2(B_R)}. \tag{6.53}$$

For $\alpha=\frac{1}{2}$, $p=2+s>2$, Proposition 47 implies then

$$\begin{aligned}\|W_\varepsilon\|_{H^1(\mathcal{S}_{\eta_\varepsilon})} &\lesssim \|W_\varepsilon - W_0 - \varepsilon W_{1,\varepsilon}\|_{H^1(\mathcal{S}_{\eta_\varepsilon})} + \|W_0+\varepsilon W_{1,\varepsilon}\|_{H^1(\mathcal{S}_{\eta_\varepsilon})} \\ &\lesssim \varepsilon^{\frac{1}{2}}\mu_d(\frac{1}{\varepsilon})^{\frac{1}{2}}\widehat{\chi_{\varepsilon,p}}\,\|W_0\|_{W^{\frac{3}{2},p}(D)} + \|W_0+\varepsilon W_{1,\varepsilon}\|_{H^1(\mathcal{S}_{\eta_\varepsilon})},\end{aligned} \tag{6.54}$$

where

$$W_{1,\varepsilon} := \sum_{i=1}^{d} \phi_i^\varepsilon \partial_i \widehat{W_0} * \xi_\varepsilon,$$

and $\widehat{\chi_{\varepsilon,p}}$ verifies (4.52). The mollifier ξ_ε is defined by (C.2) and $\widehat{W_0}$ is the Sobolev extension in $H^1(\mathbb{R}^d)$ of $W_{0|_D}$ (cf Lemma 46).
Using Lemma 51, with $f=\nabla W_0$, $r=\varepsilon\mu_d(\frac{1}{\varepsilon})$, $p=2+s$, $\alpha=\frac{1}{2}$, $q=2$, $\beta=\frac{1}{q}=\frac{1}{2}$, we obtain

$$\|\nabla W_0\|_{L^2(\mathcal{S}_{\eta_\varepsilon})} \lesssim \varepsilon^{\frac{1}{2}}\mu_d(\frac{1}{\varepsilon})^{\frac{1}{2}}\|W_0\|_{W^{\frac{3}{2},p}(D)}. \tag{6.55}$$

It also holds by the combination of (C.24) and (C.28) that

$$\varepsilon\|\nabla W_{1,\varepsilon}\|_{L^2(\mathcal{S}_{\eta_\varepsilon})} \lesssim \varepsilon^{\frac{1}{2}}\mu_d(\frac{1}{\varepsilon})^{\frac{1}{2}}\widehat{\chi_{\varepsilon,p}}\,\|W_0\|_{W^{\frac{3}{2},p}(D)}. \tag{6.56}$$

with

$$\widehat{\chi_{\varepsilon,p}} := \widetilde{\chi^2_{\varepsilon,p}} + \varepsilon^{\frac{1}{2}-\frac{1}{p}}\mu_d(\frac{1}{\varepsilon})^{1-\frac{1}{p}}\widetilde{\chi^1_{\varepsilon,p}},$$

and $\widetilde{\chi^1_{\varepsilon,p}}$, $\widetilde{\chi^2_{\varepsilon,p}}$ are defined in (C.25) and satisfy (4.52). With the same arguments, similar estimates can be derived for $\|W_0\|_{L^2(\mathcal{S}_{\eta_\varepsilon})}$ and $\varepsilon\|W_{1,\varepsilon}\|_{L^2(\mathcal{S}_{\eta_\varepsilon})}$. This yields that

$$\|W_\varepsilon\|_{H^1(\mathcal{S}_{\eta_\varepsilon})} \lesssim \varepsilon^{\frac{1}{2}}\mu_d(\frac{1}{\varepsilon})^{\frac{1}{2}}\widetilde{\chi^4_{\varepsilon,p}}\,\|h\|_{L^2(D)}, \tag{6.57}$$

where $\widetilde{\chi^4_{\varepsilon,p}} := 1 + \widehat{\chi_{\varepsilon,p}} + \widetilde{\chi^1_{\varepsilon,p}}$ satisfies (4.52).
We combine (6.50) and (6.57) to obtain

$$\|v_\varepsilon\|_{L^2(B_R)} \lesssim \varepsilon\mu_d(\frac{1}{\varepsilon})\left(\varepsilon^{\frac{1}{2}}\mu_d(\frac{1}{\varepsilon})^{\frac{1}{2}}\widetilde{\chi^1_\varepsilon} + \widetilde{\chi^3_\varepsilon\chi^4_{\varepsilon,p}}\right)\|u_0\|_{W^{2,\infty}(D)}\,. \tag{6.58}$$

Therefore, by (6.46) we get

$$\|u_\varepsilon - u_0\|_{L^2(B_R)} \lesssim \varepsilon\mu_d(\frac{1}{\varepsilon})\widehat{\chi}_\varepsilon\,\|u_0\|_{W^{2,\infty}(D)}\,, \tag{6.59}$$

where $\widehat{\chi}_\varepsilon$ defined by

$$\widehat{\chi}_\varepsilon := \chi_\varepsilon + \varepsilon^{\frac{1}{2}}\mu_d(\frac{1}{\varepsilon})^{\frac{1}{2}}\widetilde{\chi^1_\varepsilon} + \widetilde{\chi^3_\varepsilon\chi^4_{\varepsilon,2+\delta}},$$

satisfies the desired stochastic integrability thanks to the following version of Hölder's inequality [19].

Lemma 38: Hölder's inequality

For all random variables Y_1, Y_2, given $\kappa_1, \kappa_2 > 0$,

$$\text{if } \mathbb{E}[\exp(Y_1^{\kappa_1})] \le 2 \text{ and } \mathbb{E}[\exp(Y_2^{\kappa_2})] \le 2,$$
$$\text{then there exists } C > 0, \text{ such that } \mathbb{E}\left[\exp\left(\frac{1}{C}(Y_1Y_2)^{\frac{\kappa_1\kappa_2}{\kappa_1+\kappa_2}}\right)\right] < \infty. \tag{6.60}$$

□

CHAPTER 7

Asymptotic expansion of the scattered field

7.1 Main result

The convergence estimates that we established in the previous section provide an asymptotic expansion of the field at order ε. Outside D, u_ε is approximated at first-order by u_0 according to Proposition 36. Physically, u_0 corresponds to the wave that interacts with the effective medium of parameters $a^\star$ and $n^\star$. It depends on the distribution of the scatterers as $a^\star$ does but it is deterministic and thus is not characteristic of one realization in a given medium. In the context of ultrasounds the measurements are usually done using the same sensor array that transmits the plane wave excitation (ultrasonic transducers can be used as transmitters and as receivers). So u_0 contains only the contribution from the boundary ∂D while we would like to characterize the speckle field generated by the small heterogeneities. We are then interested in this section in obtaining the next order term in the expansion of the field outside of D.
We introduce G_0 the Green function associated to the homogenized problem (6.2) *i.e.* G_0 verifies in $\mathcal{D}'(B_R)$ for all $y \in B_R$,

$$\begin{cases} -\Delta G_0(\cdot,y) - k^2 n_0 G_0(\cdot,y) = \delta(\cdot - y) & \text{in } B_R \setminus \overline{D}, \\ -\nabla\cdot(a^\star \nabla G_0(\cdot,y)) - k^2 n^\star G_0(\cdot,y) = \delta(\cdot - y) & \text{in } D, \\ G_0(\cdot,y)^- = G_0(\cdot,y)^+ & \text{on } \partial D, \\ \nabla G_0(\cdot,y)^- \cdot \nu - a^\star \nabla G_0(\cdot,y)^+ \cdot \nu = 0 & \text{on } \partial D, \\ \nabla G_0 \cdot \nu = \Lambda(G_0) & \text{on } \partial B_R. \end{cases} \tag{7.1}$$

For all $\alpha > 0$, we define $D^\alpha := \{x \in B_R \,|\, dist(x,D) < \alpha\}$. For $z \in B_R \setminus \overline{D^\alpha}$, u_ε verifies the following Lippman-Schwinger equation

$$u_\varepsilon(z) = u_0(z) + \int_D (a^\star - a_\varepsilon(x)) \nabla u_\varepsilon(x) \cdot \nabla G_0(x,z) \mathrm{d}x \\ - k^2 \int_D (n^\star - n_\varepsilon(x)) u_\varepsilon(x) G_0(x,z) \mathrm{d}x. \tag{7.2}$$

We make use of the asymptotic expansion of u_ε in $H^1(D)$ and obtain for all $z \in B_R \setminus \overline{D^\alpha}$

$$\begin{aligned} u_\varepsilon(z) = u_0(z) + \int_D \sum_{i=1}^d \Big(a^\star - a_\varepsilon(x)(e_i + \varepsilon\nabla\phi_i^\varepsilon(x)\Big)\partial_i u_0(x)\cdot\nabla G_0(x,z)\mathrm{d}x \\ - k^2\int_D (n^\star - n_\varepsilon(x))u_0(x)G_0(x,z)\mathrm{d}x + J^\varepsilon(z), \end{aligned} \tag{7.3}$$

where

$$\begin{aligned} J^\varepsilon(z) := \int_D (a^\star - a_\varepsilon(x)\left(\nabla u_\varepsilon(x) - \sum_{i=1}^d (e_i + \varepsilon\nabla\phi_i^\varepsilon(x))\partial_i u_0(x)\right)\cdot\nabla G_0(x,z)\mathrm{d}x \\ - k^2\int_D (n^\star - n_\varepsilon(x))(u_\varepsilon(x) - u_0(x))G_0(x,z)\mathrm{d}x. \end{aligned} \tag{7.4}$$

Using the strong convergence estimates established in Proposition 36 and Proposition 37 leads to

$$\mathbb{E}[\|J^\varepsilon(z)\|_{L^2(B_R\setminus\overline{D^\alpha})}] \lesssim \varepsilon^{\frac{1}{2}}\mu_d(\frac{1}{\varepsilon})^{\frac{1}{2}},$$

which is not sufficient since $u_\varepsilon - u_0$ is of order ε in $L^2(B_R \setminus \overline{D})$. We thus need to estimate more sharply the weak convergence of the two quantities $(a^\star - a_\varepsilon(x))\left(\nabla u_\varepsilon - \sum_{i=1}^d (e_i + \varepsilon\nabla\phi_i^\varepsilon)\partial_i u_0\right)$ and $(n^\star - n_\varepsilon)(u_\varepsilon - u_0)$.
In [18] and [19], the authors study the fluctuations of ∇u_ε in the context of the Poisson equation in $\mathbb{R}^d$. They prove that the fluctuations of ∇u_ε and $a_\varepsilon\nabla u_\varepsilon$ can be recovered from the fluctuations of the commutator $\Xi \in L^2_{loc}(\mathbb{R}^d)^d$ defined by:

$$\forall i \in [\![1,d]\!],\ \Xi_i := (a - a^\star)(e_i + \nabla\phi_i). \tag{7.5}$$

This leads to estimate

$$\mathcal{J}^\varepsilon := \int_{\mathbb{R}^d} (a_\varepsilon - a^\star)\nabla u_\varepsilon\cdot g - \sum_{i=1}^d \Xi_i(\frac{\cdot}{\varepsilon})\partial_i u_0\cdot g \tag{7.6}$$

for all $g \in \mathcal{C}_c^\infty(\mathbb{R}^d)^d$. They show that, for all $g \in \mathcal{C}_c^\infty(\mathbb{R}^d)^d$

$$\mathrm{Var}[\mathcal{J}^\varepsilon]^{\frac{1}{2}} \lesssim \varepsilon^{\frac{d}{2}+1}\mu_d(\frac{1}{\varepsilon}). \tag{7.7}$$

We extend this result to our situation where the Poisson equation is replaced by the Helmholtz equation leading to a second term in J^ε and where we have to take into account the boundary of D as the support of G_0 is not compactly supported in D. We deal with this last point in a similar manner as in Section 6 by introducing the appropriate boundary layer. However the rate of convergence is now $1/2$ order smaller.
Our main result is stated in the following theorem.

Theorem 39: Pointwise convergence of J^ε

Let $u_\varepsilon \in H^1(B_R)$ be the almost sure solution of (6.1), $u_0 \in H^1(B_R)$ such that $u_{0|_D} \in W^{2,\infty}(D)$ be the solution of (6.2) and for $y \in B_R \setminus \overline{D^\alpha}$, let $G_0(\cdot, y) \in H^1(B_R \setminus \{y\})$ such that $G_0(\cdot, y)_D \in W^{2,\infty}(D)$ be the solution of (7.1). Define $\mathcal{U}_1 \in H^1(B_R \setminus \{y\})$ as:

$$\begin{aligned}\mathcal{U}_1 := \mathbb{E}[u_\varepsilon - u_0] + \sum_{i=1}^{d} \int_D (a^\star - a_\varepsilon(x))(e_i + \varepsilon \nabla \phi_i^\varepsilon(x)) \partial_i u_0(x) \cdot \nabla G_0(x, \cdot) \mathrm{d}x \\ - k^2 \int_D (n^\star - n_\varepsilon(x)) u_0(x) G_0(x, \cdot) \mathrm{d}x.\end{aligned} \tag{7.8}$$

Then

$$\begin{aligned}\mathbb{E}\left[|u_\varepsilon(y) - u_0(y) - \mathcal{U}_1(y)|^2\right]^{\frac{1}{2}} \\ \lesssim \varepsilon^{\frac{d+1}{2}} \mu_d(\frac{1}{\varepsilon})^{\frac{1}{2}} \|u_0\|_{W^{2,\infty}(D)} \|G_0(\cdot, y)\|_{W^{2,\infty}(D)},\end{aligned} \tag{7.9}$$

and if we further assume that $x \mapsto G(x, y)$ is in $W^{3,\infty}(D)$ for $y \in B_R \setminus \overline{D^\alpha}$, then

$$\begin{aligned}\mathbb{E}\left[|\nabla u_\varepsilon(y) - \nabla u_0(y) - \nabla \mathcal{U}_1(y)|^2\right]^{\frac{1}{2}} \\ \lesssim \varepsilon^{\frac{d+1}{2}} \mu_d(\frac{1}{\varepsilon})^{\frac{1}{2}} \|u_0\|_{W^{2,\infty}(D)} \|G_0(\cdot, y)\|_{W^{3,\infty}(D)}.\end{aligned} \tag{7.10}$$

Remark 7.1.1. *Note that for $y \in B_R \setminus \overline{D^\alpha}$, $G_0(\cdot, y)_{|_D}$ belongs to $W^{2,\infty}(D)$ in view of Proposition 44. The regularity $G_0(\cdot, y)_{|_D} \in W^{3,\infty}(D)$ can be obtained by assuming that the boundary of D is $\mathcal{C}^5$ by the Sobolev embeddings [179, Corollary 9.15].*

Corollary 40: L^2- and H^1convergence of J^ε

For all $y \in B_R \setminus \overline{D^\alpha}$,

$$\begin{aligned}\mathbb{E}\left[\|u_\varepsilon - u_0 - \mathcal{U}_1\|^2_{L^2(B_R \setminus \overline{D^\alpha})}\right]^{\frac{1}{2}} \\ \lesssim_\alpha \varepsilon^{\frac{d+1}{2}} \mu_d(\frac{1}{\varepsilon})^{\frac{1}{2}} \|u_0\|_{W^{2,\infty}(D)} \left(\int_{B_R \setminus \overline{D^\alpha}} \|G_0(\cdot, y)\|^2_{W^{2,\infty}(D)} \mathrm{d}y\right)^{\frac{1}{2}},\end{aligned} \tag{7.11}$$

and if we further assume that $G_0(\cdot,y)_{|_D}$ is in $W^{3,\infty}(D)$ for $y \in B_R \setminus \overline{D^\alpha}$, then

$$\mathbb{E}\left[\|u_\varepsilon - u_0 - \mathcal{U}_1\|^2_{H^1(B_R\setminus\overline{D^\alpha})}\right]^{\frac{1}{2}} \lesssim_\alpha \varepsilon^{\frac{d+1}{2}} \mu_d(\frac{1}{\varepsilon})^{\frac{1}{2}} \|u_0\|_{W^{2,\infty}(D)} \left(\int_{B_R\setminus\overline{D^\alpha}} \|G_0(\cdot,y)\|^2_{W^{3,\infty}(D)}\,\mathrm{d}y\right)^{\frac{1}{2}}. \tag{7.12}$$

Moreover we denote by a^* the transpose of a and ϕ^*, σ^* the adjoint correctors that solves respectively (4.30) and (6.6) with a^* instead of a. Finally, we write $\phi^{\varepsilon,*} := \phi^*(\frac{\cdot}{\varepsilon})$ and $\sigma^{\varepsilon,*} := \sigma^*(\frac{\cdot}{\varepsilon})$.
Note that, from (7.3), for all $y \in B_R \setminus \overline{D^\alpha}$,

$$\begin{aligned} u_\varepsilon(y) - u_0(y) - \mathcal{U}_1(y) = & \\ & \int_D (a^\star - a_\varepsilon(x))(\nabla u_\varepsilon(x) - \sum_{i=1}^d (e_i + \varepsilon\nabla\phi_i^\varepsilon(x)\partial_i u_0(x)) \cdot \nabla G_0(x,y)\mathrm{d}x \\ & - k^2 \int_D (n^\star - n_\varepsilon(x))(u_\varepsilon(x) - u_0(x))G_0(x,y)\mathrm{d}x - \mathbb{E}[u_\varepsilon - u_0] \\ & = J^\varepsilon(y) - \mathbb{E}[J^\varepsilon(y)]. \end{aligned} \tag{7.13}$$

We follow the strategy of [19], to show that

$$\mathrm{Var}\left[J^\varepsilon(y)\right] \lesssim \varepsilon^{d+1}\mu_d(\frac{1}{\varepsilon}) \|u_0\|^2_{W^{2,\infty}(D)} \|G_0(\cdot,y)\|^2_{W^{2,\infty}(D)}, \tag{7.14}$$

which will yield the desired result by integrating over y.
In [19], three main tools are used to show (7.7):

- the *multiscale functional inequality* Hypothesis 20 that also holds here.
- the bounds on the corrector (Proposition 22) and the convergence of the two-scale expansion (without the boundary corrector) that we showed in Proposition 36
- the large-scale (weighted) Calderón-Zygmund estimates stated in [136].

In our configuration, we can use the two first tools. However the large-scale Calderón-Zygmund estimates were developed for the Poisson equation, not for the Helmholtz equation. Instead of deriving similar estimates for Helmholtz equation, we take advantage of the boundness of the our domain D to establish the following Lemma 41.

Lemma 41

(a) There exists a constant C depending only on d such that, for any $U \in L^1(D)$ and $t > 0$,

$$\int_{\mathbb{R}^d} \left(\int_{B_t(x)\cap D} |U| \right) \mathrm{d}x \leq C t^d \int_D |U|. \tag{7.15}$$

(b) For $T > 0$, let $\rho_T(x)$ be the radial weight, for all $x \in \mathbb{R}^d$:

$$\rho_T(x) := \frac{|x|}{T} + 1.$$

Then, for $U \in L^1(D)$ and $\alpha > 0$,

$$\int_{\mathbb{R}^d} \rho_T(x)^\alpha \left(\int_{B_t(x)\cap D} |U| \right)^2 \mathrm{d}x \leq C \sup_{y\in D} \left(\frac{t+|y|}{T} + 1 \right)^\alpha t^d \left(\int_D |U| \right)^2. \tag{7.16}$$

The proof can be found in Appendix D.

The first step of the proof of Theorem 39 consists in applying the mixing condition Hypothesis 20 to $J^\varepsilon(z)$ for $z \in B_R \setminus \overline{D^\alpha}$. To simplify notations, we introduce

$$\begin{aligned} \mathcal{P}(S) := \int_D (a^\star - a_\varepsilon(x)) \left(\nabla u_\varepsilon(x) - (e_i + \nabla \phi_i(\frac{x}{\varepsilon})) \partial_i u_0(x) \right) \cdot \nabla g(x) \mathrm{d}x \\ - k^2 \int_D (n^\star - n_\varepsilon(x))(u_\varepsilon(x) - u_0(x)) g(x) \mathrm{d}x. \end{aligned} \tag{7.17}$$

where $a_\varepsilon := a_M + (a_S - a_M)\mathbb{1}_{S^\varepsilon}$, $n_\varepsilon := n_M + (n_S - n_M)\mathbb{1}_{S^\varepsilon}$ and $g \in W^{3,\infty}(D)$.
By definition, we have then $\mathcal{P}(S) = J^\varepsilon(z)$ if $g(\cdot) = G_0(\cdot, z)$, and $\mathcal{P}(S) = \partial_i J^\varepsilon(z)$ if $g(\cdot) = \partial_i G_0(\cdot, z)$, if $\partial_i G_0(\cdot, z)_{|D} \in W^{3,\infty}(D)$ where the derivative applies to the second variable.
We introduce some additional notations before considering $\partial^{osc}\mathcal{P}(S)$. Let $\ell \geq 1$ and $x \in \mathbb{R}^d$. Let S be a given realization of the scatterer process. We consider another distribution of scatterers S' satisfying the assumptions of Section 5.2 and such that $S \cap (\mathbb{R}^d \setminus B_\ell(x)) = S' \cap (\mathbb{R}^d \setminus B_\ell(x))$. We name $\mathcal{A}_\ell(x) := \{S' \,|S \cap (\mathbb{R}^d \setminus B_\ell(x)) = S' \cap (\mathbb{R}^d \setminus B_\ell(x))\}$.
For any S-dependent measurable random variable F, we denote by F' and δF the random variables:

$$F' := F(S'), \tag{7.18}$$

$$\delta F := F(S') - F(S) := F' - F. \tag{7.19}$$

By definition,

$$|\partial^{osc}_{S,B_\ell(x)}\mathcal{P}(S)| \lesssim \sup_{S'\in\mathcal{A}_\ell(x)} |\delta\mathcal{P}| \tag{7.20}$$

Here, the notation $\phi^{\varepsilon,\prime}$ stands for $\phi'(\frac{\cdot}{\varepsilon})$.
The proof is split into two. We start by deriving a representation formula for $\delta\mathcal{P}$. We then bound each term of the representation formula to get our estimate.

7.2 Representation formula for $\delta\mathcal{P}$

We recall that $\mathcal{P}$ is defined in (7.17) and $\delta\mathcal{P}$ is defined in (7.19). Then, $\delta\mathcal{P}$ admit the following form:

Lemma 42: Representation formula for $\delta\mathcal{P}$

For $g \in W^{3,\infty}(D)$,

$$\begin{aligned}
\delta\mathcal{P} = &-\sum_{j=1}^d \int_D \partial_j g(\varepsilon\nabla\phi_j^{\varepsilon,*} + e_j)\cdot\delta a_\varepsilon(\nabla u_\varepsilon' - \sum_{i=1}^d (e_i + \varepsilon\nabla\phi_i^{\varepsilon,\prime})\partial_i u_0)\\
&+\sum_{j=1}^d \int_D -(\varepsilon\phi_j^{\varepsilon,*}\nabla\partial_j g + \nabla r_j)\cdot\delta a_\varepsilon\nabla u_\varepsilon' + k^2\delta n_\varepsilon u_\varepsilon'(r_j + \varepsilon\phi_j^{\varepsilon,*}\partial_j g)\\
&+\sum_{i,j=1}^d \int_{\mathbb{R}^d} (\varepsilon\phi_j^{\varepsilon,*}\nabla\partial_j g\partial_i u_0\mathbb{1}_D - \varepsilon\nabla\cdot(\eta_\varepsilon\phi_j^{\varepsilon,*}\partial_j g\partial_i u_0)\mathbb{1}_D + \nabla R_{ij})\cdot\delta a_\varepsilon(\varepsilon\nabla\phi_i^{\varepsilon,\prime} + e_i)\\
&+\int_D k^2\delta n_\varepsilon(u_\varepsilon' - u_0)g - \varepsilon k^2\beta^\varepsilon\delta u_\varepsilon\cdot\nabla g
\end{aligned} \tag{7.21}$$

where for $j \in [\![1,d]\!]$, $r_j := -\varepsilon\partial_j g\phi_j^{\varepsilon,*}\mathbb{1}_D + \tilde{r}_j$ and $\tilde{r}_j$ is the almost sure unique solution in $H^1(B_R)$ of:

$$\begin{cases}
-\Delta\tilde{r}_j - k^2 n_0\tilde{r}_j = 0 & \text{in } B_R\setminus\overline{D},\\
-\nabla\cdot\left(a_\varepsilon^*\nabla\tilde{r}_j\right) - k^2 n_\varepsilon\tilde{r}_j = -\varepsilon\nabla\cdot((a_\varepsilon^*\phi_j^{\varepsilon,*} - \sigma_j^{\varepsilon,*})\nabla\partial_j g) & \\
\qquad\qquad + \varepsilon k^2\nabla\cdot(\beta^\varepsilon g) & \text{in } D,\\
\nabla\tilde{r}_j^-\cdot\nu - a_\varepsilon^*\nabla\tilde{r}_j^+\cdot\nu = -\varepsilon a_\varepsilon^*\phi_j^{\varepsilon,*}\nabla\partial_j g\cdot\nu + \varepsilon(\nabla\cdot\sigma_j^{\varepsilon,*})\partial_j g^+\cdot\nu & \text{on } \partial D,\\
\nabla\tilde{r}_j\cdot\nu = \Lambda(\tilde{r}_j) & \text{on } \partial B_R,
\end{cases} \tag{7.22}$$

and for $i,j \in [\![1,d]\!]$, R_{ij} is the almost sure unique solution in $\dot{H}(\mathbb{R}^d) := \{v \in H^1_{loc}(\mathbb{R}^d) \mid \nabla v \in L^2(\mathbb{R}^d)\}/\mathbb{R}$ of:

$$\begin{cases} -\nabla\cdot a(\frac{\cdot}{\varepsilon})^*\nabla R_{ij} = 0 & \text{in } \mathbb{R}^d\setminus\overline{D},\\ -\nabla\cdot a_\varepsilon^*\nabla R_{ij} = -\varepsilon\nabla\cdot(a_\varepsilon^*\phi_j^{\varepsilon,*}-\sigma_j^{\varepsilon,*})\nabla(\partial_j g\partial_i u_0) & \\ \qquad\qquad +\nabla\cdot a_\varepsilon^*\nabla(\eta_\varepsilon\phi_j^{\varepsilon,*}\partial_j g\partial_i u_0) & \text{in } D,\\ a_\varepsilon^*\nabla R_{ij}^-\cdot\nu - a_\varepsilon^*\nabla R_{ij}^+\cdot\nu = -\varepsilon(a_\varepsilon^*\phi_j^{\varepsilon,*}-\sigma_j^{\varepsilon,*})\nabla(\partial_j g\partial_i u_0)\cdot\nu & \\ \qquad\qquad +\varepsilon\nabla\cdot(\sigma_j^{\varepsilon,*}\partial_j g\partial_i u_0)\cdot\nu & \\ \qquad\qquad +\varepsilon a_\varepsilon^*\nabla(\phi_j^{\varepsilon,*}\partial_j g\partial_i u_0)\cdot\nu & \text{on } \partial D. \end{cases} \tag{7.23}$$

Remark 7.2.1. *Note that by the divergence theorem [181, theorem 3.24], since $\nabla\cdot(\nabla\cdot\sigma_j)=0$ for all $j\in[\![1,d]\!]$, we have that the normal trace $(\nabla\cdot\sigma_j)\cdot\nu \in H^{-1/2}(\partial D)$.*

Proof of the Lemma. By direct computation,

$$\begin{aligned} \delta\mathcal{P} = &-\int_D \delta a_\varepsilon\left(\nabla u_\varepsilon' - \sum_{i=1}^d (e_i+\varepsilon\nabla\phi_i^{\varepsilon,\prime})\partial_i u_0\right)\cdot\nabla g\\ &+\int_D (a^\star - a_\varepsilon)\delta\left(\nabla u_\varepsilon - \sum_{i=1}^d (e_i+\varepsilon\nabla\phi_i^{\varepsilon})\partial_i u_0\right)\cdot\nabla g\\ &+\int_D k^2\delta n_\varepsilon(u_\varepsilon'-u_0) - k^2(n^\star-n_\varepsilon)\delta u_\varepsilon g \end{aligned} \tag{7.24}$$

First notice that for $j\in[\![1,d]\!]$, $(a^\star-a_\varepsilon)e_i$ can be rewritten as:

$$(a^\star-a_\varepsilon)^* e_j = \varepsilon a_\varepsilon\nabla\phi_j^{\varepsilon,*} - \varepsilon\nabla\cdot\sigma_j^{\varepsilon,*}.$$

Moreover $\delta\phi_i$ verifies in $\mathbb{R}^d$

$$-\nabla\cdot a\nabla\delta\phi_i = \nabla\cdot\delta a(\nabla\phi_i'+e_i)$$

and δu_ε is almost sure the unique solution in $H^1(B_R)$ of:

$$\begin{cases} -\Delta\delta u_\varepsilon - k^2 n_0\delta u_\varepsilon = 0 & \text{in } \mathbb{R}^d\setminus\overline{D},\\ -\nabla\cdot(a_\varepsilon\nabla\delta u_\varepsilon) - k^2 n_\varepsilon\delta u_\varepsilon = \nabla\cdot(\delta a_\varepsilon\nabla u_\varepsilon') + k^2\delta n_\varepsilon u_\varepsilon' & \text{in } D,\\ \nabla\delta u_\varepsilon^-\cdot\nu - a_\varepsilon\nabla\delta u_\varepsilon^+\cdot\nu = \delta a_\varepsilon\nabla u_\varepsilon'^{\,+}\cdot\nu & \text{on } \partial D,\\ \nabla\delta u_\varepsilon\cdot\nu = \Lambda(\delta u_\varepsilon) & \text{on } \partial B_R. \end{cases} \tag{7.25}$$

We thus get for $i,j \in [\![1,d]\!]$

$$\begin{aligned}
&\nabla\phi_j^{\varepsilon,*}\cdot a_\varepsilon(\nabla\delta u_\varepsilon - \nabla\delta\phi_i^\varepsilon)\\
&\quad= \nabla\cdot(\phi_j^{\varepsilon,*}a_\varepsilon(\nabla\delta u_\varepsilon - \nabla\delta\phi_i^\varepsilon)) - \phi_j^{\varepsilon,*}\nabla\cdot(a_\varepsilon(\nabla\delta u_\varepsilon - \nabla\delta\phi_i^\varepsilon))\\
&\quad= \nabla\cdot(\phi_j^{\varepsilon,*}a_\varepsilon(\nabla\delta u_\varepsilon - \nabla\delta\phi_i^\varepsilon))\\
&\qquad+\phi_j^{\varepsilon,*}(\nabla\cdot(\delta a_\varepsilon\nabla u_\varepsilon') + k^2\delta n_\varepsilon u_\varepsilon' + k^2 n_\varepsilon\delta u_\varepsilon)\\
&\qquad-\phi_j^{\varepsilon,*}\nabla\cdot(\delta a_\varepsilon(\nabla\phi_i^{\varepsilon,\prime}+e_i))\\
&\quad= \nabla\cdot(\phi_j^{\varepsilon,*}a_\varepsilon(\nabla\delta u_\varepsilon - \nabla\delta\phi_i^\varepsilon))\\
&\qquad+\nabla\cdot(\phi_j^{\varepsilon,*}\delta a_\varepsilon\nabla u_\varepsilon') - \nabla\phi_j^{\varepsilon,*}\cdot\delta a_\varepsilon\nabla u_\varepsilon' + k^2\delta n_\varepsilon u_\varepsilon'\phi_j^{\varepsilon,*} + k^2 n_\varepsilon\delta u_\varepsilon\phi_j^{\varepsilon,*}\\
&\qquad-\nabla\cdot(\phi_j^{\varepsilon,*}\delta a_\varepsilon(\nabla\phi_i^{\varepsilon,\prime}+e_i)) + \nabla\phi_j^{\varepsilon,*}\cdot\delta a_\varepsilon(\nabla\phi_i^{\varepsilon,\prime}+e_i).
\end{aligned} \tag{7.26}$$

By skew-symmetry, it also holds for $i,j \in [\![1,d]\!]$

$$(\nabla\cdot\sigma_j^{\varepsilon,*})\cdot\nabla(\delta u_\varepsilon - \nabla\delta\phi_i^\varepsilon) = -\nabla\cdot\left(\sigma_j^{\varepsilon,*}(\nabla\delta u_\varepsilon - \nabla\delta\phi_i^\varepsilon)\right).$$

Similarly $n^\star - n_\varepsilon = -\varepsilon\nabla\cdot\beta^\varepsilon$ and thus,

$$(n^\star - n_\varepsilon)\delta u_\varepsilon = -\varepsilon\nabla\cdot(\beta^\varepsilon\delta u_\varepsilon) + \varepsilon\beta^\varepsilon\cdot\nabla\delta u_\varepsilon.$$

Therefore we obtain

$$\begin{aligned}
\delta\mathcal{P} = &\sum_{j=1}^d -\int_D(\varepsilon\nabla\phi_j^{\varepsilon,*}+e_j)\partial_j g\cdot\delta a_\varepsilon(\nabla u_\varepsilon' - \sum_{i=1}^d(\varepsilon\nabla\phi_i^{\varepsilon,\prime}+e_i)\partial_i u_0)\\
&-\varepsilon\int_D\phi_j^{\varepsilon,*}\nabla\partial_j g\cdot\delta a_\varepsilon\nabla u_\varepsilon' + \varepsilon\int_{\partial D}\phi_j^{\varepsilon,*}\partial_j g\cdot\delta a_\varepsilon\nabla u_\varepsilon'\cdot\nu\\
&+\varepsilon\int_D k^2\delta n_\varepsilon u_\varepsilon'\phi_j^{\varepsilon,*}\partial_j g + k^2\int_D\delta n_\varepsilon(u_\varepsilon' - u_0)g\\
&+\sum_{i=1}^d\varepsilon\int_D\phi_j^{\varepsilon,*}\nabla(\partial_j g\partial_i u_0)\cdot\delta a_\varepsilon(\varepsilon\nabla\phi_i^{\varepsilon,\prime}+e_i)\\
&-\varepsilon\int_{\partial D}\phi_j^{\varepsilon,*}\partial_j g\partial_i u_0\delta a_\varepsilon(\nabla\phi_i^{\varepsilon,\prime}+e_i)\cdot\nu\\
&+\varepsilon^2\int_D\nabla(\partial_j g\partial_i u_0)\cdot(\phi_j^{\varepsilon,*}a_\varepsilon + \sigma_j^{\varepsilon,*})\nabla\delta\phi_i^\varepsilon\\
&-\varepsilon^2\int_{\partial D}\partial_j g\partial_i u_0(\phi_j^{\varepsilon,*}a_\varepsilon + \sigma_j^{\varepsilon,*})\nabla\delta\phi_i^\varepsilon\cdot\nu\\
&-\varepsilon\int_D\nabla\partial_j g\cdot(a_\varepsilon\phi_j^{\varepsilon,*} + \sigma_j^{\varepsilon,*})\nabla\delta u_\varepsilon + \varepsilon\int_{\partial D}\partial_j g(a_\varepsilon\phi_j^{\varepsilon,*} + \sigma_j^{\varepsilon,*})\nabla\delta u_\varepsilon\cdot\nu\\
&+\varepsilon\int_D k^2 n_\varepsilon\delta u_\varepsilon\phi_j^{\varepsilon,*}\partial_j g - \varepsilon\int_D k^2\beta^\varepsilon\cdot\nabla\delta u_\varepsilon g\\
&-\varepsilon\int_D k^2\beta^\varepsilon\delta u_\varepsilon\cdot\nabla g + \varepsilon\int_{\partial D}k^2 g\beta^\varepsilon\delta u_\varepsilon\cdot\nu.
\end{aligned} \tag{7.27}$$

We simplify the terms depending on δu_ε by introducing the adjoint problem (7.22). By Proposition 43, since $\phi_j^{\varepsilon,*}$, $\sigma_j^{\varepsilon,*}$, $\beta^\varepsilon \in H^1_{loc}(\mathbb{R}^d)$ and $g \in H^2(D)$, there exists a unique solution $\tilde{r}_j$ to (7.22).
For $h \in H^1(B_R)$, $\tilde{r}_j$ verifies:

$$\begin{aligned}\int_{B_R\setminus\overline{D}} \nabla\tilde{r}_j\cdot\nabla\overline{h} - k^2 n_0\tilde{r}_j\overline{h} - \left\langle\Lambda(\tilde{r}_j),h\right\rangle_{H^{-\frac{1}{2}}(\partial B_R),H^{\frac{1}{2}}(\partial B_R)} + \int_D a_\varepsilon^*\nabla\tilde{r}_j\cdot\nabla\overline{h} - k^2 n_\varepsilon\tilde{r}_j\overline{h}\\ = \varepsilon\int_D (a_\varepsilon^*\phi_j^{\varepsilon,*} - \sigma_j^{\varepsilon,*})\nabla\partial_j g\cdot\nabla\overline{h} - k^2\beta^\varepsilon g\cdot\nabla\overline{h}\\ + \varepsilon\int_{\partial D}\sigma_j^{\varepsilon,*}\partial_j g\nabla\overline{h}\cdot\nu + k^2\beta^\varepsilon g\cdot\nu\overline{h}.\end{aligned} \tag{7.28}$$

Note that we used the skew-symmetry of σ_j to get the integration by parts

$$\left\langle\sigma_j^{\varepsilon,*},\nabla(\partial_j g\overline{h})\right\rangle_{-\frac{1}{2},\frac{1}{2}} = -\left\langle(\nabla\cdot\sigma_j^{\varepsilon,*})\cdot\nu,\partial_j g\overline{h}\right\rangle_{-\frac{1}{2},\frac{1}{2}} \tag{7.29}$$

Moreover δu_ε verifies for $h \in H^1(B_R)$

$$\begin{aligned}\int_{B_R\setminus\overline{D}} \nabla\delta u_\varepsilon\cdot\nabla\overline{h} - k^2 n_0\delta u_\varepsilon\overline{h} - \left\langle\Lambda(\delta u_\varepsilon),h\right\rangle_{H^{-\frac{1}{2}}(\partial B_R),H^{\frac{1}{2}}(\partial B_R)}\\ + \int_D a_\varepsilon\nabla\delta u_\varepsilon\cdot\nabla\overline{h} - k^2 n_\varepsilon\delta u_\varepsilon\overline{h} = \int_D -\delta a_\varepsilon\nabla u_\varepsilon'\cdot\nabla\overline{h} + k^2\delta n_\varepsilon u_\varepsilon'\overline{h},\end{aligned} \tag{7.30}$$

and

$$\begin{aligned}-\int_D a_\varepsilon\nabla\delta u_\varepsilon\cdot\nabla(\phi_j^{\varepsilon,*}\partial_j g) + \int_D k^2 n_\varepsilon\delta u_\varepsilon\phi_j^{\varepsilon,*}\partial_j g\\ = -\int_{\partial D} a_\varepsilon\phi_j^{\varepsilon,*}\partial_j g\nabla\delta u_\varepsilon\cdot\nu + \int_D\delta a_\varepsilon\nabla u_\varepsilon'\cdot\nabla(\phi_j^{\varepsilon,*}\partial_j g)\\ - \int_D k^2\delta n_\varepsilon u_\varepsilon'\phi_j^{\varepsilon,*}\partial_j g - \int_{\partial D}\delta a_\varepsilon\nabla u_\varepsilon'\cdot\nu\phi_j^{\varepsilon,*}\partial_j g.\end{aligned} \tag{7.31}$$

Therefore δu_ε satisfies

$$\begin{aligned}\int_{B_R\setminus\overline{D}} \nabla\delta u_\varepsilon\cdot\nabla r_j - k^2 n_0\delta u_\varepsilon r_j - \left\langle\Lambda(\delta u_\varepsilon),\overline{r_j}\right\rangle_{H^{-\frac{1}{2}}(\partial B_R),H^{\frac{1}{2}}(\partial B_R)}\\ + \int_D a_\varepsilon\nabla\delta u_\varepsilon\cdot\nabla r_j - k^2 n_\varepsilon\delta u_\varepsilon r_j = \int_D -\delta a_\varepsilon\nabla u_\varepsilon'\cdot\nabla r_j + k^2\delta n_\varepsilon u_\varepsilon' r_j\\ - \int_{\partial D} a_\varepsilon\phi_j^{\varepsilon,*}\partial_j g\nabla\delta u_\varepsilon\cdot\nu - \int_{\partial D}\delta a_\varepsilon\nabla u_\varepsilon'\cdot\nu\phi_j^{\varepsilon,*}\partial_j g.\end{aligned} \tag{7.32}$$

We combine (7.28) for $\overline{h} = \delta u_\varepsilon$ and (7.32) to get

$$\begin{aligned} -\int_D \delta a_\varepsilon \nabla u_\varepsilon' \cdot \nabla r_j + k^2 \delta n_\varepsilon u_\varepsilon' r_j &= \varepsilon \int_{\partial D} \phi_j^{\varepsilon,*} \partial_j g^+ \delta a_\varepsilon \nabla u_\varepsilon' \cdot \nu \\ &- \varepsilon \int_D \nabla \partial_j g \cdot (a_\varepsilon \nabla \phi_j^{\varepsilon,*} + \sigma_j^{\varepsilon,*}) \nabla \delta u_\varepsilon + \varepsilon \int_{\partial D} \partial_j g (a_\varepsilon \nabla \phi_j^{\varepsilon,*} + \sigma_j^{\varepsilon,*}) \nabla u_\varepsilon \cdot \nu \\ &+ \varepsilon \int_D k^2 \delta u_\varepsilon \phi_j^{\varepsilon,*} \partial_j g - \varepsilon \int_D k^2 \beta^\varepsilon \cdot \nabla \delta u_\varepsilon g + \varepsilon \int_{\partial D} k^2 g \beta^\varepsilon \delta u_\varepsilon \cdot \nu. \end{aligned} \tag{7.33}$$

We deal now with the terms depending on $\delta\phi_i$. R_{ij} satisfies for all $h \in \dot{H}(\mathbb{R}^d)$,

$$\begin{aligned} &\int_{\mathbb{R}^d} a(\tfrac{\cdot}{\varepsilon})^* \nabla R_{ij} \cdot \nabla \overline{h} \\ &\qquad = \varepsilon \int_D (a_\varepsilon^* \phi_j^{\varepsilon,*} - \sigma_j^{\varepsilon,*}) \nabla(\partial_j g \partial_i u_0) \cdot \nabla \overline{h} - (\nabla \cdot (\eta_\varepsilon \sigma_j^{\varepsilon,*} \partial_j g \partial_i u_0)) \cdot \nabla \overline{h} \\ &\qquad\quad - \varepsilon \int_D a_\varepsilon^* \nabla(\eta_\varepsilon \phi_j^{\varepsilon,*} \partial_j g \partial_i u_0) \cdot \nabla \overline{h} \end{aligned} \tag{7.34}$$

where we used that $\nabla \cdot \Big(\nabla \cdot (\eta_\varepsilon \sigma_j^{\varepsilon,*} \partial_j g \partial_i u_0) \Big) = 0$ by the skew-symmetry of σ_j. Subsequently the sesquilinear and linear form associated to (7.23) are respectively coercive and continuous in $\dot{H}(\mathbb{R}^d)$ equipped with the semi-norm $\|\cdot\|_{\dot{H}(\mathbb{R}^d)} = \|\nabla \cdot\|_{L^2(\mathbb{R}^d)}$ (cf [173, Chapter 2.5] for more details). Moreover,

$$\begin{aligned} &-\int_{\partial D} \phi_j^{\varepsilon,*} \partial_j g \partial_i u_0 \delta a_\varepsilon (\nabla \phi_i^{\varepsilon,\prime} + e_i) \cdot \nu - \int_{\partial D} \partial_j g \partial_i u_0 \phi_j^{\varepsilon,*} a_\varepsilon \nabla \delta \phi_i^\varepsilon \cdot \nu \\ &\qquad = -\int_D \delta a_\varepsilon (\nabla \phi_i^{\varepsilon,\prime} + e_i) \cdot \nabla(\eta_\varepsilon \phi_j^{\varepsilon,*} \partial_j g \partial_i u_0) - \nabla \delta \phi_i^\varepsilon \cdot a_\varepsilon^* \nabla(\eta_\varepsilon \phi_j^\varepsilon \partial_j g \partial_i u_0) \end{aligned} \tag{7.35}$$

and by the skew-symmetry of σ_j,

$$\begin{aligned} \int_D (\nabla \cdot (\eta_\varepsilon \sigma_j^{\varepsilon,*} \partial_j g \partial_i u_0)) \cdot \nabla \delta \phi_i^\varepsilon &= \int_{\partial D} (\nabla \cdot (\sigma_j^{\varepsilon,*} \partial_j g \partial_i u_0)) \cdot \nu \delta \phi_i^\varepsilon \\ &= -\int_{\partial D} \partial_j g \partial_i u_0 \sigma_j^{\varepsilon,*} \nabla \delta \phi_i^\varepsilon \cdot \nu. \end{aligned} \tag{7.36}$$

We combine (7.34) for $\overline{h} = \varepsilon \delta \phi_i^\varepsilon$ (which is a suitable test function), (7.35) and (7.36) to get the desired result.

□

7.3 Proof of Theorem 39

Proof of Theorem 39. Let

$$\|I\|_\ell^2 := \int_{\mathbb{R}^d} \ell^{-d} \sup_{S' \in \mathcal{A}_\ell(x)} \left| \sum_{j=1}^d \int_{D \cap B_{\varepsilon\ell}(x)} \partial_j g (\varepsilon \nabla \phi_j^{\varepsilon,*} + e_j) \cdot \delta a_\varepsilon (\nabla u_\varepsilon' - \sum_{i=1}^d (e_i + \varepsilon \nabla \phi_i^{\varepsilon,\prime}) \partial_i u_0) \right|^2 \mathrm{d}x.$$

By Cauchy-Schwarz inequality we obtain

$$\begin{aligned}\|I\|_\ell^2 &\lesssim \int_{\mathbb{R}^d} \ell^{-d} \left(\sum_{j=1}^d \int_{D\cap B_{\varepsilon\ell}(x)} |\partial_j g(\varepsilon\nabla\phi_j^{\varepsilon,*} + e_j)|^2 \right) \\ &\qquad \sup_{S'\in\mathcal{A}_\ell(x)} \left(\int_D |\nabla u'_\varepsilon - \sum_{i=1}^d (e_i + \varepsilon\nabla\phi_i'(\frac{\cdot}{\varepsilon}))\partial_i u_0|^2 \right) \mathrm{d}x \\ &\lesssim \int_{\mathbb{R}^d} \ell^{-d} \left(\sum_{j=1}^d \int_{D\cap B_{\varepsilon\ell}(x)} |\partial_j g(\varepsilon\nabla\phi_j^{\varepsilon,*} + e_j)|^2 \right) \\ &\qquad \sup_{S'\in\mathcal{A}_\ell(x)} \left(\left\| u'_\varepsilon - u_0 - \sum_{i=1}^d \varepsilon\phi_i^{\varepsilon,\prime}\partial_i u_0 \right\|_{H^1(D)}^2 \right) \mathrm{d}x.\end{aligned} \tag{7.37}$$

Using Proposition 36, we have moreover

$$\sup_{S'\in\mathcal{A}_\ell(x)} \left\| u'_\varepsilon - u_0 - \sum_{i=1}^d \varepsilon\phi_i^{\varepsilon,\prime}\partial_i u_0 \right\|_{H^1(D)}^2 \lesssim \varepsilon\mu_d(\frac{1}{\varepsilon}) \sup_{S'\in\mathcal{A}_\ell(x)} (\chi'_\varepsilon)^2 \|u_0\|_{W^{2,\infty}(D)}^2 .$$

As mentioned in [19, Remark 2.1], by following the proof of [142, Theorem 4], one has that

$$\mathcal{C}'(z) \lesssim \mathcal{C}(z). \tag{7.38}$$

where $\mathcal{C}$ is defined in Proposition 22. It particular, this implies that $\sup_{S'\in\mathcal{A}_\ell(x)}(\chi'_\varepsilon)^2$ can be bounded by χ_ε^2, which is a random variable independent of S', that satisfies the integrability (4.52). Combining this with Lemma 41 applied to $|\partial_j g(\varepsilon\nabla\phi_j^\varepsilon) + e_j|^2$ with $t = \varepsilon\ell$ and the bounds on the gradient of the corrector yields

$$\begin{aligned}\|I\|_\ell^2 &\lesssim \left(\int_{\mathbb{R}^d} \ell^{-d} \left(\sum_{j=1}^d \int_{D\cap B_{\varepsilon\ell}(x)} |\partial_j g(\varepsilon\nabla\phi_j^\varepsilon + e_j)|^2 \right) \mathrm{d}x \right) \left(\varepsilon\mu_d(\frac{1}{\varepsilon})(\chi_\varepsilon)^2 \|u_0\|_{W^{2,\infty}(D)}^2 \right) \\ &\lesssim \left(\varepsilon^d \sum_{j=1}^d \int_D |\partial_j g(\varepsilon\nabla\phi_j^\varepsilon + e_j)|^2 \right) \left(\varepsilon\mu_d(\frac{1}{\varepsilon})(\chi_\varepsilon)^2 \|u_0\|_{W^{2,\infty}(D)}^2 \right) \\ &\lesssim \varepsilon^{d+1}\mu_d(\frac{1}{\varepsilon})\widetilde{\chi_\varepsilon^4}^2(\chi_\varepsilon)^2 \|u_0\|_{W^{2,\infty}(D)}^2 \|g\|_{W^{2,\infty}(D)}^2 ,\end{aligned} \tag{7.39}$$

with $\widetilde{\chi_\varepsilon^4}$ defined as:

$$\widetilde{\chi_\varepsilon^4} := \left(\varepsilon^d \sum_{z\in P_\varepsilon(D)} (1 + r_*(z))^{2d} \right)^{\frac{1}{2}} .$$

In view of Lemma 38, $\widetilde{\chi_\varepsilon^4}^2(\chi_\varepsilon)^2$ satisfies the expected stochastic integrability.

Let

$$\|II\|_\ell^2 := \int_{\mathbb{R}^d} \ell^{-d} \sup_{S'\in\mathcal{A}_\ell(x)} \left| \sum_{j=1}^d \int_D -(\varepsilon\phi_j^{\varepsilon,*}\nabla\partial_j g + \nabla r_j)\cdot\delta a_\varepsilon \nabla u_\varepsilon' + k^2\delta n_\varepsilon u_\varepsilon'(r_j + \varepsilon\phi_j^{\varepsilon,*}\partial_j g)\right|^2 \mathrm{d}x.$$

Similarly to the analysis done with v_ε in the proof of Proposition 36, one has that r_j satisfies a similar decay rate:

$$\|r_j\|_{H^1(D)} \lesssim \varepsilon^{\frac{1}{2}}\mu_d(\frac{1}{\varepsilon})^{\frac{1}{2}}\widetilde{\chi_\varepsilon^5}\,\|g\|_{W^{2,\infty}(D)}\,, \tag{7.40}$$

for some random variable $\widetilde{\chi_\varepsilon^5}$ satisfying (4.52).
To get rid of the dependency with respect to S', note that δu_ε also satisfies

$$\begin{cases} -\Delta\delta u_\varepsilon - k^2\delta u_\varepsilon = 0 & \text{in } B_R\setminus\overline{D},\\ -\nabla\cdot\left(a_\varepsilon'\nabla\delta u_\varepsilon\right) - k^2\delta u_\varepsilon = -\nabla\cdot(\delta a_\varepsilon\nabla u_\varepsilon) - k^2\delta n_\varepsilon u_\varepsilon & \text{in } D,\\ \nabla\delta u_\varepsilon^-\cdot\nu - a_\varepsilon'\nabla\delta u_\varepsilon^+\cdot\nu = -\delta a_\varepsilon\nabla u_\varepsilon^+\cdot\nu & \text{on } \partial D,\\ \nabla\delta u_\varepsilon\cdot\nu = \Lambda(\delta u_\varepsilon) & \text{on } \partial B_R. \end{cases} \tag{7.41}$$

In particular, by Proposition 43

$$\|\delta u_\varepsilon\|_{H^1(D)} \lesssim \|u_\varepsilon\|_{H^1(B_{\varepsilon\ell}(x)\cap D)}\,. \tag{7.42}$$

This gives

$$\begin{aligned} \sup_{S'\in\mathcal{A}_\ell(x)} \left\|u_\varepsilon'\right\|_{H^1(B_{\varepsilon\ell}(x)\cap D)} &\lesssim \sup_{S'\in\mathcal{A}_\ell(x)} \|\delta u_\varepsilon\|_{H^1(D)} + \|u_\varepsilon\|_{H^1(B_{\varepsilon\ell}(x)\cap D)}\\ &\lesssim \|u_\varepsilon\|_{H^1(B_{\varepsilon\ell}(x)\cap D)}\,. \end{aligned} \tag{7.43}$$

We can finally compute $\|II\|_\ell^2$ using the Lemma 41 on u_ε and the bounds on the correctors which yields

$$\begin{aligned} \|II\|_\ell^2 &\lesssim \left(\sum_{j=1}^d \int_D |\nabla r_j|^2 + \varepsilon^2|\phi_j^{\varepsilon,*}\nabla\partial_j g|^2 + |r_j|^2 + \varepsilon^2|\phi_j^{\varepsilon,*}\partial_j g|^2\right)\\ &\qquad\qquad \times \int_{\mathbb{R}^d} \ell^{-d}\left(\sup_{S'\in\mathcal{A}_\ell(x)} \left\|u_\varepsilon'\right\|_{H^1(B_{\varepsilon\ell}(x)\cap D)}^2\right)\mathrm{d}x\\ &\lesssim \varepsilon^{d+1}\mu_d(\frac{1}{\varepsilon})\widetilde{\chi_\varepsilon^6}^2\,\|u_0\|_{W^{2,\infty}(D)}^2\,\|g\|_{W^{2,\infty}(D)}^2\,, \end{aligned} \tag{7.44}$$

for a random variable $\widetilde{\chi_\varepsilon^6}$ satisfying the desired integrability.
Let

$$\|III\|_\ell^2 = \int_{\mathbb{R}^d} \ell^{-d} \sup_{S'\in\mathcal{A}_\ell(x)} \left|\sum_{i,j=1}^d \int_D (\varepsilon\phi_j^{\varepsilon,*}\nabla\partial_j g\partial_i u_0 - \varepsilon\nabla\cdot(\eta_\varepsilon\phi_j^{\varepsilon,*}\partial_j g\partial_i u_0) + \nabla R_{ij})\cdot\delta a_\varepsilon(\varepsilon\nabla\phi_i^{\varepsilon,\prime} + e_i)\right|^2 \mathrm{d}x. \tag{7.45}$$

To estimate $\|III\|_\ell^2$, we follow the steps of the proof of [19, Proposition 2.6]. By a change of variable $y \mapsto \frac{y}{\varepsilon}$ in the integral in D and by [19, Lemma 2.9], we obtain

$$\|III\|_\ell^2 \lesssim \varepsilon^{2d} \int_{\mathbb{R}^d} \sum_{i,j=1}^d \fint_{B_{r_*(x)}(x)} \varepsilon^2 \Big[|\phi_j^{\varepsilon,*} \nabla \partial_j g \partial_i u_0 \mathbb{1}_D|^2(\varepsilon\cdot) + \varepsilon^2 |\nabla \cdot (\eta_\varepsilon \phi_j^{\varepsilon,*} \partial_j g \partial_i u_0 \mathbb{1}_D)|^2(\varepsilon\cdot) + |\nabla R_{ij}|^2(\varepsilon\cdot) \Big] \sup_{S' \in \mathcal{A}_\ell(x)} \int_{B_{2\ell + r_*(x)}(x)} |\nabla \phi_i' + e_i|^2 \mathrm{d}x. \tag{7.46}$$

Moreover from [136, Proof of Theorem 4], we obtain for $i \in [\![1, d]\!]$,

$$\sup_{S'} \int_{B_{2\ell+r_*(x)}(x)} |\nabla \phi_i' + e_i|^2 \mathrm{d}x \lesssim \int_{B_{2\ell+r_*(x)}(x)} |\nabla \phi_i + e_i|^2 \lesssim 2^d (\ell + r_*(x))^d \mathrm{d}x.$$

Thus, since for all $x \in \mathbb{R}^d$, $(\ell + r_*(x))^d \lesssim \ell^d r_*(x)^d$, we have

$$\|III\|_\ell^2 \lesssim \varepsilon^{2d} \ell^d \sum_{i,j=1}^d \int_{\mathbb{R}^d} r_*(x) \times \left(\fint_{B_{r_*(x)}(x)} \varepsilon^2 |\phi_j^{\varepsilon,*} \nabla \partial_j g \partial_i u_0 \mathbb{1}_D|^2(\varepsilon\cdot) + \varepsilon^2 |\nabla \cdot (\eta_\varepsilon \phi_j^{\varepsilon,*} \partial_j g \partial_i u_0 \mathbb{1}_D)|^2(\varepsilon\cdot) + |\nabla R_{ij}|^2(\varepsilon\cdot) \right) \mathrm{d}x. \tag{7.47}$$

We recall the following estimate [19, (3.8)] in the form: If v is the solution in $\dot{H}(\mathbb{R}^d)$ of $-\nabla \cdot a \nabla v = \nabla \cdot h$, with $h \in L^2(D)$, then for all α such that $d < \alpha < 3d$ and for all $T > 1$

$$\begin{aligned} &\int_{\mathbb{R}^d} r_*(x)^d \left(\fint_{B_{r_*(x)}(x)} |h|^2 + |\nabla v|^2 \right) \\ &\qquad \lesssim_\alpha r_*(0)^{\frac{\alpha}{2}} \left(\int_{\mathbb{R}^d} r_*^{2d} \rho_T^{-\alpha} \right)^{\frac{1}{2}} \left(\int_{\mathbb{R}^d} \rho_T^\alpha \left(\int_{B(x)} |h|^2 \right)^2 \right)^{\frac{1}{2}}, \end{aligned} \tag{7.48}$$

with ρ_T defined in Lemma 41. Note that R_{ij} verifies:

$$\begin{aligned} &-\nabla \cdot (a \nabla R_{ij}(\varepsilon\cdot)) \\ &\quad = -\varepsilon \nabla \cdot \Big(\Big(\Big((a_\varepsilon^* \phi_j^{\varepsilon,*} - \sigma_j^{\varepsilon,*}) \nabla (\partial_j g \partial_i u_0) \\ &\qquad\qquad - (\nabla \cdot (\eta_\varepsilon \sigma_j^{\varepsilon,*} \partial_j g \partial_i u_0)) - a_\varepsilon^* \nabla (\eta_\varepsilon \phi_j^{\varepsilon,*} \partial_j g \partial_i u_0) \Big) \mathbb{1}_D \Big) (\varepsilon\cdot) \Big) \\ &\quad := -\nabla (\cdot H_{ij} \mathbb{1}_D(\varepsilon\cdot)). \end{aligned} \tag{7.49}$$

Thus we can apply (7.48) to R_{ij} which yields for any α such that $d < \alpha < 3d$ and $T > 1$

$$\begin{aligned}\sum_{i,j=1}^{d} \int_{\mathbb{R}^d} r_*(x) \fint_{B_{r_*(x)}(x)} |\nabla R_{ij}|^2(\varepsilon\cdot) \\ \lesssim_\alpha \sum_{i,j=1}^{d} r_*(0)^{\frac{\alpha}{2}} \left(\int_{\mathbb{R}^d} r_*^{2d} \rho_T^{-\alpha}\right)^{\frac{1}{2}} \left(\int_{\mathbb{R}^d} \rho_T^{\alpha} \left(\int_{B(x)} |H_{ij}\mathbb{1}_D|^2(\varepsilon\cdot)\right)^2\right)^{\frac{1}{2}}.\end{aligned} \tag{7.50}$$

By denoting:

$$|(F_{ij}\mathbb{1}_D)(\varepsilon\cdot)|^2 := \varepsilon^2 |\phi_j^{\varepsilon,*} \nabla \partial_j g \partial_i u_0 \mathbb{1}_D|^2(\varepsilon\cdot) + \varepsilon^2 |\nabla\cdot(\eta_\varepsilon \phi_j^{\varepsilon,*} \partial_j g \partial_i u_0 \mathbb{1}_D|^2(\varepsilon\cdot),$$

we also have

$$\begin{aligned}\sum_{i,j=1}^{d} \int_{\mathbb{R}^d} r_*(x) \fint_{B_{r_*(x)}(x)} |F_{ij}\mathbb{1}_D|^2(\varepsilon\cdot) \\ \lesssim_\alpha \sum_{i,j=1}^{d} r_*(0)^{\frac{\alpha}{2}} \left(\int_{\mathbb{R}^d} r_*^{2d} \rho_T^{-\alpha}\right)^{\frac{1}{2}} \left(\int_{\mathbb{R}^d} \rho_T^{\alpha} \left(\int_{B(x)} |F_{ij}\mathbb{1}_D|^2(\varepsilon\cdot)\right)^2\right)^{\frac{1}{2}}.\end{aligned} \tag{7.51}$$

Similarly to the analysis done in the proof of Proposition 36, one has that

$$\left\|F_{ij}\right\|_{L^2(D)} + \left\|H_{ij}\right\|_{L^2(D)} \lesssim \varepsilon^{\frac{1}{2}} \mu_d (\frac{1}{\varepsilon})^{\frac{1}{2}} \widetilde{\chi_\varepsilon^7} \left\|u_0\right\|^2_{W^{2,\infty}(D)} \left\|g\right\|^2_{W^{2,\infty}(D)}, \tag{7.52}$$

for a random variable $\widetilde{\chi_\varepsilon^7}$ satisfying the desired integrability.
After changing variables to $x \mapsto \varepsilon x$ in the inner and outer integral and applying (7.16)

from Lemma 41 (with $U := F_{ij} + H_{ij}$) we obtain

$$\begin{aligned}
\|III\|_\ell^2 &\lesssim_\alpha \varepsilon^d \ell^d r_*(0)^{\frac{\alpha}{2}} \sum_{i,j=1}^d \left(\int_{\mathbb{R}^d} r_*^{2d} \rho_T^{-\alpha} \right)^{\frac{1}{2}} \\
&\qquad \left(\int_{\mathbb{R}^d} \rho_T^\alpha \left(\int_{B_\varepsilon(\varepsilon x)} |F_{ij}\mathbb{1}_D|^2 + |H_{ij}\mathbb{1}_D|^2 \right)^2 \right)^{\frac{1}{2}} \\
&\lesssim_\alpha \varepsilon^{d/2} \ell^d r_*(0)^{\frac{\alpha}{2}} \sum_{i,j=1}^d \left(\int_{\mathbb{R}^d} r_*^{2d} \rho_T^{-\alpha} \right)^{\frac{1}{2}} \\
&\qquad \left(\int_{\mathbb{R}^d} \rho_{\varepsilon T}^\alpha \left(\int_{B_\varepsilon(x)} |F_{ij}\mathbb{1}_D|^2 + |H_{ij}\mathbb{1}_D|^2 \right)^2 \right)^{\frac{1}{2}} \qquad (7.53) \\
&\lesssim_\alpha \varepsilon^d \ell^d r_*(0)^{\frac{\alpha}{2}} \sum_{i,j=1}^d \left(\int_{\mathbb{R}^d} r_*^{2d} \rho_T^{-\alpha} \right)^{\frac{1}{2}} \sup_{y \in D} \left(\frac{\varepsilon + y}{\varepsilon T} + 1 \right)^{\frac{\alpha}{2}} \\
&\qquad \left(\int_D |F_{ij}\mathbb{1}_D|^2 + |H_{ij}\mathbb{1}_D|^2 \right) \\
&\lesssim_\alpha \varepsilon^{d+1} \mu_d(\tfrac{1}{\varepsilon}) \widetilde{\chi_\varepsilon^7}^2 \ell^d r_*(0)^{\frac{\alpha}{2}} \left(\int_{\mathbb{R}^d} r_*^{2d} \rho_T^{-\alpha} \right)^{\frac{1}{2}} \sup_{y \in D} \left(\frac{\varepsilon + y}{\varepsilon T} + 1 \right)^{\frac{\alpha}{2}}.
\end{aligned}$$

Choosing $T = \frac{1}{\varepsilon}$ yields the desired result. Indeed, the random variables at stake r_* and $\widetilde{\chi_\varepsilon^7}$ verify the desired stochastic integrability.

Let

$$\|IV\|_\ell^2 := \ell^{-d} \int_{\mathbb{R}^d} \sup_{S' \in \mathcal{A}_\ell(x)} \left| \int_D k^2 \delta n_\varepsilon (u'_\varepsilon - u_0) g - \varepsilon k^2 \beta^\varepsilon \delta u_\varepsilon \cdot \nabla g \right|^2.$$

Proposition 37 combined with the estimate (7.38) yields

$$\sup_{S' \in \mathcal{A}_\ell(x)} \left\| u'_\varepsilon - u_0 \right\|_{L^2(D)} \lesssim \varepsilon \mu_d(\tfrac{1}{\varepsilon}) \widehat{\chi}_\varepsilon \left\| u_0 \right\|_{W^{2,\infty}(D)}.$$

Therefore, using (7.42) and Lemma 41 we get

$$\begin{aligned}
\|IV\|_\ell^2 &\lesssim \ell^{-d} \int_{\mathbb{R}^d} \sup_{S' \in \mathcal{A}_\ell(x)} \left\| u'_\varepsilon - u_0 \right\|_{L^2(D)}^2 \left(\int_{D \cap B_{\varepsilon\ell}(x))} |g|^2 \right) \\
&\qquad + \varepsilon^2 \ell^{-d} \int_{\mathbb{R}^d} \left(\int_{D \cap B_{\varepsilon\ell}(x))} |u_\varepsilon|^2 + |\nabla u_\varepsilon|^2 \right) \left\| \beta^\varepsilon \cdot \nabla g \right\|_{L^2(D)}^2 \qquad (7.54) \\
&\lesssim \varepsilon^{d+2} \mu_d(\tfrac{1}{\varepsilon})^2 \left(\widehat{\chi_\varepsilon}^2 \left\| u_0 \right\|_{W^{2,\infty}(D)}^2 \left\| g \right\|_{L^2(D)}^2 + \chi_\varepsilon^2 \left\| g \right\|_{W^{1,\infty}(D)}^2 \left\| u_\varepsilon \right\|_{H^1(D)}^2 \right) \\
&\lesssim \varepsilon^{d+2} \mu_d(\tfrac{1}{\varepsilon})^2 \widetilde{\chi_\varepsilon^9}^2 \left\| u_0 \right\|_{W^{2,\infty}(D)}^2 \left\| g \right\|_{W^{2,\infty}(D)}^2,
\end{aligned}$$

with $\widetilde{\chi_\varepsilon^9}^2 := \widehat{\chi_\varepsilon}^2 + \chi_\varepsilon^2$. □

CHAPTER 8

Numerical illustrations

In this section, we illustrate numerically the different asymptotic expansion of u_ε, *i.e.* the results of Proposition 37 and Corollary 40. Especially, we recover the predicted convergence rates.

8.1 Geometry and choice of parameters

We choose D as the two-dimensional square $(-L_D/2, L_D/2)^2$, with $L_D = 5$. All the inclusions are disks of equal radius. The centers of the inclusions of size 1 are sampled according to a Matèrn point process [134, Section 6.5.2] in a domain $\mathcal{Q}_L := (-\frac{L}{2}, \frac{L}{2})^d$ with $L \gg 1$. To compute the correctors and the associated homogenized coefficients, we will use periodization [141] and thus the Matèrn process is periodized in $\mathcal{Q}_L$. The different parameters chosen for the simulation are summarized in Table 8.1. Note in

Parameter	Value
Angle of the incident wave u^i	0 (From left to right)
h	0.07
k	5
(a_M, a_S)	$(2.0, 3.5)$
(n_M, n_S)	$(1.5, 0.5)$
ε	Between 0.18 and 0.09
Volumic fraction of inclusions	$\approx 22.6\%$

Table 8.1: Parameters of the simulation

particular that L_D is of the order of a few wavelengths.
The solutions are computed with $XLiFE++$ [182], an open source FEM, BEM, and FEM-BEM solver. In order to avoid significant discretization errors and distinguish them from the homogenization error, the mesh step h is taken sufficiently small, *i.e.* much smaller than ε. We choose a $P1$ mesh. All the equations defined in B_R are implemented with a classical FEM-BEM coupling to avoid numerically computing the corresponding Dirichlet-to-Neumann operators on ∂B_R. We choose $P2$ elements both

for the FEM and the BEM unknown. For a single realization, with the set of parameters of Table 8.1, the problems u_ε, u_0 and $\mathcal{U}_1$ could be simulated in a few minutes on a personal laptop. All the following simulations were obtained using a server with bi-processors, AMD EPYC Processor 7452 2.35 GHz with 128 threads, 2 chips, 32 cores/chip, 2 threads/core with RAM of 256 Go.

8.2 Computation of the reference solution

We describe here the procedure to simulate u_ε. The computation of u_0 and $\mathcal{U}_1$ will be done similarly. We solve simultaneously $u_\varepsilon^+ \in H^1(D)$, the solution of the equation for u_ε inside D and the flux $p_\varepsilon^+ \in H^{-\frac{1}{2}}(\partial D)$,

$$p_\varepsilon^+ := a_\varepsilon \nabla u_\varepsilon^+ \cdot \nu.$$

Since the outside domain is homogeneous, by knowing only u_ε^+ and p_ε^+, we can compute $u_\varepsilon(y)$ for $y \in B_R \setminus \overline{D}$ using the Green function $\mathcal{G}$ of the free space:

$$\mathcal{G}(x,y) := \begin{cases} \dfrac{i}{4} H_0^{(1)}(k|x-y|) & \text{if } d=2, \\ \dfrac{\exp(ik|x-y|)}{4\pi|x-y|} & \text{if } d=3, \end{cases} \tag{8.1}$$

where $H_0^{(1)}$ is the first Hankel function of the first kind [108]. u_ε satisfies for $y \in B_R \setminus \overline{D}$

$$u_\varepsilon(y) = u^i(y) + \int_{\partial D} \nabla \mathcal{G}(\cdot, y) \cdot \nu u_\varepsilon^- - \nabla u_\varepsilon^- \cdot \nu \mathcal{G}(\cdot, y),$$

i.e.

$$u_\varepsilon(y) = u^i(y) + \int_{\partial D} \nabla \mathcal{G}(\cdot, y) \cdot \nu u_\varepsilon^+ - p_\varepsilon^+ \mathcal{G}(\cdot, y). \tag{8.2}$$

Then u_ε^+ is the solution in $H^1(D)$ of:

$$\begin{cases} -\nabla \cdot \left(a_\varepsilon \nabla u_\varepsilon^+\right) - k^2 n_\varepsilon u_\varepsilon^+ = 0 & \text{in } D, \\ a_\varepsilon \nabla u_\varepsilon^+ \cdot \nu = p_\varepsilon^+ & \text{on } \partial D. \end{cases} \tag{8.3}$$

The equation for the flux p_ε^+ on ∂D is obtained by taking the normal trace of (8.2). Using the classical jump formula for the single layer potential [108, (2.64)], we have

$$\frac{u_\varepsilon^+(y)}{2} = u^i(y) + \int_{\partial D} \nabla \mathcal{G}(\cdot, y) \cdot \nu u_\varepsilon^+ - p_\varepsilon^+ \mathcal{G}(\cdot, y). \tag{8.4}$$

By coupling (8.3) and (8.4), this yields the following variational formulation: find $(u_\varepsilon^+, p_\varepsilon^+) \in H^1(D) \times H^{-\frac{1}{2}}(D)$ such that for all $(v,q) \in H^1(D) \times H^{\frac{1}{2}}(D)$,

$$\begin{aligned}\int_D a_\varepsilon \nabla u_\varepsilon^+ \cdot \nabla v - k^2 n^\star u_\varepsilon^+ v - \int_{\partial D} p_\varepsilon^+ v + \frac{u_\varepsilon^+(y)}{2} q \\ + \iint_{\partial D \times \partial D} \Big(-u_\varepsilon^+(x) \nabla \mathcal{G}(x,y) \cdot \nu(x) q(y) + p_\varepsilon^+(x) \mathcal{G}(x,y) q(y) \Big) d\sigma(x) d\sigma(y) \\ = \int_{\partial D} u^i q.\end{aligned} \tag{8.5}$$

The simulation of u_0 is done similarly by replacing the coefficient fields a_ε and n_ε with $a^\star$ and $n^\star$.

8.3 Computation of the correctors and effective parameters

As it is customary in stochastic homogenization, we choose to compute ϕ with periodic boundary condition and a regularization term. We compute the periodized correctors $\phi_i^{T,L}$ solutions in

$$H^1_{per}(\mathcal{Q}_L) := \{\phi \in H^1_{loc}(\mathbb{R}^d) \mid \phi \ \mathcal{Q}_L\text{-periodic}\}$$

of

$$\frac{1}{T}\phi_i^{T,L} - \nabla \cdot a(\nabla \phi_i^{T,L} + e_i) = 0.$$

The massive term ensures $\int_{\mathcal{Q}_L} \phi_i^{T,L} = 0$. If one computes $\widetilde{a^\star}$ as

$$[\widetilde{a^\star}]_{i,j} := \mathbb{E}\left[\fint_{(-\frac{L}{2},\frac{L}{2})^d} a(e_i + \nabla \phi_i^{T,L}) \cdot (e_j + \nabla \phi_j^{T,L}) \right],$$

then one has that $\lim_{T,L \longrightarrow \infty} \left[\widetilde{a^\star}\right]_{i,j} = [a^\star]_{i,j}$.
Furthermore, from [135, Proposition 2], we know that the corrector ϕ^T posed in the entire space $\mathbb{R}^d$ without periodic condition satisfies for $T \gg 1$,

$$\mathbb{E}[|\nabla \phi_T - \nabla \phi|^2] \lesssim \begin{cases} T^{-1} & \text{if } d = 2, \\ T^{-\frac{3}{2}} & \text{if } d = 3. \end{cases} \tag{8.6}$$

Therefore, for T and L sufficiently large, $\phi_i^{T,L}$ is a good approximation of ϕ_i [138].
To compute the numerical approximations of $a^\star$ and $n^\star$ that we call $a^\star_{num}$ and $n^\star_{num}$, we

use a Monte-Carlo algorithm. For a fixed number N of distinct periodic realizations we compute

$$[a^\star_{num}]_{ij} := \frac{1}{N}\sum_{m=1}^{N}\int_{(-\frac{L}{2},\frac{L}{2})^d} a^m(e_i+\nabla\phi_i^{T,L,m})\cdot(e_j+\nabla\phi_j^{T,L,m}),$$

and

$$n^\star_{num} := \frac{1}{N}\sum_{m=1}^{N}\int_{(-\frac{L}{2},\frac{L}{2})^d} n^m,$$

where a^k, n^k and $\phi_i^{T,L,k}$ are respectively the coefficients for the k-th realization and the solution of the periodized corrector equation for the k-th realization.

We choose $T = 10^7$, $L = 50$ and $N = 20$. For the set of parameters described in Table 8.1, we find the following homogenized coefficients:

$$a^\star_{num} := \begin{bmatrix} 2.27054991565 & 0.000164757342405 \\ 0.000164757342405 & 2.27054991565 \end{bmatrix},$$

and

$$n^\star_{num} := 1.2735108046.$$

To simulate $\mathcal{U}_1$, we remark that $\mathcal{U}_1$ is the solution in $H^1(B_R)$ of

$$\begin{cases} -\Delta\mathcal{U}_1 - k^2\mathcal{U}_1 = 0 & \text{in } B_R\setminus\overline{D}, \\ -\nabla\cdot(a^\star\nabla\mathcal{U}_1) - k^2 n^\star\mathcal{U}_1 = -\nabla\cdot\mathcal{H}_\varepsilon - k^2(n^\star - n_\varepsilon)u_0 & \text{in } D, \\ \mathcal{U}_1^- - \mathcal{U}_1^+ = 0 & \text{on } \partial D, \\ \nabla\mathcal{U}_1^-\cdot\nu - a^\star\nabla\mathcal{U}_1^+\cdot\nu = -\mathcal{H}_\varepsilon\cdot\nu & \text{on } \partial D, \\ \nabla\mathcal{U}_1\cdot\nu = \Lambda(\mathcal{U}_1) & \text{on } \partial B_R, \end{cases} \tag{8.7}$$

with $\mathcal{H}_\varepsilon$ defined as

$$\mathcal{H}_\varepsilon := (a^\star - a_\varepsilon)(e_i+\nabla\phi_i^\varepsilon)\partial_i u_0,$$

so that $\mathcal{U}_1$ can be simulated just as u_0 with the correct source term.

8.4 Numerical results

We show here the results of the computations of u_ε, u_0 and $\mathcal{U}_1$ on Figure 8.1 and Figure 8.2. We plot the mesh and the solutions associated with one realization. We also plot and compare the error terms and the correction $\mathcal{U}_1$ to illustrate both Proposition 36 and Theorem 39.

The Monte-Carlo process to compute the average error is done with 30 realizations on Figure 8.3.

One can see on Figure 8.3, that the expected error decay of order $\varepsilon^{\frac{d+1}{2}}\mu_d(\frac{1}{\varepsilon})^{\frac{1}{2}} = \varepsilon^{\frac{3}{2}}|\log(\varepsilon)|^{\frac{1}{2}}$ in Theorem 39 is obtained. For values of ε of order 0.1,

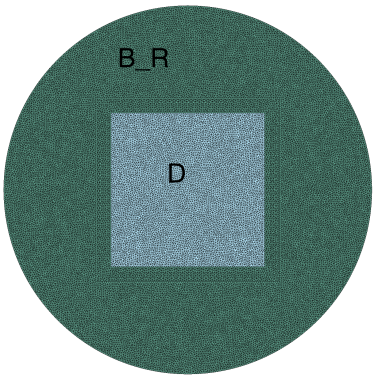

(a) Mesh with domains

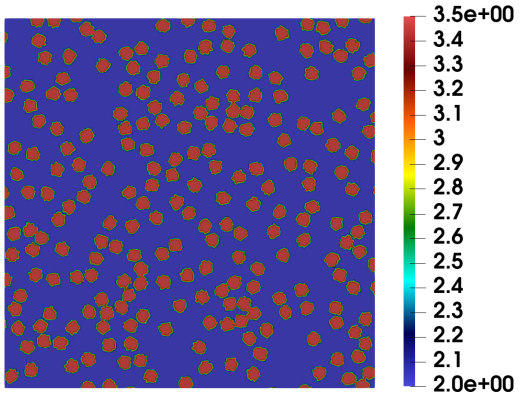

(b) Realization of a_ε with $\varepsilon = 0.09$ in D

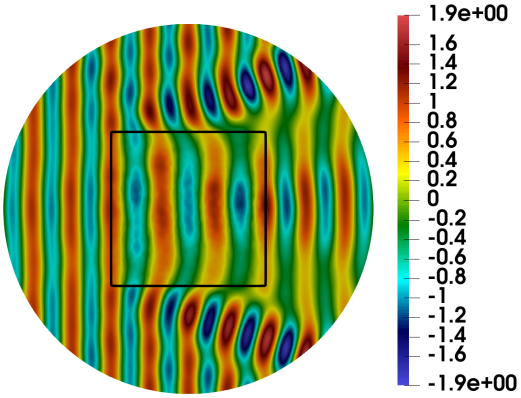

(c) Solution u_ε with $\varepsilon = 0.09$

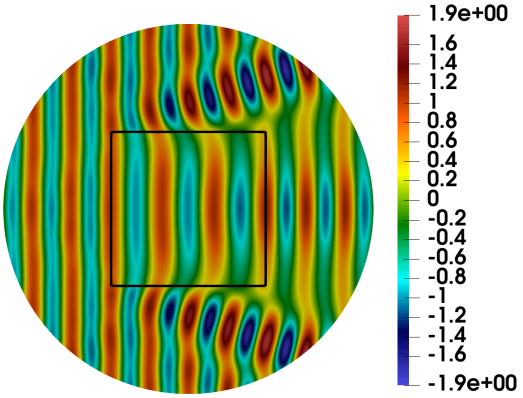

(d) Solution u_0

Figure 8.1: (a) Mesh, (b) a_ε for a realization of S with $\varepsilon = 0.09$, (c) corresponding u_ε and (d) homogenized solution u_0 for an incident plane wave along $(1, 0)$.

the asymptotic expansion $u_0 + \varepsilon \mathcal{U}_1$ is already a very good approximation of the field u_ε.

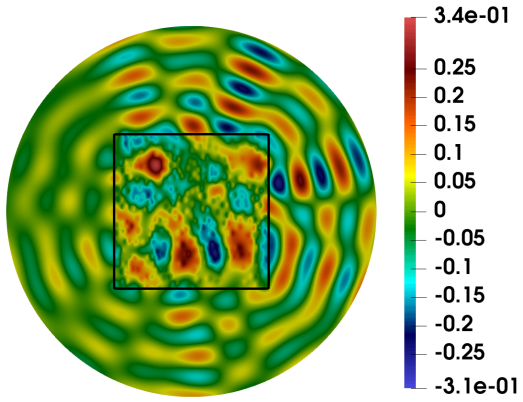

(a) $u_\varepsilon - u_0$ for the realization of S in Figure 8.1b ($\varepsilon = 0.09$)

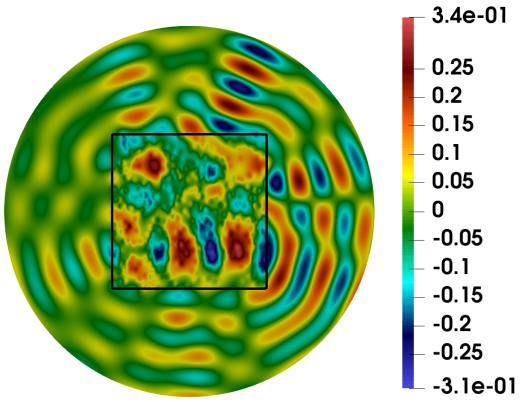

(b) $\mathcal{U}_1$ for the realization of S in Figure 8.1b ($\varepsilon = 0.09$)

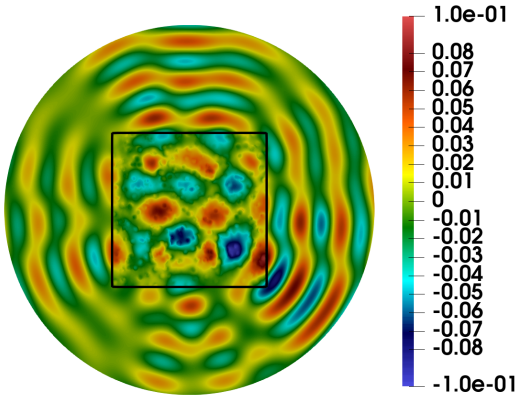

(c) $u_\varepsilon - u_0 - \mathcal{U}_1$ for the realization of S in Figure 8.1b ($\varepsilon = 0.09$)

Figure 8.2: For the realization S shown in Figure 8.1b, (a) error term $u_\varepsilon - u_0$, (b) correction term $\mathcal{U}_1$, (c) error term term $u_\varepsilon - u_0 - \mathcal{U}_1$.

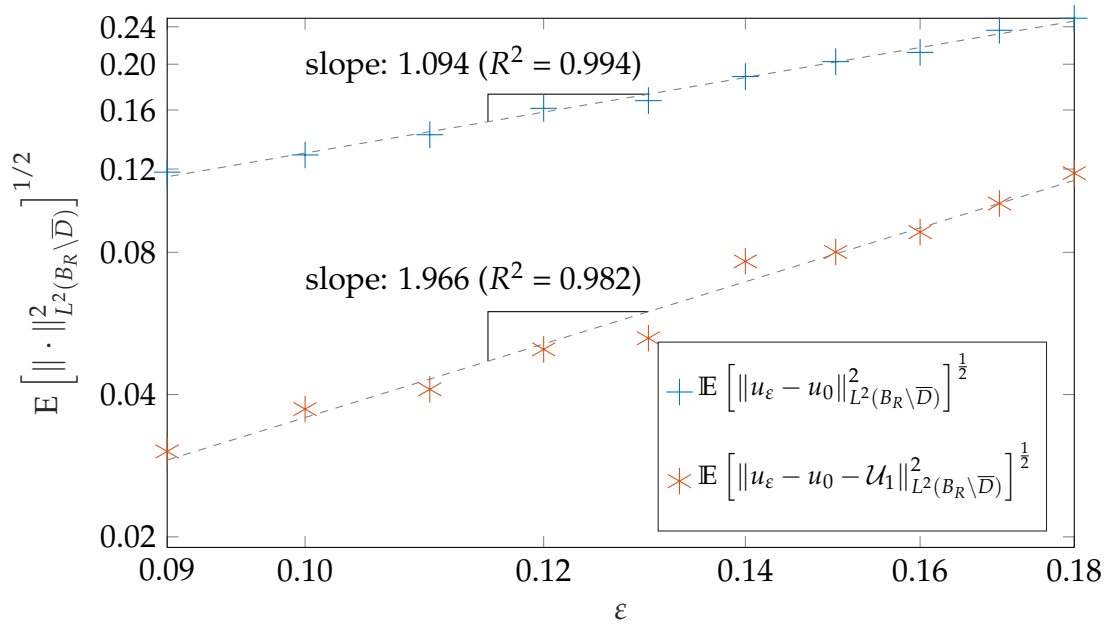

Figure 8.3: Error decay and linear regression.

Appendices

APPENDIX A

Well-posedness of the scattering problem and H^S-regularity

We show in this appendix that the scattering problems are well-posed in $H^1(B_R \setminus \overline{D}) \times H^1(D)$ with a control of u_ε that is independent on ε and the randomness. To do so, we suppose that the bilinear form associated to (6.1) is coercive. Finally, we prove that u_0 can be more regular than H^1 under regularity assumptions on the boundary of D and the source terms. The coercivity of the bilinear form is not a restrictive hypothesis. It can be shown for example under either one of the following sufficient conditions [183]

1. $\Im k > 0$

2. kR is small enough (low frequency).

Proposition 43: Uniform stability under coercivity assumption

Let $D \subset \mathbb{R}^d$ be a non-empty, open, and bounded set having $\mathcal{C}^2$- boundary ∂D such that the exterior domain $\mathbb{R}^d \setminus \overline{D}$ is connected. Let $A : \overline{D} \mapsto \mathbb{C}^{d\times d}$ and $n : \overline{D} \mapsto \mathbb{C}$. We suppose that $A(x)$, $x \in \overline{D}$, is a definite positive matrix that satisfies, $\xi \cdot A\xi \geq \Lambda_A^- |\xi|^2$ and $|A\xi| \leq \Lambda_A^+ |\xi|$ for all $\xi \in \mathbb{C}^3$ and $x \in D$, and that $\Lambda_n^+ \geq n \geq \Lambda_n^- > 0$ where Λ_A^+, Λ_A^-, Λ_n^+, Λ_n^- are positive constants.

Let $f \in L^2(D)$, $g \in H^{\frac{1}{2}}(\partial D)$ and $h \in H^{-\frac{1}{2}}(\partial D)$. Then, there exists a unique $u \in H^1(B_R \setminus \overline{D}) \times H^1(D)$ solution of the transmission problem

$$\begin{cases} -\Delta u^- - k^2 n_0 u^- = 0 & \text{in } B_R \setminus \overline{D}, \\ -\nabla \cdot \left(A \nabla u^+\right) - k^2 n u^+ = f & \text{in } D, \\ u^- - u^+ = g & \text{on } \partial D, \\ \nabla u^- \cdot \nu - A \nabla u^+ \cdot \nu = h & \text{on } \partial D, \\ \nabla u \cdot \nu = \Lambda(u) & \text{on } \partial B_R, \end{cases} \tag{A.1}$$

which satisfies the uniform control:

$$\|u\|_{H^1(B_R \setminus \overline{D})} + \|u\|_{H^1(D)} \lesssim \|f\|_{L^2(D)} + \|g\|_{H^{\frac{1}{2}}(\partial D)} + \|h\|_{H^{-\frac{1}{2}}(\partial D)}. \tag{A.2}$$

We also need a regularity result on the homogenized solution u_0 that we recall here.

Proposition 44: H^s- regularity for the transmission problem

Let $s \geq 2$. Let D be a bounded domain of class $\mathcal{C}^s$. If $A, n \in \mathcal{C}^{s-2}(\overline{D})$, $f \in H^{s-2}(D)$ $g \in H^{s-\frac{1}{2}}(\partial D)$ and $h \in H^{s-\frac{3}{2}}(\partial D)$, then the unique solution $u \in H^1(D) \times H^1(B_R \setminus \overline{D})$ of (A.1) belongs to $H^s(D) \times H^s(B_R \setminus \overline{D})$. Moreover the following estimate holds:

$$\|u\|_{H^s(B_R \setminus \overline{D})} + \|u\|_{H^s(D)} \lesssim \|f\|_{H^{s-2}(D)} + \|g\|_{H^{s-\frac{1}{2}}(\partial D)} + \|h\|_{H^{s-\frac{3}{2}}(\partial D)}. \tag{A.3}$$

Proof. We rely on elliptic regularity results proved in [184] to establish our result. We first prove that u belongs to $H^2(D)$. Since $u \in H^1(D)$, its trace on ∂D belongs to $H^{\frac{1}{2}}(\partial D)$. Let $\widetilde{u} \in H^1(D)$ be the unique solution of

$$\begin{cases} -\nabla \cdot (A \nabla \widetilde{u}) - k^2 n \widetilde{u} = 0 & \text{in } D, \\ \widetilde{u} = u & \text{on } \partial D. \end{cases} \tag{A.4}$$

Then $\widetilde{u}$ satisfies the hypotheses of [184, Theorem 3.4.1] and therefore $\widetilde{u}$ is in $H^2(D)$. By uniqueness of the solution of (A.4), we also have:

$$\widetilde{u} = u \quad \text{in } D.$$

Therefore $u \in H^2(D)$. Using the same reasoning in $B_R \setminus \overline{D}$ with a Dirichlet-to-Neumann operator on the boundary of B_R, one concludes that $u \in H^2(B_R \setminus \overline{D})$. Similarly we can now apply [184, Theorem 2.3.2 (ii)] to show that u belongs in fact to $H^s(D) \times H^s(B_R \setminus \overline{D})$ and get the estimate. □

APPENDIX B

Qualitative homogenization

We detail here the proof of the convergence of u_ε towards u_0 strongly in $L^2(B_R)$ and weakly in $H^1(B_R)$ by the method of oscillating test functions.

Proposition 45: Homogenization of the scattering problem in $H^1(B_R)$

Let u_ε be the almost sure unique solution in $H^1(B_R)$ of (6.1) and $u_0 \in H^1(B_R)$ be the solution of (6.2). Then we have the following convergence results as ε goes to 0

$$\begin{cases} u_\varepsilon \xrightarrow{L^2(B_R)} u_0, \\ \nabla u_\varepsilon \xrightarrow{L^2(B_R)} \nabla u_0, \\ a_\varepsilon \nabla u_\varepsilon \xrightarrow{L^2(B_R)} a^\star \nabla u_0. \end{cases} \tag{B.1}$$

Here, we extend $a^\star$ by I in $B_R \setminus \overline{D}$.

Proof. Since almost surely u_ε is uniformly bounded in $H^1(B_R)$ independently of ε, by Rellich-Kondrachov theorem, we can extract a subsequence, still denoted u_ε such that

$$u_\varepsilon \xrightarrow{H^1(B_R)} u, \tag{B.2}$$

for a certain $u \in H^1(B_R)$. By Rellich's theorem we have then $u_\varepsilon \xrightarrow{L^2(B_R)} u$. Similarly thanks to the uniform ellipticity of a, we have:

$$\|a_\varepsilon \nabla u_\varepsilon\|_{L^2(B_R)} \leq \Lambda_a \|\nabla u_\varepsilon\|_{L^2(B_R)} \lesssim \left\|u^i\right\|_{H^1(B_R)}.$$

Therefore we can also extract a subsequence of $a_\varepsilon \nabla u_\varepsilon$ such that

$$a_\varepsilon \nabla u_\varepsilon \xrightarrow{L^2(B_R)} F^\star$$

for some $F^\star \in L^2(B_R)$.
We show that $u = u_0$ and $F^\star = a^\star \nabla u_0$.

By Birkhoff's ergodic theorem and the strong convergence of u_ε to u in $L^2(D)$, we have that

$$n_\varepsilon u_\varepsilon \xrightarrow{L^2(B_R)} \mathbb{E}[n]u = n^\star u.$$

Furthermore, the DtN operator is continuous from $H^{\frac{1}{2}}(\partial B_R)$ to $H^{-\frac{1}{2}}(\partial B_R)$ and the trace operator is continuous from $H^1(B_R)$ to $H^{\frac{1}{2}}(\partial B_R)$. Thus

$$\Lambda(u_\varepsilon) \xrightarrow{H^{-\frac{1}{2}}(\partial B_R)} \Lambda(u).$$

By passing to the limit inside the variational formulation of (6.1) for u_ε, one finds that, for all $v \in H^1(B_R)$,

$$\begin{aligned}\int_D F^\star \cdot \nabla \overline{v} - k^2 n^\star u \overline{v} + \int_{B_R \setminus \overline{D}} F^\star \cdot \nabla \overline{v} - k^2 n_0 u \overline{v} \\ - \langle \Lambda(u), v \rangle_{H^{-\frac{1}{2}}(\partial B_R), H^{\frac{1}{2}}(\partial B_R)} = \left\langle \Lambda(u^i), v \right\rangle_{H^{-\frac{1}{2}}(\partial B_R), H^{\frac{1}{2}}(\partial B_R)}.\end{aligned} \tag{B.3}$$

For $i \in [\![1, d]\!]$, let $\psi_i \in H^1_{loc}(\mathbb{R}^d)$ be the adjoint corrector satisfying

$$-\nabla \cdot a^*(\nabla \psi_i + e_i) = 0 \quad \text{in } \mathcal{D}'(\mathbb{R}^d), \tag{B.4}$$

with the anchoring condition $\frac{1}{|\square_0|}\int_{\square_0} \psi_i = 0$.
Moreover, $\nabla \psi_i$ is stationary, verifies $\mathbb{E}[\nabla \psi_i] = 0$ and admits finite second order moment. Now for all $x \in \mathbb{R}^d$, let

$$\alpha_i(x) := x_i + \psi_i(x),$$

and

$$\alpha_i^\varepsilon(x) := \varepsilon \alpha_i(\frac{x}{\varepsilon}) = x_i + \varepsilon \psi_i(\frac{x}{\varepsilon}).$$

Thanks to the sublinearity of ψ_i, $\alpha_i^\varepsilon \xrightarrow{L^2(B_R)} x_i$. Moreover by Birkhoff's theorem $\nabla \alpha_i^\varepsilon \xrightarrow{L^2(B_R)} e_i$. Thus

$$\alpha_i^\varepsilon \xrightarrow{H^1(B_R)} x_i.$$

Similarly by Birkhoff's theorem, $a_\varepsilon^* \nabla \alpha_i^\varepsilon \xrightarrow{L^2(B_R)} \mathbb{E}[a^* \nabla \alpha_i] = \mathbb{E}[a^*(e_i + \nabla \psi_i)]$.
Moreover, since $\mathbb{E}[\nabla \phi_j \cdot a^*(e_i + \nabla \psi_i)] = \mathbb{E}[\nabla \psi_i \cdot a(e_j + \nabla \phi_j)] = 0$ for $i, j \in [\![1, d]\!]$,

$$\begin{aligned}\mathbb{E}[e_j \cdot a^* \nabla \alpha_i] &= \mathbb{E}[(e_j + \nabla \phi_j) \cdot a^*(e_i + \nabla \psi_i) \\ &= \mathbb{E}[a(e_j + \nabla \phi_j) \cdot e_i \\ &= a^\star_{ji} = e_i \cdot a^\star e_j.\end{aligned} \tag{B.5}$$

For $\zeta \in C_c^\infty(B_R)$ consider the variational formulation of the problem solved by u_ε with the test function $\zeta\alpha_i^\varepsilon$,

$$\begin{aligned} 0 &= \int_{B_R} a_\varepsilon \nabla u_\varepsilon \cdot \nabla(\overline{\zeta}\alpha_i^\varepsilon) - k^2 n_\varepsilon u_\varepsilon \overline{\zeta}\alpha_i^\varepsilon \\ &= \int_{B_R} a_\varepsilon \nabla u_\varepsilon \cdot (\nabla\overline{\zeta})\alpha_i^\varepsilon - (\nabla\overline{\zeta})u_\varepsilon \cdot a_\varepsilon^* \nabla\alpha_i^\varepsilon - k^2 n_\varepsilon u_\varepsilon \overline{\zeta}\alpha_i^\varepsilon. \end{aligned} \tag{B.6}$$

Then, by passing to the limit

$$\begin{aligned} \int_D F^\star \cdot (\nabla\zeta)x_i - (\nabla\zeta)u \cdot (a^\star)^* e_i - k^2 n^\star u\zeta x_i \\ + \int_{B_R\setminus\overline{D}} F^\star \cdot (\nabla\zeta)x_i - a^\star(\nabla\zeta)u \cdot e_i - k^2 n_0 u\zeta x_i = 0. \end{aligned} \tag{B.7}$$

Moreover by (B.3)

$$\begin{aligned} \int_{B_R} F^\star \cdot (\nabla\overline{\zeta})x_i &= \int_{B_R} F^\star \cdot \nabla(\overline{\zeta}x_i) - F \cdot \overline{\zeta}e_i \\ &= \int_{B_R\setminus\overline{D}} k^2 n_0 u\overline{\zeta}x_i + \int_D k^2 n^\star u\overline{\zeta}x_i - \int_{B_R} F^\star \cdot \overline{\zeta}e_i. \end{aligned} \tag{B.8}$$

Since $\zeta u \in H_0^1(B_R)$, an integration by parts yields

$$\int_{B_R} a^\star(\nabla\overline{\zeta})u \cdot e_i = \int_{B_R} -a^\star\nabla u \cdot \overline{\zeta}e_i \tag{B.9}$$

from which we obtain that for any $\zeta \in C_c^\infty(B_R)$ and for any $i \in [\![1, d]\!]$,

$$\int_{B_R} \overline{\zeta}e_i \cdot (a^\star\nabla u - F^\star) = 0. \tag{B.10}$$

This implies that almost surely $F^\star = a^\star\nabla u$ in $\mathcal{D}'(B_R)$, thus in $L^2(B_R)$.
Finally, (B.3) can then be rewritten as

$$\begin{aligned} \int_{B_R} a^\star\nabla u \cdot \nabla\overline{v} - k^2 n^\star u\overline{v} - \langle \Lambda(u), v\rangle_{H^{-\frac{1}{2}}(\partial B_R), H^{\frac{1}{2}}(\partial B_R)} = \\ \left\langle \Lambda(u^i), v\right\rangle_{H^{-\frac{1}{2}}(\partial B_R), H^{\frac{1}{2}}(\partial B_R)}. \end{aligned} \tag{B.11}$$

We get $u = u_0$. Moreover by uniqueness of the limit, we proved convergence of u_ε and $a_\varepsilon\nabla u_\varepsilon$ and not just of a subsequence. □

APPENDIX C

Homogenization with a less regular solution

In Section 6 Proposition 36, we proved an error estimate for the two-scale expansion when $u_{0|_D} \in W^{2,\infty}(D)$. This result still holds for less regular u_0 as stated in Proposition 47.
As done in [119], we consider an extension of $u_{0|_D}$ that we denote $\widehat{u_0} \in W^{1+\alpha,p}(\mathbb{R}^d)$. $\widehat{u_0}$ is defined through the Sobolev extension theorem stated below.

Lemma 46: Sobolev extension theorem [119, Proposition B.14]

Let D be a bounded Lipschitz domain, $\alpha \in (0,\infty)$ and $p \in (1,\infty)$. The restriction operator $W^{\alpha,p}(\mathbb{R}^d) \to W^{\alpha,p}(D)$ has a bounded linear right inverse. That is, there exists a linear operator

$$\mathrm{Ext} : W^{\alpha,p}(D) \to W^{\alpha,p}(\mathbb{R}^d),$$

such that, for every $u \in W^{\alpha,p}(D)$,

$$\mathrm{Ext}(u) = u \text{ a.e. in } D,$$

and

$$\|\mathrm{Ext}(u)\|_{W^{\alpha,p}(\mathbb{R}^d)} \lesssim \|u\|_{W^{\alpha,p}(D)}.$$

We derive a convergence rate of u_ε towards the two-scale expansion when $u_{0|_D} \in W^{1+\alpha,p}(D)$.

Proposition 47: H^1- convergence of the two-scale expansion for $u_{0|_D} \in W^{1+\alpha,p}(D)$

For $p \in (2,\infty]$, $\alpha \in (\frac{1}{p},1]$, suppose that $u_0 \in H^1(B_R)$ such that $u_{0|_D} \in W^{1+\alpha,p}(D)$ then

$$\|u_\varepsilon - u_0\|_{H^1(B_R\setminus\overline{D})} + \|u_\varepsilon - u_0 - \widehat{u_{1,\varepsilon}}\|_{H^1(D)} \lesssim \varepsilon^{\frac{1}{2}}\mu_d(\frac{1}{\varepsilon})^{\frac{1}{2}}\widehat{\chi_{\varepsilon,p}}\,\|u_0\|_{W^{1+\alpha,p}(D)}, \quad \text{(C.1)}$$

where $\widehat{u}_{1,\varepsilon}$ is defined by

$$\widehat{u}_{1,\varepsilon}(x) := \mathbb{1}_D(x)\sum_{i=1}^{d}\phi_i\left(\frac{x}{\varepsilon}\right)\partial_i\widehat{u}_0 * \xi_\varepsilon(x) \quad \text{for } x \in B_R,$$

with the standard mollifier ξ_ε defined by

$$\xi_\varepsilon(x) := \varepsilon^{-d}\begin{cases} c_d\exp(-\dfrac{1}{1-|\frac{x}{\varepsilon}|^2}) & \text{for } |\frac{x}{\varepsilon}| < 1, \\ 0 & \text{for } |\frac{x}{\varepsilon}| \geq 1, \end{cases} \quad \text{(C.2)}$$

and c_d is such that

$$\int_{\mathbb{R}^d}\xi_\varepsilon(x)\mathrm{d}x = 1.$$

Here $\widehat{\chi_{\varepsilon,p}}$ denotes a random variable satisfying the stochastic integrability (4.52).

In order to prove the previous theorem, we introduce the boundary corrector and start by proving the result with the boundary corrector.

Proposition 48: H^1- convergence of the two-scale expansion with the boundary corrector for $u_{0|_D} \in W^{1+\alpha,p}(D)$

For $p \in (2,\infty]$, $\alpha \in (0,1]$, suppose that $u_0 \in H^1(B_R)$ such that $u_{0|_D} \in W^{1+\alpha,p}(D)$ then

$$\|u_\varepsilon - u_0 - \widehat{u}_{1,\varepsilon} - \widehat{v}_\varepsilon\|_{H^1(B_R)} \lesssim \varepsilon^\alpha\mu_d(\frac{1}{\varepsilon})\chi_{\varepsilon,p}\,\|u_0\|_{W^{1+\alpha,p}(D)}, \quad \text{(C.3)}$$

where the boundary corrector $\widehat{v}_\varepsilon \in H^1(B_R\setminus\overline{D}) \times H^1(D)$ is the solution of

$$\begin{cases} -\Delta\widehat{v_\varepsilon} - k^2\widehat{v_\varepsilon} = 0 & \text{in } B_R \setminus \overline{D}, \\ -\nabla\cdot a_\varepsilon\nabla\widehat{v_\varepsilon} - k^2 n_\varepsilon\widehat{v_\varepsilon} = 0 & \text{in } D, \\ \widehat{v_\varepsilon}^- - \widehat{v_\varepsilon}^+ = \varepsilon\widehat{u}_{1,\varepsilon} & \text{on } \partial D, \\ \nabla\widehat{v_\varepsilon}^-\cdot\nu - a_\varepsilon\nabla\widehat{v_\varepsilon}^+\cdot\nu = \varepsilon\left(\nabla\cdot(\sigma_i^\varepsilon\partial_i\widehat{u_0} * \xi_\varepsilon)^+\right)\cdot\nu & \\ \qquad\qquad - k^2\varepsilon(\beta^\varepsilon\widehat{u_0} * \xi_\varepsilon)^+\cdot\nu & \text{on } \partial D, \\ \nabla\widehat{v_\varepsilon}\cdot\nu = \Lambda(\widehat{v_\varepsilon}) & \text{on } \partial B_R. \end{cases} \tag{C.4}$$

$\chi_{\varepsilon,p}$ is a random variable defined as

$$\chi_{\varepsilon,p} := \left(\varepsilon^d \sum_{z\in P_\varepsilon(D)} \mathcal{C}(z)^{\frac{2p}{p-2}}\right)^{\frac{p-2}{2p}}, \tag{C.5}$$

with $\mathcal{C}$ denoting the constant in Proposition 22. Moreover $\chi_{\varepsilon,p}$ satisfies the stochastic integrability (4.52).

Both results of Proposition 47 and Proposition 48 were established for the Poisson equation in a bounded domain with Dirichlet or Neumann condition in [119, Chapter 6]. The proofs below use similar arguments as the ones developed in [119].

Proof of Proposition 48. We denote $\widehat{Z_\varepsilon} := u_\varepsilon - u_0 - \varepsilon\widehat{u_{1,\varepsilon}}$.
As in Proposition 35, the boundary layer $\widehat{v_\varepsilon}$ solution of (C.4) is constructed such that $\widehat{Z_\varepsilon} - \widehat{v_\varepsilon}$ is the unique solution in $H^1(B_R)$ of

$$\begin{cases} -\nabla\cdot a_\varepsilon\nabla(\widehat{Z_\varepsilon} - \widehat{v_\varepsilon}) - k^2 n_\varepsilon(\widehat{Z_\varepsilon} - \widehat{v_\varepsilon}) = \nabla\cdot\widehat{F_\varepsilon} + k^2\widehat{G_\varepsilon} & \text{in } B_R, \\ \nabla(\widehat{Z_\varepsilon} - \widehat{v_\varepsilon})\cdot\nu = \Lambda(\widehat{Z_\varepsilon} - \widehat{v_\varepsilon}) & \text{on } \partial B_R, \end{cases} \tag{C.6}$$

where $\widehat{F_\varepsilon}$ and $\widehat{G_\varepsilon}$ are defined by

$$\widehat{F_\varepsilon} := \varepsilon(a_\varepsilon\phi_i^\varepsilon - \sigma_i^\varepsilon)\nabla(\partial_i\widehat{u_0} * \xi_\varepsilon) + (a_\varepsilon - a^\star)\nabla(\widehat{u_0} * \xi_\varepsilon - u_0) + \varepsilon k^2\beta^\varepsilon\widehat{u_0} * \xi_\varepsilon, \tag{C.7}$$

and

$$\widehat{G_\varepsilon} := \varepsilon\left((n_\varepsilon\phi_i^\varepsilon - \beta_i^\varepsilon)\partial_i\widehat{u_0} * \xi_\varepsilon\right) + (n_\varepsilon - n^\star)(u_0 - \widehat{u_0} * \xi_\varepsilon). \tag{C.8}$$

Moreover, $\widehat{Z_\varepsilon} - \widehat{v_\varepsilon}$ verifies almost surely

$$\left\|\widehat{Z_\varepsilon} - \widehat{v_\varepsilon}\right\|_{H^1(B_R)} \lesssim \left\|\widehat{F_\varepsilon}\right\|_{L^2(D)} + \left\|\widehat{G_\varepsilon}\right\|_{L^2(D)}. \tag{C.9}$$

To prove (C.1), we hence need to prove that

$$\left\|\widehat{F_\varepsilon}\right\|_{L^2(D)} + \left\|\widehat{G_\varepsilon}\right\|_{L^2(D)} \lesssim \varepsilon^\alpha\mu_d(\frac{1}{\varepsilon})\chi_{\varepsilon,p}\left\|u_0\right\|_{W^{1+\alpha,p}(D)}.$$

By the triangle inequality, we immediately get

$$\begin{aligned}&\left\|\widehat{F_\varepsilon}\right\|_{L^2(D)}+\left\|\widehat{G_\varepsilon}\right\|_{L^2(D)}\\&\qquad\lesssim \varepsilon\,\||\phi^\varepsilon-\sigma^\varepsilon||\nabla\nabla\widehat{u_0}*\xi_\varepsilon|\|_{L^2(D)}+\varepsilon\,\||\beta^\varepsilon||\widehat{u_0}*\xi_\varepsilon|\|_{L^2(D)}\\&+\varepsilon\,\||\phi^\varepsilon-\beta^\varepsilon|\nabla\widehat{u_0}*\xi_\varepsilon\|_{L^2(D)}+\|\nabla(\widehat{u_0}*\xi_\varepsilon-u_0)\|_{L^2(D)}+\|\widehat{u_0}*\xi_\varepsilon-u_0\|_{L^2(D)}\,.\end{aligned}\tag{C.10}$$

It remains to estimate these five terms.
We recall a useful Lemma, proved in [119], which allows us to estimate the three first terms of (C.10).

Lemma 49: [119, Lemma 6.8]

Fix $\alpha\in(0,1]$ and $p\in(2,\infty)$. Let $f\in L^2(D+2\varepsilon\square_0)$, $g\in L^p(D+2\varepsilon\square_0)$ and its Sobolev extension $\widehat{g}\in L^p(\mathbb{R}^d)$. Then

$$\|f|\widehat{g}*\xi_\varepsilon|\|_{L^2(D)}\lesssim\left(\varepsilon^d\sum_{z\in P_\varepsilon(D)}\|f\|^{\frac{2p}{p-2}}_{\underline{L}^2(z+2\varepsilon\square_0)}\right)^{\frac{p-2}{2p}}\|g\|_{L^p(D+2\varepsilon\square_0)}\,,\tag{C.11}$$

where $\|f\|_{\underline{L}^2(z+2\varepsilon\square_0)}:=\|f\|_{\underline{L}^2(z+2\varepsilon\square_0)}:=\left(\fint_{z+2\varepsilon\square_0}|f|^2\right)^{\frac12}$.
Moreover, if $g\in W^{\alpha,p}(D+2\varepsilon\square_0)$, then

$$\|f|\nabla(\widehat{g}*\xi_\varepsilon)|\|_{L^2(D)}\lesssim\varepsilon^{\alpha-1}\left(\varepsilon^d\sum_{z\in P_\varepsilon(D)}\|f\|^{\frac{2p}{p-2}}_{\underline{L}^2(z+2\varepsilon\square_0)}\right)^{\frac{p-2}{2p}}\|g\|_{W^{\alpha,p}(D+2\varepsilon\square_0)}\,.\tag{C.12}$$

Now, using (C.12), with $f=\phi^\varepsilon$ and $g=\nabla\widehat{u_0}$ and the corrector estimate of Proposition 22, we obtain

$$\begin{aligned}&\||\phi^\varepsilon|\ |\nabla(\nabla\widehat{u_0}*\xi_\varepsilon)|\|_{L^2(D)}\\&\qquad\lesssim\varepsilon^{\alpha-1}\left(\varepsilon^d\sum_{z\in P_\varepsilon(D)}\|\phi^\varepsilon\|^{\frac{2p}{p-2}}_{\underline{L}^2(z+2\varepsilon\square_0))}\right)^{\frac{p-2}{2p}}\|\nabla\widehat{u_0}\|_{W^{\alpha,p}(D+2\varepsilon\square_0)}\\&\qquad\lesssim\varepsilon^{\alpha-1}\left(\varepsilon^d\sum_{z\in P_\varepsilon(D)}\|\phi\|^{\frac{2p}{p-2}}_{\underline{L}^2(2\square_0)}\right)^{\frac{p-2}{2p}}\|\nabla u_0\|_{W^{\alpha,p}(D)}\\&\qquad\lesssim\varepsilon^{\alpha-1}\mu_d(\frac{1}{\varepsilon})\left(\varepsilon^d\sum_{z\in P_\varepsilon(D)}\mathcal{C}(z)^{\frac{2p}{p-2}}\right)^{\frac{p-2}{2p}}\|\nabla u_0\|_{W^{\alpha,p}(D)}\,.\end{aligned}\tag{C.13}$$

Similarly, with $f = \phi^\varepsilon - \beta^\varepsilon$ and $g = \widehat{u_0}$,

$$\| |\phi^\varepsilon - \beta^\varepsilon| |\nabla \widehat{u_0} * \xi_\varepsilon| \|_{L^2(D)} \lesssim \varepsilon^{\alpha-1} \mu_d(\frac{1}{\varepsilon}) \left(\varepsilon^d \sum_{z \in P_\varepsilon(D)} \mathcal{C}(z)^{\frac{2p}{p-2}} \right)^{\frac{p-2}{2p}} \|u_0\|_{W^{\alpha,p}(D)} . \quad \text{(C.14)}$$

Now, using (C.11) with $f = \beta^\varepsilon$ and $g = u_0$, we get

$$\| |\beta^\varepsilon| |u_0 * \xi_\varepsilon| \|_{L^2(D)} \lesssim \mu_d(\frac{1}{\varepsilon}) \left(\varepsilon^d \sum_{z \in P_\varepsilon(D)} \mathcal{C}(z)^{\frac{2p}{p-2}} \right)^{\frac{p-2}{2p}} \|u_0\|_{L^p(D)} . \quad \text{(C.15)}$$

To estimate the last two terms of (C.10), we recall another useful lemma.

Lemma 50: [119, Lemma 6.7]

Fix $1 \leq q \leq p < \infty$ and $0 < \alpha \leq 1$. Let $g \in W^{\alpha,p}(D + 2\varepsilon\square_0)$ and its Sobolev extension $\widehat{g} \in W^{\alpha,p}(\mathbb{R}^d)$. Then

$$\|g - (\widehat{g} * \xi_\varepsilon)\|_{L^q(D)} \lesssim |D|^{\frac{1}{q}-\frac{1}{p}} \varepsilon^\alpha \|g\|_{W^{\alpha,p}(D+2\varepsilon\square_0)} . \quad \text{(C.16)}$$

Using this Lemma, with $g = \nabla u_0$, $q = 2$, and $p > 2$, we have

$$\|\nabla u_0 - (\nabla \widehat{u_0}) * \xi_\varepsilon\|_{L^2(D)} \lesssim \varepsilon^\alpha \|\nabla \widehat{u_0}\|_{W^{\alpha,p}(D+2\varepsilon\square_0)} \lesssim \varepsilon^\alpha \|u_0\|_{W^{1+\alpha,p}(D)} \quad \text{(C.17)}$$

and with $g = u_0$ we obtain similarly

$$\|u_0 - \widehat{u_0} * \xi_\varepsilon\|_{L^2(D)} \lesssim \varepsilon^\alpha \|\widehat{u_0}\|_{W^{\alpha,p}(D+2\varepsilon\square_0)} \lesssim \varepsilon^\alpha \|u_0\|_{W^{\alpha,p}(D)} . \quad \text{(C.18)}$$

Inserting (C.13), (C.14), (C.15), (C.17), (C.18) into (C.10) gives us (C.1), concluding the proof of Proposition 35.

□

By estimating the H^1-norm of the boundary corrector $\widehat{v_\varepsilon}$, we can now prove Proposition 47.

Proof of Proposition 47. We consider $\widehat{V_\varepsilon} := \widehat{v_\varepsilon} - \varepsilon \eta_\varepsilon \widehat{u_{1,\varepsilon}}$ the almost sure unique solution in $H^1(B_R)$ of

$$\begin{cases} -\Delta \widehat{V_\varepsilon} - k^2 \widehat{V_\varepsilon} = 0 & \text{in } B_R \setminus \overline{D}, \\ -\nabla \cdot a_\varepsilon \nabla \widehat{V_\varepsilon} - k^2 n_\varepsilon \widehat{V_\varepsilon} = -\varepsilon \nabla \cdot a_\varepsilon \nabla (\eta_\varepsilon \widehat{u_{1,\varepsilon}}) + \varepsilon k^2 n_\varepsilon \eta_\varepsilon \widehat{u_{1,\varepsilon}} & \text{in } D, \\ \nabla \widehat{V_\varepsilon}^- \cdot \nu - a_\varepsilon \nabla \widehat{V_\varepsilon}^+ \cdot \nu = \varepsilon a_\varepsilon \nabla (\eta_\varepsilon \widehat{u_{1,\varepsilon}}) \cdot \nu + \varepsilon \left(\nabla \cdot (\sigma_i^\varepsilon \partial_i \widehat{u_0} * \xi_\varepsilon)^+ \right) \cdot \nu \\ \qquad\qquad - k^2 \varepsilon (\beta^\varepsilon \widehat{u_0} * \xi_\varepsilon)^+ \cdot \nu & \text{on } \partial D, \\ \nabla \widehat{V_\varepsilon} \cdot \nu = \Lambda(\widehat{V_\varepsilon}) & \text{on } \partial B_R. \end{cases} \quad \text{(C.19)}$$

As in the proof of Proposition 36, we estimate $\left\|\widehat{V_\varepsilon}\right\|_{H^1(B_R)}$ by writing the variational formulation. For $w \in H^1(B_R)$,

$$\begin{aligned}\int_{B_R} a_\varepsilon \nabla \widehat{V}_\varepsilon \cdot \nabla \overline{w} - k^2 n_\varepsilon \widehat{V}_\varepsilon \overline{w} - \left\langle \Lambda(\widehat{V}_\varepsilon), w \right\rangle_{H^{-\frac{1}{2}}(\partial B_R), H^{\frac{1}{2}}(\partial B_R)} \\ = \int_D -\varepsilon a_\varepsilon \nabla(\eta_\varepsilon \widehat{u_{1,\varepsilon}}) \cdot \nabla \overline{w} + \varepsilon k^2 n_\varepsilon (\eta_\varepsilon \widehat{u_{1,\varepsilon}}) - \varepsilon \nabla \cdot (\sigma_i^\varepsilon \eta_\varepsilon \partial_i \widehat{u}_0 * \xi_\varepsilon) \cdot \nabla \overline{w} \\ - k^2 \varepsilon \nabla \cdot (\beta^\varepsilon \widehat{u}_0 * \xi_\varepsilon \eta_\varepsilon) \overline{w} + k^2 \varepsilon \beta^\varepsilon \widehat{u}_0 * \xi_\varepsilon \eta_\varepsilon \cdot \nabla \overline{w}.\end{aligned} \tag{C.20}$$

In particular, by the coercivity of the sesquilinear form, we get

$$\begin{aligned}\|\widehat{v}_\varepsilon\|_{H^1(D)} + \|\widehat{v}_\varepsilon\|_{H^1(B_R \setminus \overline{D})} \lesssim \varepsilon \|\eta_\varepsilon \widehat{u_{1,\varepsilon}}\|_{H^1(D)} + \varepsilon \left\| \sum_{i=1}^d \nabla \cdot (\sigma_i^\varepsilon \partial_i \widehat{u}_0 * \xi_\varepsilon \eta_\varepsilon) \right\|_{L^2(D)} + \\ \varepsilon \|\nabla \cdot (\beta^\varepsilon \widehat{u}_0 * \xi_\varepsilon \eta_\varepsilon)\|_{L^2(D)} + \varepsilon \|\beta^\varepsilon \widehat{u}_0 * \xi_\varepsilon \eta_\varepsilon\|_{L^2(D)}.\end{aligned} \tag{C.21}$$

Let us now estimate $\|\eta_\varepsilon \widehat{u_{1,\varepsilon}}\|_{H^1(D)} = \|\eta_\varepsilon \phi_i^\varepsilon \partial_i \widehat{u}_0 * \xi_\varepsilon\|_{H^1(D)}$. The three other terms can then be estimated using similar arguments. First

$$\begin{aligned}\|\nabla(\eta_\varepsilon \phi_i^\varepsilon \partial_i \widehat{u}_0 * \xi_\varepsilon)\|_{L^2(D)} &\lesssim \|(\nabla \eta_\varepsilon) \phi_i^\varepsilon \partial_i \widehat{u}_0 * \xi_\varepsilon + \eta_\varepsilon \nabla(\phi_i^\varepsilon \partial_i \widehat{u}_0 * \xi_\varepsilon)\|_{L^2(D)} \\ &\lesssim \left\| \left(\frac{1}{\mu_d(\frac{1}{\varepsilon})} |\nabla \widehat{u}_0 * \xi_\varepsilon| + \varepsilon |\nabla(\nabla \widehat{u}_0 * \xi_\varepsilon)| \right) |\phi^\varepsilon| + |\nabla \phi| |\nabla \widehat{u}_0 * \xi_\varepsilon| \right\|_{L^2(\mathcal{S}_{\eta_\varepsilon})}.\end{aligned} \tag{C.22}$$

Eq (C.11) combined with the bounds on the corrector implies

$$\left\| \frac{1}{\mu_d(\frac{1}{\varepsilon})} |\nabla \widehat{u}_0 * \xi_\varepsilon| |\phi^\varepsilon| \right\|_{L^2(\mathcal{S}_{\eta_\varepsilon})} \lesssim \varepsilon^{\frac{p-2}{2p}} \mu_d(\frac{1}{\varepsilon})^{\frac{p-2}{2p}-1} \widetilde{\chi^1_{\varepsilon,p}} \|\nabla \widehat{u}_0\|_{L^p(\mathcal{S}_{\eta_\varepsilon} + 2\varepsilon \square_0)} \tag{C.23}$$

and

$$\left\| |\nabla \widehat{u}_0 * \xi_\varepsilon| |\nabla \phi^\varepsilon| \right\|_{L^2(\mathcal{S}_{\eta_\varepsilon})} \lesssim \varepsilon^{\frac{p-2}{2p}} \mu_d(\frac{1}{\varepsilon})^{\frac{p-2}{2p}} \widetilde{\chi^2_{\varepsilon,p}} \|\nabla \widehat{u}_0\|_{L^p(\mathcal{S}_{\eta_\varepsilon} + 2\varepsilon \square_0)} \tag{C.24}$$

where the random variables $\widetilde{\chi^1_{\varepsilon,p}}$ and $\widetilde{\chi^2_{\varepsilon,p}}$ are defined as

$$\begin{cases} \widetilde{\chi^1_{\varepsilon,p}} := \left(\dfrac{\varepsilon^d}{\varepsilon \mu_d(\frac{1}{\varepsilon})} \displaystyle\sum_{z \in P_\varepsilon(\mathcal{S}_{\eta_\varepsilon})} \mathcal{C}(z)^{\frac{2p}{p-2}} \right)^{\frac{p-2}{2p}}, \\ \widetilde{\chi^2_{\varepsilon,p}} := \left(\dfrac{\varepsilon^d}{\varepsilon \mu_d(\frac{1}{\varepsilon})} \displaystyle\sum_{z \in P_\varepsilon(\mathcal{S}_{\eta_\varepsilon})} (1 + r_*(z))^{d \frac{2p}{p-2}} \right)^{\frac{p-2}{2p}}. \end{cases} \tag{C.25}$$

We use the following Lemma to estimate $\|\nabla \widehat{u_0}\|_{L^p(\mathcal{S}_{\eta_\varepsilon}+2\varepsilon\square_0)}$.

Lemma 51: [119, Lemma 6.12]

Fix $p \in (1,\infty)$, $\alpha > \frac{1}{p}$, $q \in [1,p]$ and $\beta \in \left(0, \frac{1}{q}\right]$. For every $f \in W^{\alpha,p}(\mathbb{R}^d)$ and $r \in (0,1]$,

$$\|f\|_{L^q(\partial D + B_r)} \lesssim r^\beta \|f\|_{W^{\alpha,p}(\mathbb{R}^d)}. \tag{C.26}$$

Applying (C.26) with $f = \nabla \widehat{u_0}$, $r = 4\varepsilon\mu_d(\frac{1}{\varepsilon})$, $q = p$, $\alpha > \frac{1}{p}$, $\beta = \frac{1}{q} = \frac{1}{p}$ yields

$$\|\nabla \widehat{u_0}\|_{L^p(\mathcal{S}_{\eta_\varepsilon}+2\varepsilon\square_0)} \lesssim \varepsilon^{\frac{1}{p}} \mu_d(\frac{1}{\varepsilon})^{\frac{1}{p}} \|\nabla u_0\|_{W^{\alpha,p}(D)}. \tag{C.27}$$

Furthermore, using (C.12), we get

$$\begin{aligned} \left\| \varepsilon |\nabla(\nabla \widehat{u_0} * \xi_\varepsilon)||\phi^\varepsilon| \right\|_{L^2(\mathcal{S}_{\eta_\varepsilon})} &\lesssim \varepsilon^\alpha \mu_d(\frac{1}{\varepsilon}) \varepsilon^{\frac{p-2}{2p}} \mu_d(\frac{1}{\varepsilon})^{\frac{p-2}{2p}} \widetilde{\chi^1_{\varepsilon,p}} \|\nabla u_0\|_{W^{\alpha,p}(\mathcal{S}_{\eta_\varepsilon}+2\varepsilon\square_0)} \\ &\lesssim \varepsilon^{\frac{1}{2}} \mu_d(\frac{1}{\varepsilon})^{\frac{1}{2}} \varepsilon^{\alpha-\frac{1}{p}} \mu_d(\frac{1}{\varepsilon})^{1-\frac{1}{p}} \widetilde{\chi^1_{\varepsilon,p}} \|\nabla u_0\|_{W^{\alpha,p}(D)}. \end{aligned} \tag{C.28}$$

Combining the last estimates (C.23), (C.24), (C.27) and (C.28), and the fact that $\alpha > \frac{1}{p}$, one has that

$$\begin{aligned} &\|\nabla(\eta_\varepsilon \phi_i^\varepsilon \ \partial_i \widehat{u_0} * \xi_\varepsilon)\|_{L^2(D)} \\ &\quad\lesssim \varepsilon^{\frac{1}{2}} \mu_d(\frac{1}{\varepsilon})^{\frac{1}{2}} \left(\mu_d(\frac{1}{\varepsilon})^{-1} \chi^1_{\varepsilon,p} + \chi^2_{\varepsilon,p} + \varepsilon^{\alpha-\frac{1}{p}} \mu_d(\frac{1}{\varepsilon})^{1-\frac{1}{p}} \chi^1_{\varepsilon,p} \right) \|\nabla u_0\|_{W^{\alpha,p}(D)} \\ &\quad\lesssim \varepsilon^{\frac{1}{2}} \mu_d(\frac{1}{\varepsilon})^{\frac{1}{2}} \widetilde{\chi^3_{\varepsilon,p}} \|u_0\|_{W^{1+\alpha,p}(D)}, \end{aligned} \tag{C.29}$$

where the random variable $\widetilde{\chi^3_{\varepsilon,p}}$ is defined as

$$\widetilde{\chi^3_{\varepsilon,p}} := \mu_d(\frac{1}{\varepsilon})^{-1} \widetilde{\chi^1_{\varepsilon,p}} + \widetilde{\chi^2_{\varepsilon,p}} + \varepsilon^{\alpha-\frac{1}{p}} \mu_d(\frac{1}{\varepsilon})^{1-\frac{1}{p}} \widetilde{\chi^1_{\varepsilon,p}},$$

and satisfies the stochastic integrability (4.52).
We finally proved that

$$\|\widetilde{v_1}\|_{H^1(D)} + \|\widetilde{v_1}\|_{H^1(B_R\setminus\overline{D})} \lesssim \varepsilon^{\frac{1}{2}} \mu_d(\frac{1}{\varepsilon})^{\frac{1}{2}} \widetilde{\chi^3_{\varepsilon,p}} \|u_0\|_{W^{1+\alpha,p}(D)}. \tag{C.30}$$

□

APPENDIX D

Proof of Lemma 41

Proof of Lemma 41. (a) First note that for $y \in \mathbb{R}^d$,

$$\int_{\mathbb{R}^d} \mathbb{1}_{B_t(x)}(y)\mathrm{d}x = \int_{\mathbb{R}^d} \mathbb{1}_{B_t(y)}(x)\mathrm{d}x = Ct^d,$$

where C depends only on d.
We have also for $y, z \in \mathbb{R}^d$,

$$\int_{\mathbb{R}^d} \mathbb{1}_{B_t(x)}(y)\mathbb{1}_{B_t(x)}(z)\mathrm{d}x \leq \int_{\mathbb{R}^d} \mathbb{1}_{B_t(x)}(y)\mathrm{d}x = Ct^d.$$

Let $U \in L^1(D)$ and $t > 0$. By Fubini's theorem,

$$\begin{aligned}
\int_{\mathbb{R}^d} \left(\int_{B_t(x)\cap D} |U| \right) \mathrm{d}x &= \int_{\mathbb{R}^d} \int_D |U(y)| \mathbb{1}_{B_t(x)}(y)\mathrm{d}y\mathrm{d}x \\
&= \int_D |U(y)| \left(\int_{\mathbb{R}^d} \mathbb{1}_{B_t(x)}(y)\mathrm{d}x \right) \mathrm{d}y \\
&\leq Ct^d \int_D |U(y)|\mathrm{d}y \\
&\leq Ct^d \left(\int_D |U| \right).
\end{aligned} \tag{D.1}$$

(b) Similarly,

$$\begin{aligned}
&\int_{\mathbb{R}^d} \rho_T(x)^\alpha \left(\int_{B_t(x)\cap D} |U| \right)^2 \mathrm{d}x \\
&\quad = \int_{\mathbb{R}^d} \rho_T(x)^\alpha \left(\int_D |U(y)| \mathbb{1}_{B_t(x)}(y)\mathrm{d}y \right) \left(\int_D |U(z)| \mathbb{1}_{B_t(x)}(z)\mathrm{d}z \right) \mathrm{d}x \\
&\quad = \int_D |U(y)| \int_D |U(z)| \left(\int_{\mathbb{R}^d} \rho_T(x)^\alpha \mathbb{1}_{B_t(x)}(y) \mathbb{1}_{B_t(x)}(z)\mathrm{d}x \right) \mathrm{d}y\mathrm{d}z.
\end{aligned} \tag{D.2}$$

Since $\mathbb{1}_{B_t(x)}(y)\mathbb{1}_{B_t(x)}(z) = 0$ if $|x-y| > t$ or $|x-z| > t$, one can bound $\rho_T(x)^\alpha$ in the third integral by $\sup_{y\in D}\left(\frac{t+y}{T}+1\right)^\alpha$ yielding the result.

□

PART III

VIRTUAL GUIDE STAR FOR SPEED OF SOUND ESTIMATION

CHAPTER 9

Introduction

Abstract

The medical ultrasound images are now expected not only to provide structural accurate representations of the imaged medium but also to quantitatively assess the quality of the reconstructed images or estimate relevant physical parameters. In this context, we design an estimator of the effective speed of sound inside a random multi-scale medium with acoustic properties modeling those of a biological tissue. We consider the Kirchhoff migration and study the influence on the image of a mismatch between the backpropagation speed of sound and the actual speed. We first study the effect on the point spread function (image of a point-like scatterer) in a homogeneous medium. The position of the focal spot on the image moves when we change the backpropagation speed, and the overall displayed amplitude decreases when the speed of sound is not the actual speed of sound inside the medium. Therefore by tracking the maximum of amplitude on the image, we can recover the true speed of sound. The position of the reflector on the image acts as a guide star at which we adapt our focusing to recover the speed of sound. We then consider the image of the random multi-scale medium. In this medium, there is no guide star, as the image is a random speckle pattern. However, as we exhibit the dependency of the position of the focal spot with respect to the backpropagation speed, we can always focus on the same point whatever the backpropagation speed and thus create a virtual guide star. By focusing on this virtual guide star and maximizing the amplitude on the image, we can recover the effective speed of sound.

Keywords: Inverse problem, quantitative ultrasound imaging, asymptotic analysis

French abstract

Les techniques d'imagerie ultrasonores médicales sont désormais censées non seulement fournir des représentations structurelles précises du milieu imagé, mais aussi évaluer quantitativement la qualité des images reconstruites ou estimer des paramètres physiques pertinents. Dans ce contexte, nous concevons un estimateur

de la vitesse effective du son à l'intérieur d'un milieu multi-échelle aléatoire dont les propriétés acoustiques modélisent celles d'un tissu biologique. Nous considérons la migration de Kirchhoff et étudions l'influence sur l'image d'un décalage entre la vitesse du son par rétropropagation et la vitesse réelle à l'intérieur du milieu. Nous étudions d'abord l'effet sur la *point spread function* (image d'un diffuseur ponctuel) dans un milieu homogène. La position de la tâche focale sur l'image se déplace lorsque nous modifions la vitesse de rétropropagation, et l'amplitude globale affichée diminue lorsque la vitesse du son n'est pas la vitesse réelle du son à l'intérieur du milieu. Par conséquent, en suivant le maximum d'amplitude sur l'image, nous pouvons récupérer la vitesse réelle du son. La position du réflecteur sur l'image sert d'*étoile guide* à laquelle nous adaptons notre mise au point pour retrouver la vitesse du son. Nous considérons ensuite l'image d'un milieu aléatoire à plusieurs échelles. Dans ce milieu, il n'y a pas d'étoile guide, car l'image est un motif de *speckle* aléatoire. Cependant, comme nous arrivons à exhbiber la dépendance de la position de la tâche focale par rapport à la vitesse de rétropropagation, nous pouvons toujours nous focaliser sur le même point, quelle que soit la vitesse de rétropropagation, et créer ainsi une *étoile guide virtuelle*. En se concentrant sur cette *étoile guide virtuelle* et en maximisant l'amplitude sur l'image, nous pouvons récupérer la vitesse effective du son.

Mots-clés: Problème inverse, imagerie ultrasonore quantitative, analyse asymptotique

Introduction

The ultrasound images are computed by delay and sum beamforming or Kirchhoff migration, assuming a known speed of sound inside the medium under investigation. However, discrepancies between the speed of sound of the actual medium and the backpropagation speed of sound results in nonphysical artifacts and aberrations on the image. Furthermore, the effective properties of the medium can be used as biomarkers for the diagnosis of breast cancers or steatosis of the liver.
In this context, Alexandre Aubry and Mathias Fink have carried out experimental works [17, 46] to establish a quantitative estimator of the actual speed of sound inside the medium. Driven by their results, we try to theoreticaly understand the dependency of the reconstruction algorithm with respect to the input backpropagation speed of sound. This requires a precise modeling of the propagation of ultrasounds inside the biological tissues, which was the topic of Part II. Building on these results, in this Part III, we study the estimator of the effective speed of sound introduced by Aubry for the model of tissue mimicking medium described in Section 3.3.1.

Main contribution

We are interested in recovering the underlying speed of sound of acoustic waves in soft biological tissues by using ultrasound measurements.
To construct this estimator, we perform an asymptotic analysis of the Kirchhoff migration imaging functional in the paraxial regime of Figure 10.1 (also see *e.g.* [55]). Before considering tissue-mimicking media, the asymptotic analysis is carried in the Chapter 11, on a simpler model of a homogeneous medium in which lies a single isolated point-like scatterer. This allows to compute the point spread function (PSF) of the imaging system, and to show its dependence on the backpropagation speed of sound. The point spread function of an imaging system is the pattern produced on the image by a point-like object. When the theoretical point spread function of a given system is known, the comparison with the pattern of a given image allows for an assessment of the quality of the image (blurring, aberration, presence of artifacts). The point spread function for ultrasound imaging system is well-known when the backpropagation speed is the speed of sound inside the medium [55].
In this simple setting, we show that the point-like object can be used to calibrate the speed of sound inside the medium. Indeed, the position of the focal spot on the image depends on the backpropagation speed and the returned echo amplitude decreases whenever the backpropagation speed is not the true speed of the tissue. Therefore, by following the amplitude at the center of the focal spot, we can recover the speed of sound.
However, in biological tissues, the backscattered field is not produced by isolated targets but by numerous unresolved randomly distributed scatterers. In Part II, we obtained a simple form of the scattered field by using quantitative stochastic homogenization techniques. Using this expansion, in Chapter 12, we show that for a given backpropagation speed, the imaging function is in fact asymptotically locally a stationary and ergodic random field (with respect to the spatial variable). Therefore, by locally spatially averaging the imaging function, we can extract coherent data from the measurements and recover the effective speed of sound.
The Part III is organized as follows:

- In Chapter 10 we briefly recall the model that we use and introduce the asymptotic framework.
- In Chapter 11, we analyze the dependency of point spread function in a homogeneous medium with respect to the backpropagation speed of sound and establish an estimator of the actual speed of sound of the homogeneous medium.
- In Chapter 12, we use the asymptotic expansion of Theorem 39 to describe the scattered field. Using this expansion, we establish in Theorem 57 the asymptotic form of the imaging function in tissue mimicking media. Based on this result, we show in Lemma 58 that the imaging function is locally stationary. The speed of sound is then recovered by local spatial averages of the amplitude the imaging

function. In fact, the speed of sound can be also recovered by a singular values decomposition of the matrix $K_{\tilde{\xi},t}$ described in Section 12.3.

- In Chapter 13, we perform numerical simulations to illustrate the theoretical results developed in the two previous Chapter 11 and Chapter 12.

CHAPTER 10

Presentation of the model

In this section, we present a mathematical model for medical ultrasound imaging experiments. We first describe how the set of measurements is done in practice. We then detail the geometry of the problem and the governing equation. In a last subsection, we introduce the asymptotic regime in which the computations are done.

10.1 Physical experiment

We recall that the acoustic properties of a medium can be described by its density (denoted ρ) and its bulk modulus (denoted κ) as described in Section 3.3. A soft biological tissue can be modeled by an incompressible homogeneous medium in which lie numerous underresolved contrasted heterogeneities. The image is then done as follows. A set of ultrasound transducers generates a wave that propagates throughout the medium. The contrasted heterogeneities produce a backscattered wave that is recorded by the transducers. Assuming a constant speed for the propagation of ultrasounds, the image is then computed by applying proper time delays to the time data of the different sensors and summing them (see (3.2)).

10.2 Mathematical model

We describe here the mathematical model that we use. We assume that the propagation medium presents a constant density, so that its acoustic properties are characterized by the propagation speed of ultrasonic waves $c := \sqrt{\frac{\kappa}{\rho}}$. We suppose that the propagation medium is infinite and that the speed of sound is a constant $c_0 > 0$ outside of a compact domain $D \subset \mathbb{R}^d$, for $d = 2$ or $d = 3$. D is the medium of interest to be imaged. The transducer array denoted by $\mathcal{A} := [-a, a]^{d-1} \times \{0\}$, $a > 0$ lies outside of D. The bandwidth of each transducer is denoted by $\mathcal{B} \subset \mathbb{R}_*^+$. Without loss of generality, we will assume that the medium is illuminated with spherical incident waves u^i with

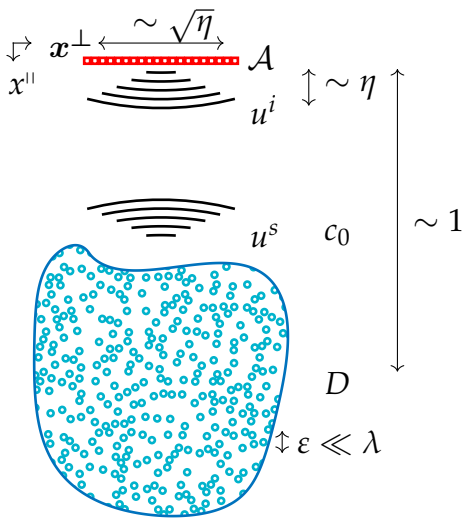

Figure 10.1: Schema of an ultrasound experiment

angular frequency ω, *i.e.*:

$$u^i(\boldsymbol{x_e}, \boldsymbol{x}, \omega) := G^{\frac{\omega}{c_0}}(\boldsymbol{x} - \boldsymbol{x_e}), \text{ for } \boldsymbol{x_e} \in \mathcal{A}, \boldsymbol{x} \in \mathbb{R}^d \setminus \{x_e\}, \omega \in \mathcal{B}. \tag{10.1}$$

where G^k is the Green function associated to the Helmholtz equation at wavenumber k *i.e.* the outgoing solution in $\mathcal{D}'(\mathbb{R}^d)$ of

$$-\Delta G^k - k^2 G^k = \delta. \tag{10.2}$$

We recall [108, Lemma 2.21]:

$$G^k(\boldsymbol{z}) = \begin{cases} \dfrac{i}{4} \mathrm{H}_0^1(k|\boldsymbol{z}|) & \text{if } d = 2, \\ \dfrac{\exp(ik|\boldsymbol{z}|)}{4\pi|z|} & \text{if } d = 3, \end{cases} \tag{10.3}$$

where $\mathrm{H}_0^{(1)}$ is the Hankel function of the first kind. The scattered field $u^s(\boldsymbol{x_e}, \cdot, \omega)$ is the unique solution in $H^1_{loc}(\mathbb{R}^d)$ of:

$$\begin{cases} -\Delta(u^s + u^i)(\boldsymbol{x_e}, \cdot, \omega) - \dfrac{\omega^2}{c_0^2}(1 + n(\cdot))(u^s + u^i)(\boldsymbol{x_e}, \cdot, \omega) = 0 \quad \text{in } \mathbb{R}^d \\ \lim\limits_{|\boldsymbol{x}| \to \infty} |\boldsymbol{x}|^{\frac{d-1}{2}} \left(\dfrac{\partial}{\partial |\boldsymbol{x}|} u^s(\boldsymbol{x_e}, \boldsymbol{x}, \omega) - i\dfrac{\omega}{c_0} u^s(\boldsymbol{x_e}, \boldsymbol{x}, \omega) \right) = 0 \end{cases} \tag{10.4}$$

where $n \in L^\infty$, and $\mathrm{supp}(n) \subset D$ and $1 + n > 0$. n models the variations of the sound velocity inside the medium. The well-posedness of (10.4) is addressed for example in

[185] in dimension $d = 2$ and in [186] in dimension $d = 3$. A review of the well-posedness results for the Helmholtz equation in heterogenous media is presented in [187].
The scattered field u^s is then measured at every $\boldsymbol{x_r} \in \mathcal{A}$. We thus have access to the measurement map

$$M \in L^2((\mathcal{A} \times \mathcal{A}), L^2(\mathcal{B}))$$

defined by

$$M(\boldsymbol{x_e}, \boldsymbol{x_r}, \omega) := u(\boldsymbol{x_e}, \boldsymbol{x_r}, \omega). \tag{10.5}$$

10.3 Imaging functional

The ultrasound images are then computed by a sum and delay algorithm or equivalently a Kirchhoff migration algorithm [6, 188]. Usually, the speed of sound c_0 is known. The imaging function depends then only on the point at which the image is computed. Here we study the dependency on the back propagation speed used as an input. For a given back propagation speed $c_s \in [c_{\min}, c_{\max}]$, the imaging function $\mathcal{I} \in L^2(D \times [c_{\min}, c_{\max}])$ at a given point $\boldsymbol{x_s} \in \mathbb{R}^d$, is given by

$$\mathcal{I}(\boldsymbol{x_s}, c_s) := \int_{(\mathcal{A}\times\mathcal{A}\times\mathcal{B})} \overline{M(\boldsymbol{x_e}, \boldsymbol{x_r}, \omega)} G^{\frac{\omega}{c_s}}(\boldsymbol{x_e} - \boldsymbol{x_s}) G^{\frac{\omega}{c_s}}(\boldsymbol{x_s} - \boldsymbol{x_r}) d\boldsymbol{x_e} d\boldsymbol{x_r} d\omega. \tag{10.6}$$

This imaging function is the usual definition of the Kirchhoff migration, where the measurements M are backpropagated at the speed c_s inside the medium. In a medium where single scattering dominates, the intensity $|\mathcal{I}(\boldsymbol{x_s}, c_0)|$ is then an indicator of the presence (or absence) of contrasted scatterers at $\boldsymbol{x_s}$. When $c_s \neq c_0$, the image is deteriorated. In this section, we study this effect.

10.4 Asymptotic assumptions

The problem of medical ultrasound imaging is a multi-scale problem in which the size of the domain is larger than wavelength, itself larger than the typical size of the heterogeneities. In clinical situations, the typical central frequency of the transducer is of the order of $1 - 10$ Mhz, the speed of sound varies from $c \sim 1400 - 1600$ m.s^{-1}, and thus the wavelength is $\lambda \sim 0.8 - 1$ mm while $\mathrm{diam}(D) \sim 8 - 10$ cm. Finally the size of the transducer array is of order $\mathrm{diam}(\mathcal{A}) \approx 40$ mm (see [17, Table 2.2]).
Therefore, in order to obtain simple and explicit formulas, we will carry out an asymptotic analysis. The particular geometry of ultrasound imaging is well-described by paraxial regime [55].
We introduce a small dimensionless parameter $\eta \ll 1$. We consider that $\frac{\lambda}{\mathrm{diam}(D)}$ is of the order η. Thus we scale the bandwidth as $\mathcal{B} := \frac{\mathcal{B}_0}{\eta}$ where $\mathcal{B}_0 := [\omega_0 - B/2, \omega_0 + B/2]$, where ω_0 is the normalized central frequency and B is the effective bandwidth.

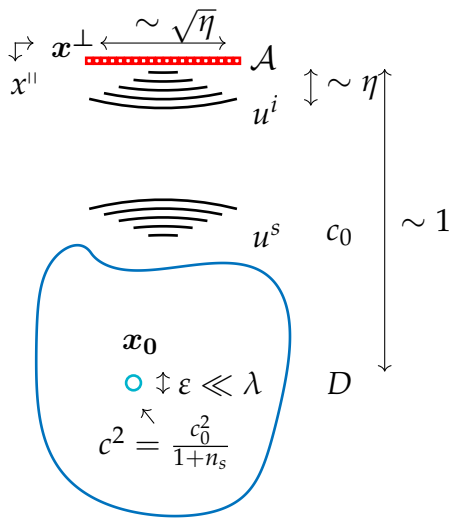

Figure 10.2: Asymptotic regime and point like reflector

The size of the transducer array is typically inbetween the size of D and the wavelength. As in [55], we consider that $\frac{\text{diam}(\mathcal{A})}{\text{diam}(D)}$ is of the order $\eta^{\frac{1}{2}}$. We write $\mathcal{A} := \eta^{\frac{1}{2}} a_0 \mathcal{A}_0 := \eta^{\frac{1}{2}} [-a_0, a_0]^{d-1} \times \{0\}$ where $a_0 = \eta^{\frac{1}{2}} a$ is the normalized size of the transducer array and $\mathcal{A}_0 := [-1,1]^{d-1} \times \{0\}$ is the normalized shape of $\mathcal{A}$. The asymptotic regime is illustrated on Figure 10.2. In this regime, the following holds, for $z \in D$ and $\omega \in \mathcal{B}$ (see [94, (9.2.3)]

$$\mathrm{H}_0^1\left(\frac{\omega}{c_0}|z|\right) \sim \left(\frac{2}{\pi \frac{\omega}{c_0}|z|}\right)^{\frac{1}{2}} \exp\left(i\frac{\omega}{c_0}|z| - i\frac{\pi}{4}\right), \tag{10.7}$$

as $\frac{\omega}{c_0}|z| \gg 1$.
In order to distinguish the rescaled variables from the the physical variables, we use the notation $\tilde{\cdot}$ for the rescaled variables. In the paraxial regime, the axial propagation distances are way larger than the transverse distances and the points $x \in \mathbb{R}^d$ will be denoted as

$$x = (\eta^{\frac{1}{2}} \tilde{x}^\perp, x^{||}).$$

where $\tilde{x}^\perp \in \mathbb{R}^{d-1}$ is the normalized transverse coordinate and $x^{||} \in \mathbb{R}^+$ is the axial coordinate. Thus, $\widetilde{x} \in \mathbb{R}^d$ designates the point

$$\widetilde{x} = (\tilde{x}^\perp, x^{||}).$$

This setting is illustrated on Figure 10.2.

CHAPTER 11

Analysis of the point spread function in the paraxial regime

The point spread function (PSF) is the response of an imaging system to an isolated point-like object. This point like object will usually appear as a spot on the image, called the focal spot. The typical size of the focal spot gives the resolution that one can expect from the imaging system. The point spread function of ultrasound imaging systems has been widely studied when the propagation speed c_0 is constant and known (see for example [55, Chapter 6]). However, if an incorrect propagation speed is used to compute the image, the image will appear as a distorted focal spot. In this section, we carry out an analysis of the point spread function with respect to the backpropagation speed used in the imaging function.
We show that for a small point-like target centered at $\boldsymbol{x_0}$ the focal spot is shifted, distorted and that the value of $\mathcal{I}$ at the point in the center of the focal spot (which is not $\boldsymbol{x_0}$) exhibits a phase shift around the correct speed of sound. This allows to build an estimator of the speed of sound inside the medium (see Theorem 54). To understand and analyze these effects, we consider a toy model with one isolated point-like reflector.
We thus consider a homogeneous medium with one small (with respect to the wavelength) scatterer at $\boldsymbol{x_0} = (\eta^{\frac{1}{2}}\tilde{\boldsymbol{x_0}}^{\perp}, x_0^{\shortparallel})$. We then assume

$$n(\boldsymbol{x}) := (n_S - 1)\mathbb{1}_{B(\boldsymbol{x_0},\varepsilon)}(\boldsymbol{x})$$

where $n_S > 0$, $\varepsilon \ll \lambda$, and $\boldsymbol{x_0} \in D$. In this regime, as we consider a point-like object, we assume that there exists $\alpha > 1$, such that $\varepsilon = \eta^{\alpha} r_0$ for some normalized radius r_0. In this configuration, the monopole approximation holds [189, 107] and we have

Lemma 52: Monopole approximation of the scattered field

For all $\omega \in \mathcal{B}$, and $\boldsymbol{x_e}, \boldsymbol{x_r} \in \mathcal{A}$,

$$u^s(\boldsymbol{x_e}, \boldsymbol{x_r}, \omega) = \varepsilon^d n_S \left(\frac{\omega}{c_0}\right)^2 G^{\frac{\omega}{c_0}}(\boldsymbol{x_r} - \boldsymbol{x_0}) G^{\frac{\omega}{c_0}}(\boldsymbol{x_e} - \boldsymbol{x_0}) + \mathcal{O}\left(\varepsilon^{d+1} \left(\frac{\omega}{c_0}\right)^d |\boldsymbol{x_e} - \boldsymbol{x_0}|^{-\frac{d-1}{2}} |\boldsymbol{x_r} - \boldsymbol{x_0}|^{-\frac{d-1}{2}}\right). \quad (11.1)$$

The proof is done in Appendix E. This simple formula for u will be used to carry out an asymptotic analysis of the imaging function and to obtain explicit formulas for the point spread function.

11.1 Asymptotic analysis of $\mathcal{I}$

This section is devoted to the asymptotic analysis of $\mathcal{I}$ in the paraxial regime for a given backpropagation c_s which is not necessary the speed of sound inside the medium c_0. In particular, in Theorem 54, we obtain a simple formula for the point spread function which we will use to analyze an estimator of the speed of sound inside the medium (see Theorem 54).
We introduce F defined by

$$F(\boldsymbol{x}, \boldsymbol{y}, c_0, c_s, \omega) := \left\langle G^{\frac{\omega}{c_s}}(\cdot - \boldsymbol{y}), G^{\frac{\omega}{c_0}}(\cdot - \boldsymbol{x}) \right\rangle_{\mathcal{A}} \quad (11.2)$$

for $\boldsymbol{x}, \boldsymbol{y} \in \mathbb{R}^d$ and where the notation

$$\langle f, g \rangle_{\mathcal{A}} := \int_{\mathcal{A}} f(\boldsymbol{x}) \overline{g}(\boldsymbol{x}) d\sigma(\boldsymbol{x})$$

stands for the standard $L^2(\mathcal{A})$-product. By Lemma 52, the imaging function $\mathcal{I}$ can be approximated by

$$\mathcal{I}(\boldsymbol{x_s}, c_s) = \varepsilon^d n_S \int_{\mathcal{B}} \frac{\omega^2}{c_0^2} F(\boldsymbol{x_0}, \boldsymbol{x_s}, c_0, c_s, \omega)^2 \, d\omega + \int_{\mathcal{A}\times\mathcal{A}\times\mathcal{B}} R_{\eta,\varepsilon}(\boldsymbol{x_e}, \boldsymbol{x_r}, \omega) G^{\frac{\omega}{c_s}}(\boldsymbol{x_e} - \boldsymbol{y}) G^{\frac{\omega}{c_s}}(\boldsymbol{x_r} - \boldsymbol{y}) d\sigma(\boldsymbol{x_e}) d\sigma(\boldsymbol{x_r}) d\omega \quad (11.3)$$

for some function $R_{\eta,\varepsilon}$ that satisfies

$$R_{\eta,\varepsilon}(\boldsymbol{x_e}, \boldsymbol{x_r}, \omega) = \mathcal{O}\left(\varepsilon^{d+1} \left(\frac{\omega}{c_0}\right)^d |\boldsymbol{x_e} - \boldsymbol{x_0}|^{-\frac{d-1}{2}} |\boldsymbol{x_r} - \boldsymbol{x_0}|^{-\frac{d-1}{2}}\right).$$

We recall that

$$|\mathcal{A}| = \eta^{\frac{d-1}{2}} a_0^{d-1} |\mathcal{A}_0|,$$

and that

$$\left\| G^{\frac{\omega}{c_s}}(\cdot - \boldsymbol{x_s}) \right\|^2_{L^\infty(\mathcal{A})} \leq \begin{cases} \dfrac{R_d(\boldsymbol{x_s}, c_s)}{\omega} & \text{if } d = 2 \\ R_d(\boldsymbol{x_s}, c_s) & \text{if } d = 3, \end{cases} \tag{11.4}$$

for some function $R_d \in L^\infty(D \times [c_{\min}, c_{\max}])$ and independent on ω. Therefore, with the scaling of the paraxial regime, where $\omega \in \frac{\mathcal{B}_0}{\eta}$, the imaging function can thus be approximated as

$$\mathcal{I}(\boldsymbol{x_s}, c_s) = \varepsilon^d n_S \int_{\mathcal{B}} \frac{\omega^2}{c_0^2} F\left(\boldsymbol{x_0}, \boldsymbol{x_s}, c_0, c_s, \omega\right)^2 d\omega + R^1_{\varepsilon,\eta}(\boldsymbol{x_s}, c_s), \tag{11.5}$$

with $R^1_{\varepsilon,\eta}(\boldsymbol{x_s}, c_s) = \mathcal{O}\left(\varepsilon^{d+1}\eta^{2-d}\right)$.
The analysis of $\mathcal{I}$ can be then carried out by studying, for a search point $\boldsymbol{x_s} = (\eta^{\frac{1}{2}}\widetilde{\boldsymbol{x}}^\perp_{\boldsymbol{s}}, x^{\shortparallel}_s) \in D$ and for $\omega \in \mathcal{B}$, the function $F(\boldsymbol{x_0}, \boldsymbol{x_s}, c_0, c_s, \omega)$.
In the following computations, to simplify the expression we use the variable

$$v := \frac{c_0}{c_s}.$$

We first derive an asymptotic expression for F.

Lemma 53: Asymptotic expression of F

Let $\boldsymbol{x} = (\eta^{\frac{1}{2}}\widetilde{\boldsymbol{x}}^\perp, x^{\shortparallel}), \boldsymbol{y} = (\eta^{\frac{1}{2}}\widetilde{\boldsymbol{y}}^\perp, y^{\shortparallel}) \in \mathbb{R}^d$, $c_s = \frac{c_0}{v} \in [c_{\min}, c_{\max}]$ and $\omega = \frac{\tilde{\omega}}{\eta} \in \mathcal{B}$, then,

$$\begin{aligned} &F\left(\boldsymbol{x}, \boldsymbol{y}, c_0, c_s = \frac{c_0}{v}, \omega\right) \\ &\quad = \frac{\eta^{\frac{5-d}{2}} c_0^{3-d} a_0^{d-1}}{4\pi^{d-1}\tilde{\omega}^{3-d} v^{\frac{3-d}{2}} (x^{\shortparallel} y^{\shortparallel})^{\frac{d-1}{2}}} \exp\left(\frac{i\tilde{\omega}}{c_0\eta}\left(v y^{\shortparallel} - x^{\shortparallel} + \eta\frac{v|\widetilde{\boldsymbol{y}}^\perp|^2}{2y^{\shortparallel}} - \eta\frac{|\widetilde{\boldsymbol{x}}^\perp|^2}{2x^{\shortparallel}}\right)\right) \\ &\qquad \times \mathcal{G}\left(\frac{\tilde{\omega} a_0}{c_0}\left(\frac{v\widetilde{\boldsymbol{y}}^\perp}{y^{\shortparallel}} - \frac{\widetilde{\boldsymbol{x}}^\perp}{x^{\shortparallel}}\right), \frac{\tilde{\omega} a_0}{c_0}\left(\frac{v}{y^{\shortparallel}} - \frac{1}{x^{\shortparallel}}\right)\right) \\ &\qquad + \eta^{\frac{d+1}{2}} R(\boldsymbol{x}, \boldsymbol{y}, \tilde{\omega}), \end{aligned} \tag{11.6}$$

where $\mathcal{G} : (\mathbb{R}^{d-1} \times \mathbb{R}) \to \mathbb{C}$ is defined by

$$\mathcal{G}(\boldsymbol{\xi_1}, \xi_2) := \frac{1}{|\mathcal{A}_0|} \int_{\mathcal{A}_0} \exp\left(-i\widetilde{\boldsymbol{x_e}}^\perp \cdot \boldsymbol{\xi_1} + i\frac{|\widetilde{\boldsymbol{x_e}}^\perp|^2}{2}\xi_2\right) d\sigma(\widetilde{\boldsymbol{x_e}}) \tag{11.7}$$

and for some remainder $R \in L^1_{loc}(\mathbb{R}^d \times \mathbb{R}^d, L^1(\mathcal{B}_0))$.

Proof. The proof is done for $d = 3$. In dimension $d = 2$, the amplitude must be modified and in particular the dependency on ω must be taken into account to obtain the result (11.6).
By the definition of the Green function,

$$F(\boldsymbol{x}, \boldsymbol{y}, c_0, c_s = \frac{c_0}{v}, \omega) = \frac{1}{16\pi^2} \int_{\mathcal{A}} \frac{\exp\left(\frac{i\omega}{c_0}(v|\boldsymbol{x_e} - \boldsymbol{y}| - |\boldsymbol{x_e} - \boldsymbol{x}|)\right)}{|\boldsymbol{x_e} - \boldsymbol{x}||\boldsymbol{x_e} - \boldsymbol{y}|} d\sigma(\boldsymbol{x_e}). \tag{11.8}$$

With the scaling of the paraxial regime, we write $\omega := \frac{\tilde{\omega}}{\eta}$, $\boldsymbol{x_e} = (\eta^{\frac{1}{2}}\widetilde{\boldsymbol{x_e}}^{\perp}, 0)$. As $\boldsymbol{x} = (\eta^{\frac{1}{2}}\widetilde{\boldsymbol{x}}^{\perp}, x^{\shortparallel})$ by a Taylor expansion, we have that

$$|\boldsymbol{x_e} - \boldsymbol{x}| = x^{\shortparallel} + \eta \frac{|\widetilde{\boldsymbol{x_e}}^{\perp} - \widetilde{\boldsymbol{x}}^{\perp}|^2}{2x^{\shortparallel}} + \eta^2 R_0(\boldsymbol{x}), \tag{11.9}$$

for some $R_0 \in L^1_{loc}(\mathbb{R}^d)$. Therefore,

$$\begin{aligned} F(\boldsymbol{x},&\boldsymbol{y}, c_0, c_s = \frac{c_0}{v}, \omega) \\ &= \frac{\eta}{4\pi^2|\boldsymbol{x}||\boldsymbol{y}|}\left(\exp\left(\frac{i\tilde{\omega}}{c_0\eta}\left(vy^{\shortparallel} - x^{\shortparallel} + \eta\frac{v|\widetilde{\boldsymbol{y}}^{\perp}|^2}{2y^{\shortparallel}} - \eta\frac{|\widetilde{\boldsymbol{x}}^{\perp}|^2}{2x^{\shortparallel}}\right)\right)\right. \\ &\quad \left.\times \frac{1}{4}\int_{a_0\mathcal{A}_0} \exp\left(i\frac{\tilde{\omega}}{c_0}\left(\widetilde{\boldsymbol{x_e}}^{\perp} \cdot \left(\frac{v\widetilde{\boldsymbol{y}}^{\perp}}{y^{\shortparallel}} - \frac{\boldsymbol{x}^{\perp}}{x^{\shortparallel}}\right) + \frac{|\widetilde{\boldsymbol{x_e}}^{\perp}|^2}{2}\left(\frac{1}{x^{\shortparallel}} - \frac{v}{y^{\shortparallel}}\right)\right)\right) d\sigma(\widetilde{\boldsymbol{x_e}})\right. \\ &\qquad + \eta^2 R(\boldsymbol{x}, \boldsymbol{y}, \tilde{\omega}), \end{aligned} \tag{11.10}$$

for some $R \in L^1_{loc}(\mathbb{R}^d \times \mathbb{R}^d, L^1(\mathcal{B}_0))$. The result (11.6) is then obtained by the change of variable $\widetilde{\boldsymbol{z_e}} := \frac{\widetilde{\boldsymbol{x_e}}}{a_0}$. □

We can now resume the study of $\mathcal{I}$. We show in the next proposition that an error in the backpropagation speed of sound has two effects on the image. First, the focal spot is not centered at $\boldsymbol{x_0}$. In the paraxial regime it is located at

$$\boldsymbol{x}_f(\boldsymbol{x_0}, v) := (\eta^{\frac{1}{2}}\frac{\widetilde{\boldsymbol{x_0}}^{\perp}}{v^2}, \frac{x_0^{\shortparallel}}{v}).$$

Secondly, the shape of the focal spot is altered as we can see on Figure 13.3.
To study these effects, we use a Taylor expansion around the center of the focal spot. We consider for a point $\boldsymbol{r_s}(v) = (\eta^{\frac{1}{2}}\frac{\widetilde{\boldsymbol{r_s}}^{\perp}}{v^2}, \eta\frac{r_s^{\shortparallel}}{v}) \in \mathbb{R}^d$, the following parametrization for the search point:

$$\boldsymbol{x_s} = \boldsymbol{x}_f(\boldsymbol{x_0}, v) + \boldsymbol{r_s}(v) = \left(\eta^{\frac{1}{2}}\frac{\widetilde{\boldsymbol{x_0}}^{\perp} + \widetilde{\boldsymbol{r_s}}^{\perp}}{v^2}, \frac{x_0^{\shortparallel} + \eta r_s^{\shortparallel}}{v}\right).$$

The dependency in v on $\boldsymbol{r_s}$ allows to obtain a simple asymptotic form. The scaling $\eta^{\frac{1}{2}}$ in the transverse direction and η in the axial direction are the expected scaling and corresponds to the scaling of the focal spot when $c_s = c_0$ [55, Proposition 6.4]. We establish a formula for the point spread function:

Theorem 54: Asymptotic expression of $\mathcal{I}$ with an isolated target

Let $\boldsymbol{x_f}(\boldsymbol{x_0}, v) := (\eta^{\frac{1}{2}} \frac{\widetilde{\boldsymbol{x_0}}^{\perp}}{v^2}, \frac{x_0^{\shortparallel}}{v})$ and $\boldsymbol{r_s}(v) = (\eta^{\frac{1}{2}} \frac{\widetilde{\boldsymbol{r_s}}^{\perp}}{v^2}, \eta \frac{r_s^{\shortparallel}}{v}) \in \mathbb{R}^d$ and $c_s \in [c_{\min}, c_{\max}]$. We then parametrize the search point as

$$\boldsymbol{x_s} = \boldsymbol{x_f}(v) + \boldsymbol{r_s}(v) \in \mathbb{R}^d.$$

Then the imaging function of (10.6) has the simple form:

$$\mathcal{I}\left(\boldsymbol{x_s}, c_s = \frac{c_0}{v}\right) = \varepsilon^d \eta^{2-d} C_a n_S \mathcal{P}_0\left(\widetilde{\boldsymbol{x_0}}, \widetilde{\boldsymbol{r}}_{\boldsymbol{s}}, v\right) + \mathcal{O}(\varepsilon^d \eta^{3-d}), \tag{11.11}$$

with $\mathcal{P}_0 : (\mathbb{R}^d \times \mathbb{R}^d \times \mathbb{R}_*^+) \to \mathbb{C}$ the point spread function defined by:

$$\begin{aligned}\mathcal{P}_0\left(\widetilde{\boldsymbol{x_0}}, \widetilde{\boldsymbol{r}}_{\boldsymbol{s}}, v\right) := \int_{\mathcal{B}_0} &\left(\frac{v^2\tilde{\omega}^2}{(x_0^{\shortparallel})^2 c_0^2}\right)^{d-2} \frac{1}{(x_0^{\shortparallel})^2} \\ &\times \exp\left(\frac{2i\tilde{\omega}}{c_0}\left(r_s^{\shortparallel} - \frac{v^2|\widetilde{\boldsymbol{x_0}}^{\perp}|^2 - |\widetilde{\boldsymbol{x_0}}^{\perp} + \widetilde{\boldsymbol{r}}_{\boldsymbol{s}}^{\perp}|^2}{2v^2 x_0^{\shortparallel}}\right)\right) \\ &\times \mathcal{G}\left(\frac{a_0\tilde{\omega}}{x_0^{\shortparallel} c_0}\widetilde{\boldsymbol{r}}_{\boldsymbol{s}}^{\perp}, \frac{a_0^2\tilde{\omega}}{x_0^{\shortparallel} c_0}(v^2 - 1)\right)^2 d\tilde{\omega}\end{aligned} \tag{11.12}$$

and the amplitude

$$C_a := \frac{a_0^{2(d-1)}}{16\pi^2(d-1)}. \tag{11.13}$$

The function $\mathcal{G}$ is defined in (11.7).

The formula can be even simplified in the narrowband case, when the central frequency is larger than the bandwidth, *i.e.* $\frac{B}{\omega_0} \ll 1$. This yields the following:

Corollary 55: Point spread function for narrowband signal

(Narrowband signal) Assume that $B \ll \omega_0$, $\mathcal{P}_0$ is approximated by:

$$\begin{aligned}\mathcal{P}_0(\widetilde{\boldsymbol{x_0}}, \widetilde{\boldsymbol{r}_s}, v) &= \left(\frac{v^2\omega_0^2}{(x_0^{\shortparallel})^2 c_0^2}\right)^{d-2} \frac{B}{(x_0^{\shortparallel})^2} \exp\left(\frac{2i\omega_0}{c_0}\left(r_s^{\shortparallel} - \frac{v^2|\widetilde{\boldsymbol{x_0}}^{\perp}|^2 - |\widetilde{\boldsymbol{x_0}}^{\perp} + \widetilde{\boldsymbol{r}_s}^{\perp}|^2}{2v^2 x_0^{\shortparallel}}\right)\right) \\ &\times \operatorname{sinc}\left(\frac{B}{c_0} r_s^{\shortparallel}\right) \times \mathcal{G}\left(\frac{a_0\omega_0}{x_0^{\shortparallel} c_0}\widetilde{\boldsymbol{r}_s}^{\perp}, \frac{a_0^2\omega_0}{x_0^{\shortparallel} c_0}\left(v^2 - 1\right)\right)^2 \left(1 + \mathcal{O}\left(\frac{B}{\omega_0}\right)\right). \quad (11.14)\end{aligned}$$

Remark 11.1.1. *This result is an extension of the point spread function found e.g. in [55, Proposition 6.4], for $c_0 \neq c_s$. We show an image of the point spread function for several backpropagation speeds of sound on Figure 13.3.*
In this analysis, we considered, without loss of generality that the Fourier transform of the source is $\hat{S}(\boldsymbol{x_e}, \boldsymbol{x}, \omega) := \delta(\boldsymbol{x} - \boldsymbol{x_e})\mathbb{1}_{\mathcal{B}}(\omega)$. The result of Corollary 55 remains true for any source with a more realistic frequency content, that is a real measurable signal with a Fourier transform of the form for $\omega \in \mathcal{B}$,

$$\hat{S}(\boldsymbol{x_e}, \boldsymbol{x}, \omega) = \delta(\boldsymbol{x} - \boldsymbol{x_e})\hat{f}_0\left(\frac{\omega_0 - \varepsilon\omega}{B}\right)$$

for some $\hat{f}_0 \in L^2(\mathcal{B})$. As we consider In the formula (11.14), one must then replace $\operatorname{sinc}\left(\frac{B}{c_0} v x_s^{\shortparallel}\right)$ *with* $f_0\left(\frac{B}{c_0} v x_s^{\shortparallel}\right)$.

Proof of Theorem 54. By (11.5), and the change of variable $\omega := \frac{\tilde{\omega}}{\eta}$, it holds that

$$\mathcal{I}(\boldsymbol{x_s}, c_s) = \varepsilon^d n_S \eta^{-3} \int_{\mathcal{B}_0} \frac{\tilde{\omega}^2}{c_0^2} F(\boldsymbol{x_0}, \boldsymbol{x_s}, c_0, c_s, \frac{\tilde{\omega}}{\eta})^2 d\tilde{\omega} + \mathcal{O}(\varepsilon^{d+1}\eta^{2-d}). \quad (11.15)$$

We use the asymptotic expression (11.6) of Lemma 53 with $\boldsymbol{x} = \boldsymbol{x_0}$ and $\boldsymbol{y} = \boldsymbol{x_s}$, which yields:

$$\begin{aligned}\mathcal{I}\left(\boldsymbol{x_s}, c_s = \frac{c_0}{v}\right) &= \varepsilon^d \eta^{2-d} \frac{a_0^{2d-2}}{16\pi^{2d-2}} \frac{1}{(x_0^{\shortparallel})^{d-1}(x_0^{\shortparallel} + \eta r_s^{\shortparallel})^{d-1}} \\ &\times \int_{\mathcal{B}_0} \left(\frac{v^2\tilde{\omega}^2}{c_0^2}\right)^{d-2} \exp\left(\frac{2i\tilde{\omega}}{c_0}\left(r_s^{\shortparallel} - \frac{|\widetilde{\boldsymbol{x_0}}^{\perp}|^2}{2x_0^{\shortparallel}} + \frac{|\widetilde{\boldsymbol{x_0}}^{\perp} + \widetilde{\boldsymbol{r}_s}^{\perp}|^2}{2v^2(x_0^{\shortparallel} + \eta r_s^{\shortparallel})}\right)\right) \\ &\times \mathcal{G}\left(\frac{\tilde{\omega} a_0}{c_0}\left(\frac{\widetilde{\boldsymbol{x_0}}^{\perp} + \widetilde{\boldsymbol{r}_s}^{\perp}}{x_0^{\shortparallel} + \eta r_s^{\shortparallel}} - \frac{\widetilde{\boldsymbol{x_0}}^{\perp}}{x_0^{\shortparallel}}\right), \frac{a_0^2\tilde{\omega}}{c_0}\left(\frac{v^2}{x_0^{\shortparallel} + \eta r_s^{\shortparallel}} - \frac{1}{x_0^{\shortparallel}}\right)\right)^2 d\tilde{\omega} \\ &+ \mathcal{O}(\varepsilon^{d+1}\eta^{2-d}) + \mathcal{O}(\varepsilon^d \eta^{3-d}). \quad (11.16)\end{aligned}$$

We want to compare $\mathcal{O}(\varepsilon^{d+1}\eta^{2-d})$ and $\mathcal{O}(\varepsilon^{d}\eta^{3-d})$. We recall that $\eta = \frac{\lambda}{\mathrm{diam(D)}}$ is a dimensionless parameter while $\varepsilon \ll \lambda$ corresponds to the typical radius size of the reflector. However, by assuming that $\varepsilon = \eta^{\alpha} r_0$, we have that, $\varepsilon^{d+1}\eta^{2-d} \leq r_0 \varepsilon^{d}\eta^{3-d}$. The result (11.11) is then obtained from a Taylor expansion with respect to η in (11.16). □

Proof of Corollary 55. We prove (11.14). We use the change of variable $\zeta := \frac{\tilde{\omega}-\omega_0}{B}$, so that:

$$\begin{aligned}\mathcal{P}_0\left(\widetilde{\boldsymbol{x_0}}, \widetilde{\boldsymbol{r}_s}, v\right) = \left(\frac{v^2}{(x_0^{\shortparallel})^2 c_0^2}\right)^{d-2} \frac{B}{(x_0^{\shortparallel})^2} \exp\left(\frac{2i\omega_0}{c_0}\left(r_s^{\shortparallel} - \frac{v^2|\widetilde{\boldsymbol{x_0}}^{\perp}|^2 - |\widetilde{\boldsymbol{x_0}}^{\perp} + \widetilde{\boldsymbol{r}_s}^{\perp}|^2}{2v^2 x_0^{\shortparallel}}\right)\right) \\ \times \int_{[-\frac{1}{2},\frac{1}{2}]} (B\zeta + \omega_0)^{2(d-2)} \exp\left(\frac{2iB\zeta}{c_0}\left(r_s^{\shortparallel} - \frac{v^2|\widetilde{\boldsymbol{x_0}}^{\perp}|^2 - |\widetilde{\boldsymbol{x_0}}^{\perp} + \widetilde{\boldsymbol{r}_s}^{\perp}|^2}{2v^2 x_0^{\shortparallel}}\right)\right) \\ \times \mathcal{G}\left(\frac{a_0(B\zeta+\omega_0)}{x_0^{\shortparallel} c_0}\widetilde{\boldsymbol{r}_s}^{\perp}, \frac{a_0^2(B\zeta+\omega_0)}{x_0^{\shortparallel} c_0}(v^2-1)\right)^2 d\zeta.\end{aligned} \tag{11.17}$$

A Taylor expansion in $\frac{B}{\omega_0}$ then gives:

$$\begin{aligned}\mathcal{P}_0\left(\widetilde{\boldsymbol{x_0}}, \widetilde{\boldsymbol{r}_s}, v\right) = \left(\frac{v^2\omega_0^2}{(x_0^{\shortparallel})^2 c_0^2}\right)^{d-2} \frac{B}{(x_0^{\shortparallel})^2} \exp\left(\frac{2i\omega_0}{c_0}\left(r_s^{\shortparallel} - \frac{v^2|\widetilde{\boldsymbol{x_0}}^{\perp}|^2 - |\widetilde{\boldsymbol{x_0}}^{\perp} + \widetilde{\boldsymbol{r}_s}^{\perp}|^2}{2v^2 x_0^{\shortparallel}}\right)\right) \\ \times \operatorname{sinc}\left(\frac{B}{c_0}\left(r_s^{\shortparallel} - \frac{v^2|\widetilde{\boldsymbol{x_0}}^{\perp}|^2 - |\widetilde{\boldsymbol{x_0}}^{\perp} + \widetilde{\boldsymbol{r}_s}^{\perp}|^2}{2x_0^{\shortparallel}}\right)\right) \\ \times \mathcal{G}\left(\frac{a_0\omega_0}{x_0^{\shortparallel} c_0}\widetilde{\boldsymbol{r}_s}^{\perp}, \frac{a_0^2\omega_0}{x_0^{\shortparallel} c_0}(v^2-1)\right)^2 \left(1 + \mathcal{O}\left(\frac{B}{\omega_0}\right)\right).\end{aligned} \tag{11.18}$$

Furthermore, with the change of variable $\widetilde{\boldsymbol{\chi}_s}^{\perp} = \omega_0 \widetilde{\boldsymbol{r}_s}^{\perp}$,

$$\begin{aligned}\operatorname{sinc}\left(\frac{B}{c_0}\left(r_s^{\shortparallel} - \frac{v^2|\widetilde{\boldsymbol{x_0}}^{\perp}|^2 - |\frac{\widetilde{\boldsymbol{\chi}_s}^{\perp}}{\omega_0} + \widetilde{\boldsymbol{x_0}}^{\perp}|^2}{2v^2 x_0^{\shortparallel}}\right)\right) \times \mathcal{G}\left(\frac{a_0}{x_0^{\shortparallel} c_0}\widetilde{\boldsymbol{\chi}_s}^{\perp}, \frac{a_0^2\omega_0}{x_0^{\shortparallel} c_0}(v^2-1)\right)^2 \\ = \operatorname{sinc}\left(\frac{B}{c_0}\left(r_s^{\shortparallel} - \frac{|\widetilde{\boldsymbol{x_0}}^{\perp}|^2}{2v^2 x_0^{\shortparallel}}(v^2-1)\right)\right) \times \mathcal{G}\left(\frac{a_0\omega_0}{x_0^{\shortparallel} c_0}\widetilde{\boldsymbol{r}_s}^{\perp}, \frac{a_0^2\omega_0}{x_0^{\shortparallel} c_0}(v^2-1)\right)^2 \\ \times \left(1 + \mathcal{O}\left(\frac{B}{\omega_0}\right)\right).\end{aligned} \tag{11.19}$$

Finally, with the change of variable $p = \omega_0(v^2 - 1)$ *i.e.* $v^2 = \frac{p}{\omega_0} + 1$,

$$\operatorname{sinc}\left(\frac{B}{c_0} r_s^{\shortparallel} - \frac{B}{\omega_0} \frac{|\widetilde{\boldsymbol{x_0}}^{\perp}|^2}{2c_0 x_0^{\shortparallel}} \frac{p}{\frac{p}{\omega_0} + 1}\right) \times \mathcal{G}\left(\frac{a_0\omega_0}{x_0^{\shortparallel} c_0} \widetilde{\boldsymbol{r_s}}^{\perp}, \frac{a_0^2}{x_0^{\shortparallel} c_0} p\right)^2$$
$$= \operatorname{sinc}\left(\frac{B}{c_0} x_s^{\shortparallel}\right) \times \mathcal{G}\left(\frac{a_0\omega_0}{x_0^{\shortparallel} c_0} \widetilde{\boldsymbol{r_s}}^{\perp}, \frac{a_0^2}{x_0^{\shortparallel} c_0}(v^2 - 1)\right)^2 \left(1 + \mathcal{O}\left(\frac{B}{\omega_0}\right)\right). \quad (11.20)$$

Inserting the approximations (11.19) and (11.20) into (11.18) gives the desired result. □

The results of Theorem 54 indicate that the overall intensity $|\mathcal{I}|$ is lowered when $c_s \neq c_0$. Indeed, the function $\mathcal{G}$ is peak function centered at the origin (see [55, Chapter 6] for an analysis of $\mathcal{G}$). The loss of amplitude on the image can be used to design an estimator of the speed of sound inside the medium. This is the topic of the next section.

11.2 Estimator of the speed of sound

The spatial resolution of an imaging system is defined as its ability to differentiate between two close points. It can be characterized by the typical size of the focal spot of the point spread function. In Theorem 54, we recover the well-known resolutions [55] in axial and transverse directions:

- The axial resolution is $\frac{c_0}{B}$.
- The transverse resolution is $\frac{c_0 x_0^{\shortparallel}}{a_0\omega_0}$.

We also have that the point spread function is centered at $\boldsymbol{x_f}(\boldsymbol{x_0}, v)$, and its amplitude maximum at this point. At this particular point, the point spread function has the form,

$$\mathcal{I}\left(\boldsymbol{x_f}(\boldsymbol{x_0}, \frac{c_0}{c_s}), c_s\right) := \mathcal{P}_c\left(c_s = \frac{c_0}{v}\right)$$
$$:= v^{2(d-2)} \exp\left(\frac{2i\omega_0 |\boldsymbol{x_0}^{\perp}|^2}{2x_0^{\shortparallel} c_0}\left(\frac{v^2 - 1}{v^2}\right)\right) \mathcal{G}\left(0, \frac{a_0^2\omega_0}{x_0^{\shortparallel} c_0}(v^2 - 1)\right)^2. \quad (11.21)$$

Therefore, the behavior of the point spread function with respect to the backpropagation speed is mainly driven by the behavior of

$$\mathcal{G}(0, \beta)^2 = \frac{2^{d+1}}{\beta^{2(d-1)}} \left(C + iS\right)^{2(d-1)} \left(\frac{\sqrt{\beta}}{\sqrt{2}}\right),$$

where C and S are the Fresnel integrals,

$$C(u) := \int_0^u \cos(t^2) dt \quad S(u) := \int_0^u \sin(t^2) dt.$$

We plot in dimension for $d = 2$, the functions $|\mathcal{G}(0,\beta)^2|$ and $\mathrm{Im}(\mathcal{G}(0,\beta)^2)$ on Figure 11.1. $|\mathcal{G}(0,\beta)^2|$ is a peak function which is maximum a $\beta = 0$. Furthermore, $\mathrm{Im}(\mathcal{G}(0,\beta)^2)$ has its steepest slope at $\beta = 0$. This allows to establish two estimators of c_0 that we denote $\hat{c}_1$ and $\hat{c}_2$. They are defined by:

$$\hat{c}_1 := \underset{c_s}{\mathrm{argmax}} \max_{\boldsymbol{x_s}} |\mathcal{I}(\boldsymbol{x_s}, c_s)|, \tag{11.22}$$

and

$$\hat{c}_2 := \underset{c_s}{\mathrm{argmax}} \frac{\partial \mathrm{Im}(\mathcal{I})}{\partial c_s}(\boldsymbol{x}^\star(c_s), c_s) \text{ for } \boldsymbol{x}^\star(c_s) = \underset{x_s}{\mathrm{argmax}} |\mathcal{I}(\boldsymbol{x_s}, c_s)|. \tag{11.23}$$

$\hat{c}_1$ corresponds to the speed of sound that give the highest intensity on the image while $\hat{c}_2$ allows to recover the speed at which occurs shift of the imaginary part of the function in the center of the focal spot. Both estimators allows to recover the true speed of sound c_0. These two estimators are plotted on Figure 13.5 and are commented in Section 13.

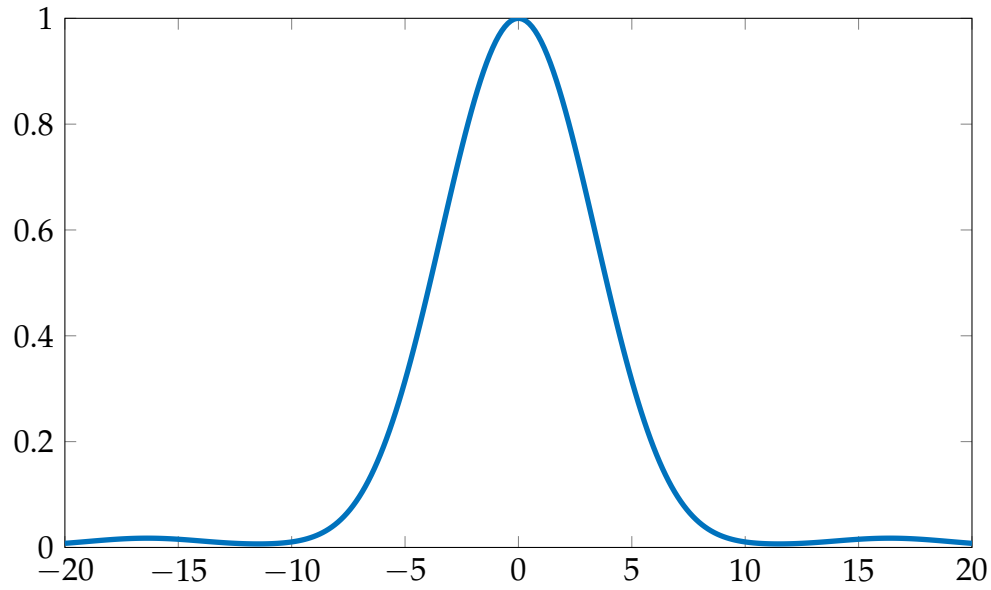

(a) $|\mathcal{G}(0,\beta)^2|$

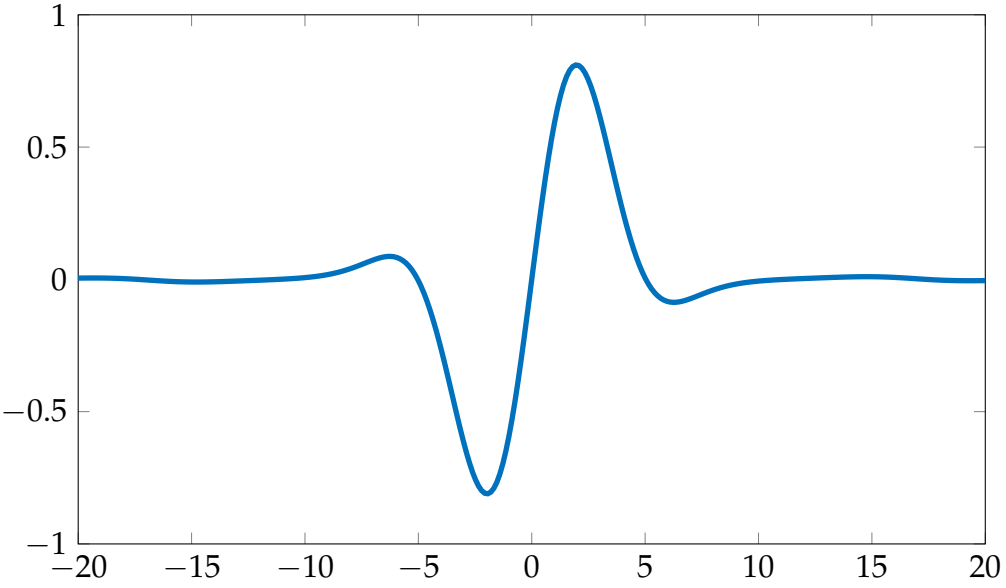

(b) $\mathrm{Im}(\mathcal{G}(0,\beta)^2)$

Figure 11.1: Plots of $|\mathcal{G}(0,\beta)^2|$ and $\mathrm{Im}(\mathcal{G}(0,\beta)^2)$.

CHAPTER 12

Estimation of the speed of sound in tissue mimicking media

In medical ultrasound imaging, the measured backscattered field does not come from isolated target but from a large collection of unresolved scatterers. In this configuration, it is not possible to use the previous estimators to recover the speed of sound c_0. In this section, we study the imaging functional for the model of Section 3.3.1 modeling the biological tissues. We then study the estimators of the effective speed of sound introduced by Aubry in [17]. The main results of this chapter are then Theorem 57, Proposition 59 and Proposition 61. It is well-known in physics that the imaging process consists in focusing a wave at $\boldsymbol{x}$ and imaging a local (virtual) reflector at $\boldsymbol{x}$. If this is true when the backpropagation speed of sound $c_s = c_0$, it is also known that a mismatch $c_s \neq c_0$ induces spatial errors on the image. We recover mathematically these results in Theorem 57 for the model of Section 12.1. Building on the result of Theorem 57, we show in Lemma 58 that the imaging function is locally (at the order of the wavelength) a stationary process. Therefore spatial averages on the image allows to recover statistical data. Proposition 59 and Proposition 61 are asymptotic formulas for respectively the *incoherent* and *coherent* operator introduced by Aubry. The *incoherent* estimator consists in maximizing the (local) spatial average of the amplitude of the imaging function with respect to several speeds of sound. The *coherent* estimator is built upon the first right singular vector in the decomposition of the matrix whose lines are the imaging function of point in a small area of interest and the columns are the several backpropagation speeds to compute these images.

12.1 Model of the medium

We consider the model described in Section 3.3.1 that we quickly recall here. As, the acoustic properties of the medium oscillate rapidly compared to the wavelength we introduce ε which denotes the typical radius of the small heterogeneities inside the medium. In this regime, it holds that

$$\varepsilon \ll \lambda \ll 1.$$

We assume that $\varepsilon = r_0^\alpha$ for some normalized radius r_0 and exponent α which will be discussed in the end of this section. We recall that λ is of typical order $\eta \mathrm{diam}(D)$. The position of the centers of the heterogeneities is random. We introduce the probability space $(\Omega, \mathcal{F}, \mathbb{P})$. We emphasize that the realizations of the random medium are denoted $\varpi \in \Omega$ while the notation $\omega \in \mathcal{B}$ is kept for the angular frequency.
In this Part III, we will only consider fluctuations of the speed of sound around a homogeneous speed c_0. More precisely, we will use the framework of the stochastic homogenization already used in Part II, which is a standard and non-restrictive framework. We thus assume, that n_ε is the realization of a stationary ergodic process (see Section 4.3 for a full definition). We write:

$$n_\varepsilon(\boldsymbol{x}) := \psi\left(\frac{\boldsymbol{x}}{\varepsilon}\right), \text{ for } \boldsymbol{x} \in D \tag{12.1}$$

where $\psi \in L^2(\Omega, L^\infty(\mathbb{R}^d))$, is a zero-mean, measurable, stationary and mixing random field, with covariance function given for all $\boldsymbol{x} \in \mathbb{R}^d$ by

$$\Sigma(\boldsymbol{x}) := \mathrm{Cov}(\psi(\boldsymbol{x}), \psi(0)). \tag{12.2}$$

We specified in Section 4.4.2, the exact mixing assumption, Hypothesis 20, that we consider. We recall that these assumptions imply in particular that $\Sigma \in L^1(\mathbb{R}^d)$ and has exponential decay. The coefficient $n_\varepsilon \in L^2(\Omega, L^\infty(\mathbb{R}^d))$ models the presence of unresolved scatterers. As the physical parameters υ and κ stay positive and finite in biological tissues, it is natural to assume that $-1 < n^- < n < n^+ < \infty$ for some constant n^-, n^+. Moreover, as we consider a bounded zone of interest, we assume $\mathrm{supp}(n) \subset D$. For almost every $\varpi \in \Omega$, the scattered field $u_\varepsilon^s(\boldsymbol{x_e}, \cdot, \omega) \in H^1_{loc}(\mathbb{R}^d)$ for an incident wave $u^i(\boldsymbol{x_e}, \cdot, \omega)$ is then the almost sure unique solution of

$$\begin{cases} -\Delta(u_\varepsilon^s + u^i)(\boldsymbol{x_e}, \cdot, \omega) - \dfrac{\omega^2}{c_0^2}(1 + n_\varepsilon(\cdot))(u_\varepsilon^s + u^i)(\boldsymbol{x_e}, \cdot, \omega) = 0 \quad \text{in } \mathbb{R}^d \setminus \{\boldsymbol{x_e}\}, \\ \lim\limits_{|\boldsymbol{x}|\to\infty} |\boldsymbol{x}|^{\frac{d-1}{2}} \left(\dfrac{\partial}{\partial|\boldsymbol{x}|} u_\varepsilon^s(\boldsymbol{x_e}, \boldsymbol{x}, \omega) - i\dfrac{\omega}{c_0} u_\varepsilon^s(\boldsymbol{x_e}, \boldsymbol{x}, \omega) \right) = 0, \end{cases} \tag{12.3}$$

where $c_0 > 0$ is the unknown background speed of sound. We wish to apply the homogenization results developped in Part II to characterize the total field $u_\varepsilon := u_\varepsilon^s + u^i$. The analysis of the well-posedness of (12.3) is done in Part II with $\omega \in \mathbb{C}$ such that $\mathrm{Im}(\omega) > 0$, and the radiation condition is replaced with a Dirichlet-to-Neumann operator on the ball B_R of radius $R > 0$ that contains D.
For a given $\varepsilon > 0$ and a given $\varpi \in \Omega$, the problem (12.3) is well-posed. However, the difficulty lies in finding a uniform control in ε and ϖ, which is the first step to apply any homogenization techniques. $\mathrm{Im}(\omega) > 0$ ensures the coercivity of the problem, so that the desired uniform bound can be obtained.
We recall the definition of the homogenized total field $u_0 = u^i + u_0^s$ with $u_0^s(\boldsymbol{x_e}, \cdot, \omega) \in$

$H^1_{loc}(\mathbb{R}^d)$ is the solution of

$$\begin{cases} -\Delta(u_0^s + u^i)(\boldsymbol{x_e}, \cdot, \omega) - \dfrac{\omega^2}{c_0^2}(1 + \mathbb{E}[\psi])(u_0^s + u^i)(\boldsymbol{x_e}, \cdot, \omega) = 0 \quad \text{in } \mathbb{R}^d \setminus \{\boldsymbol{x_e}\}, \\ \lim\limits_{|\boldsymbol{x}|\to\infty} |\boldsymbol{x}|^{\frac{d-1}{2}} \left(\dfrac{\partial}{\partial|\boldsymbol{x}|} u_0^s(\boldsymbol{x_e}, \boldsymbol{x}, \omega) - i\dfrac{\omega}{c_0} u_0^s(\boldsymbol{x_e}, \boldsymbol{x}, \omega) \right) = 0. \end{cases} \tag{12.4}$$

With the assumption of zero-mean on ψ, we have in our case that the homogenized field can be written as

$$u_0(\boldsymbol{x_e}, \boldsymbol{x}, \omega) = G^{\frac{\omega}{c_0}}(\boldsymbol{x} - \boldsymbol{x_e}).$$

This hypothesis of zero-mean allows to have explicit results and is non restrictive.

We use the results of Theorem 39 to describe our measurement data. As we assume the coefficient a_ε of (3.11) to be constant equal to 1, the problem simplifies and it holds the following version of Theorem 39:

Proposition 56: Expression of the scattered field in the homogenization regime

For $\boldsymbol{x_e}, \boldsymbol{x_r} \in \mathcal{A}$ and $\omega \in \mathcal{B}$, let

$$U_\varepsilon^s(\boldsymbol{x_e}, \boldsymbol{x_r}, \omega) := \frac{\omega^2}{c_0^2} \int_D \psi_\varepsilon(\boldsymbol{x}) G^{\frac{\omega}{c_0}}(\boldsymbol{x_e} - \boldsymbol{x}) G^{\frac{\omega}{c_0}}(\boldsymbol{x} - \boldsymbol{x_r}) d\boldsymbol{x}. \tag{12.5}$$

Under the assumption that ∂D is regular enough and $\mathrm{Im}(\omega) > 0$, for all $\boldsymbol{x_e}, \boldsymbol{x_r} \in \mathcal{A}$, $\omega := \frac{\tilde{\omega}}{\eta} \in \mathcal{B}$,

$$\begin{aligned} &\|u_\varepsilon^s(\boldsymbol{x_e}, \boldsymbol{x_r}, \omega) - U_\varepsilon^s(\boldsymbol{x_e}, \boldsymbol{x_r}, \omega)\|_{L^2(\Omega)} \\ &\quad \leq C\omega^2 \varepsilon^{\frac{d+1}{2}} \mu_d \left(\frac{1}{\varepsilon}\right)^{\frac{1}{2}} \left\| G^{\frac{\omega}{c_0}}(\cdot - \boldsymbol{x_e}) \right\|_{W^{1,\infty}(D)} \left\| G^{\frac{\omega}{c_0}}(\cdot - \boldsymbol{x_r}) \right\|_{W^{1,\infty}(D)}, \end{aligned} \tag{12.6}$$

where μ_d is defined in (4.50) and for some $C > 0$.

Remark 12.1.1. *We recall that the error term $u_\varepsilon^s - U_\varepsilon^s$ verifies, in view of (7.2):*

$$(u_\varepsilon^s - u_0^s)(\boldsymbol{x_e}, \boldsymbol{x_r}, \omega) = -\frac{\omega^2}{c_0^2} \int_D \psi_\varepsilon(\boldsymbol{x}) u_\varepsilon(\boldsymbol{x_e}, \boldsymbol{x}, \omega) G^{\frac{\omega}{c_0}}(\boldsymbol{x} - \boldsymbol{x_r}) dx. \tag{12.7}$$

We make three observations.

- *The derivative of G^k is not involved in this representation which allows to improve the $W^{2,\infty}(D)$-norm of $G^k(\cdot - \boldsymbol{x_e})$ in Theorem 39 to a $W^{1,\infty}(D)$-norm.*
- *It is clear that the rest $(u_\varepsilon^s - U_\varepsilon^s)(\boldsymbol{x_e}, \boldsymbol{x_r}, \omega)$ is proportional to $\frac{\omega^2}{c_0^2}$.*

- *With the result of Theorem 39, we obtain an estimate of* $Var\left[|u_\varepsilon^s(\boldsymbol{x_e}, \boldsymbol{x_r}, \omega) - U_\varepsilon^s(\boldsymbol{x_e}, \boldsymbol{x_r}, \omega)|\right]^{\frac{1}{2}}$. *However, in view of Lemma 65, the result also holds in the* $L^2(\Omega)$*-norm, as* $\mathbb{E}[u_\varepsilon - u_0] = \mathcal{O}(\varepsilon^d k^6)$ *which is negligible in front of the right hand side of* (12.6).

We recall that by (11.4), for $x \in D$, $\left\| G^{\frac{\omega}{c_0}}(\cdot - \boldsymbol{x}) \right\|^2_{L^\infty(\mathcal{A})} = \mathcal{O}\left(\eta^{3-d}\right)$. It also holds that for $\boldsymbol{x_e} \in \mathcal{A}$, $\left\| G^{\frac{\omega}{c_0}}(\cdot - \boldsymbol{x_e}) \right\|^2_{W^{1,\infty}(D)} = \mathcal{O}\left(\eta^{1-d}\right)$.
The measurement map is now random variable

$$M \in L^2(\Omega, L^2((\mathcal{A} \times \mathcal{A}), L^2(\mathcal{B})))$$

which is then approximated with (12.5) by

$$M(\boldsymbol{x_e}, \boldsymbol{x_r}, \omega) = U_\varepsilon^s(\boldsymbol{x_e}, \boldsymbol{x_r}, \omega) + \eta^{-1-d}\varepsilon^{\frac{d+1}{2}}\mu_d\left(\frac{1}{\varepsilon}\right)^{\frac{1}{2}} R_\varepsilon(\boldsymbol{x_e}, \boldsymbol{x_r}, \omega). \tag{12.8}$$

where the remainder $R_\varepsilon(\boldsymbol{x_e}, \boldsymbol{x_r}, \omega) \in L^2(\Omega)$ is a random that verifies $\|R_\varepsilon(\boldsymbol{x_e}, \boldsymbol{x_r}, \omega)\|_{L^2(\Omega)} \leq C$, for some $C > 0$ independent of $\boldsymbol{x_e}, \boldsymbol{x_r}, \omega$ and ε.

In view of Lemma 64,

$$\|U_\varepsilon^s\|_{L^2(\Omega)} = \eta^{1-d}\varepsilon^{\frac{d}{2}},$$

Therefore, for the model (12.8) to be accurate, it requires to have

$$r_0^{\frac{1}{2}}\eta^{1-d}\varepsilon^{\frac{d}{2}} \geq \eta^{-1-d}\varepsilon^{\frac{d+1}{2}}\mu_d\left(\frac{1}{\varepsilon}\right)^{\frac{1}{2}},$$

which is verified when $\alpha > 4$ in dimension $d = 2$ and $\alpha \geq 4$ in dimension $d = 3$.

We have now a description of the measured data. To study the estimators of the effective speed of sound, we derive an expression of the imaging function when the medium verifies the hypotheses of Section 12.1. This is the subject of the next section.

12.2 Asymptotic analysis of $\mathcal{I}$

We first derive asymptotic results for $\mathcal{I}$, similar to Theorem 54 but which holds for the tissue mimicking medium. We show the following:

Theorem 57: Asymptotic of $\mathcal{I}$

Let $\boldsymbol{x_s} = (\eta^{\frac{1}{2}}\widetilde{\boldsymbol{x}}_{\boldsymbol{s}}^{\perp}, x_s^{\shortparallel}) \in D, c_s \in [c_{\min}, c_{\max}]$. Then the imaging function of (10.6) is approximated almost surely by:

$$\mathcal{I}\left(\boldsymbol{x_s}, c_s = \frac{c_0}{v}\right) \quad = \quad \eta^{d-2} C_a \mathcal{I}_0^M \left(\boldsymbol{x_s}, c_s = \frac{c_0}{v}\right) + \eta^{d-2}\varepsilon^{\frac{d}{2}} R_\varepsilon(\boldsymbol{x_s}, c_s, M). \quad (12.9)$$

The function $\mathcal{I}_0^M$ is defined by:

$$\mathcal{I}_0^M \left(\boldsymbol{x_s}, c_s = \frac{c_0}{v}\right) := \eta^{\frac{d+1}{2}} \int_{B(0,M)} \psi_\varepsilon\left(\boldsymbol{x_f}\left(\boldsymbol{x_s}, \frac{1}{v}\right) + \boldsymbol{s}(\widetilde{\boldsymbol{r}}, v)\right) \times \mathcal{P}_1(\widetilde{\boldsymbol{x_s}}, \widetilde{\boldsymbol{r}}, v) d\widetilde{\boldsymbol{r}}, \quad (12.10)$$

with $\boldsymbol{x_f}\left(\boldsymbol{x_s}, \frac{1}{v}\right) = (\eta^{\frac{1}{2}} v^2 \widetilde{\boldsymbol{x_s}}^{\perp}, \eta v x_s^{\shortparallel})$ and $\boldsymbol{s}(\widetilde{\boldsymbol{r}}, v) = \left(\eta^{\frac{1}{2}} v^2 \widetilde{\boldsymbol{r}}^{\perp}, \eta v r^{\shortparallel}\right) \in \mathbb{R}^d$.
$\mathcal{P}_1 : (\mathbb{R}^d \times \mathbb{R}^d \times \mathbb{R}_+^*) \to \mathbb{C}$ is the point spread function given by

$$\begin{aligned} \mathcal{P}_1\left(\widetilde{\boldsymbol{x_s}}, \widetilde{\boldsymbol{r}}, v\right) := \int_{\mathcal{B}_0} & \left(\frac{\tilde{\omega}^2}{(x_s^{\shortparallel})^2 c_0^2}\right)^{d-2} \frac{1}{v^2 (x_s^{\shortparallel})^2} \\ & \times \exp\left(\frac{2i\tilde{\omega}}{c_0}\left(-v r^{\shortparallel} + \frac{v^2 |\widetilde{\boldsymbol{x_s}}^{\perp}|^2 - v^4 |\widetilde{\boldsymbol{x_s}}^{\perp} + \widetilde{\boldsymbol{r}}^{\perp}|^2}{2 v x_s^{\shortparallel}}\right)\right) \\ & \times \mathcal{G}\left(-\frac{a_0 \tilde{\omega}}{v x_s^{\shortparallel} c_0} \widetilde{\boldsymbol{r}}^{\perp}, \frac{a_0^2 \tilde{\omega}}{v x_s^{\shortparallel} c_0}(v^2 - 1)\right)^2 d\tilde{\omega}. \end{aligned} \quad (12.11)$$

The remainder $R_\varepsilon(\boldsymbol{x_s}, c_s, M) \in L^2(\Omega)$ is a random variable that verifies, $\|R_\varepsilon(\boldsymbol{x_s}, c_s, M)\|_{L^2(\Omega)} \leq C(M)$ with $C(M) \to 0$.

Remark 12.2.1. *In view of Lemma 64 for all $\boldsymbol{x_s}, c_s$,*

$$\left|\mathcal{I}_0^M \left(\boldsymbol{x_s}, c_s = \frac{c_0}{v}\right)\right| = \mathcal{O}(\varepsilon^{\frac{d}{2}})$$

and is bounded in η, which is due to the η-dependency in the oscillations of the coefficient ψ_ε so that the second term of (12.9) is indeed smaller than the first one.

In practice, the number M introduced in the proof corresponds to the full width at half maximum of $\mathcal{P}_1$ and is of the typical order $\max\left(\frac{c_0 x_s^{\shortparallel}}{a_0 \omega_0}, \frac{c_0}{B}\right)$ which are the expected resolution of the imaging system as discussed in Section 11.2.
To image the medium $\boldsymbol{x}$, a wave is focused at $\boldsymbol{x}$ assuming a propagation speed of sound c_s. The point $\boldsymbol{x}$ then scatters the wave and the scattered field allows to compute the image. When the speed of sound is not the actual propagation speed, spatial error can

be seen on the image. Theorem 57 is just a mathematical transcription of this idea. In Theorem 57, we also explicitly obtain the dependency on the error in the backpropagation speed for the medium of Section 12.1 which will be used in Section 12.3 to build an estimator of the effective speed of sound inside the medium. We begin with the proof of Theorem 57

Proof of Theorem 57. Using (12.8), we have for all $\boldsymbol{x_s} \in D$,

$$\mathcal{I}(\boldsymbol{x_s}, c_s) = \int_{\mathcal{B}} \frac{\omega^2}{c_0^2} \int_D \psi_\varepsilon(\boldsymbol{x}) \left(\left\langle G^{\frac{\omega}{c_s}}(\cdot - \boldsymbol{x_s}), G^{\frac{\omega}{c_0}}(\cdot - \boldsymbol{x}) \right\rangle_{\mathcal{A}} \right)^2 d\boldsymbol{x} d\omega$$
$$+ \eta^{-1-d} \varepsilon^{\frac{d+1}{2}} \mu_d \left(\frac{1}{\varepsilon}\right)^{\frac{1}{2}} \int_{\mathcal{A}\times\mathcal{A}\times\mathcal{B}} R_\varepsilon(\boldsymbol{x_e}, \boldsymbol{x_r}, \omega) G^{\frac{\omega}{c_s}}(\boldsymbol{x_e} - \boldsymbol{x_s})$$
$$\times G^{\frac{\omega}{c_s}}(\boldsymbol{x_r} - \boldsymbol{x_s}) d\sigma(\boldsymbol{x_e}) d\sigma(\boldsymbol{x_r}) d\omega. \quad (12.12)$$

We recall that $|\mathcal{A}|^2 = \eta^{d-1} a_0^{2(d-1)} |\mathcal{A}_0|^2$ and $|\mathcal{B}| = B\eta^{-1}$. Furthermore, by (11.4),

$$\left\| G^{\frac{\omega}{c_s}}(\cdot - \boldsymbol{x_s}) \right\|^2_{L^\infty(\mathcal{A})} = \mathcal{O}\left(\eta^{3-d}\right).$$

Therefore, by the the uniform bounds on $\|R_\varepsilon\|_{L^2(\Omega)}$ in $\boldsymbol{x_e}, \boldsymbol{x_r}, \omega$,

$$\left\| \int_{\mathcal{A}\times\mathcal{A}\times\mathcal{B}} R_\varepsilon(\boldsymbol{x_e}, \boldsymbol{x_r}, \omega) G^{\frac{\omega}{c_s}}(\boldsymbol{x_e} - \boldsymbol{x_s}) G^{\frac{\omega}{c_s}}(\boldsymbol{x_r} - \boldsymbol{x_s}) d\sigma(\boldsymbol{x_e}) d\sigma(\boldsymbol{x_r}) d\omega \right\|_{L^2(\Omega)} = \mathcal{O}(\eta).$$

By the change of variable $\omega = \frac{\tilde{\omega}}{\eta}$,

$$\mathcal{I}(\boldsymbol{x_s}, c_s) = \eta^{-3} \int_{\mathcal{B}_0} \frac{\tilde{\omega}^2}{c_0^2} \int_D \psi_\varepsilon(\boldsymbol{x}) F\left(\boldsymbol{x}, \boldsymbol{x_s}, c_0, c_s, \frac{\tilde{\omega}}{\eta}\right)^2 d\boldsymbol{x} d\tilde{\omega}$$
$$+ \eta^{-d} \varepsilon^{\frac{d+1}{2}} \mu_d \left(\frac{1}{\varepsilon}\right)^{\frac{1}{2}} R^1_\varepsilon(\boldsymbol{x_s}, c_s), \quad (12.13)$$

for some random variable $R^1_\varepsilon(\boldsymbol{x_s}, c_s) \in L^2(\Omega)$ uniformly bounded in $\boldsymbol{x_s}$, c_s and ε in $L^2(\Omega)$, and where F is defined in (11.2). Note that in view of the above estimations and (11.2), and Lemma 64,

$$\left\| \int_{\mathcal{B}_0} \frac{\tilde{\omega}^2}{c_0^2} \int_D \psi_\varepsilon(\boldsymbol{x}) F\left(\boldsymbol{x}, \boldsymbol{x_s}, c_0, c_s, \frac{\tilde{\omega}}{\eta}\right)^2 d\boldsymbol{x} d\tilde{\omega} \right\|_{L^2(\Omega)} = \mathcal{O}(\varepsilon^{\frac{d}{2}} \eta^{2-d}).$$

We want to use Lemma 53. However the points in D are not all in the paraxial regime. That is why we will use the result of Lemma 63 (in appendix G), which is an extension Lemma 53 when the points are not in the paraxial regime. We use the asymptotic

expression of F given in Lemma 63 to obtain:

$$\mathcal{I}\left(\boldsymbol{x_s}, c_s = \frac{c_0}{v}\right) = \eta^{2-d}\int_D \frac{\psi_\varepsilon(\boldsymbol{x})}{(|x||x_s|)^{d-1}}\int_{\mathcal{B}_0}\frac{\tilde{\omega}^{2d-4}C_a}{c_0^{2d-4}v^{3-d}}\left(\exp\left(\frac{2i\tilde{\omega}}{c_0\eta}(v|x_s|-|x|)\right)\right.$$
$$\left.\times\,\mathcal{G}\left(\frac{\tilde{\omega}a_0}{\eta^{\frac{1}{2}}c_0}\left(\frac{v\boldsymbol{x_s^\perp}}{|x_s|}-\frac{\boldsymbol{x}^\perp}{|x|}\right),\frac{\tilde{\omega}a_0}{c_0}\left(\frac{v(x_s^{\shortparallel})^2}{|x_s|^3}-\frac{(x^{\shortparallel})^2}{|x|^3}\right)\right)\right)^2$$
$$\times\left(1+\eta^{\frac{1}{2}}\mathcal{O}\left(\frac{\tilde{\omega}(x^{\shortparallel})^2|\boldsymbol{x}^\perp|}{c_0|\boldsymbol{x}|^3}+\frac{\tilde{\omega}v(x_s^{\shortparallel})^2|\boldsymbol{x_s^\perp}|}{c_0|\boldsymbol{x_s}|^5}\right)\right)d\tilde{\omega}d\boldsymbol{x}+\eta^{-d}\varepsilon^{\frac{d+1}{2}}\mu_d\left(\frac{1}{\varepsilon}\right)^{\frac{1}{2}}R_\varepsilon^1(\boldsymbol{x_s},c_s). \tag{12.14}$$

We recall that $\boldsymbol{x_s}$ is in the paraxial regime and thus,

$$\mathcal{I}(\boldsymbol{x_s}, c_s = \frac{c_0}{v}) = \eta^{2-d}\int_D \frac{\psi_\varepsilon(\boldsymbol{x})}{(|x|x_s^{\shortparallel})^{d-1}}\int_{\mathcal{B}_0}\exp\left(\frac{2i\tilde{\omega}}{c_0\eta}\left(vx_s^{\shortparallel}+\eta v\frac{(\widetilde{\boldsymbol{x}}_{\boldsymbol{s}}^\perp)^2}{2x_s^{\shortparallel}}-|x|\right)\right)$$
$$\times\frac{\tilde{\omega}^{2d-4}C_a}{c_0^{2d-4}v^{3-d}}\mathcal{G}\left(\frac{\tilde{\omega}a_0}{\eta^{\frac{1}{2}}c_0}\left(\frac{\eta^{\frac{1}{2}}v\widetilde{\boldsymbol{x}}_{\boldsymbol{s}}^\perp}{x_s^{\shortparallel}}-\frac{\boldsymbol{x}^\perp}{|\boldsymbol{x}|}\right),\frac{\tilde{\omega}a_0}{c_0}\left(\frac{v}{x_s^{\shortparallel}}-\frac{(x^{\shortparallel})^2}{|\boldsymbol{x}|^3}\right)\right)^2$$
$$\times\left(1+\eta^{\frac{1}{2}}\mathcal{O}\left(\frac{(x^{\shortparallel})^2|\boldsymbol{x}^\perp|}{|\boldsymbol{x}|^5}\right)\right)d\tilde{\omega}d\boldsymbol{x}+\eta^{3-d}\varepsilon^{\frac{d}{2}}R_\varepsilon^2(\boldsymbol{x_s},c_s)+\eta^{-d}\varepsilon^{\frac{d+1}{2}}\mu_d\left(\frac{1}{\varepsilon}\right)^{\frac{1}{2}}R_\varepsilon^1(\boldsymbol{x_s},c_s), \tag{12.15}$$

with $R_\varepsilon^2(\boldsymbol{x_s},c_s)\in L^2(\Omega)$ with $\left\|R_\varepsilon^2(\boldsymbol{x_s},c_s)\right\|_{L^2(\Omega)}\leq C$ for some $C>0$.

Even if the main term of (12.15) in an integral which is on the whole domain D, in reality only a small region around the point

$$\boldsymbol{x_f}\left(\boldsymbol{x_s},\frac{1}{v}\right):=\left(v^2\eta^{\frac{1}{2}}\widetilde{\boldsymbol{x}}_s^\perp,vx_s^{\shortparallel}\right)$$

actually contributes to the integral. Indeed, if the point $|\boldsymbol{x}|$ is too far away from the search point $\boldsymbol{x}_f(v)$, *i.e.* does *not* verify

$$\begin{cases}|vx_s^{\shortparallel}-|\boldsymbol{x}||=\mathcal{O}(\eta vx_s^{\shortparallel}),\\ \left|\dfrac{\eta^{\frac{1}{2}}v\widetilde{\boldsymbol{x}}_{\boldsymbol{s}}^\perp}{x_s^{\shortparallel}}-\dfrac{\boldsymbol{x}^\perp}{|\boldsymbol{x}|}\right|=\mathcal{O}\left(\eta^{\frac{1}{2}}\right),\end{cases}$$

then the phase terms

$$\frac{2i\tilde{\omega}}{c_0\eta}\left(vx_s^{\shortparallel}+\eta v\frac{(\widetilde{\boldsymbol{x}}_{\boldsymbol{s}}^\perp)^2}{2x_s^{\shortparallel}}-|x|\right)\text{ and }\frac{\tilde{\omega}a_0}{\eta^{\frac{1}{2}}c_0}\left(\frac{\eta^{\frac{1}{2}}v|\widetilde{\boldsymbol{x}}_{\boldsymbol{s}}^\perp|}{x_s^{\shortparallel}}-\frac{|\boldsymbol{x}^\perp|}{|\boldsymbol{x}|}\right)$$

are arbitrary large and the integral becomes negligible. More precisely, for $M > 0$, we define the domain

$$\mathcal{D}_\eta(\boldsymbol{x}_s, M) := \left\{\boldsymbol{x} \in D,\ |vx_s^{||} - |\boldsymbol{x}|| < M\eta\right\} \cap \left\{\boldsymbol{x} \in D,\ |\eta^{\frac{1}{2}}v^2|\widetilde{\boldsymbol{x}}_{\boldsymbol{s}}^{\perp}| - |\boldsymbol{x}^{\perp}|| < M\eta^{\frac{1}{2}}\right\}$$

then as $\mathcal{G}$ is peak function centered in 0, $\mathcal{I}$ can be approximated by:

$$\begin{aligned}\mathcal{I}(\boldsymbol{x}_{\boldsymbol{s}}, c_s = \frac{c_0}{v}) = \eta^{2-d}\int_{\mathcal{D}_\eta(\boldsymbol{x}_{\boldsymbol{s}},M)} \frac{\psi_\varepsilon(\boldsymbol{x})}{(|x|x_s^{||})^{d-1}} \int_{\mathcal{B}_0} \exp\left(\frac{2i\tilde{\omega}}{c_0\eta}(vx_s^{||} + \eta v\frac{(\widetilde{\boldsymbol{x}}_{\boldsymbol{s}}^{\perp})^2}{2x_s^{||}} - |x|)\right) \\ \times \frac{\tilde{\omega}^{2d-4}C_a}{c_0^{2d-4}v^{3-d}}\mathcal{G}\left(\frac{\tilde{\omega}a_0}{\eta^{\frac{1}{2}}c_0}\left(\frac{\eta^{\frac{1}{2}}v|\widetilde{\boldsymbol{x}}_{\boldsymbol{s}}^{\perp}|}{x_s^{||}} - \frac{|\boldsymbol{x}^{\perp}|}{|\boldsymbol{x}|}\right), \frac{\tilde{\omega}a_0}{c_0}\left(\frac{v}{x_s^{||}} - \frac{(x^{||})^2}{|\boldsymbol{x}|^3}\right)\right)^2 d\tilde{\omega}d\boldsymbol{x} \\ + \varepsilon^{2-d}R_\varepsilon(\boldsymbol{x}_{\boldsymbol{s}}, c_s, M),\end{aligned} \tag{12.16}$$

where the random variable R_ε verifies the desired properties. We almost recognize the point spread function from equation (11.12) with the roles of the variables exchanged: $\boldsymbol{x_s}$ now plays the role of the position of the reflector $\boldsymbol{x_0}$, and the point $\boldsymbol{x}$ the role of the search point $\boldsymbol{x_s}$. Just as before, we expand the imaging functional around the center of the focal spot $\boldsymbol{x_f}(\boldsymbol{x_s}, \frac{1}{v})$ by setting

$$\boldsymbol{x} = \boldsymbol{x_f}\left(\boldsymbol{x_s}, \frac{1}{v}\right) + \boldsymbol{s}(\boldsymbol{r}, v) \in \mathbb{R}^d$$

with $\boldsymbol{s}(\widetilde{\boldsymbol{r}}, v) = (\eta^{\frac{1}{2}}v^2\widetilde{\boldsymbol{r}}^{\perp}, \eta v r^{||})$ for $\widetilde{\boldsymbol{r}} \in \mathbb{R}^d$. By integrating with respect to the variable $\widetilde{\boldsymbol{r}} := (\widetilde{\boldsymbol{r}}_{\boldsymbol{s}}^{\perp}, r_s^{||})$, and a last Taylor expansion with respect to η, we obtain the result (12.9). □

An ultrasound image is a map of the reflectivity of a medium. Here the reflectivity is modeled by n_ε. To compute the imaging function at $\boldsymbol{x_s}$, we focus a wave at $\boldsymbol{x_s}$ and listen to the returning echoes from which we expect to compute $n_\varepsilon(\boldsymbol{x_s})$ or a spatial average of n_ε in a small ball around $\boldsymbol{x_s}$. However, Theorem 54 indicates that this is not exactly the case. If $v \neq 1$, due to the mismatch between the speed of sound of the medium c_0 and the backpropagation speed c_s, we are not focusing the wave at $\boldsymbol{x_s}$, but at $\boldsymbol{x_f}\left(\boldsymbol{x_s}, \frac{1}{v}\right)$ and therefore not listening to the echoes returning from $\boldsymbol{x_s}$. Still, the listened echoes come not only from $\boldsymbol{x_f}\left(\boldsymbol{x_s}, \frac{1}{v}\right)$ but in fact from a small area around it, of typical size $\eta^{\frac{1}{2}}$.
In other words, it means that the focusing of the wave at $\boldsymbol{x_s}$ can be seen as the creation of a (small) virtual reflector centered at $\boldsymbol{x_f}\left(\boldsymbol{x_s}, \frac{1}{v}\right)$ which radiates. The echoes are measured and the averaged reflectivity is computed.
From these observations, our goal is now to identify the speed of sound of the medium. We are able to use the maximum of intensity on the image when we have a real target

inside the medium. However, in this configuration, the image is a random speckle pattern and it is not possible to follow a bright pixel from one image computed with one speed of sound c_s to another. Nevertheless, we show in the next section that following Aubry's work [17], we can extract, via a local spatial averaging and a singular value expansion, coherent signal that allows this virtual reflector to be used as a guide star.

12.3 From spatial averaging to ensemble averaging

By Theorem 57, when we compute the image at $\boldsymbol{x_s}$ with backpropagation speed c_s, we are actually focusing on a virtual reflector at $\boldsymbol{x_f}\left(\boldsymbol{x_s}, \frac{1}{v}\right) = (v^2\eta^{\frac{1}{2}}\widetilde{\boldsymbol{x}}_{\boldsymbol{s}}^{\perp}, vx_s^{||})$. To always focus on one particular chosen point, it is natural to parametrize the points by $\bar{\boldsymbol{x}}_{\boldsymbol{s}}(c_s) = (\eta^{\frac{1}{2}}c_s^2\widetilde{\boldsymbol{\xi}}, c_s t)$ for $t > 0$ and $\widetilde{\boldsymbol{\xi}} \in \mathbb{R}^{d-1}$. By doing so, for a given $\widetilde{\boldsymbol{\xi}} \in \mathbb{R}^{d-1}$ and $t > 0$, the focal spot is always localized at $\boldsymbol{x}_{\widetilde{\boldsymbol{\xi}},t} := (\eta^{\frac{1}{2}}c_0^2\widetilde{\boldsymbol{\xi}}, c_0 t)$. In particular, we always recreate at virtual reflector at the point $\boldsymbol{x}_{\widetilde{\boldsymbol{\xi}},t}$ for every backpropagation speed of sound c_s, and this point is going to be our guide star.
To obtain an estimator of the effective sound speed that does not depend of the random fluctuations, we want to average over several realizations of the medium. However, in practice we only have access to one realization $\mathcal{O}$ of the medium. By Theorem 57, the computation of the imaging function at $\boldsymbol{x}$ corresponds to the computation of the local reflectivity in a neighborhood of $\boldsymbol{x_f}\left(\boldsymbol{x}, \frac{1}{v}\right)$. Intuitively, for two points less than a wavelength apart *i.e.* at scale η, we expect the average reflectivity to not have changed by a lot. However, the displayed images is a speckle pattern due to the random oscillations of the reflectivity which occurs at the typical scale ε. The random oscillations are modeled by a stationary process (which means that the distribution law of the scatterers is invariant by translation). The idea is then to show that the reflectivity map around a point $\boldsymbol{y}$ can be interpreted as the reflectivity map around the point $\boldsymbol{x}$ for a new realization $\mathcal{O}'$ *i.e.* $\mathcal{I}^{\mathcal{O}}(\boldsymbol{y}, c_s) \approx \mathcal{I}^{\mathcal{O}'}(\boldsymbol{x}, c_s)$. We show that this is true at first order in η in Lemma 58. Then, when we are focusing on a series of points $\boldsymbol{y}$ in a small region of interest, it is as if we had access to several realizations of the disorder. Indeed, under the mixing assumption the spatial average of a stationary process over a domain, which is much larger than the typical scale at which the random process oscillates *i.e.* ε, is an approximation of its expectation. It means that we can compute spatial averages of $\mathcal{I}$ to recover averaged quantities. In particular, we show that we can recover the effective speed of sound c_0.
This idea was developed by the team of Alexandre Aubry [17] and is the topic of this section. We define the function $K_{\widetilde{\boldsymbol{\xi}},t}$ by:

$$K_{\widetilde{\boldsymbol{\xi}},t}(\widetilde{\boldsymbol{\Delta\xi}}, \widetilde{\Delta t}, c_s) := \mathcal{I}\left(c_s^2(\eta^{\frac{1}{2}}\widetilde{\boldsymbol{\xi}} + \eta\widetilde{\boldsymbol{\Delta\xi}}), c_s(t + \eta\widetilde{\Delta t}), c_s\right), \tag{12.17}$$

for $\widetilde{\Delta\boldsymbol{\xi}} \in I_{\widetilde{\boldsymbol{\xi}}} := [\widetilde{\boldsymbol{\xi}_-}, \widetilde{\boldsymbol{\xi}_+}]^{d-1}$ and $\widetilde{\Delta t} \in I_t := [-\widetilde{t_-}, \widetilde{t_+}]$. $K_{\widetilde{\boldsymbol{\xi}},t}$ corresponds to the imaging function on a small area of size $\eta I_{\widetilde{\boldsymbol{\xi}}} \times \eta I_t$ around $\boldsymbol{x}_{\widetilde{\boldsymbol{\xi}},t}$. We show in this section, in Lemma 58, that at first order in η, $K_{\widetilde{\boldsymbol{\xi}},t}(\cdot,\cdot,c_s)$ is stationary in the sense of Definition 8. Thanks to its ergodic properties, spatially averaging on a large domain is equivalent to an ensemble average. In particular we show in Proposition 59, that the spatial average of the intensity of the imaging function contains the deterministic information about the homogenized speed of sound that we can use to establish an estimator of the latter.

Lemma 58: Local stationarity of $K_{\widetilde{\boldsymbol{\xi}},t}$

For $M > 0$, $K_{\widetilde{\boldsymbol{\xi}},t}$ defined in (12.17) can be approximated by:

$$K_{\widetilde{\boldsymbol{\xi}},t}(\widetilde{\Delta\boldsymbol{\xi}}, \widetilde{\Delta t}, c_s) = \eta^{2-d} C_a K^M_{\widetilde{\boldsymbol{\xi}},t}(\widetilde{\Delta\boldsymbol{\xi}}, \widetilde{\Delta t}, c_s) + \eta^{2-d}\varepsilon^{\frac{d}{2}} R_{\varepsilon,\widetilde{\boldsymbol{\xi}},t}(\widetilde{\Delta\boldsymbol{\xi}}, \widetilde{\Delta t}, c_s, M). \quad (12.18)$$

The function K^M is defined by,

$$K^M_{\widetilde{\boldsymbol{\xi}},t}(\widetilde{\Delta\boldsymbol{\xi}}, \widetilde{\Delta t}, c_s) := \eta^{\frac{d+1}{2}} \int_{B(0,M)} \psi_\varepsilon(\boldsymbol{x}_{\widetilde{\boldsymbol{\xi}},t} + s(\widetilde{\boldsymbol{r}}, v) + p(\widetilde{\Delta\boldsymbol{\xi}}, \widetilde{\Delta t})) \times \mathcal{P}_1(\widetilde{\boldsymbol{x}}_{\widetilde{\boldsymbol{\xi}},t}, \widetilde{\boldsymbol{r}}, v) d\widetilde{\boldsymbol{r}}, \quad (12.19)$$

with $\boldsymbol{x}_{\widetilde{\boldsymbol{\xi}},t} := (\eta^{\frac{1}{2}} c_0^2 \widetilde{\boldsymbol{\xi}}, c_0 t)$, $s(\widetilde{\boldsymbol{r}}, v) = \left(\eta^{\frac{1}{2}} v^2 \widetilde{\boldsymbol{r}}^\perp, \eta v r^{\shortparallel}\right) \in \mathbb{R}^d$ and $p(\widetilde{\Delta\boldsymbol{\xi}}, \widetilde{\Delta t}) := (\eta c_0^2 \widetilde{\Delta\boldsymbol{\xi}}, \eta c_0 \widetilde{\Delta t})$ and the remainder $R_{\varepsilon,\widetilde{\boldsymbol{\xi}},t}(\widetilde{\Delta\boldsymbol{\xi}}, \widetilde{\Delta t}, c_s, M) \in L^2(\Omega)$ is a random variable that verifies $\left\| R_{\varepsilon,\widetilde{\boldsymbol{\xi}},t} \right\|_{L^2(\Omega)} \leq C(M)$ with $C(M) \xrightarrow[M\to\infty]{} 0$. In particular, $K^M_{\widetilde{\boldsymbol{\xi}},t}(\cdot,\cdot,c_s)$ is stationary in the sense of Definition 8.

Proof. By definition (12.17) and the asymptotic formula of Theorem 57,

$$K_{\widetilde{\boldsymbol{\xi}},t}(\widetilde{\Delta\boldsymbol{\xi}}, \widetilde{\Delta t}, c_s) = \eta^{\frac{5-d}{2}} C_a \int_{B(0,M)} \psi_\varepsilon(\boldsymbol{x}_{\widetilde{\boldsymbol{\xi}},t} + s(\widetilde{\boldsymbol{r}}, v) + p(\widetilde{\Delta\boldsymbol{\xi}}, \widetilde{\Delta t})) \times \mathcal{P}_1\left(\widetilde{\boldsymbol{x}}_{\widetilde{\boldsymbol{\xi}},t} + (\eta^{\frac{1}{2}}\widetilde{\Delta\boldsymbol{\xi}}, \eta\widetilde{\Delta t}), \widetilde{\boldsymbol{r}}, v\right) d\widetilde{\boldsymbol{r}} + \eta^{2-d}\varepsilon^{\frac{d}{2}} R_{\varepsilon,\widetilde{\boldsymbol{\xi}},t}(\widetilde{\Delta\boldsymbol{\xi}}, \widetilde{\Delta t}, c_s, M), \quad (12.20)$$

for a random variable $R_{\widetilde{\boldsymbol{\xi}},t}(\widetilde{\Delta\boldsymbol{\xi}}, \widetilde{\Delta t}, c_s, M, \varepsilon)$ with the desired properties. A Taylor expansion in η inside $\mathcal{P}_1$ yields the result and the remainder is estimated by applying Lemma 64. □

Therefore, building on the result of Lemma 58, we can use the ergodicity property of $K^M_{\widetilde{\boldsymbol{\xi}},t}(\cdot,\cdot,c_s)$ via the Birkhoff ergodic Theorem 10 and the mixing Hypothesis 20. In particular, we can spatially average $K^M_{\widetilde{\boldsymbol{\xi}},t}(\cdot,\cdot,c_s)$ to average in the probability space. We recall that we aim to recover the effective speed of sound.

The first idea to recover the speed of sound, using the ergodicity property is then to sum the amplitude of the imaging function over several close points. This corresponds to the *incoherent* estimator introduced by Aubry [17].
We thus introduce $C(\boldsymbol{\xi}, t, c_s)^2$ the local average of the intensity of the imaging function defined by

$$C(\widetilde{\boldsymbol{\xi}}, t, c_s)^2 := \int_{I_{\widetilde{\boldsymbol{\xi}}} \times I_t} |K_{\widetilde{\boldsymbol{\xi}},t}(\widetilde{\boldsymbol{\Delta\xi}}, \widetilde{\Delta t}, c_s)|^2 d\widetilde{\boldsymbol{\Delta\xi}} d\widetilde{\Delta t}. \tag{12.21}$$

In the following Proposition 59, we prove an asymptotic form of this local average. We show the following:

Proposition 59: Local average of the intensity of $\mathcal{I}$

For $M > 0$, $c_s \in [c_{\min}, c_{\max}]$, $\widetilde{\boldsymbol{\xi}} \in \mathbb{R}^d$ and $t > 0$,

$$C(\widetilde{\boldsymbol{\xi}}, t, c_s)^2 = \eta^{4-2d} \varepsilon^d C_a^2 C^M(\widetilde{\boldsymbol{\xi}}, t, c_s)^2 + \eta^{4-2d} \varepsilon^d R_\varepsilon(\widetilde{\boldsymbol{\xi}}, t, c_s, M) \tag{12.22}$$

with

$$C^M(\widetilde{\boldsymbol{\xi}}, t, c_s)^2 := \left(\int_{\mathbb{R}^d} \Sigma(\boldsymbol{z}) d\boldsymbol{z} \right) \times \int_{B(0,M)} \left| v^{-2d+1} \mathcal{P}_1(\boldsymbol{x}_{\widetilde{\boldsymbol{\xi}},t}, \boldsymbol{r}, v) \right|^2 d\boldsymbol{r}. \tag{12.23}$$

Σ is the covariance function of ψ defined in (12.2), and the remainder $R_\varepsilon(\widetilde{\boldsymbol{\xi}}, t, c_s, M) \in L^1(\Omega)$ verifies, $\left\| R_\varepsilon(\widetilde{\boldsymbol{\xi}}, t, c_s, M) \right\|_{L^1(\Omega)} \leq C(M)$ with $C(M) \xrightarrow[M \to \infty]{} 0$.

In the narrowband case, the expression of C^M is explicit:

Corollary 60: Narrowband approximation of C

(Narrowband signal) Assume that $B \ll \omega_0$,

$$C^M(\widetilde{\boldsymbol{\xi}}, t, c_s)^2 = \left(\int_{\mathbb{R}^d} \Sigma(\boldsymbol{z}) d\boldsymbol{z} \right) \mathcal{H}^M\left(\boldsymbol{x}_{\widetilde{\boldsymbol{\xi}},t}, v \right)^2 + \frac{B}{\omega_0} R(\widetilde{\boldsymbol{\xi}}, t, c_s, M). \tag{12.24}$$

$\mathcal{H}^M$ is the peak function defined by,

$$\mathcal{H}^M(\boldsymbol{x}_{\widetilde{\boldsymbol{\xi}},t},v)^2 := \left(\frac{\omega_0^4}{c_0^8t^4}\right)^{d-2}\frac{1}{v^2c_0^4t^4}\int_{B(0,M)}\left|\mathrm{sinc}\left(\frac{B}{c_0}vr^{\shortparallel}\right)\right|^2 \times\left|\mathcal{G}\left(-\frac{a_0\omega_0}{c_0^2t}\widetilde{\boldsymbol{r}}^{\perp},\frac{a_0^2\omega_0}{c_0^2t}(v^2-1)\right)\right|^4 d\boldsymbol{r}, \quad (12.25)$$

and the (deterministic) remainder $R(\widetilde{\boldsymbol{\xi}},t,c_s,M)$ is uniformly bounded in $\widetilde{\boldsymbol{\xi}}$, t and c_s.

Remark 12.3.1. *Corollary 60 is written to keep a local estimator in the sense that we work at a given $\boldsymbol{\xi}\in\mathbb{R}^{d-1}$ and $t>0$ and recover the local speed of sound at $\boldsymbol{x}_{\widetilde{\boldsymbol{\xi}},t}$. However, in our study, the random distribution of the reflectivity is spatially invariant everywhere. We can get explicit formulas, by approximating in the definition the peak function $\mathcal{H}^M$ the integral on $B(0,M)$ by the integral over $\mathbb{R}^d$ to get the following $C_{\mathcal{H}}\mathcal{H}\left(\frac{a_0^2\omega_0}{c_0^2x_s^{\shortparallel}}(v^2-1)\right)$, where $\mathcal{H}$ is the normalized peak function defined by:*

$$\mathcal{H}(\beta)^2 := \left(\frac{2}{3\pi}\right)^{d-1}\int_{\mathbb{R}^{d-1}}\left|\mathcal{G}\left(\widetilde{\boldsymbol{z}}^{\perp},\beta\right)\right|^4 d\widetilde{\boldsymbol{z}}^{\perp}, \quad (12.26)$$

and

$$C_{\mathcal{H}} := \frac{\pi}{vBc_0^3t^4}\left(\frac{v^4\omega_0^4}{c_0^8t^4}\right)^{d-2}\left(\frac{c_0^2t}{a_0\omega_0}\frac{3\pi}{2}\right)^{d-1}.$$

The result (12.26) is obtained by Lebesgue's dominated convergence theorem applied to the integral on $r^{\shortparallel}$ of the right hand side of (12.25), analytically integrating this integral over $r^{\shortparallel}\in\mathbb{R}$, and by the change of variable $\widetilde{\boldsymbol{z}}^{\perp}=\frac{a_0\omega_0}{c_0^2t}\widetilde{\boldsymbol{r}}^{\perp}$.

Proof of Proposition 59. We have by Lemma 58,

$$C(\widetilde{\boldsymbol{\xi}},t,c_s)^2 = \eta^{4-2d}\int_{I_{\widetilde{\boldsymbol{\xi}}}\times I_t}\left|C_aK^M_{\widetilde{\boldsymbol{\xi}},t}(\widetilde{\boldsymbol{\Delta\xi}},\widetilde{\Delta t},c_s)+\varepsilon^{\frac{d}{2}}R_{\varepsilon,\widetilde{\boldsymbol{\xi}},t}(\widetilde{\boldsymbol{\Delta\xi}},\widetilde{\Delta t},c_s,M)\right|^2 d\widetilde{\boldsymbol{\Delta\xi}}d\widetilde{\Delta t}$$

Note that $\mathcal{P}_1(\widetilde{\boldsymbol{x}}_{\widetilde{\boldsymbol{\xi}},t},\cdot,v)\in\mathcal{C}^1(\mathbb{R}^d)$, so that we obtain by Lemma 64:

$$\mathbb{E}\left[|K^M_{\widetilde{\boldsymbol{\xi}},t}(0,0,c_s)|^2\right] = v^{-2d+1}\left(\int_{\mathbb{R}^d}\varepsilon^d\Sigma(\boldsymbol{z})d\boldsymbol{z}\right)\times\int_{B(0,M)}\left|\mathcal{P}_1(\widetilde{\boldsymbol{x}}_{\widetilde{\boldsymbol{\xi}},t},\widetilde{\boldsymbol{r}},v)\right|^2 d\widetilde{\boldsymbol{r}} + \frac{\varepsilon^{d+1}}{\eta}R(\widetilde{\boldsymbol{\xi}},t,c_s,M), \quad (12.27)$$

for some (deterministic) remainder $R(\widetilde{\boldsymbol{\xi}}, t, c_s, M)$ uniformly bounded in $\widetilde{\boldsymbol{\xi}}$, t, and c_s. Therefore, we have for fixed $\widetilde{\boldsymbol{\xi}}$ and t by Theorem 10 and the quantitative mixing hypothesis Hypothesis 20,

$$C(\widetilde{\boldsymbol{\xi}}, t, c_s)^2 \quad = \quad \eta^{4-2d} C_a^2 |I_{\widetilde{\xi}}||I_t| \mathbb{E}\left[|K^M{}_{\widetilde{\boldsymbol{\xi}},t}(0,0,c_s)|^2\right] + \eta^{4-2d}\varepsilon^d R_\varepsilon^1(\widetilde{\boldsymbol{\xi}}, t, c_s, M) \quad (12.28)$$

for some remainder random variable $R_\varepsilon^1(\widetilde{\boldsymbol{\xi}}, t, c_s, M) \in L^1(\Omega)$ that verifies the required properties. □

Proof of Corollary 60. Following the proof of Corollary 55, we have in the narrowband case that,

$$\mathcal{P}_1(\widetilde{\boldsymbol{x}}_{\widetilde{\boldsymbol{\xi}},t}, \widetilde{\boldsymbol{r}}, v) = \left(\frac{\omega_0^2 v^2}{t^2 c_0^4}\right)^{d-2} \frac{1}{c_0^2 t^2} \exp\left(\frac{2i\omega_0}{c_0}\left(-vr^{\shortparallel} + \frac{|c_0^2\widetilde{\boldsymbol{\xi}}|^2 - v^2|c_0^2\widetilde{\boldsymbol{\xi}} + v^2\widetilde{\boldsymbol{r}}^{\perp}|^2}{2v^2 c_0 t}\right)\right)$$
$$\times \operatorname{sinc}\left(\frac{B}{c_0} v r^{\shortparallel}\right) \times \mathcal{G}\left(\frac{a_0\omega_0}{c_0^2 t}\widetilde{\boldsymbol{r}}^{\perp}, \frac{a_0^2\omega_0}{c_0^2 t}\left(v^2 - 1\right)\right)^2 + \frac{B}{\omega_0} R^1_{\widetilde{\boldsymbol{\xi}},t}(\boldsymbol{r}), \quad (12.29)$$

for some (deterministic) remainder $R^1_{\widetilde{\boldsymbol{\xi}},t}(\boldsymbol{r}) \in L^2(B(0,M))$. Equation (12.24) is then obtained by integrating the square of (12.29). □

As $v \mapsto \mathcal{P}_1(\cdot,\cdot,v)$ defined by (12.11) is a peak function (maximum for $v = 1$), we have that $C(\widetilde{\boldsymbol{\xi}}, t, c_s)$ is maximum for $c_s = c_0$ by Proposition 59. We can then recover c_0 by the following estimator:

$$\hat{c}_3(\boldsymbol{x}_{\widetilde{\xi},t}) = \operatorname*{argmax}_{c_s} C(\widetilde{\boldsymbol{\xi}}, t, c_s). \quad (12.30)$$

We plot $C(\widetilde{\boldsymbol{\xi}}, t, c_s)$ on Figure 13.8a.
In the narrowband setup, the behavior of C is driven by $\mathcal{H}^M(\boldsymbol{x}_{\widetilde{\boldsymbol{\xi}},t})$. This peak function is very similar to $|\mathcal{G}(0,\beta)|^4$.
However, as we considered the average of the amplitude of the function, we have lost all the information about the imaginary part of $\mathcal{G}(0,\beta)$ that we previously used in (11.23) and which displays a better resolution as the width of peak is narrower (see Figure 13.5). This explains why the *incoherent* estimator $\hat{c}_3$ established in [17] by Alexandre Aubry and his team was improved to a *coherent* estimator by applying a singular value decomposition (SVD) to the kernel operator with kernel $K_{\widetilde{\boldsymbol{\xi}},t}$. This is the subject of the next section.
We also point out that for technical reasons, we considered a medium in which the underlying homogenized speed of sound is constant and does not depend on the position $\boldsymbol{x}_{\widetilde{\xi},t}$. However, we explicit the dependency to $\boldsymbol{x}_{\widetilde{\xi},t}$ as we could extend the theoretical results to a more complex speed of sound map.

12.4 Singular value expansion of K

When we have a medium with a target, we can use the maximum of the derivative of the imaginary part at the brightest pixel to recover the speed of sound. By focusing at $\boldsymbol{x_s}(c_s) = (c_s^2\eta^{\frac{1}{2}}\widetilde{\boldsymbol{\xi}}, c_s t)$ for some $\widetilde{\boldsymbol{\xi}} \in \mathbb{R}^{d-1}$ and $t > 0$, we create a virtual target at $\boldsymbol{x}_{\widetilde{\boldsymbol{\xi}},t}$ and the position of this target does not depend on the input backpropagting speed of sound as proven in Theorem 57. By spatially averaging the imaging function in a small area, we obtain deterministic information about the medium as proven in Lemma 58. We show in this section that we are able to recover the coherent and deterministic information about the imaginary part of $\mathcal{G}$ by considering another type of average of $K_{\widetilde{\boldsymbol{\xi}},t}$ defined by (12.17) via a singular value decomposition.
This heuristic was put in practice by Alexandre Aubry and his team and he experimentally showed in [17] that the first right singular vector V of the kernel operator $\mathcal{R}_{\widetilde{\boldsymbol{\xi}},t} : L^2([c_{\min}, c_{\max}] \to L^2(I_{\widetilde{\boldsymbol{\xi}}} \times I_{\widetilde{t}})$ with kernel $K_{\widetilde{\boldsymbol{\xi}},t}$, is such that $\frac{\partial \mathrm{Im}(V)}{\partial c_s}(c_s)$ is maximal when $c_s = c_0$. The operator $\mathcal{R}_{\widetilde{\boldsymbol{\xi}},t}$ is defined by:

$$\mathcal{R}_{\widetilde{\boldsymbol{\xi}},t} : \begin{cases} L^2([c_{\min}, c_{\max}]) & \longrightarrow & L^2(I_{\widetilde{\boldsymbol{\xi}}} \times I_t) \\ f & \longmapsto & (\mathcal{R}_{\widetilde{\boldsymbol{\xi}},t} f)(\widetilde{\boldsymbol{\Delta\xi}}, \widetilde{\Delta t}) = \displaystyle\int_{[c_{\min}, c_{\max}]} K_{\widetilde{\boldsymbol{\xi}},t}(\widetilde{\boldsymbol{\Delta\xi}}, \widetilde{\Delta t}, c) f(c) dc. \end{cases} \tag{12.31}$$

We propose here to theoretically prove the result of Aubry. First, note that $\mathcal{R}_{\widetilde{\boldsymbol{\xi}},t}$ is a Hilbert-Schmidt integral operator as $K_{\widetilde{\boldsymbol{\xi}},t}(\widetilde{\boldsymbol{\Delta\xi}}, \widetilde{\Delta t}, c) \in L^2((I_{\widetilde{\boldsymbol{\xi}}} \times I_{\widetilde{t}}) \times [c_{\min}, c_{\max}])$. Indeed, $K_{\widetilde{\boldsymbol{\xi}},t}$ depends on $\widetilde{\boldsymbol{\Delta\xi}}, \widetilde{\Delta t}$ and c only via the Green function which is uniformly bounded. A singular value decomposition (SVD) can thus be performed (see *e.g.* [190]). The right singular vectors of $\mathcal{R}_{\widetilde{\boldsymbol{\xi}},t}$ are the eigenvectors of $\mathcal{S}_{\widetilde{\boldsymbol{\xi}},t} : L^2([c_{\min}, c_{\max}]) \to L^2([c_{\min}, c_{\max}])$ defined by

$$\mathcal{S}_{\widetilde{\boldsymbol{\xi}},t} := \mathcal{R}^*_{\widetilde{\boldsymbol{\xi}},t} \mathcal{R}_{\widetilde{\boldsymbol{\xi}},t},$$

where $\mathcal{R}^*_{\widetilde{\boldsymbol{\xi}},t}$ is the adjoint of $\mathcal{R}_{\widetilde{\boldsymbol{\xi}},t}$. We show in this section, that $\mathcal{S}_{\widetilde{\boldsymbol{\xi}},t}$ at first order in η is the kernel operator with kernel

$$\mathbb{E}[\overline{K}_{\widetilde{\boldsymbol{\xi}},t}(0,0,c_1) K_{\widetilde{\boldsymbol{\xi}},t}(0,0,c_2)]$$

for $c_1, c_2 \in [c_{\min}, c_{\max}]$. For a given $\widetilde{\boldsymbol{\xi}} \in \mathbb{R}^{d-1}$ and $t > 0$, $C(\widetilde{\boldsymbol{\xi}}, t, \cdot)$ introduced in (12.21) corresponds to the diagonal of $\mathcal{S}_{\widetilde{\boldsymbol{\xi}},t}$. We show that the eigenvectors of $\mathcal{S}_{\widetilde{\boldsymbol{\xi}},t}$ can be used to estimate c_0. To that aim, we first carry an asymptotic analysis of $\mathcal{S}_{\widetilde{\boldsymbol{\xi}},t}$:

Proposition 61: Asymptotic of $\mathcal{S}_{\widetilde{\boldsymbol{\xi}},t}$

For $M > 0$, $\mathcal{S}_{\widetilde{\boldsymbol{\xi}},t} : L^2([c_{\min}, c_{\max}]) \to L^2([c_{\min}, c_{\max}])$ can be approximated by

$$|||\mathcal{S}_{\widetilde{\boldsymbol{\xi}},t} - \eta^{4-2d}\varepsilon^d \mathcal{S}^M{}_{\widetilde{\boldsymbol{\xi}},t}||| \leq \eta^{4-2d}\varepsilon^d R_\varepsilon(\widetilde{\boldsymbol{\xi}}, t, M) \tag{12.32}$$

with $\mathcal{S}^M_{\widetilde{\boldsymbol{\xi}},t} : L^2([c_{\min}, c_{\max}]) \to L^2([c_{\min}, c_{\max}])$ defined for $f \in L^2([c_{\min}, c_{\max}])$ by

$$\begin{aligned}(\mathcal{S}^M_{\widetilde{\boldsymbol{\xi}},t} f)(c_s) := C_a^2 \left(\int_{\mathbb{R}^d} \Sigma(\boldsymbol{z}) d\boldsymbol{z}\right) \int_{[c_{\min}, c_{\max}]} f(c) \\ \times \frac{c^{2d-1} c_s^{2d-1}}{c_0^{4d-2}} \int_{B(0, \frac{c_0}{c_s}M) \cap B(0, \frac{c_0}{c}M)} \overline{\mathcal{P}_1}\left(\widetilde{\boldsymbol{x}}_{\widetilde{\boldsymbol{\xi}},t}, \boldsymbol{s}\left(\widetilde{\boldsymbol{r}}, \frac{c_0}{c_s}\right), \frac{c_0}{c_s}\right) \\ \times \mathcal{P}_1\left(\widetilde{\boldsymbol{x}}_{\widetilde{\boldsymbol{\xi}},t}, \boldsymbol{s}\left(\widetilde{\boldsymbol{r}}, \frac{c_0}{c}\right), \frac{c_0}{c}\right) d\widetilde{\boldsymbol{r}} dc\end{aligned} \tag{12.33}$$

with $\boldsymbol{s}(\widetilde{\boldsymbol{r}}, v) = (v^2 \widetilde{\boldsymbol{r}^\perp}, v r^{||})$ and the remainder $R_\varepsilon(\widetilde{\boldsymbol{\xi}}, t, M) \in L^1(\Omega)$ is a random variable that verifies, $\left\| R_\varepsilon(\widetilde{\boldsymbol{\xi}}, t, M) \right\|_{L^1(\Omega)} \leq C(M)$ with $C(M) \xrightarrow[M\to\infty]{} 0$.

When the source term has a narrow bandwidth, $\mathcal{S}^M_{\widetilde{\boldsymbol{\xi}},t}$ has a form:

Corollary 62: Narrowband asymptotic of $\mathcal{S}_{\widetilde{\boldsymbol{\xi}},t}$

(Narrowband signal) Assume that $B \ll \omega_0$, then it holds

$$|||\mathcal{S}^M{}_{\widetilde{\boldsymbol{\xi}},t} - \widetilde{\mathcal{S}^M}_{\widetilde{\boldsymbol{\xi}},t}||| \leq \frac{B}{\omega_0} R(\widetilde{\boldsymbol{\xi}}, t, M) \tag{12.34}$$

where

$$(\widetilde{\mathcal{S}^M}_{\widetilde{\boldsymbol{\xi}},t} f)(c_s) = C_a^2 \left(\int_{\mathbb{R}^d} \Sigma(\boldsymbol{z}) d\boldsymbol{z}\right) \times \int_{[c_{\min}, c_{\max}]} f(c) \mathcal{L}^M\left(\widetilde{\boldsymbol{x}}_{\widetilde{\boldsymbol{\xi}},t}, \frac{c_0}{c}, \frac{c_0}{c_s}\right) dc. \tag{12.35}$$

$\mathcal{L}^M$ is the kernel defined by,

$$\mathcal{L}^M(\widetilde{\boldsymbol{x}}_{\widetilde{\boldsymbol{\xi}},t}, v_1, v_2) := \left(\frac{\omega_0^4}{c_0^8 t^4}\right)^{d-2} \frac{1}{v_1 v_2 c_0^4 t^4}$$
$$\times \int_{B(0,\frac{c_0}{c_s}M)\cap B(0,\frac{c_0}{c}M)} \exp\left(\frac{2i\omega_0}{c_0}\left(\frac{|c_0^4\widetilde{\boldsymbol{\xi}} + \widetilde{\boldsymbol{r}}^{\perp}|^2 - |c_0^4\widetilde{\boldsymbol{\xi}} + \widetilde{\boldsymbol{r}}^{\perp}|^2}{2c_0 t}\right)\right)$$
$$\times \operatorname{sinc}\left(\frac{B}{c_0} r^{\shortparallel}\right)^2$$
$$\times \overline{\mathcal{G}}\left(-\frac{a_0\omega_0}{c_0^2 t} v_1^2 \widetilde{\boldsymbol{r}}^{\perp}, \frac{a_0^2\omega_0}{c_0^2 t}(v_1^2 - 1)\right)^2 \mathcal{G}\left(-\frac{a_0\omega_0}{c_0^2 t} v_2^2 \widetilde{\boldsymbol{r}}^{\perp}, \frac{a_0^2\omega_0}{c_0^2 t}(v_2^2 - 1)\right)^2 d\widetilde{\boldsymbol{r}}, \quad (12.36)$$

and the (deterministic) remainder $R(\widetilde{\boldsymbol{\xi}}, t, M)$ is uniformly bounded in $\widetilde{\boldsymbol{\xi}}$ and t.

$\mathcal{R}_{\widetilde{\boldsymbol{\xi}},t}$ corresponds a matrix whose rows are the imaging function for points in a neighborhood (of the order of the wavelength) of $\boldsymbol{x}_{\widetilde{\boldsymbol{\xi}},t}$ and whose columns are the back-propagation speeds of sound c_s at which the imaging functional is computed. The *coherent* estimator of Aubry is built upon the first right singular of this matrix $\mathcal{R}_{\widetilde{\boldsymbol{\xi}},t}$. In Proposition 61, we obtain an asymptotic form of for $\mathcal{S}_{\widetilde{\boldsymbol{\xi}},t} = \mathcal{R}^*_{\widetilde{\boldsymbol{\xi}},t}\mathcal{R}_{\widetilde{\boldsymbol{\xi}},t}$. The *coherent* estimator is then the maximum of amplitude of the first eigenvector of $\mathcal{S}_{\widetilde{\boldsymbol{\xi}},t}$. The asymptotic form of Proposition 61 is numerically computed and we numerically show in Section 13 that its first eigenvector can indeed be used to recover the effective speed of sound.

Proof of Proposition 61. We first show that the adjoint $\mathcal{R}^*_{\widetilde{\boldsymbol{\xi}},t} : L^2(I_{\widetilde{\boldsymbol{\xi}}} \times I_t) \to L^2([c_{\min}, c_{\max}])$ is defined by

$$(\mathcal{R}^*_{\widetilde{\boldsymbol{\xi}},t} g)(c_s) := \int_{I_{\widetilde{\boldsymbol{\xi}}}\times I_t} \overline{K}_{\widetilde{\boldsymbol{\xi}},t}(\widetilde{\boldsymbol{\Delta\xi}}, \widetilde{\Delta t}, c_s) g(\widetilde{\boldsymbol{\Delta\xi}}, \widetilde{\Delta t}) d\widetilde{\boldsymbol{\Delta\xi}} d\widetilde{\Delta t}. \quad (12.37)$$

Indeed, we have for $f \in L^2([c_{\min}, c_{\max}])$, $g \in L^2(I_{\widetilde{\boldsymbol{\xi}}} \times I_t)$,

$$\begin{aligned}\left\langle \mathcal{R}_{\widetilde{\boldsymbol{\xi}},t} f, g\right\rangle_{L^2(I_{\widetilde{\boldsymbol{\xi}}}\times I_t)} &= \int_{[c_{\min},c_{\max}]} f(c)\left(\int_{I_{\widetilde{\boldsymbol{\xi}}}\times I_t} K_{\widetilde{\boldsymbol{\xi}},t}(\widetilde{\boldsymbol{\Delta\xi}}, \widetilde{\Delta t}, c)\overline{g}(\widetilde{\boldsymbol{\Delta\xi}}, \widetilde{\Delta t}) d\widetilde{\boldsymbol{\Delta\xi}} d\widetilde{\Delta t}\right) dc \\ &= \left\langle f, \mathcal{R}^*_{\widetilde{\boldsymbol{\xi}},t} g\right\rangle_{L^2([c_{\min},c_{\max}])}.\end{aligned}$$

$\mathcal{S}_{\widetilde{\boldsymbol{\xi}},t} : L^2([c_{\min}, c_{\max}]) \to L^2([c_{\min}, c_{\max}])$ is then defined by

$$(\mathcal{S}_{\widetilde{\boldsymbol{\xi}},t} f)(c_s) := \int_{[c_{\min},c_{\max}]}\left(\int_{I_{\widetilde{\boldsymbol{\Delta\xi}}}\times I_{\widetilde{\Delta t}}} \overline{K}_{\widetilde{\boldsymbol{\xi}},t}(\widetilde{\boldsymbol{\Delta\xi}}, \widetilde{\Delta t}, c_s) K_{\widetilde{\boldsymbol{\xi}},t}(\widetilde{\boldsymbol{\Delta\xi}}, \widetilde{\Delta t}, c) d\widetilde{\boldsymbol{\Delta\xi}} d\widetilde{\Delta t}\right) f(c) dc. \quad (12.38)$$

We proceed as in the proof of Proposition 59. First, by Lemma 58,

$$K_{\widetilde{\boldsymbol{\xi}},t}(\widetilde{\boldsymbol{\Delta\xi}},\widetilde{\Delta t},c)=\eta^{4-2d}\left(C_a K^M{}_{\widetilde{\boldsymbol{\xi}},t}(\widetilde{\boldsymbol{\Delta\xi}},\widetilde{\Delta t},c)+\varepsilon^{\frac{d}{2}}R_{\varepsilon,\widetilde{\boldsymbol{\xi}},t}(\widetilde{\boldsymbol{\Delta\xi}},\widetilde{\Delta t},c_s,M)\right). \tag{12.39}$$

Moreover, by Lemma 64,

$$\begin{aligned}\mathbb{E}\left[\overline{K^M}_{\widetilde{\boldsymbol{\xi}},t}(0,0,c_s)K^M_{\widetilde{\boldsymbol{\xi}},t}(0,0,c)\right]&=\frac{c^{2d-1}c_s^{2d-1}}{c_0^{4d-2}}\varepsilon^d\left(\int_{\mathbb{R}^d}\Sigma(\boldsymbol{z})d\boldsymbol{z}\right)\\&\times\int_{B(0,\frac{c_0}{c_s}M)\cap B(0,\frac{c_0}{c}M)}\overline{\mathcal{P}_1}\left(\widetilde{\boldsymbol{x}}_{\widetilde{\boldsymbol{\xi}},t},\boldsymbol{s}\left(\widetilde{\boldsymbol{r}},\frac{c_s}{c_0}\right),\frac{c_0}{c_s}\right)\mathcal{P}_1\left(\widetilde{\boldsymbol{x}}_{\widetilde{\boldsymbol{\xi}},t},\boldsymbol{s}\left(\widetilde{\boldsymbol{r}},\frac{c}{c_0}\right),\frac{c_0}{c}\right)d\widetilde{\boldsymbol{r}}\\&+\eta^{-1}\varepsilon^{d+1}R^1(\widetilde{\boldsymbol{\xi}},t,c_s,M),\end{aligned} \tag{12.40}$$

for some (deterministic) remainder $R^1(\widetilde{\boldsymbol{\xi}},t,c_s,M)$ uniformly bounded with respect to $\widetilde{\boldsymbol{\xi}}$, t, c_s and ε. Then using Theorem 10 and the mixing Hypothesis 20, it holds,

$$\begin{aligned}(\mathcal{S}_{\widetilde{\boldsymbol{\xi}},t}f)(c_s):=\eta^{4-2d}\int_{[c_{\min},c_{\max}]}&C_a^2|I_{\widetilde{\boldsymbol{\xi}}}||I_{\widetilde{t}}|\mathbb{E}\left[\overline{K^M}_{\widetilde{\boldsymbol{\xi}},t}(0,0,c_s)K^M{}_{\widetilde{\boldsymbol{\xi}},t}(0,0,c)\right]\\&+\eta^{4-2d}\varepsilon^d\int_{[c_{\min},c_{\max}]}R_\varepsilon^2(\widetilde{\boldsymbol{\xi}},t,c,M)f(c)dc,\end{aligned} \tag{12.41}$$

for some remainder $R_\varepsilon^2(\widetilde{\boldsymbol{\xi}},t,c,M)\in L^1(\Omega)$ that satisfies the required properties *i.e.* $\left\|R_\varepsilon^2(\widetilde{\boldsymbol{\xi}},t,M)\right\|_{L^1(\Omega)}\leq C(M)$ with $C(M)\xrightarrow[M\to\infty]{}0$. In particular, using the uniform bound in c, it holds

$$\begin{aligned}&\left\|(\mathcal{S}_{\widetilde{\boldsymbol{\xi}},t}f)\right\|_{L^2([c_{\min},c_{\max}])}\\&\quad\leq\eta^{4-2d}\varepsilon^dC_a^2|I_{\widetilde{\boldsymbol{\xi}}}||I_{\widetilde{t}}|\left(\int_{[c_{\min},c_{\max}]}\mathbb{E}\left[\overline{K^M}_{\widetilde{\boldsymbol{\xi}},t}(0,0,c_s)K^M{}_{\widetilde{\boldsymbol{\xi}},t}(0,0,c)\right]f(c)\right)^2dc\\&\qquad+\eta^{4-2d}\varepsilon^dR_\varepsilon^3(\widetilde{\boldsymbol{\xi}},t,M)\left\|f\right\|^2_{L^2([c_{\min},c_{\max}])},\end{aligned} \tag{12.42}$$

for some remainder $R_\varepsilon^3(\widetilde{\boldsymbol{\xi}},t,M)\in L^1(\Omega)$ that verifies $\left\|R_\varepsilon^3(\widetilde{\boldsymbol{\xi}},t,M)\right\|_{L^1(\Omega)}\leq C(M)$ with $C(M)\xrightarrow[M\to\infty]{}0$. This yields the desired result by inserting (12.40) into (12.42). □

Proof of Corollary 62. We proceed as in the proof of Corollary 60, by a Taylor expansion $\frac{B}{\omega_0}$ inside the equation of $\mathcal{P}_1\left(\widetilde{\boldsymbol{x}}_{\widetilde{\boldsymbol{\xi}},t},\boldsymbol{s}\left(\widetilde{\boldsymbol{r}},\frac{c_0}{c_s}\right),\frac{c_0}{c_s}\right)$ to an equivalent of (12.29). We then insert this equivalent into the definition of (12.33) to obtain (12.35). □

When we compute the operator $\mathcal{S}_{\widetilde{\boldsymbol{\xi}},t}$, we compute in fact the ensemble average of $\mathbb{E}[\overline{K}_{\widetilde{\boldsymbol{\xi}},t}(0,0,c_1)K_{\widetilde{\boldsymbol{\xi}},t}(0,0,c_2)]$ for different $c_1\neq c_2$. When we compute function $C(\widetilde{\boldsymbol{\xi}},t,\cdot)$

defined by (12.21), we only compute the ensemble average $\mathbb{E}[|K_{\widetilde{\boldsymbol{\xi}},t}(0,0,c_1)|^2$.
In that sense, $\mathcal{S}_{\widetilde{\boldsymbol{\xi}},t}$ contains more exploitable information to recover the speed of sound. We can for example compute the eigenvectors of $\mathcal{S}_{\widetilde{\boldsymbol{\xi}},t}$. Numerically, we observe that the first eigenvector $V_{\widetilde{\boldsymbol{\xi}},t}$ of $\mathcal{S}_{\widetilde{\boldsymbol{\xi}},t}$ can be used to recover the sound speed c_0. $V_{\widetilde{\boldsymbol{\xi}},t}$ is maximal for $c_s = c_0$ (see Figure 13.8b). Furthermore, $\frac{\partial \mathrm{Im}(V_{\widetilde{\boldsymbol{\xi}},t})}{\partial c_s}$ is maximal when $c_s = c_0$ (see Figure 13.8c). V shows the properties of $\mathcal{P}_c$ defined by (11.21), that we used to recover the speed of sound in a homogeneous medium. We thus define the two estimators:

$$\hat{c}_4(\boldsymbol{x}_{\widetilde{\boldsymbol{\xi}},t}) = \underset{c_s}{\mathrm{argmax}} \left| V_{\widetilde{\boldsymbol{\xi}},t}(c_s) \right|, \tag{12.43}$$

and

$$\hat{c}_5(\boldsymbol{x}_{\widetilde{\boldsymbol{\xi}},t}) = \underset{c_s}{\mathrm{argmax}} \left| \frac{\partial \mathrm{Im}(V_{\widetilde{\boldsymbol{\xi}},t})}{\partial c_s}(c_s) \right|. \tag{12.44}$$

These two estimators are plotted on Figure 13.4. Even if the effective speed of sound is here constant in the entire medium, we still keep the $\boldsymbol{x}_{\widetilde{\boldsymbol{\xi}},t}$-dependency on $\hat{c}_4$ and $\hat{c}_5$ as they are local estimators, in the sense that we could estimate c_0 in a series of points $(\boldsymbol{x}_{\widetilde{\boldsymbol{\xi}},t})_{(\widetilde{\boldsymbol{\xi}} \in \mathbb{R}^{d-1},\, t>0)}$ to compute a local map of speed of sound.

CHAPTER 13

Numerical illustrations

In this section, we illustrate the results of Theorem 54 and Theorem 57 and the estimators of the speed of sound in the two regimes described in Section 11 and Section 12. The simulations are done in dimension $d = 2$.

13.1 Simulation of the direct problem

In practice, the measurements are done in the time domain and we have access to $\mathcal{F}^{-1}(M(\boldsymbol{x_e}, \boldsymbol{x_r}, \cdot))(t)$ where $\mathcal{F}$ is the Fourier transform. We thus decide to perform numerical simulations in the time domain by using the K-Wave library [191]. For a given $\boldsymbol{x_e} \in \mathbb{R}^d$, and a given end time $T > 0$, we simulate $U(\boldsymbol{x_e}, x, t) := \mathcal{F}^{-1}(u(\boldsymbol{x_e}, x, \cdot))(t)$, the solution in $L^2([0,T], H^1(\mathbb{R}^d \setminus \{\boldsymbol{x_e}\}))$ of:

$$\begin{cases} -\Delta U(\boldsymbol{x_e}, \boldsymbol{x}, t) + \dfrac{n(\boldsymbol{x})}{c_0^2}\partial_{tt}^2 U(\boldsymbol{x_e}, \boldsymbol{x}, t) = \delta(\boldsymbol{x} - \boldsymbol{x_e})f(t), \quad \text{for } x \in \mathbb{R}^d \setminus \{\boldsymbol{x_e}\},\ t \in [0,T] \\ U(\boldsymbol{x_e}, \boldsymbol{x}, 0) = \partial_t U(\boldsymbol{x_e}, \boldsymbol{x}, 0) = 0, \end{cases} \tag{13.1}$$

with $f(t) \in C^0([0,T])$ (see Figure 13.1). The signal $U(\boldsymbol{x_e}, \boldsymbol{x_r}, t)$ is then recorded on the transducers at x_r.
By considering $N_e = 15$ incident waves emitted at $\{\boldsymbol{x_e^i}\}_{i=1...N_e}$ and $N_r = 64$ recording sensors placed at $\{\boldsymbol{x_r^j}\}_{j=1...N_r}$, we have access to the matrix of data $M(\omega_k) \in \mathbb{C}^{N_e \times N_r}$ where

$$M_{i,j}(\omega_k) = \mathcal{F}^{-1}(U(\boldsymbol{x_e^i}, \boldsymbol{x_r^j}, \cdot))(\omega_k)$$

and $\{\omega_k\}_{k=1...N_\omega}$ are the sampling frequencies that are sampled from 100 to $\times 10^8$ rad (which is the frequency content of the source f). Here $N_\omega = 1000$. The sensors $\{x_e^i\}_{i=1...N_e}$ and $\{x_r^j\}_{j=1...N_r}$ are equally spaced on the segment $[-a_0, a_0] \times \{0\}$ with $a_0 = 1.5 \times 10^{-2}$ m.
As the problem is a multi-scale problem, the simulation of M can hardly be done on a personal laptop. Indeed, it requires to mesh the small inclusions to capture their effects. By the CFL condition (taken here to be 0.4), the computations can become quite long. However, for $i = 1...N_e$, the simulations of $U(\boldsymbol{x_e^i}, \cdot, \cdot)$ can be done in parallel, and are

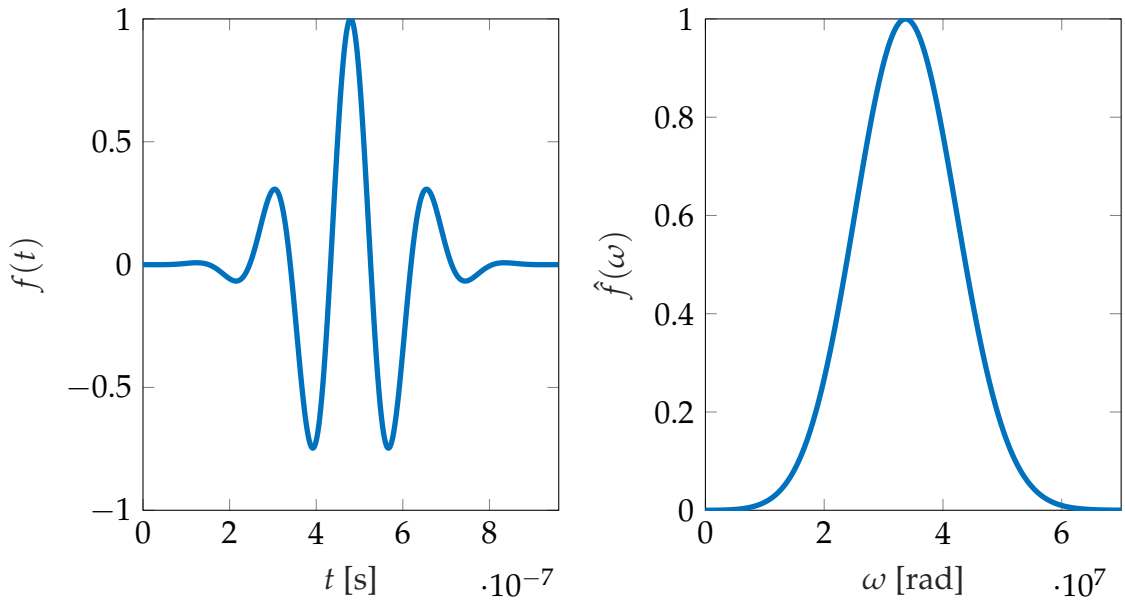

(a) Input signal $g(t)$

(b) Normalized Fourier transform of $g(t)$

Figure 13.1: Source term used in the simulation. $f(t)$ is chosen as the derivative of $g(t) = \sin(\omega_0(t-t_0))\exp(-\frac{\omega_0^2(t-t_0)^2}{\tau^2})$, centered in $\omega_0 \approx 3.14 \times 10^7$ rad, $\tau = 0.8$ and $t_0 = 1.2$.

then computed on Nvidia Tesla V100 GPUs. For the choice of parameters, it takes ~ 10 hours per problem.
The inverse problem is done by computing the integral of the matrix M. The number $N_e \times N_r \times N_\omega$ drives its size. The parameters N_e, N_r and N_ω are chosen such that the matrix M can be processed on a personal laptop.

For the imaging problem, we consider two media. One homogeneous medium with one small target, which illustrate the work of Section 11. We recover the point spread function of Theorem 54. We then consider a medium with tens of thousands unresolved scatterers, which corresponds to the regime described in Section 12. In the two cases, we estimate the underlying speed of sound with our estimators.

13.2 Point spread function in a homogeneous medium

We first consider a medium with one circular point like reflector at $\boldsymbol{x_0} = (0, 61 \times 10^{-3})$ m inside a homogeneous medium with speed of sound $c_0 = 1500$ m.s^{-1}. For a given emission point $\boldsymbol{x_e}$, we first plot the time series recorded by several sensors on Figure 13.2.

We compute the imaging function given by (10.6). This illustrate to the situation

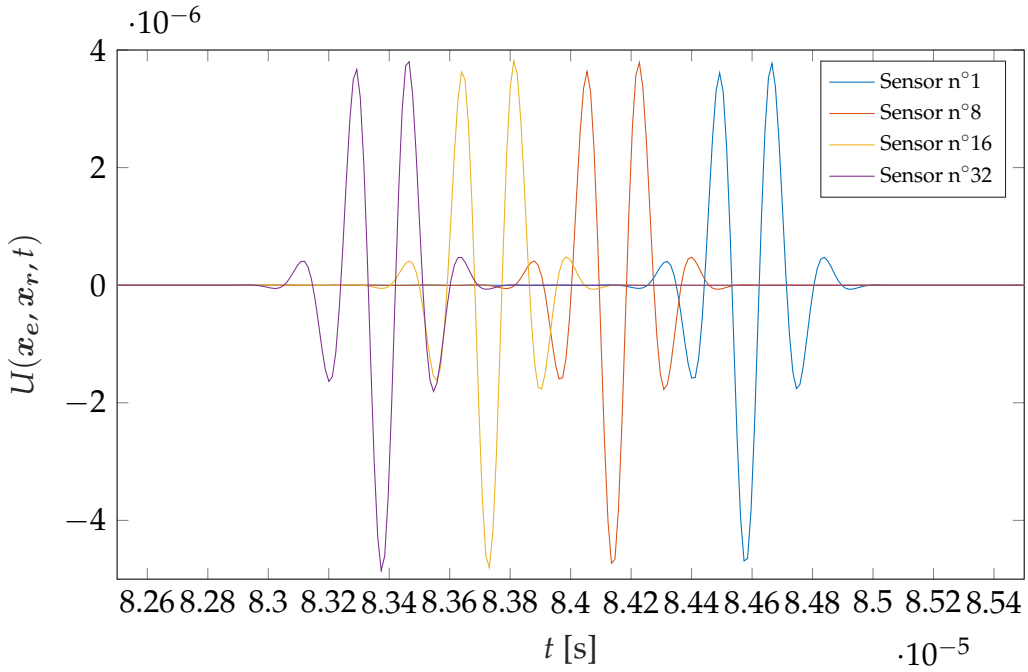

Figure 13.2: Solution $U(x_e, x_r, t)$ for a given emission point x_e on 4 sensors on a given time interval. The solution is 0 out of the interval.

of Section 11. We plot the resulting image for several backpropagation speeds on Figure 13.3. The resulting image corresponds to the point spread function described by(11.12) with the expected resolution.
As predicted by Theorem 54, the shape of the point spread function differs alongside the backpropagation speed and the center of the focal spot is at $\boldsymbol{x_f}(\boldsymbol{x_0}, v) := \left(\frac{\boldsymbol{x_0^\perp}}{v^2}, \frac{x_0^{||}}{v}\right)$. Moreover, the intensity is lowered when $v \neq 1$. The results are shown on Figure 13.3.
We then compute the theoretical and the simulated function $\mathcal{I}(\boldsymbol{x_f}(\boldsymbol{x_0}, v = \frac{c_0}{c_s}), c_s)$ from which we compute the estimators of c_0 described in (11.22) and (11.23). To numerically access $\mathcal{I}(\boldsymbol{x_f}(\boldsymbol{x_0}, v = \frac{c_0}{c_s}), c_s)$ for a given c_s, we take the maximum of amplitude on the image. We then plot on Figure 13.4a and Figure 13.4b the theoretical and numerical estimators defined (11.22) and (11.23). The derivation of the imaginary part is done by first order finite differences.
One can see on Figure 13.5a that the peak function obtained by the derivation of the imaginary part of $\mathcal{I}$ is narrower, more sensitive to an error in the backpropagating speed. Note that in the physical experimental setups, the typical value of $\frac{a_0^2\omega_0}{x_0^{||}c_0}$ is of the order 10^2-10^3 (see for example the transducers described in [17, Table 2.2]). Due to computational limitations, we restrain the simulation to $\frac{x_0^{||}c_0^2}{a_0^2\omega_0} \approx 70$. It means that the displayed peaks computed with real (and perfect) experimental data should be even narrower.
We also investigate the numerical stability of the estimator with respect to measurement noise. We add a Gaussian white noise to our data with increasing amplitude and plot the results on Figure 13.5. The measurement noise has only a small impact on the recovery of the speed of sound.

13.3 Simulation in the tissue mimicking medium

We now consider the medium of Figure 13.6 which is composed on many unresolved scatterers. We set the density of scatterers but the number and the position of the scatterers is random and given by a Matèrn point process (see [134, Section 6.5.2]). In Figure 13.6, there are 22710 scatterers with up to 30% contrast in the speed of sound and a typical radius $\varepsilon = 7.5 \times 10^{-5}$ m. This corresponds to a density of 15%. We consider the three estimators described in Section 12 and given by (12.30), (12.43) and (12.44).

We want to recover the (local) speed of sound. Here, we only describe the computing process that allows to recover the speed of sound in one point, but this could be done for any point in D. We set the coordinates $\widetilde{\boldsymbol{\xi}} \in \mathbb{R}^{d-1}$, $t > 0$ and we want to recover the speed of sound at $\boldsymbol{x}_{\widetilde{\boldsymbol{\xi}},t}$. For the numerical example, we choose $\widetilde{\boldsymbol{\xi}} = 0$ m^{-2}.s^2 and $t = 3 \times 10^{-5}$ s. As $c_0 = 1500$ m.s^{-1}, this corresponds to $\boldsymbol{x}_{\widetilde{\boldsymbol{\xi}},t} = (0, 45)$ mm.
As a first step, we compute the matrix $K_{\widetilde{\boldsymbol{\xi}},t}$ given by (12.17). To this matter, we consider

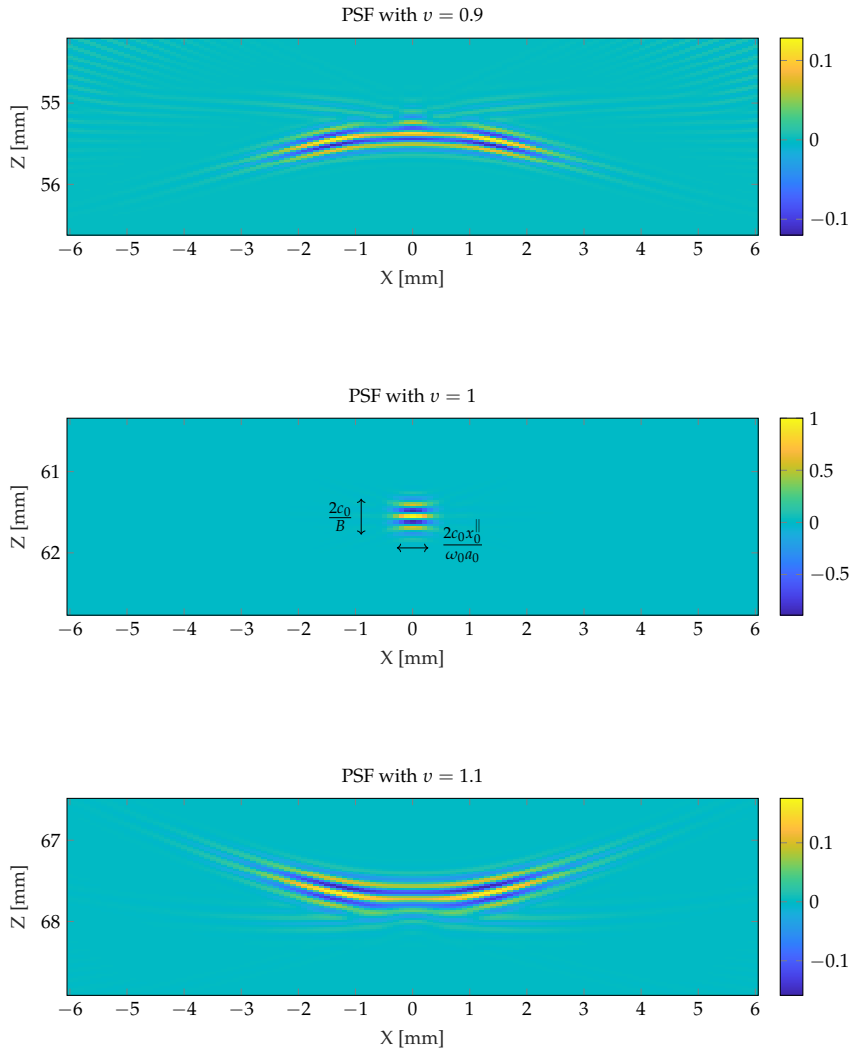

Figure 13.3: Point spread function for several backpropagation speeds. The intensity is normalized to the maximum of $\mathcal{I}$.

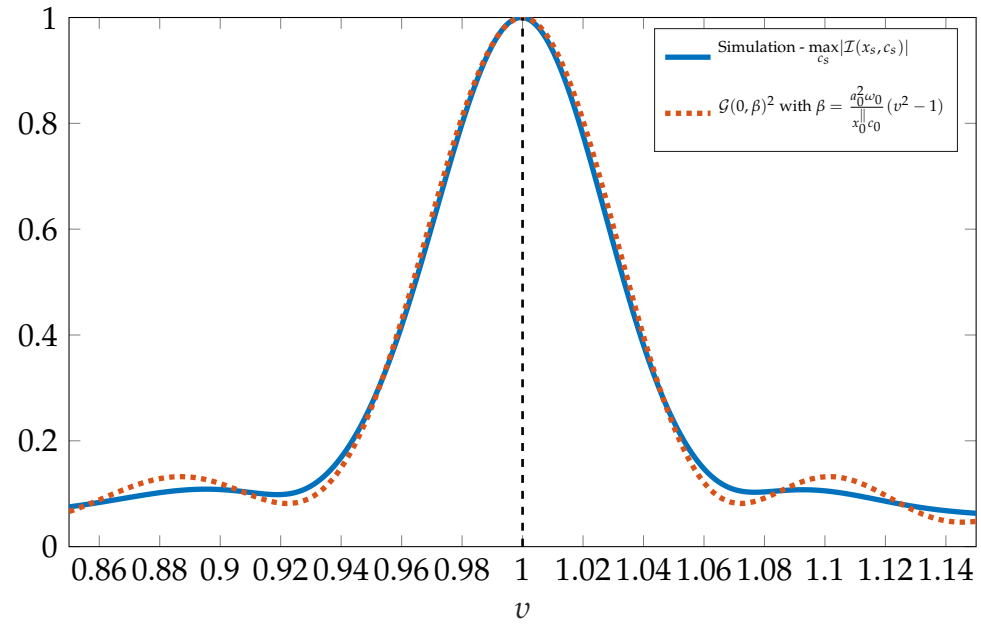

(a) Estimator of c_0 using the modulus of $\mathcal{I}(\boldsymbol{x_f}(\boldsymbol{x_0}, v), v)$.

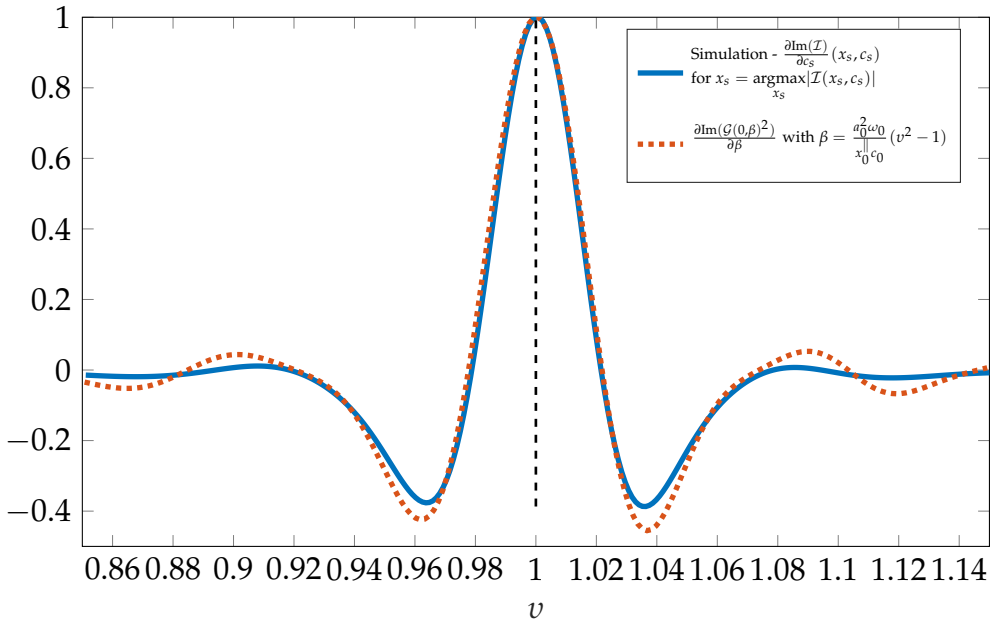

(b) Estimator of c_0 using the derivative of the imaginary part of $\mathcal{I}(\boldsymbol{x_f}(\boldsymbol{x_0}, v), v)$.

Figure 13.4: Estimators of the speed of sound in the homogeneous medium.

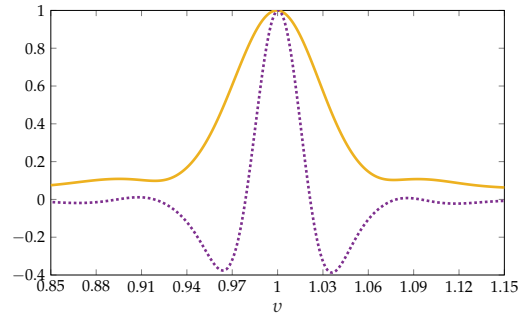

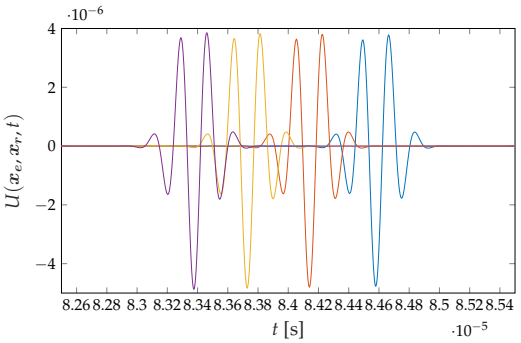

(▬) : $\max_{x_s} |\mathcal{I}(x_s, c_s)|$

(┅) : $\frac{\partial \mathrm{Im}(\mathcal{I})}{\partial c_s}(x_s, c_s)$ for $x_s = \operatorname{argmax}_{x_s} |\mathcal{I}(x_s, c_s)|$

(▬) : Sensor 1 (┅) : Sensor 8

(┅) : Sensor 16 (▬) : Sensor 32

(a) The two estimators (left) for the associated measurements (right) with 0% of noise.

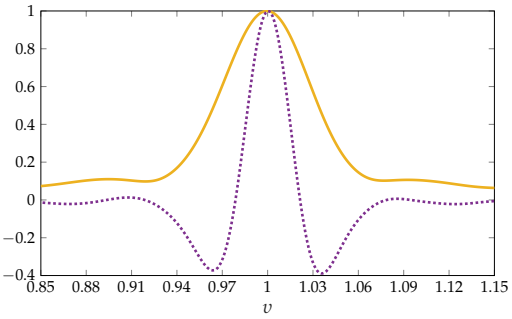

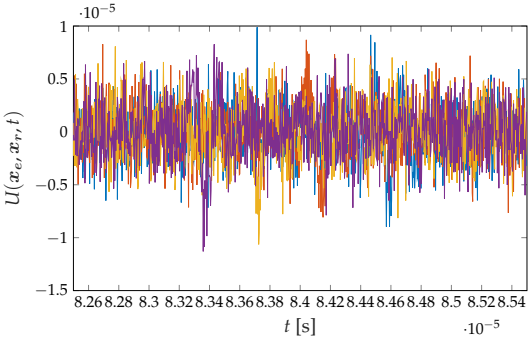

(▬) : $\max_{x_s} |\mathcal{I}(x_s, c_s)|$

(┅) : $\frac{\partial \mathrm{Im}(\mathcal{I})}{\partial c_s}(x_s, c_s)$ for $x_s = \operatorname{argmax}_{x_s} |\mathcal{I}(x_s, c_s)|$

(▬) : Sensor 1 (▬) : Sensor 8

(▬) : Sensor 16 (▬) : Sensor 32

(b) The two estimators (left) for the associated measurements (right) with 50% of noise

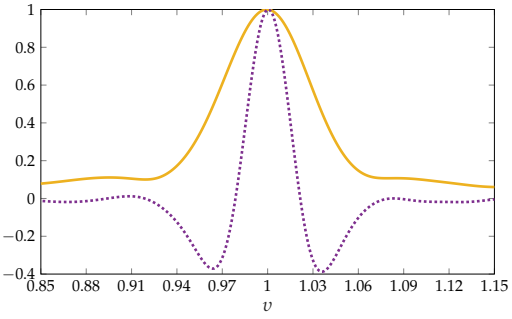

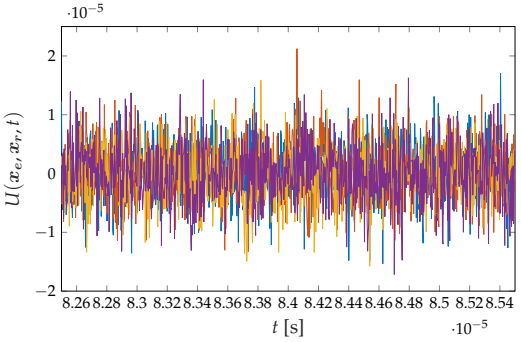

(▬) : $\max_{x_s} |\mathcal{I}(x_s, c_s)|$

(┅) : $\frac{\partial \mathrm{Im}(\mathcal{I})}{\partial c_s}(x_s, c_s)$ for $x_s = \operatorname{argmax}_{x_s} |\mathcal{I}(x_s, c_s)|$

(▬) : Sensor 1 (▬) : Sensor 8

(▬) : Sensor 16 (▬) : Sensor 32

(c) The two estimators (left) for the associated measurements (right) with 100% of noise

Figure 13.5: Comparison of the two peak functions used to estimate c_0 with several levels of noise.

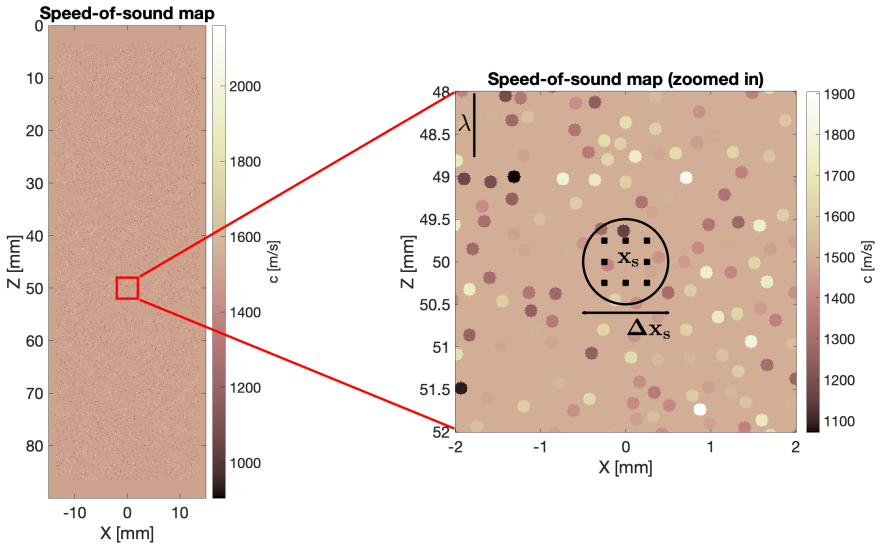

Figure 13.6: Tissue mimicking medium.

a set of points in a neighborhood $\mathcal{V}(\boldsymbol{x_s}(c_s))$ of $\boldsymbol{x_s}(c_s) = (c_s^2\widetilde{\boldsymbol{\xi}}, c_s t)$ and compute the imaging function in these points. These points denoted $\boldsymbol{y_s}(c_s) \in \mathcal{V}(\boldsymbol{x_s}(c_s))$ are chosen to be at most 4 wavelengths away from $\lambda(c_s) = \frac{c_s}{\omega_0}$ of $\boldsymbol{x_s}$. We then compute both the local average of $|K_{\widetilde{\boldsymbol{\xi}},t}|^2$ given by $C(\widetilde{\boldsymbol{\xi}}, t, c_s)$ in (12.21) and the first right singular vector of the matrix $K_{\widetilde{\boldsymbol{\xi}},t}$. In fact, the singular vectors of $K_{\widetilde{\boldsymbol{\xi}},t}$ are defined up to a constant phase $p_0 \in [-\pi, \pi]$. By a singular value decomposition, we do not have access to the vector $V_{\widetilde{\boldsymbol{\xi}},t}$ but in fact to $W_{\widetilde{\boldsymbol{\xi}},t} := V_{\widetilde{\boldsymbol{\xi}},t} \exp(ip_0)$. In particular, we cannot use the imaginary part of $W_{\widetilde{\boldsymbol{\xi}},t}$ to recover c_0. We first need to estimate p_0. To that aim, we remark that the theoretical singular vector $V_{\widetilde{\boldsymbol{\xi}},t}(c_0)$ plotted on Figure 13.7 satisfies:

$$\frac{\partial \mathrm{Re}(V_{\widetilde{\boldsymbol{\xi}},t}(c_0))}{\partial_{c_s}} = 0 \tag{13.2}$$

whilst

$$\frac{\partial \mathrm{Im}(V_{\widetilde{\boldsymbol{\xi}},t}(c_0))}{\partial_{c_s}} \text{ is maximum.} \tag{13.3}$$

as shown on Figure By using these two conditions (13.2) and (13.3), we can estimate both p_0 and c_0. We recover p_0 by the following procedure. For $p_s \in [-\pi, \pi]$, we compute

$$\hat{c}(p_s) := \underset{c_s}{\mathrm{argmax}} \left| \frac{\partial \mathrm{Im}(W_{\widetilde{\boldsymbol{\xi}},t} \exp(-ip_s))}{\partial c_s} \right|.$$

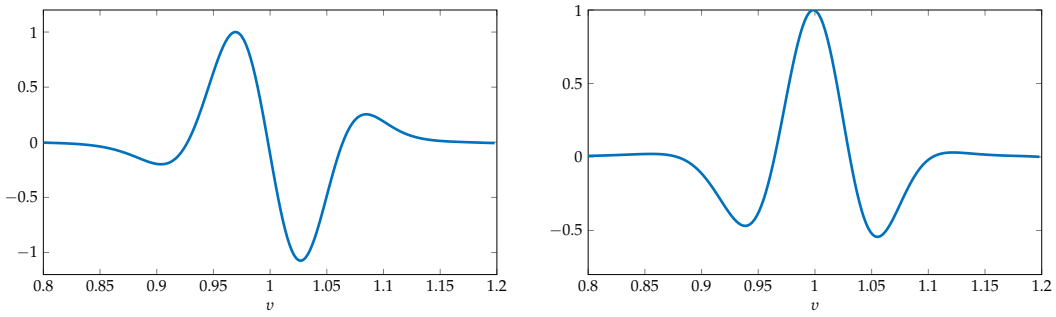

Real part Imaginary part

Figure 13.7: Real and imaginary of the first eigenvector of $\mathcal{S}_{\widetilde{\boldsymbol{\xi}},t}$.

From that estimation $\hat{c}(p_s)$ we compute

$$Q(p_s) := \left| \frac{\partial \mathrm{Re}(W_{\widetilde{\boldsymbol{\xi}},t}(\hat{c}(p_s))\exp(-ip_s))}{\partial c_s} \right|.$$

Then, we estimate p_0 by:

$$\hat{p}_0 := \underset{p_s}{\mathrm{argmin}}\, Q(p_s).$$

This procedure ensures that (13.2) and (13.3) are satisfied. The singular vector $\hat{V}_{\widetilde{\boldsymbol{\xi}},t}(c_s)$ is then recovered by:

$$\hat{V}_{\widetilde{\boldsymbol{\xi}},t}(c_s) := W_{\widetilde{\boldsymbol{\xi}},t}(c_s)\exp(-i\hat{p}_0),$$

and the estimator of c_0 is then given by:

$$\hat{c}_0 := \underset{c_s}{\mathrm{argmax}}\, \frac{\partial \mathrm{Im}(\hat{V}_{\widetilde{\boldsymbol{\xi}},t}(c_s))}{\partial c_s}.$$

The three functions $C(\widetilde{\boldsymbol{\xi}},t,c_s)$, $|\hat{V}_{\widetilde{\boldsymbol{\xi}},t}|$ and $\frac{\partial \hat{V}_{\widetilde{\boldsymbol{\xi}},t}}{\partial c_s}$ are plotted on Figure 13.8a, Figure 13.8b and Figure 13.8c respectively. We also plot the asymptotic theoretical shape of these three objects given by the results of Corollary 60 and Corollary 62 in the narrowband case. As already mentioned in the previous section, the peak function obtained by looking at $\frac{\partial V_{\widetilde{\boldsymbol{\xi}},t}}{\partial c_s}$ is narrower than the two other peaks, more sensitive to an error in the backpropagation speed.
The matrix $K_{\widetilde{\boldsymbol{\xi}},t}$ is displayed on Figure 13.10 and is a random speckle pattern. When we compute the matrix

$$\mathcal{T}_{\widetilde{\boldsymbol{\xi}},t} := K^*_{\widetilde{\boldsymbol{\xi}},t} K_{\widetilde{\boldsymbol{\xi}},t}$$

which corresponds to the kernel of $\mathcal{S}_{\widetilde{\boldsymbol{\xi}},t}$, we see a spot centered in $v = 1$ displayed on Figure 13.11. $C(\widetilde{\boldsymbol{\xi}},t,c_s)$ is in fact the diagonal of $\mathcal{T}_{\widetilde{\boldsymbol{\xi}},t}$.

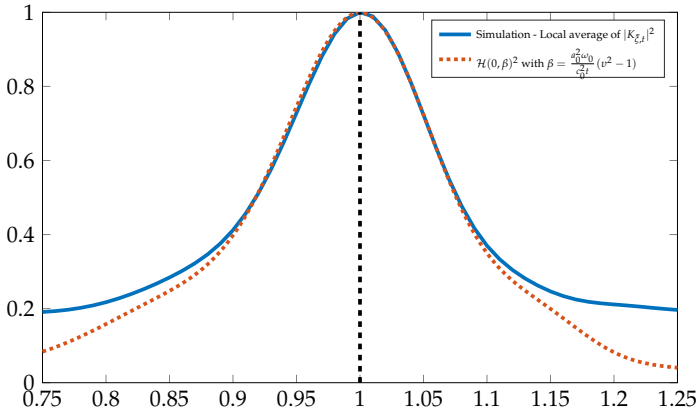

(a) Estimator of c_0 using the spatial average of $|K_{\tilde{\xi},t}|^2$.

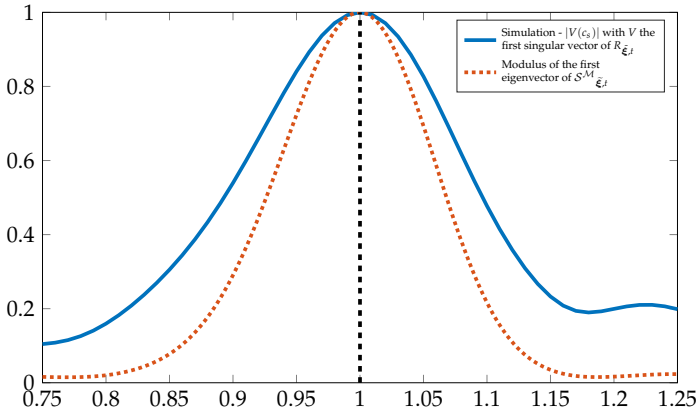

(b) Estimator of c_0 using the modulus of the first singular vector of $K_{\tilde{\xi},t}$.

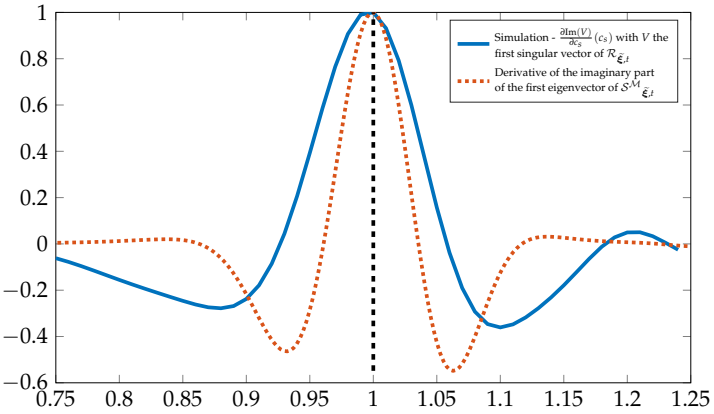

(c) Estimator of c_0 using the derivative of the imaginary part of the first singular vector of $K_{\tilde{\xi},t}$.

Figure 13.8: Estimators of the effective speed of sound in the stochastic homogenization regime

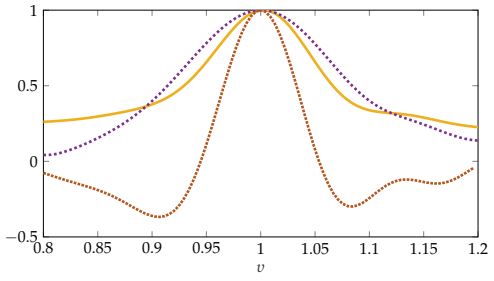

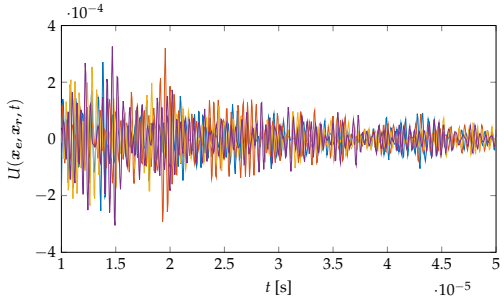

(▬) : Local average of $|K_{\tilde{\xi},t}|^2$
(▪▪▪) : Modulus of the first singular vector of $K_{\tilde{\xi},t}$
(▪▪▪) : Derivative of the imaginary part of the first singular vector of $K_{\tilde{\xi},t}$

(▬) : Sensor 33 (▬) : Sensor 40
(▬) : Sensor 56 (▬) : Sensor 64

(a) The two estimators (left) for the associated measurements around $t = 3 \times 10^{-5}$ s (right) with 0% of noise

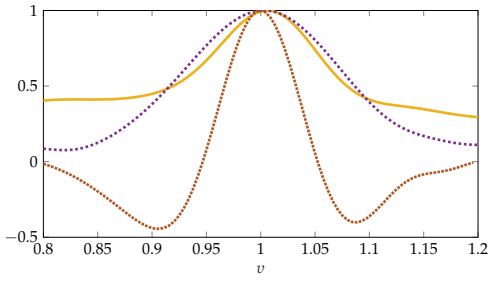

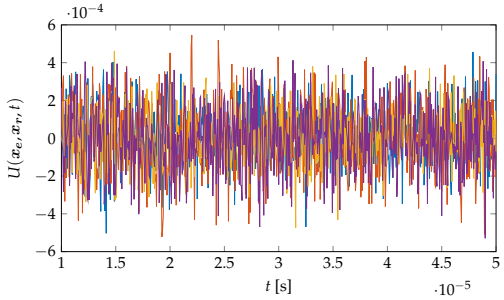

(▬) : Local average of $|K_{\tilde{\xi},t}|^2$
(▪▪▪) : Modulus of the first singular vector of $K_{\tilde{\xi},t}$
(▪▪▪) : Derivative of the imaginary part of the first singular vector of $K_{\tilde{\xi},t}$

(▬) : Sensor 33 (▬) : Sensor 40
(▬) : Sensor 56 (▬) : Sensor 64

(b) The three estimators (left) for the associated measurements around $t = 3 \times 10^{-5}$ s (right) with 50% of noise

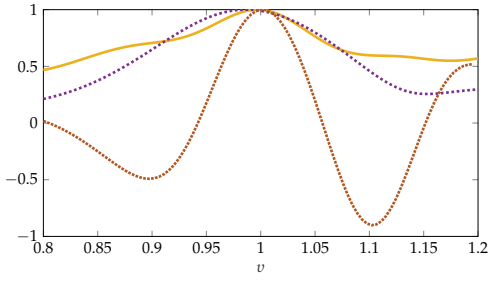

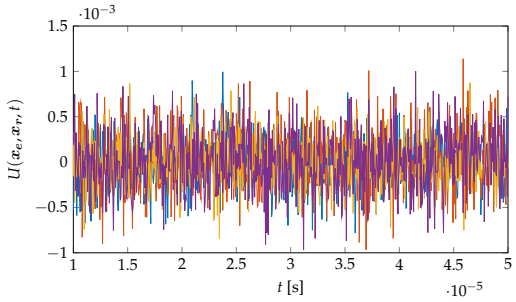

(▬) : Local average of $|K_{\tilde{\xi},t}|^2$
(▪▪▪) : Modulus of the first singular vector of $K_{\tilde{\xi},t}$
(▪▪▪) : Derivative of the imaginary part of the first singular vector of $K_{\tilde{\xi},t}$

(▬) : Sensor 33 (▬) : Sensor 40
(▬) : Sensor 56 (▬) : Sensor 64

(c) The three estimators (left) for the associated measurements around $t = 3 \times 10^{-5}$ s (right) with 100% of noise

Figure 13.9: Comparison of the three peak functions used to estimate c_0 in the stochastic homogenization regime with several levels of noise.

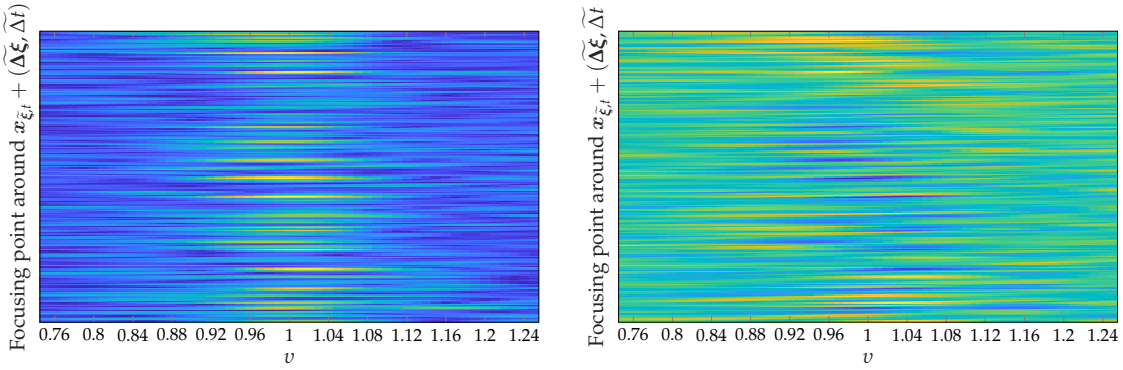

(a) Modulus the matrix $K_{\widetilde{\xi},t}$. (b) Imaginary part of the matrix $K_{\widetilde{\xi},t}$

Figure 13.10: Modulus and imaginary part of the matrix $K_{\widetilde{\xi},t}$.

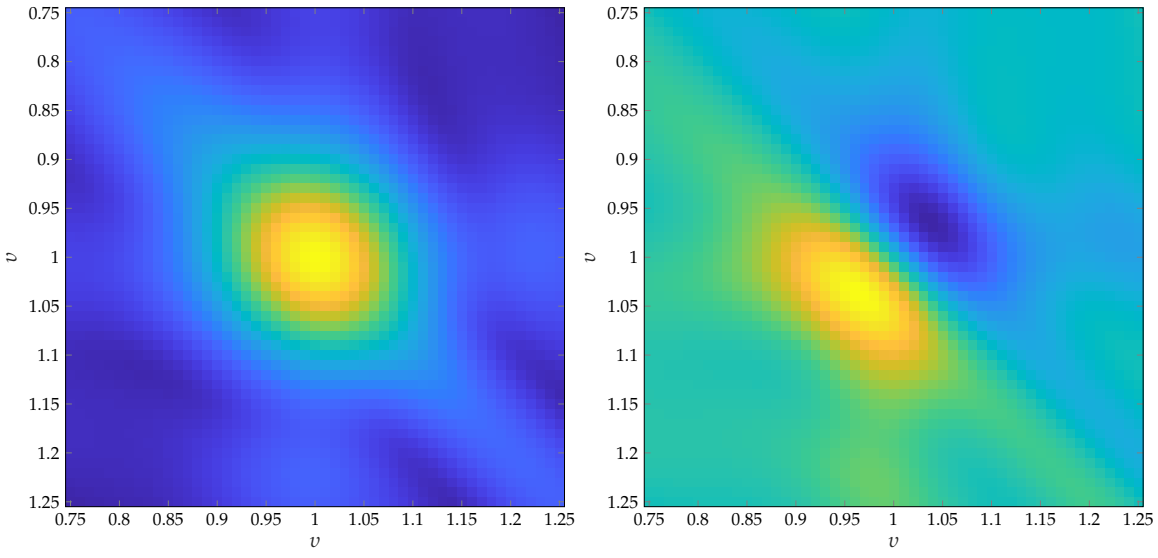

(a) Modulus the matrix $\mathcal{T}_{\widetilde{\xi},t}$. (b) Imaginary part of the matrix $\mathcal{T}_{\widetilde{\xi},t}$

Figure 13.11: Modulus and imaginary part of the matrix $\mathcal{T}_{\widetilde{\xi},t}$.

Appendices

APPENDIX E

Proof of the monopole approximation

Proof of Lemma 52. The proof follows from [107, Chapter 8]. It states that for all $x \in \mathbb{R}^d$, the total field $u = u^s + u^i$ can be represented by ([107, (8.13)]),

$$u(\boldsymbol{x_e}, \boldsymbol{x}, \omega) = u^i(\boldsymbol{x_e}, \boldsymbol{x}, \omega) + n_S \left(\frac{\omega}{c_0}\right)^2 \int_{B(\boldsymbol{x_0}, \varepsilon)} G^{\frac{\omega}{c_0}}(\boldsymbol{x} - \boldsymbol{y}) u(\boldsymbol{x_e}, \boldsymbol{y}, \omega) d\boldsymbol{y}. \tag{E.1}$$

Let $v^s = u^s_{|B(\boldsymbol{x_0}, \varepsilon)}$, then

$$u^s(\boldsymbol{x_e}, \boldsymbol{x}, \omega) = \begin{cases} v^s(\boldsymbol{x_e}, \boldsymbol{x}, \omega) & \text{if } \boldsymbol{x} \in B(\boldsymbol{x_0}, \varepsilon), \\ n_S(\frac{\omega}{c_0})^2 \int_{B(\boldsymbol{x_0}, \varepsilon)} G^{\frac{\omega}{c_0}}(\boldsymbol{x} - \boldsymbol{y}) v^s(\boldsymbol{x_e}, \boldsymbol{y}, \omega) d\boldsymbol{y}. & \text{if } \boldsymbol{x} \in \mathbb{R}^d \setminus \overline{B(\boldsymbol{x_0}, \varepsilon)}, \end{cases} \tag{E.2}$$

where $v^s \in L^2(B(\boldsymbol{x_0}, \varepsilon))$ satisfies:

$$v^s(\boldsymbol{x_e}, \boldsymbol{x}, \omega) = (I - T^\omega_\varepsilon)^{-1} u^i(\boldsymbol{x_e}, \boldsymbol{x}, \omega) \tag{E.3}$$

and the Lippmann-Schwinger operator $T^\omega_\varepsilon \in L^2(B(\boldsymbol{x_0}, \varepsilon)) \to L^2(B(\boldsymbol{x_0}, \varepsilon))$ is defined by

$$T^\omega_\varepsilon[f](\boldsymbol{x}) := n_s(\frac{\omega}{c_0})^2 \int_{B(\boldsymbol{x_0}, \varepsilon)} G^{\frac{\omega}{c_0}}(\boldsymbol{x} - \boldsymbol{y}) f(\boldsymbol{y}) dy. \tag{E.4}$$

We show that in this configuration the Neumann series $N(T^\omega_\varepsilon)$ of T^ω_ε defined by

$$N(T^\omega_\varepsilon) = \sum_{k=0}^{\infty} (T^\omega_\varepsilon)^k$$

converges. The convergence of this series is a consequence of the control on $|||T^\omega_\varepsilon|||$. We thus estimate $|||T^\omega_\varepsilon|||$. By the change of variable $\boldsymbol{y} := \boldsymbol{x_0} + \varepsilon\widetilde{y}$, for

$$T^\omega_\varepsilon f(\boldsymbol{x}) = \varepsilon^d n_s(\frac{\omega}{c_0})^2 \int_{B(0,1)} G^{\frac{\omega}{c_0}}(\boldsymbol{x} - \boldsymbol{x_0} - \varepsilon\widetilde{\boldsymbol{y}}) f(\boldsymbol{x_0} + \varepsilon\widetilde{\boldsymbol{y}}) d\widetilde{\boldsymbol{y}}. \tag{E.5}$$

Therefore, we have that

$$\|T^\omega_\varepsilon f\|_{L^2(B(\boldsymbol{x_0}, \varepsilon))} = \varepsilon^{2d} \int_{B(0,1)\times B(0,1)} G^{\frac{\omega}{c_0}}(\varepsilon(\widetilde{\boldsymbol{x}} - \widetilde{\boldsymbol{y}})) f(\boldsymbol{x_0} + \varepsilon\widetilde{\boldsymbol{y}}) d\widetilde{\boldsymbol{y}} d\widetilde{\boldsymbol{x}}. \tag{E.6}$$

This yields that

$$|||T_\varepsilon^\omega||| \leq \varepsilon^d \left\| G^{\frac{\omega}{c_0}}(\varepsilon(\cdot - \cdot)) \right\|_{L^2(B(0,1)\times B(0,1))}. \tag{E.7}$$

We recall [108, Lemma 2.21]:

$$\forall z \in \mathbb{R}^d,\ G^k(\boldsymbol{z}) = \begin{cases} \frac{i}{4} \mathrm{H}_0^{(1)}(k|\boldsymbol{z}|) & \text{if } d = 2, \\ \frac{\exp(ik|\boldsymbol{z}|)}{4\pi|\boldsymbol{z}|} & \text{if } d = 3, \end{cases} \tag{E.8}$$

where $\mathrm{H}_0^{(1)}$ is the Hankel function of the first kind. In particular,

$$|||T_\varepsilon^\omega||| \leq \varepsilon^2 (\frac{\omega}{c_0})^2 \begin{cases} \left\| \frac{i}{4} \mathrm{H}_0^{(1)}(\frac{\varepsilon\omega}{c_0}|\cdot - \cdot|) \right\|_{L^2(B(0,1)\times B(0,1))} & \text{if } d = 2. \\ \left\| \frac{\exp(i\frac{\varepsilon\omega}{c_0}|\cdot - \cdot|)}{4\pi|\cdot - \cdot|} \right\|_{L^2(B(0,1)\times B(0,1))} & \text{if } d = 3, \end{cases} \tag{E.9}$$

At the origin, $|\boldsymbol{z}| \to 0$, $\mathrm{H}_0^{(1)}(|z|) \sim \frac{2i}{\pi}\log(|z|)$ (see *e.g.* [108, Chapter 2.2.1]). Therefore,

$$|||T_\varepsilon^\omega||| \leq C \begin{cases} \varepsilon^2 (\frac{\omega}{c_0})^2 \log(\varepsilon(\frac{\omega}{c_0})) & \text{if } d = 2. \\ \varepsilon^2 (\frac{\omega}{c_0})^2 & \text{if } d = 3. \end{cases} \tag{E.10}$$

In particular, for $\varepsilon(\frac{\omega}{c_0})$ sufficiently small, the series $N(T_\varepsilon^\omega)$ converges and:

$$v^s(\boldsymbol{x_e}, \boldsymbol{x}, \omega) = u^i(\boldsymbol{x_e}, \boldsymbol{x}, \omega) + \begin{cases} \mathcal{O}\left(\varepsilon^4 (\frac{\omega}{c_0})^4 \log(\varepsilon(\frac{\omega}{c_0}))^2\right) & \text{if } d = 2. \\ \mathcal{O}(\varepsilon^4 (\frac{\omega}{c_0})^4) & \text{if } d = 3. \end{cases} \tag{E.11}$$

We can now use (E.11) inside (E.2) and the change of variable $\boldsymbol{y} = \boldsymbol{x_0} + \varepsilon\widetilde{\boldsymbol{y}}$ to get for all $x \notin D$,

$$\begin{aligned} u^s(\boldsymbol{x_e}, \boldsymbol{x}, \omega) = n_S \varepsilon^d \left(\frac{\omega}{c_0}\right)^2 \int_{B(0,1)} G^{\frac{\omega}{c_0}}(\boldsymbol{x} - \boldsymbol{x_0} - \varepsilon\widetilde{\boldsymbol{y}}) u^i(\boldsymbol{x_e}, \boldsymbol{x_0} + \varepsilon\widetilde{\boldsymbol{y}}, \omega) d\widetilde{\boldsymbol{y}} \\ + \begin{cases} \mathcal{O}(\varepsilon^4 (\frac{\omega}{c_0})^4 \log(\varepsilon(\frac{\omega}{c_0}))^2) & \text{if } d = 2. \\ \mathcal{O}(\varepsilon^4 (\frac{\omega}{c_0})^4) & \text{if } d = 3. \end{cases} \end{aligned} \tag{E.12}$$

We have that

$$G^{\frac{\omega}{c_0}}(\boldsymbol{x} - \boldsymbol{x_0} - \varepsilon\widetilde{\boldsymbol{y}}) = G^{\frac{\omega}{c_0}}(\boldsymbol{x} - \boldsymbol{x_0}) \left(1 + \mathcal{O}\left(\frac{\varepsilon\widetilde{\boldsymbol{y}}}{|\boldsymbol{x} - \boldsymbol{x_0}|}\right) + \mathcal{O}\left(\frac{\varepsilon\omega}{c_0|\boldsymbol{x} - \boldsymbol{x_0}|}\right)\right). \tag{E.13}$$

Moreover, for $\frac{\omega}{c_0}|\boldsymbol{x}-\boldsymbol{x_0}| \gg 1$, we have by (10.7) for dimension 2 and by (10.3) that

$$|G^{\frac{\omega}{c_0}}(\boldsymbol{x}-\boldsymbol{x_0})| = \begin{cases} \mathcal{O}\left((\frac{c_0}{\omega}|\boldsymbol{x}-\boldsymbol{x_0}|)^{\frac{1}{2}}\right) & \text{if } d=2 \\ \mathcal{O}(1) & \text{if } d=3 \end{cases}. \tag{E.14}$$

Recalling that

$$u^i(\boldsymbol{x_e},\boldsymbol{x},\omega) = G^{\frac{\omega}{c_0}}(\boldsymbol{x}-\boldsymbol{x_0}),$$

the result follows by inserting (E.13) and (E.14) in (E.12).

□

APPENDIX F

Homogenization result in large domains

Proof of Proposition 56. The homogenization result of Theorem 39 has been obtained in a domain D of typical size 1 and a wavelength λ of order 1. We prove that this holds in the setting where $\frac{\lambda}{\text{diam}(D)} = \eta$. First we rewrite the problem. To that aim, for $\boldsymbol{x}', \boldsymbol{y}' \in \mathbb{R}^d$ and $\tilde{\omega} \in \mathcal{B}_0$, we introduce

$$v^s_{\varepsilon,\eta}(\boldsymbol{x}', \boldsymbol{y}', \tilde{\omega}) := u^s_\varepsilon\left(\eta \boldsymbol{x}', \eta \boldsymbol{y}', \frac{\tilde{\omega}}{\eta}\right),$$

and

$$v^i_\eta(\boldsymbol{x}', \boldsymbol{y}', \tilde{\omega}) := u^i\left(\eta \boldsymbol{x}', \eta \boldsymbol{y}', \frac{\tilde{\omega}}{\eta}\right).$$

Then, for $\boldsymbol{x}'_{\boldsymbol{e}} \in \frac{\mathcal{A}}{\eta}$, the scattered field $v^s_{\varepsilon,\eta}(\boldsymbol{x}'_{\boldsymbol{e}}, \widetilde{\boldsymbol{y}}, \tilde{\omega}) \in H^1_{loc}(\mathbb{R}^d)$ is then the solution of

$$\begin{cases} -\Delta(v^s_{\varepsilon,\eta} + v^i_\eta)(\boldsymbol{x}'_{\boldsymbol{e}}, \cdot, \tilde{\omega}) - \dfrac{\tilde{\omega}^2}{c_0^2}(1 + n_\varepsilon(\eta\cdot))(v^s_{\varepsilon,\eta} + v^i_\eta)(\boldsymbol{x}'_{\boldsymbol{e}}, \cdot, \tilde{\omega}) = 0 \quad \text{in } \mathbb{R}^d \setminus \{\boldsymbol{x}'_{\boldsymbol{e}}\} \\ \lim\limits_{|\boldsymbol{x}|\to\infty} |\boldsymbol{x}|^{\frac{d-1}{2}}\left(\dfrac{\partial}{\partial|\boldsymbol{x}|} v^s_{\varepsilon,\eta}(\boldsymbol{x}'_{\boldsymbol{e}}, \boldsymbol{x}, \tilde{\omega}) - i\dfrac{\tilde{\omega}}{c_0} v^s_{\varepsilon,\eta}(\boldsymbol{x}'_{\boldsymbol{e}}, \boldsymbol{x}, \tilde{\omega})\right) = 0 \end{cases} \tag{F.1}$$

For this problem, it has been shown in Theorem 39 under the Hypothesis 20 that for all $\boldsymbol{x}'_{\boldsymbol{e}}, \boldsymbol{x}'_{\boldsymbol{r}} \in \frac{\mathcal{A}}{\eta}$:

$$\begin{aligned} &\mathbb{E}\left[|v^s_{\varepsilon,\eta}(\boldsymbol{x}'_{\boldsymbol{e}}, \boldsymbol{x}'_{\boldsymbol{r}}, \tilde{\omega}) - V^s_{\varepsilon,\eta}(\boldsymbol{x}'_{\boldsymbol{e}}, \boldsymbol{x}'_{\boldsymbol{r}}, \tilde{\omega})|^2\right]^{\frac{1}{2}} \\ &\qquad \leq C(\tilde{\omega}, \eta)\varepsilon^{\frac{d+1}{2}}\mu_d\left(\frac{1}{\varepsilon}\right)^{\frac{1}{2}} \left\|G^{\frac{\tilde{\omega}}{c_0}}(\cdot - \boldsymbol{x}'_{\boldsymbol{e}})\right\|_{W^{2,\infty}(\frac{D}{\eta})} \left\|G^{\frac{\tilde{\omega}}{c_0}}(\cdot - \boldsymbol{x}'_{\boldsymbol{r}})\right\|_{W^{2,\infty}(\frac{D}{\eta})} \end{aligned} \tag{F.2}$$

with

$$V^s_{\varepsilon,\eta}(\boldsymbol{x}'_{\boldsymbol{e}}, \boldsymbol{x}'_{\boldsymbol{r}}, \tilde{\omega}) := \frac{\tilde{\omega}^2}{c_0^2}\int_{\frac{D}{\eta}} \psi_\varepsilon(\eta \boldsymbol{x}) G^{\frac{\tilde{\omega}}{c_0}}(\boldsymbol{x}'_{\boldsymbol{e}} - \boldsymbol{x}) G^{\frac{\tilde{\omega}}{c_0}}(\boldsymbol{x} - \boldsymbol{x}'_{\boldsymbol{r}}) d\boldsymbol{x}. \tag{F.3}$$

We show here that C_η grows with η^{-d} *i.e.* with the volume of $\frac{D}{\eta}$. In Part II, the result of (F.2) is obtained by the estimation of the L^2-norm of the correctors (6.28). In the setting of Part III, we only consider contrasts in the index n. Therefore, we only need to estimate $\left\|\beta(\frac{\eta\cdot}{\varepsilon})\right\|_{L^2(\frac{D}{\eta})}$ with respect to η and ε. We recall that the corrector $\beta \in H^1_{loc}(\mathbb{R}^d)^d$ is the almost sure unique solution in $\mathcal{D}'(\mathbb{R}^d)$ of (see Definition 31):

$$-\Delta\beta_i = \partial_i n \tag{F.4}$$

It holds (see (6.28)):

$$\begin{aligned}\|\beta^\varepsilon(\eta\cdot)\|^2_{L^2(\frac{D}{\eta})} &= \eta^{-d}\|\beta^\varepsilon\|^2_{L^2(D)} \\ &\leq C\eta^{-d}\mu_d\left(\frac{1}{\varepsilon}\right)^2\left(\varepsilon^d\sum_{\boldsymbol{z}\in P_\varepsilon(D)}\mathcal{C}(\boldsymbol{z})^2\right),\end{aligned} \tag{F.5}$$

where $P_\varepsilon(D)$ defined in (6.23) is the set of the centers of the covering of D with squares of size ε. Thus, by following the proof of Theorem 39, we obtain that for all $\boldsymbol{x_e}, \boldsymbol{x_r} \in \mathcal{A}$, $\omega = \frac{\tilde{\omega}}{\eta} \in \mathcal{B}$,

$$\begin{aligned}&\mathbb{E}\left[|u^s_\varepsilon(\boldsymbol{x_e},\boldsymbol{x_r},\omega) - V^s_{\varepsilon,\eta}(\boldsymbol{x_e},\boldsymbol{x_r},\tilde{\omega})|^2\right]^{\frac{1}{2}} \\ &\qquad\leq C\eta^{-d}\varepsilon^{\frac{d+1}{2}}\mu_d\left(\frac{1}{\varepsilon}\right)^{\frac{1}{2}}\left\|G^{\frac{\tilde{\omega}}{c_0}}(\cdot-\frac{\boldsymbol{x_e}}{\eta})\right\|_{W^{2,\infty}(\frac{D}{\eta})}\left\|G^{\frac{\tilde{\omega}}{c_0}}(\cdot-\frac{\boldsymbol{x_r}}{\eta})\right\|_{W^{2,\infty}(\frac{D}{\eta})}.\end{aligned} \tag{F.6}$$

By the change of variable $\boldsymbol{z} = \eta\boldsymbol{x}$,

$$\begin{aligned}V^s_{\varepsilon,\eta}(\boldsymbol{x_e},\boldsymbol{x_r},\tilde{\omega}) &= \eta^{-d}\int_D \psi_\varepsilon(\boldsymbol{z})G^{\frac{\tilde{\omega}}{c_0}}(\frac{1}{\eta}(\boldsymbol{x_e}-\boldsymbol{z}))G^{\frac{\tilde{\omega}}{c_0}}\left(\frac{1}{\eta}(\boldsymbol{x_r}-\boldsymbol{z})\right)d\boldsymbol{z} \\ &= U^s_{\varepsilon,\eta}(\boldsymbol{x_e},\boldsymbol{x_r},\omega)\end{aligned} \tag{F.7}$$

where we used that,

$$G^{\frac{\tilde{\omega}}{c_0}}\left(\frac{1}{\eta}(\boldsymbol{x_e}-\boldsymbol{y})\right) = \eta^{d-2}G^{\frac{\omega}{c_0}}(\boldsymbol{x_e}-\boldsymbol{y})$$

which ends the proof. □

APPENDIX G

Lemma 53 in a more general case

When the points $\boldsymbol{x}$ and $\boldsymbol{y}$ are not in the paraxial case, an approximation of F can still be found:

Lemma 63: Asymptotic expression of F when the points are not in the paraxial regime

Let $\boldsymbol{x} = (\boldsymbol{x}^\perp, x^{\shortparallel}), \boldsymbol{y} = (\boldsymbol{y}^\perp, y^{\shortparallel}) \in \mathbb{R}^d$, $c_s = \frac{c_0}{v} \in [c_{\min}, c_{\max}]$ and $\omega = \frac{\tilde{\omega}}{\eta} \in \mathcal{B}$, then,

$$\begin{aligned} &F\left(\boldsymbol{x}, \boldsymbol{y}, c_0, c_s = \frac{c_0}{v}, \omega\right) \\ &\quad = \frac{\eta^{\frac{5-d}{2}} c_0^{3-d} a_0^{d-1}}{4\pi^{d-1}\tilde{\omega}^{3-d} v^{\frac{3-d}{2}} (|x||y|)^{\frac{d-1}{2}}} \left(\exp\left(\frac{i\tilde{\omega}}{c_0\eta}(v|y| - |x|)\right)\right. \\ &\quad \times \mathcal{G}\left(\frac{\tilde{\omega} a_0}{\eta^{\frac{1}{2}} c_0}\left(\frac{v\tilde{\boldsymbol{y}}^\perp}{|y|} - \frac{\tilde{\boldsymbol{x}}^\perp}{|x|}\right), \frac{\tilde{\omega} a_0}{c_0}\left(\frac{v(y^{\shortparallel})^2}{|y|^3} - \frac{(x^{\shortparallel})^2}{|x|^3}\right)\right) \\ &\quad \left. \times \left(1 + \eta^{\frac{1}{2}}\mathcal{O}\left(\frac{\tilde{\omega}(x^{\shortparallel})^2|\boldsymbol{x}^\perp|}{c_0|\boldsymbol{x}|^3} + \frac{\tilde{\omega} v (y^{\shortparallel})^2 |\boldsymbol{y}^\perp|}{c_0|\boldsymbol{y}|^3}\right)\right)\right), \end{aligned} \tag{G.1}$$

where $\mathcal{G}$ is defined by (11.7).

Proof. As in the proof of Lemma 53, the computation of the proof is done in $d = 3$. In dimension $d = 2$, the amplitude is different and must be tracked to obtain the result (G.1).

Doing a change of variable $\widetilde{\boldsymbol{x_e}} = \eta^{-\frac{1}{2}}\boldsymbol{x_e}$ in (11.2),

$$F(\boldsymbol{x}, \boldsymbol{y}, c_0, c_s, \omega) = \frac{\eta}{16\pi^2}\int_{\mathcal{A}_0} \frac{\exp\left(\frac{i\tilde{\omega}}{c_0\eta}(v|\eta^{\frac{1}{2}}\widetilde{\boldsymbol{x_e}} - \boldsymbol{y}| - |\eta^{\frac{1}{2}}\widetilde{\boldsymbol{x_e}} - \boldsymbol{x}|)\right)}{|\eta^{\frac{1}{2}}\widetilde{\boldsymbol{x_e}} - \boldsymbol{x}||\eta^{\frac{1}{2}}\widetilde{\boldsymbol{x_e}} - \boldsymbol{y}|} d\sigma(\widetilde{\boldsymbol{x_e}}). \tag{G.2}$$

Then, by a Taylor expansion,

$$\left|\eta^{\frac{1}{2}}\widetilde{\boldsymbol{x_e}} - \boldsymbol{x}\right| = |\boldsymbol{x}| - \eta^{\frac{1}{2}}\widetilde{\boldsymbol{x_e}}^\perp \cdot \frac{\boldsymbol{x}^\perp}{|\boldsymbol{x}|} + \eta\frac{|\widetilde{\boldsymbol{x_e}}^\perp|^2}{2}\frac{(x^{\shortparallel})^2}{|\boldsymbol{x}|^3} + C\eta^{\frac{3}{2}}\frac{(x^{\shortparallel})^2|\boldsymbol{x}^\perp|}{|\boldsymbol{x}|^3}. \tag{G.3}$$

Thus,

$$F(\boldsymbol{x},\boldsymbol{y},c_0,c_s,\omega)=\frac{\eta}{16\pi^2|\boldsymbol{x}||\boldsymbol{y}|}\left(\exp\left(\frac{i\tilde{\omega}}{c_0\eta}(v|\boldsymbol{y}|-|\boldsymbol{x}|)\right)\right.$$
$$\times\int_{a_0\mathcal{A}_0}\exp\left(i\widetilde{\boldsymbol{x_e}}^{\perp}\cdot\frac{\tilde{\omega}}{\eta^{\frac{1}{2}}c_0}\left(\frac{\boldsymbol{x}^{\perp}}{|\boldsymbol{x}|}-\frac{v\boldsymbol{y}^{\perp}}{|\boldsymbol{y}|}\right)+i\frac{|\widetilde{\boldsymbol{x_e}}^{\perp}|^2}{2}\frac{\tilde{\omega}}{c_0}\left(\frac{v(y^{\shortparallel})^2}{|\boldsymbol{y}|^3}-\frac{(x^{\shortparallel})^2}{|\boldsymbol{x}|^3}\right)\right)d\sigma(\widetilde{\boldsymbol{x_e}})$$
$$\left.\times\left(1+\eta^{\frac{1}{2}}\mathcal{O}\left(\frac{\tilde{\omega}(x^{\shortparallel})^2|\boldsymbol{x}^{\perp}|}{c_0|\boldsymbol{x}|^3}+\frac{\tilde{\omega}v(y^{\shortparallel})^2|\boldsymbol{y}^{\perp}|}{c_0|\boldsymbol{y}|^3}\right)\right)\right. \quad \text{(G.4)}$$

which yields the result by the change of variable $\widetilde{\boldsymbol{x_e}}=\frac{\widetilde{\boldsymbol{z_e}}}{a_0}$. □

APPENDIX H

Important lemmas

To carry out the asymptotic analysis, we need to the study of the behavior of the weak limit of $\mathrm{Cov}(n_\varepsilon(\boldsymbol{x}), n_\varepsilon(\boldsymbol{y}))$. This is the topic of the following lemma:

Lemma 64: Covariance approximation

For any deterministic function $f \in \mathcal{C}^1(D)$, $g \in \mathcal{C}^0(D)$,

$$\int_{D\times D} \mathrm{Cov}(n_\varepsilon(\boldsymbol{x}), n_\varepsilon(\boldsymbol{y}))f(\boldsymbol{x})\overline{g}(y)d\boldsymbol{x}d\boldsymbol{y} = \left(\int_{\mathbb{R}^d} \varepsilon^d \Sigma(\boldsymbol{z})d\boldsymbol{z}\right)\int_D f(\boldsymbol{x})\overline{g}(\boldsymbol{x})d\boldsymbol{x} + \mathcal{O}(\varepsilon^{d+1}) \tag{H.1}$$

Proof. By definition and by a change of variable

$$\begin{aligned}\int_{D\times D} \mathrm{Cov}(n_\varepsilon(\boldsymbol{x}), n_\varepsilon(\boldsymbol{y}))f(x)\overline{g}(\boldsymbol{y})d\boldsymbol{x}d\boldsymbol{y} &= \int_{D\times D} \Sigma(\frac{\boldsymbol{x}-\boldsymbol{y}}{\varepsilon})f(x)\overline{g}(\boldsymbol{y})d\boldsymbol{x}d\boldsymbol{y} \\ &= \varepsilon^d \int_D \left(\int_{\frac{D}{\varepsilon}} \Sigma(\boldsymbol{z})f(\varepsilon\boldsymbol{z}+\boldsymbol{y})d\boldsymbol{z}\right)\overline{g}(\boldsymbol{y})d\boldsymbol{y}.\end{aligned}$$

Therefore,

$$\begin{aligned}&\left|\int_{D\times D} \mathrm{Cov}(n_\varepsilon(\boldsymbol{x}), n_\varepsilon(\boldsymbol{y}))f(\boldsymbol{x})\overline{g}(\boldsymbol{y})d\boldsymbol{x}d\boldsymbol{y} - \left(\varepsilon^d \int_{\frac{D}{\varepsilon}} \Sigma(\boldsymbol{z})d\boldsymbol{z}\right)\int_D f(\boldsymbol{x})\overline{g}(\boldsymbol{x})d\boldsymbol{x}\right| \\ &\qquad \lesssim \varepsilon^d \int_{\frac{D}{\varepsilon}} \left(\int_D |g(\boldsymbol{y})|\Big|f(\varepsilon\boldsymbol{z}+\boldsymbol{y}) - f(\boldsymbol{y})\Big|d\boldsymbol{y}\right)|\Sigma(z)|d\boldsymbol{z} \\ &\qquad \lesssim \varepsilon^{d+1}\left(\int_{\frac{D}{\varepsilon}} |\Sigma(\boldsymbol{z})||\boldsymbol{z}|d\boldsymbol{z}\right)\left(\int_D |\nabla f(\boldsymbol{y})||g(\boldsymbol{y})|\Big|d\boldsymbol{y}\right)\end{aligned}$$

Finally,

$$\int_{\frac{D}{\varepsilon}} \Sigma(\boldsymbol{z})d\boldsymbol{z} = \int_{\mathbb{R}^d} \Sigma(\boldsymbol{z})d\boldsymbol{z} + \mathcal{O}(\varepsilon)$$

as Σ has exponential decay. This yields the result. □

We also prove that the term $\mathbb{E}[u_\varepsilon - u_0]$ is small.

Lemma 65: Estimation of $\mathbb{E}[u_\varepsilon - u_0]$

Let $u_\varepsilon \in H^1_{loc}(\mathbb{R}^d)$ be the solution of (12.3) and $u_0 \in H^1_{loc}(\mathbb{R}^d)$ be the associated homogenized solution that solved (12.4). For all $\boldsymbol{x_e}, \boldsymbol{x_r} \in \mathcal{A}$, $\omega \in \mathcal{B}$, it holds

$$\mathbb{E}\left[(u_\varepsilon - u_0)(\boldsymbol{x_e}, \boldsymbol{x_r}, \omega)\right] \lesssim C\varepsilon^d \left(\frac{\omega}{c_0}\right)^6 \tag{H.2}$$

for some $C > 0$ independent on $\boldsymbol{x_e}$, $\boldsymbol{x_r}$, ω and ε.

Proof. Our starting point is (7.2) which reads here as:

$$u_\varepsilon(y) = u_0(y) + \int_D k^2 \psi_\varepsilon G^k(\cdot, y) u_\varepsilon,$$

where $k^2 = \frac{\omega^2}{c_0^2}$, and $\boldsymbol{y} \in \mathbb{R}^d$. By iterating in the previous equation, it holds that:

$$\begin{aligned} u_\varepsilon(y) = u_0(y) &+ \int_D k^2 \psi_\varepsilon(x) G^k(x, y) u_0(x) dx \\ &+ k^4 \int_D \int_D \psi_\varepsilon(x_1)\psi_\varepsilon(x_2) G^k(x_2, x_1) G^k(x_1, y) u_0(x_2) dx_1 dx_2 \\ &+ k^6 \int_D \left(\int_D \int_D \psi_\varepsilon(x_1)\psi_\varepsilon(x_2) G^k(x_3, x_2) G^k(x_2, x_1) G^k(x_1, y) dx_1 dx_2 \right) \psi_\varepsilon(x_3) u_\varepsilon(x_3) dx_3 \\ := u_0(y) &+ \int_D k^2 \psi_\varepsilon G^k(x, y) u_0(x) dx + k^4 I + k^6 II. \end{aligned} \tag{H.3}$$

Since ψ has zero-mean, we have that

$$\mathbb{E}[\int_D k^2 \psi_\varepsilon G^k(x, y) u_0(x) dx] = 0.$$

We treat both terms I and II independently. It holds that,

$$\mathbb{E}[I] = \int_D \int_D \mathrm{Cov}\left[\psi_\varepsilon(x_1)\psi_\varepsilon(x_2)\right] u_0(x_2) G^k(x_2, x_1) G^k(x_1, y) dx_1 dx_2.$$

By Lemma 64, $\mathbb{E}[I] = \mathcal{O}\left(\varepsilon^d \left\|G^k\right\|^2_{L^\infty(D)} \|u_0\|_{L^\infty(D)}\right)$.

To estimate $\mathbb{E}[II]$, we use [154, Lemma 2.1] which states that for random variable with covariance Σ such that $\Sigma^{\frac{1}{2}} \in L^1(\Omega)$ then,

$$|\mathbb{E}[\psi(x_1)\psi(x_2)\psi(x_3)\psi(x_4)]| \leq C \sup_{\{y_k\}_{1\leq k\leq 4} = \{x_k\}_{1\leq k\leq 4}} \Sigma(y_1 - y_3)^{\frac{1}{2}} \Sigma(y_2 - y_4)^{\frac{1}{2}}.$$

Then, by the uniform boundness of $u_\varepsilon \in L^2(D)$.

$$\begin{aligned}
\mathbb{E}\left[II^2\right] &= \mathbb{E}\left[\left|\int_D \left(\iint_{D^2} \psi_\varepsilon(x_1)\psi_\varepsilon(x_2)G^k(x_3,x_2)G^k(x_2,x_1)G^k(x_1,y)dx_1dx_2\right)\psi_\varepsilon(x_3)u_\varepsilon(x_3)dx_3\right|^2\right] \\
&\leq \mathbb{E}\left[\int_D \left|\iint_{D^2} \psi_\varepsilon(x_1)\psi_\varepsilon(x_2)G^k(x_3,x_2)G^k(x_2,x_1)G^k(x_1,y)dx_1dx_2\right|^2\right. \\
&\qquad \left.\times \int_D \psi_\varepsilon(x_3)^2|u_\varepsilon(x_3)|^2dx_3\right] \\
&\leq C\left\|u^i\right\|_{H^1(D)} \int_D \iiiint_{D^4} \mathbb{E}\left[\psi_\varepsilon(x_1)\psi_\varepsilon(x_2)\psi_\varepsilon(x_3)\psi_\varepsilon(x_4)\right] \\
&\qquad \times G^k(z,x_2)G^k(x_2,x_1)G^k(x_1,y)\overline{G^k}(z,x_4)\overline{G^k}(x_4,x_3)\overline{G^k}(x_3,y)dx_1dx_2dx_3dx_4dz \\
&\leq C\left\|u^i\right\|_{H^1(D)} \varepsilon^{2d}\left\|G^k\right\|^6_{L^2(D)}.
\end{aligned} \tag{H.4}$$

Therefore, we conclude that

$$\begin{aligned}
|\mathbb{E}\left[u_\varepsilon(y)-u_0(y)\right]| &\leq k^4\mathbb{E}[I]+k^6\mathbb{E}[II] \\
&\leq C\varepsilon^d\left(k^4\left\|G^k\right\|^2_{L^2(D)}\|u_0\|_{L^\infty(D)}+\left\|u^i\right\|_{H^1(D)}\left\|G^k\right\|^3_{L^2(D)}\right).
\end{aligned} \tag{H.5}$$

□

PART IV

CONCLUSION AND PERSPECTIVES

CHAPTER 14

Conclusion and perspectives

The main goal of the thesis was to establish a mathematical framework for understanding and analyzing the experiment of Aubry to establish an estimator of the effective speed of sound inside the soft biological tissues by using ultrasound measurements. In order to design a quantitative estimator, the first step was to quantitatively link the parameters of interest with the ultrasound measurements corresponding to the scattered field. As the backscattered field originates form the small heterogeneities of the tissues, we modeled the tissues by micro-structured heterogeneous bounded media in which lie numerous unresolved and randomly distributed scatterers. This model was used throughout the entire thesis.
While the Born approximation is commonly used to describe the backscattered field, we decided to use quantitative stochastic homogenization. A high-order asymptotic expansion was derived, from which we were able to define the effective speed of sound inside the tissue. The derivation of this expansion required to use state of the art techniques such as the multiscale variance inequality that was introduced only recently. Furthermore, we had to introduce and characterize boundary layer correctors for a transmission problem in the stochastic homogenization framework. The formalism that we propose could be extended to more complex transmission problems, for example between several domains, each having their own random distribution of unresolved scatterers. The model considered in this thesis allows to recover a constant homogenized speed of sound but could be extended to take into account the interfaces between the different layers of the tissues (fat, muscle...). Moreover, the effective speed of sound is actually not constant in each layer, and one could also want to model these variations on the effective speed of sound. This could be possible by adding a dependency on the slow variable $x \in D$ in the coefficients n and a of (3.11). However, this would require the introduction of local correctors for each fixed $x \in D$. The study of the boundary corrector problem might also be more complex.

The homogenization model that we developed was then used to establish an estimator of the speed of sound. Before using the newly derived model, we carried out an asymptotic analysis in the paraxial regime of the point spread function with respect to the backpropagation speed of sound c_s. This allowed to point out the effect of a mismatch between c_s and the actual speed of sound c_0 on the focal spot. In particular, its

position and shape of the focal spot on the image are altered and the global displayed amplitude diminishes. By maximizing this amplitude, one recovers the speed of sound c_0 inside the medium. In the complex heterogeneous medium, the picture is different, as there is no isolated target resulting in a focal spot on the image. The image is in fact a speckle pattern. However, by an asymptotic analysis of the imaging function, we are able to identify that the displayed amplitude at $\boldsymbol{x_s}$ is similar to the amplitude that would be produced by a virtual reflector at $\boldsymbol{x}_f(\boldsymbol{x_s}, \frac{c_s}{c_0}) = (\tilde{\boldsymbol{x_s}}^{\perp}\frac{c_0^2}{c_s^2}, x_s^{||}\frac{c_0}{c_s})$. A further study using the stationary and ergodic assumptions allows to build an estimator of the effective speed of sound.
In this entire study, we assumed the density or equivalently a to be constant and worked only on the variation of the speed of sound or equivalently the variation of n. The theory that we developed could be extended to the cases where both coefficients vary. Several differences must be pointed out. First, it would not only require to characterize F introduced by (11.2) but also

$$F_i^a(\boldsymbol{x}, \boldsymbol{y}, c_0, c_s, \omega) := \left\langle e_i \cdot \nabla G^{\frac{\omega}{c_s}}(\cdot - \boldsymbol{y}), G^{\frac{\omega}{c_0}}(\cdot - \boldsymbol{x}) \right\rangle_{\mathcal{A}}, \tag{14.1}$$

for $i = 1...d$, as the gradient of G^k is involved in the approximation of Theorem 39. Moreover, it requires to prove an equivalent of Lemma 64 when both coefficients a and n are varying, and in particular to characterize the limit of the covariance function of

$$I_\varepsilon(F) := \int_D F(x) \cdot (a^\star - a)(e_i + \nabla\phi_i)(\frac{x}{\varepsilon})dx,$$

for $F \in L^2(D)$. This was the topic of [156] for Gaussian correlated fields in unbounded domains and for $F \in \mathcal{C}_c^\infty(\mathbb{R}^d)$.
Nevertheless, by adding a x dependency on a or n, the study of the inverse problem of Part III would remain substantially identical. Though, the recovered speed of sound $\hat{c}_0(z)$ would surely not be an estimation of the local speed of sound at depth z but under certain geometries and hypotheses, it would be the integrated speed of sound satisfying [17]:

$$\frac{z}{\hat{c}_0(z)} = \int_0^z \frac{d\tilde{z}}{c(\tilde{z})}, \tag{14.2}$$

where c is the true speed of sound.

Finally, the model that we derived is very flexible and allows to model complex micro-layered media such as the biological tissues. We are able to capture the micro-scale effects on the macroscopic behavior of the effective properties of the medium. In particular, the resulting homogenized medium that we obtain in Part II is not always an isotropic medium. Our model could be used for the wave propagation in muscles which are anisotropic structures composed of elongated fibers. The mathematical framework that we developed could be also used to study other wave propagation problems (linear elasticity, Maxwell equations) and be used in other case studies such

as the wave propagation inside the earth crust or for industrial non-destructive testing applications.

BIBLIOGRAPHY

Bibliography

[1] Reimar Pohlman. Die ultraschalltherapie. *Stuttgart. Thieme.*, pages 17–20, 1940.

[2] NHS England and N Improvement. Diagnostic imaging dataset annual statistical release. london: Department of health, 2024.

[3] Jin Hyun Kim, Sunmi Yeo, Min Kim, Sangbum Kye, Youngbae Lee, and Taikyong Song. A smart-phone based portable ultrasound imaging system for point-of-care applications. In *2017 10th International Congress on Image and Signal Processing, BioMedical Engineering and Informatics (CISP-BMEI)*, pages 1–5. IEEE, 2017.

[4] K Kirk Shung. *Diagnostic ultrasound: Imaging and blood flow measurements*. CRC press, 2005.

[5] Boris Tutschek. Simple virtual reality display of fetal volume ultrasound. *Ultrasound in Obstetrics and Gynecology: The Official Journal of the International Society of Ultrasound in Obstetrics and Gynecology*, 32(7):906–909, 2008.

[6] Norman Bleistein, Jack K Cohen, JW Stockwell Jr, and JG Berryman. Mathematics of multidimensional seismic imaging, migration, and inversion. interdisciplinary applied mathematics, vol 13. *Appl. Mech. Rev.*, 54(5):B94–B96, 2001.

[7] Mathias Fink. Time reversal of ultrasonic fields. i. basic principles. *IEEE transactions on ultrasonics, ferroelectrics, and frequency control*, 39(5):555–566, 1992.

[8] Guy Cloutier, Francois Destrempes, Fei Yu, and An Tang. Quantitative ultrasound imaging of soft biological tissues: a primer for radiologists and medical physicists. *Insights Imaging*, 12(1):127, Sep 2021.

[9] Ali Mohammad Pirmoazen, Anjali Khurana, Ahmed El Kaffas, and Aya Kamaya. Quantitative ultrasound approaches for diagnosis and monitoring hepatic steatosis in nonalcoholic fatty liver disease. *Theranostics*, 10(9):4277–4289, Mar 2020.

[10] Tadashi Yamaguchi. Basic concept and clinical applications of quantitative ultrasound (qus) technologies. *Journal of Medical Ultrasonics*, 48(4):391–402, 2021.

[11] B. H. Malik and J. C. Klock. Breast cyst fluid analysis correlations with speed of sound using transmission ultrasound. *Academic Radiology*, 26(1):76–85, 2019.

[12] C. Li, N. Duric, P. Littrup, and L. Huang. In vivo breast sound-speed imaging with ultrasound tomography. *Ultrasound in Medicine & Biology*, 35(10):1615–1628, 10 2009.

[13] R. G. Pratt, L. Huang, N. Duric, and P. Littrup. Sound-speed and attenuation imaging of breast tissue using waveform tomography of transmission ultrasound data. In *Medical Imaging 2007: Physics of Medical Imaging*, volume 6510, page 65104S. International Society for Optics and Photonics, 03 2007.

[14] C. Li, G. Y. Sandhu, M. Boone, and N. Duric. Breast imaging using waveform attenuation tomography. In *Medical Imaging 2017: Ultrasonic Imaging and Tomography*, volume 10139, page 101390A. International Society for Optics and Photonics, 2017.

[15] B. Malik, R. Terry, J. Wiskin, and M. Lenox. Quantitative transmission ultrasound tomography: Imaging and performance characteristics. *Medical Physics*, 45(7):3063–3075, 2018.

[16] S. Johnson, T. Abbott, R. Bell, M. Berggren, D. Borup, D. Robinson, J. Wiskin, S. Olsen, and B. Hanover. Non-invasive breast tissue characterization using ultrasound speed and attenuation. In M. P. André, I. Akiyama, M. Andre, W. Arnold, J. Bamber, V. Burov, N. Chubachi, K. Erikson, H. Ermert, M. Fink, W. S. Gan, B. Granz, J. Greenleaf, J. Hu, J. P. Jones, P. Khuri-Yakub, P. Laugier, H. Lee, S. Lees, V. M. Levin, R. Maev, L. Masotti, A. Nowicki, W. O'Brien, M. Prasad, P. Rafter, D. Rouseff, J. Thijssen, B. Tittmann, P. Tortoli, A. Van der Steen, R. Waag, and P. Wells, editors, *Acoustical Imaging*, Acoustical Imaging, pages 147–154. Springer Netherlands, 2007.

[17] Flavien Bureau. *Multi-dimensional analysis of the reflection matrix for quantitative ultrasound imaging*. Theses, Université Paris sciences et lettres, July 2023.

[18] Mitia Duerinckx, Antoine Gloria, and Felix Otto. The structure of fluctuations in stochastic homogenization. *Communications in Mathematical Physics*, 377(1):259–306, 2020.

[19] Mitia Duerinckx, Antoine Gloria, and Felix Otto. Robustness of the pathwise structure of fluctuations in stochastic homogenization. *Probability theory and related fields*, 178:531–566, 2020.

[20] Jacques Curie and Pierre Curie. Développement par compression de l'électricité polaire dans les cristaux hémièdres à faces inclinées. *Bulletin de minéralogie*, 3(4):90–93, 1880.

[21] Warren P Mason. Piezoelectricity, its history and applications. *The journal of the Acoustical Society of America*, 70(6):1561–1566, 1981.

[22] Paul Langevin. The employment of ultra-sonic waves for echo sounding. *Hydrographic Rev*, 2(1):57–91, 1924.

[23] FA Duck and A Thomas. Paul langevin (1872-1946): The father of ultrasonics. *Medical Physics*, 10(1), 2022.

[24] Francis Duck. Ultrasound–the first fifty years. *Med Phys Int J. History of Medical Physics*, 5:470–498, 2020.

[25] Pohlman R Lassen sich durch Ultraschall. therapeutische wirkungen erzielen. *Forsch u Fortsch*, 15(14):187–188, 1939.

[26] Joseph Woo. A short history of the development of ultrasound in obstetrics and gynecology. *History of Ultrasound in Obstetrics and Gynecology*, 3:1–25, 2002.

[27] WN McDicken and CM Moran. History of medical ultrasound. *MEDICAL PHYSICS INTERNATIONAL Journal*, Special Issue History of Medical Physics 6, 1939.

[28] Alan Gordon Fraser. Inge edler and the origins of clinical echocardiography. *European Journal of Echocardiography*, 2(1), 2001.

[29] Jørgen Arendt Jensen. Medical ultrasound imaging. *Progress in biophysics and molecular biology*, 93(1-3):153–165, 2007.

[30] LFGON CALVES, W Lee, J Espinoza, and R Romero. Examination of the fetal heart by four-dimensional (4d) ultrasound with spatio-temporal image correlation (stic). *Ultrasound Obstet Gynecol*, 27:336–348, 2006.

[31] Douglas L Miller, Nadine B Smith, Michael R Bailey, Gregory J Czarnota, Kullervo Hynynen, Inder Raj S Makin, and Bioeffects Committee of the American Institute of Ultrasound in Medicine. Overview of therapeutic ultrasound applications and safety considerations. *Journal of ultrasound in medicine*, 31(4):623–634, 2012.

[32] SV Ranganayakulu, N Ramakoteswara Rao, and Leena Gahane. Ultrasound applications in medical sciences. *IJMTER*, 3(02):287–293, 2016.

[33] Rongrong Guo, Guolan Lu, Binjie Qin, and Baowei Fei. Ultrasound imaging technologies for breast cancer detection and management: a review. *Ultrasound in medicine & biology*, 44(1):37–70, 2018.

[34] Sylvain Poinard, Alice Ganeau, Maxime Lafond, Oliver Dorado, Stefan Catheline, Cyril Lafon, Florent Aptel, Gilles Thuret, and Philippe Gain. Ultrasound applications in ophthalmology: a review. *IRBM*, page 100828, 2024.

[35] Alan D Pierce. *Basic linear acoustics*. Springer, , 2007.

[36] Mickael Tanter and Mathias Fink. Ultrafast imaging in biomedical ultrasound. *IEEE transactions on ultrasonics, ferroelectrics, and frequency control*, 61(1):102–119, 2014.

[37] Claire Prada and Mathias Fink. Eigenmodes of the time reversal operator: A solution to selective focusing in multiple-target media. *Wave motion*, 20(2):151–163, 1994.

[38] Claire Prada, Sébastien Manneville, Dimitri Spoliansky, and Mathias Fink. Decomposition of the time reversal operator: Detection and selective focusing on two scatterers. *The Journal of the Acoustical Society of America*, 99(4):2067–2076, 1996.

[39] Claire Prada and Jean-Louis Thomas. Experimental subwavelength localization of scatterers by decomposition of the time reversal operator interpreted as a covariance matrix. *The Journal of the Acoustical Society of America*, 114(1):235–243, 2003.

[40] Mickaël Tanter, Jean-Louis Thomas, and Mathias Fink. Time reversal and the inverse filter. *The Journal of the Acoustical Society of America*, 108(1):223–234, 2000.

[41] Michael Tanter, J-F Aubry, J Gerber, J-L Thomas, and M Fink. Optimal focusing by spatio-temporal inverse filter. i. basic principles. *The Journal of the Acoustical Society of America*, 110(1):37–47, 2001.

[42] J-F Aubry, M Tanter, J Gerber, J-L Thomas, and M Fink. Optimal focusing by spatio-temporal inverse filter. ii. experiments. application to focusing through absorbing and reverberating media. *The Journal of the Acoustical Society of America*, 110(1):48–58, 2001.

[43] Sébastien Michel Popoff, Alexandre Aubry, Geoffroy Lerosey, Mathias Fink, Albert-Claude Boccara, and Sylvain Gigan. Exploiting the time-reversal operator for adaptive optics, selective focusing and scattering pattern analysis. In *2012 Conference on Lasers and Electro-Optics (CLEO)*, pages 1–2. IEEE, 2012.

[44] Claire Prada, Mickael Tanter, and Mathias Fink. Flaw detection in solid with the dort method. In *1997 IEEE Ultrasonics Symposium Proceedings. An International Symposium (Cat. No. 97CH36118)*, volume 1, pages 679–683. IEEE, 1997.

[45] Patrick Tremblay, Daniel Richard, and H Ann. Development and validation of a full matrix capture solution. In *9th International Conference on NDE in Relation to Structural Integrity for Nuclear and Pressurized Components*, pages 457–466, 2012.

[46] William Lambert, Laura A Cobus, Mathieu Couade, Mathias Fink, and Alexandre Aubry. Reflection matrix approach for quantitative imaging of scattering media. *Physical Review X*, 10(2):021048, 2020.

[47] William Lambert, Justine Robin, Laura A Cobus, Mathias Fink, and Alexandre Aubry. Ultrasound matrix imaging—part i: The focused reflection matrix, the f-factor and the role of multiple scattering. *IEEE Transactions on Medical Imaging*, 41(12):3907–3920, 2022.

[48] William Lambert, Laura A Cobus, Justine Robin, Mathias Fink, and Alexandre Aubry. Ultrasound matrix imaging part ii: The distortion matrix for aberration correction over multiple isoplanatic patches. *IEEE Transactions on Medical Imaging*, 41(12):3921–3938, 2022.

[49] Cécile Brûtt, Benoit Gérardin, Alexandre Aubry, Arnaud Derode, and Claire Prada. A model of ultrasonic reflection matrix for multiple scattering evaluation. In *Forum Acusticum*, pages 1419–1419, 2020.

[50] Cécile Brütt, Alexandre Aubry, Benoît Gérardin, Arnaud Derode, and Claire Prada. Weight of single and recurrent scattering in the reflection matrix of complex media. *Physical Review E*, 106(2):025001, 2022.

[51] Cécile Brutt. *Imagerie ultrasonore multi-éléments de solides anisotropes et multiplement diffusants par analyse de la matrice de réflexion*. PhD thesis, Université Paris sciences et lettres, 2021.

[52] Francis A Duck. Acoustic properties of tissue at ultrasonic frequencies. *Physical Properties of Tissues*, pages 73–135, 1990.

[53] Alexandre Aubry and Arnaud Derode. Multiple scattering of ultrasound in weakly inhomogeneous media: Application to human soft tissues. *The Journal of the Acoustical Society of America*, 129(1):225–233, 2011.

[54] Max Born and Emil Wolf. *Principles of optics: electromagnetic theory of propagation, interference and diffraction of light*. Elsevier, 2013.

[55] Josselin Garnier and George Papanicolaou. *Passive imaging with ambient noise*. Cambridge University Press, 2016.

[56] AP Sarvazyan, AR Skovoroda, SY Emelianov, JB Fowlkes, JG Pipe, RS Adler, RB Buxton, and PL Carson. Biophysical bases of elasticity imaging. *Acoustical imaging*, pages 223–240, 1995.

[57] Arsenii V Telichko, Rehman Ali, Thurston Brevett, Huaijun Wang, Jose G Vilches-Moure, Sukumar U Kumar, Ramasamy Paulmurugan, and Jeremy J Dahl. Noninvasive estimation of local speed of sound by pulse-echo ultrasound in a rat model of nonalcoholic fatty liver. *Physics in Medicine & Biology*, 67(1):015007, 2022.

[58] Thomas Deffieux, Charlie Demené, and Mickael Tanter. Functional ultrasound imaging: a new imaging modality for neuroscience. *Neuroscience*, 474:110–121, 2021.

[59] Jonathan Ophir, Ignacio Cespedes, Hari Ponnekanti, Youseph Yazdi, and Xin Li. Elastography: a quantitative method for imaging the elasticity of biological tissues. *Ultrasonic imaging*, 13(2):111–134, 1991.

[60] J-L Gennisson, Thomas Deffieux, Mathias Fink, and Michaël Tanter. Ultrasound elastography: principles and techniques. *Diagnostic and interventional imaging*, 94(5):487–495, 2013.

[61] Hiroyasu Morikawa, Katsuhiko Fukuda, Sawako Kobayashi, Hideki Fujii, Shuji Iwai, Masaru Enomoto, Akihiro Tamori, Hiroki Sakaguchi, and Norifumi Kawada. Real-time tissue elastography as a tool for the noninvasive assessment of liver stiffness in patients with chronic hepatitis c. *Journal of gastroenterology*, 46:350–358, 2011.

[62] Rosa MS Sigrist, Joy Liau, Ahmed El Kaffas, Maria Cristina Chammas, and Juergen K Willmann. Ultrasound elastography: review of techniques and clinical applications. *Theranostics*, 7(5):1303, 2017.

[63] Minghua Xu and Lihong V Wang. Photoacoustic imaging in biomedicine. *Review of scientific instruments*, 77(4), 2006.

[64] Amalina Binte Ebrahim Attia, Ghayathri Balasundaram, Mohesh Moothanchery, US Dinish, Renzhe Bi, Vasilis Ntziachristos, and Malini Olivo. A review of clinical photoacoustic imaging: Current and future trends. *Photoacoustics*, 16:100144, 2019.

[65] Peter Frinking, Tim Segers, Ying Luan, and François Tranquart. Three decades of ultrasound contrast agents: a review of the past, present and future improvements. *Ultrasound in medicine & biology*, 46(4):892–908, 2020.

[66] Stefanie Dencks and Georg Schmitz. Ultrasound localization microscopy. *Zeitschrift für Medizinische Physik*, 2023.

[67] Eric Betzig, George H Patterson, Rachid Sougrat, O Wolf Lindwasser, Scott Olenych, Juan S Bonifacino, Michael W Davidson, Jennifer Lippincott-Schwartz, and Harald F Hess. Imaging intracellular fluorescent proteins at nanometer resolution. *science*, 313(5793):1642–1645, 2006.

[68] Samuel T Hess, Thanu PK Girirajan, and Michael D Mason. Ultra-high resolution imaging by fluorescence photoactivation localization microscopy. *Biophysical journal*, 91(11):4258–4272, 2006.

[69] Michael J Rust, Mark Bates, and Xiaowei Zhuang. Sub-diffraction-limit imaging by stochastic optical reconstruction microscopy (storm). *Nature methods*, 3(10):793–796, 2006.

[70] Olivier Couture, Benoit Besson, Gabriel Montaldo, Mathias Fink, and Mickael Tanter. Microbubble ultrasound super-localization imaging (musli). In *2011 IEEE International Ultrasonics Symposium*, pages 1285–1287. IEEE, 2011.

[71] Kirsten Christensen-Jeffries, Olivier Couture, Paul A Dayton, Yonina C Eldar, Kullervo Hynynen, Fabian Kiessling, Meaghan O'Reilly, Gianmarco F Pinton, Georg Schmitz, Meng-Xing Tang, et al. Super-resolution ultrasound imaging. *Ultrasound in medicine & biology*, 46(4):865–891, 2020.

[72] Benoit Beliard, Chaimae Ahmanna, Elodie Tiran, Kadia Kanté, Thomas Deffieux, Mickael Tanter, Fatiha Nothias, Sylvia Soares, and Sophie Pezet. Ultrafast doppler imaging and ultrasound localization microscopy reveal the complexity of vascular rearrangement in chronic spinal lesion. *Scientific Reports*, 12(1):6574, 2022.

[73] Monica Siepmann, Georg Schmitz, Jessica Bzyl, Moritz Palmowski, and Fabian Kiessling. Imaging tumor vascularity by tracing single microbubbles. In *2011 IEEE International Ultrasonics Symposium*, pages 1906–1909. IEEE, 2011.

[74] Melvin Linzer. The ultrasonic tissue characterization seminar: an assessment. *Journal of Clinical Ultrasound*, 4(2):97–100, 1976.

[75] Jonathan Mamou and Michael L Oelze. *Quantitative ultrasound in soft tissues*. Springer, 2013.

[76] JC Bamber and CR Hill. Acoustic properties of normal and cancerous human liver—i. dependence on pathological condition. *Ultrasound in medicine & biology*, 7(2):121–133, 1981.

[77] Marion Imbault, Alex Faccinetto, Bruno-Félix Osmanski, Antoine Tissier, Thomas Deffieux, Jean-Luc Gennisson, Valérie Vilgrain, and Mickaël Tanter. Robust sound speed estimation for ultrasound-based hepatic steatosis assessment. *Physics in Medicine & Biology*, 62(9):3582, 2017.

[78] Marion Imbault, Marco Dioguardi Burgio, Alex Faccinetto, Maxime Ronot, Hanna Bendjador, Thomas Deffieux, Emma Ollivier Triquet, Pierre-Emmanuel Rautou, Laurent Castera, Jean-Luc Gennisson, et al. Ultrasonic fat fraction quantification using in vivo adaptive sound speed estimation. *Physics in Medicine & Biology*, 63(21):215013, 2018.

[79] Marco Dioguardi Burgio, Marion Imbault, Maxime Ronot, Alex Faccinetto, Bernard E Van Beers, Pierre-Emmanuel Rautou, Laurent Castera, Jean-Luc Gennisson, Mickael Tanter, and Valérie Vilgrain. Ultrasonic adaptive sound speed estimation for the diagnosis and quantification of hepatic steatosis: a pilot study. *Ultraschall in der Medizin-European Journal of Ultrasound*, 40(06):722–733, 2019.

[80] SW Flax and Matthew O'Donnell. Phase-aberration correction using signals from point reflectors and diffuse scatterers: Basic principles. *IEEE transactions on ultrasonics, ferroelectrics, and frequency control*, 35(6):758–767, 1988.

[81] Levin Nock, Gregg E Trahey, and Stephen W Smith. Phase aberration correction in medical ultrasound using speckle brightness as a quality factor. *The Journal of the Acoustical Society of America*, 85(5):1819–1833, 1989.

[82] David Napolitano, Ching-Hua Chou, Glen McLaughlin, Ting-Lan Ji, Larry Mo, Derek DeBusschere, and Robert Steins. Sound speed correction in ultrasound imaging. *Ultrasonics*, 44:e43–e46, 2006.

[83] MH Cho, LH Kang, JS Kim, and SY Lee. An efficient sound speed estimation method to enhance image resolution in ultrasound imaging. *Ultrasonics*, 49(8):774–778, 2009.

[84] KW Hollman, KW Rigby, and M O'donnell. Coherence factor of speckle from a multi-row probe. In *1999 IEEE Ultrasonics Symposium. Proceedings. International Symposium (Cat. No. 99CH37027)*, volume 2, pages 1257–1260. IEEE, 1999.

[85] Gabriel Montaldo, Mickaël Tanter, Jérémy Bercoff, Nicolas Benech, and Mathias Fink. Coherent plane-wave compounding for very high frame rate ultrasonography and transient elastography. *IEEE transactions on ultrasonics, ferroelectrics, and frequency control*, 56(3):489–506, 2009.

[86] Ho-Chul Shin, Richard Prager, Henry Gomersall, Nick Kingsbury, Graham Treece, and Andrew Gee. Estimation of average speed of sound using deconvolution of medical ultrasound data. *Ultrasound in medicine & biology*, 36(4):623–636, 2010.

[87] Ho-Chul Shin, Richard Prager, Henry Gomersall, Nick Kingsbury, Graham Treece, and Andrew Gee. Estimation of speed of sound in dual-layered media using medical ultrasound image deconvolution. *Ultrasonics*, 50(7):716–725, 2010.

[88] William Lambert, Laura A Cobus, Thomas Frappart, Mathias Fink, and Alexandre Aubry. Distortion matrix approach for ultrasound imaging of random scattering media. *Proceedings of the National Academy of Sciences*, 117(26):14645–14656, 2020.

[89] Michael Jaeger, Georg Held, Sarah Peeters, Stefan Preisser, Michael Grünig, and Martin Frenz. Computed ultrasound tomography in echo mode for imaging speed of sound using pulse-echo sonography: proof of principle. *Ultrasound in Medicine & Biology*, 41(1):235–250, Jan 2015.

[90] Micha Feigin, Daniel Freedman, and Brian W Anthony. A deep learning framework for single-sided sound speed inversion in medical ultrasound. *IEEE Transactions on Biomedical Engineering*, 67(4):1142–1151, 2019.

[91] Stephen J Norton and Melvin Linzer. Ultrasonic reflectivity imaging in three dimensions: exact inverse scattering solutions for plane, cylindrical, and spherical apertures. *IEEE Transactions on biomedical engineering*, (2):202–220, 1981.

[92] Habib Ammari and Hyeonbae Kang. *Polarization and moment tensors: with applications to inverse problems and effective medium theory*, volume 162. Springer Science & Business Media, 2007.

[93] Timothée Noé Pouchon. Effective models and numerical homogenization methods for long time wave propagation in heterogeneous media. Technical report, EPFL, 2017.

[94] Milton Abramowitz and Irene A Stegun. *Handbook of mathematical functions with formulas, graphs, and mathematical tables*, volume 55. US Government printing office, 1968.

[95] Jean-Pierre Fouque, Josselin Garnier, George Papanicolaou, and Knut Solna. *Wave propagation and time reversal in randomly layered media*, volume 56. Springer Science & Business Media, 2007.

[96] Alain Bensoussan, Jacques-Louis Lions, and George Papanicolaou. *Asymptotic analysis for periodic structures*, volume 374. American Mathematical Soc., 2011.

[97] Guillaume Bal and Leonid Ryzhik. Time reversal and refocusing in random media. *SIAM Journal on Applied Mathematics*, 63(5):1475–1498, 2003.

[98] Liliana Borcea, George Papanicolaou, Chrysoula Tsogka, and James Berryman. Imaging and time reversal in random media. *Inverse Problems*, 18(5):1247, 2002.

[99] Mathias Fink and Claire Prada. Acoustic time-reversal mirrors. *Inverse problems*, 17(1):R1, 2001.

[100] Liliana Borcea, Josselin Garnier, George Papanicolaou, and Chrysoula Tsogka. Enhanced statistical stability in coherent interferometric imaging. *Inverse problems*, 27(8):085004, 2011.

[101] Liliana Borcea, George Papanicolaou, and Chrysoula Tsogka. Adaptive interferometric imaging in clutter and optimal illumination. *Inverse problems*, 22(4):1405, 2006.

[102] Liliana Borcea, George Papanicolaou, and Chrysoula Tsogka. Interferometric array imaging in clutter. *Inverse Problems*, 21(4):1419, 2005.

[103] Liliana Borcea, George Papanicolaou, and Chrysoula Tsogka. Coherent interferometric imaging in clutter. 2008.

[104] Nikolai M Shapiro, Michel Campillo, Laurent Stehly, and Michael H Ritzwoller. High-resolution surface-wave tomography from ambient seismic noise. *Science*, 307(5715):1615–1618, 2005.

[105] R Alonso, Liliana Borcea, George Papanicolaou, and Chrysoula Tsogka. Detection and imaging in strongly backscattering randomly layered media. *Inverse Problems*, 27(2):025004, 2011.

[106] Liliana Borcea, George Papanicolaou, and Chrysoula Tsogka. Time and direction of arrival detection and filtering for imaging in strongly scattering random media. *Waves in Random and Complex Media*, 27(4):664–689, 2017.

[107] David Colton and Rainer Kress. *Inverse Acoustic and Electromagnetic Scattering Theory*. Applied Mathematical Sciences. Springer New York, New York, NY, 3 edition, 2013. Published: 26 October 2012.

[108] Habib Ammari, Josselin Garnier, Wenjia Jing, Hyeonbae Kang, Mikyoung Lim, Knut Sølna, and Han Wang. *Mathematical and statistical methods for multistatic imaging*, volume 2098. Springer, 2013.

[109] Alexandre Aubry and Arnaud Derode. Detection and imaging in a random medium: A matrix method to overcome multiple scattering and aberration. *Journal of Applied Physics*, 106(4), 2009.

[110] Antton Goïcoechea, Cécile Brütt, Arthur Le Ber, Flavien Bureau, William Lambert, Claire Prada, Arnaud Derode, and Alexandre Aubry. Reflection measurement of the scattering mean free path at the onset of multiple scattering, 2024.

[111] Paul A Martin. Acoustic scattering by inhomogeneous obstacles. *SIAM Journal on Applied Mathematics*, 64(1):297–308, 2003.

[112] Kimberly Kilgore, Shari Moskow, and John C Schotland. Inverse born series for scalar waves. *Journal of Computational Mathematics*, pages 601–614, 2012.

[113] Kimberly Kilgore, Shari Moskow, and John C Schotland. Convergence of the born and inverse born series for electromagnetic scattering. *Applicable analysis*, 96(10):1737–1748, 2017.

[114] Shari Moskow and John C Schotland. Numerical studies of the inverse born series for diffuse waves. *Inverse Problems*, 25(9):095007, 2009.

[115] Simon Arridge, Shari Moskow, and John C Schotland. Inverse born series for the calderon problem. *Inverse Problems*, 28(3):035003, 2012.

[116] Shermila B Singham and Gary C Salzman. Evaluation of the scattering matrix of an arbitrary particle using the coupled dipole approximation. *The Journal of Chemical Physics*, 84(5):2658–2667, 1986.

[117] Maxence Cassier and Christophe Hazard. Multiple scattering of acoustic waves by small sound-soft obstacles in two dimensions: mathematical justification of the foldy–lax model. *Wave Motion*, 50(1):18–28, 2013.

[118] Martin Costabel, Monique Dauge, and Khadijeh Nedaiasl. Stability analysis of a simple discretization method for a class of strongly singular integral equations. *Integral Equations and Operator Theory*, 95(4):29, 2023.

[119] Scott Armstrong, Tuomo Kuusi, and Jean-Christophe Mourrat. *Quantitative stochastic homogenization and large-scale regularity*, volume 352. Springer, 2019.

[120] E De Giorgi-S Spagnolo. Sulla convergenza degli integrali dell'energia per operatori ellittici del secondo ordine. *Ennio De Giorgi*, page 380, 1973.

[121] Sergio Spagnolo. Sulla convergenza di soluzioni di equazioni paraboliche ed ellittiche. *Annali della Scuola Normale Superiore di Pisa-Scienze Fisiche e Matematiche*, 22(4):571–597, 1968.

[122] Sergio Spagnolo. Convergence in energy for elliptic operators. In *Numerical Solution of Partial Differential Equations–III*, pages 469–499. Elsevier, 1976.

[123] Doina Cioranescu and Patrizia Donato. *An introduction to homogenization*. Oxford university press, 1999.

[124] Vasili Vasilievitch Jikov, Sergei M Kozlov, and Olga Arsenievna Oleinik. *Homogenization of differential operators and integral functionals*. Springer Science & Business Media, 2012.

[125] Luc Tartar. Compensated compactness and applications to partial differential equations. In *Nonlinear analysis and mechanics: Heriot-Watt symposium*, volume 4, pages 136–212, 1979.

[126] François Murat. Compacité par compensation. *Annali della Scuola Normale Superiore di Pisa-Classe di Scienze*, 5(3):489–507, 1978.

[127] Grégoire Allaire. Homogenization and two-scale convergence. *SIAM Journal on Mathematical Analysis*, 23(6):1482–1518, 1992.

[128] Grégoire Allaire and Micol Amar. Boundary layer tails in periodic homogenization. *ESAIM: Control, Optimisation and Calculus of Variations*, 4:209–243, 1999.

[129] Clément Beneteau. *Modeles homogénéisés enrichis en présence de bords: Analyse et traitement numérique*. PhD thesis, Institut polytechnique de Paris, 2021.

[130] G. C. Papanicolaou and S. R. S. Varadhan. Boundary value problems with rapidly oscillating random coefficients. In *Random fields, Vol. I, II (Esztergom, 1979)*, volume 27 of *Colloq. Math. Soc. János Bolyai*, pages 835–873. North-Holland, Amsterdam-New York, 1981.

[131] Serguei M. Kozlov. Averaging of random operators. *Mathematics of The Ussr-sbornik*, 37:167–180, 1980.

[132] Ulrich Krengel. *Ergodic Theorems*. De Gruyter, Berlin, New York, 1985.

[133] Albert N Shiryaev. *Probability-1*, volume 95. Springer, 2016.

[134] Janine Illian, Antti Penttinen, Helga Stoyan, and Dietrich Stoyan. *Statistical analysis and modelling of spatial point patterns*. John Wiley & Sons, 2008.

[135] Antoine Gloria and Felix Otto. Quantitative results on the corrector equation in stochastic homogenization. *Journal of the European mathematical society*, 19(11):3489–3548, 2017.

[136] Antoine Gloria, Stefan Neukamm, and Felix Otto. A regularity theory for random elliptic operators. *arXiv preprint arXiv:1409.2678*, 2014.

[137] Yu Gu. High order correctors and two-scale expansions in stochastic homogenization. *Probability Theory and Related Fields*, 169:1221–1259, 2017.

[138] Alain Bourgeat and Andrey Piatnitski. Approximations of effective coefficients in stochastic homogenization. In *Annales de l'IHP Probabilités et statistiques*, volume 40, pages 153–165, 2004.

[139] Toufik Kanit, Samuel Forest, Isabelle Galliet, Valérie Mounoury, and Dominique Jeulin. Determination of the size of the representative volume element for random composites: statistical and numerical approach. *International Journal of solids and structures*, 40(13-14):3647–3679, 2003.

[140] Antoine Gloria. Numerical approximation of effective coefficients in stochastic homogenization of discrete elliptic equations. *ESAIM: Mathematical Modelling and Numerical Analysis*, 46(1):1–38, 2012.

[141] Nicolas Clozeau, Marc Josien, Felix Otto, and Qiang Xu. Bias in the representative volume element method: periodize the ensemble instead of its realizations. *Foundations of Computational Mathematics*, pages 1–83, 2023.

[142] Antoine Gloria, Stefan Neukamm, and Felix Otto. Quantitative estimates in stochastic homogenization for correlated coefficient fields. *Analysis & PDE*, 14(8):2497–2537, 2021.

[143] Scott Armstrong, Tuomo Kuusi, and Jean-Christophe Mourrat. Scaling limits of energies and correctors. *arXiv preprint arXiv:1603.03388*, 2016.

[144] Scott Armstrong, Tuomo Kuusi, and Jean-Christophe Mourrat. The additive structure of elliptic homogenization. *Inventiones mathematicae*, 208(3):999–1154, 2017.

[145] Alain Bourgeat and Andrey Piatnitski. Estimates in probability of the residual between the random and the homogenized solutions of one-dimensional second-order operator. *Asymptotic Analysis*, 21(3-4):303–315, 1999.

[146] Guillaume Bal, Josselin Garnier, Sébastien Motsch, and Vincent Perrier. Random integrals and correctors in homogenization. *Asymptotic Analysis*, 59(1-2):1–26, 2008.

[147] David Nualart. *The Malliavin calculus and related topics*, volume 1995. Springer, 2006.

[148] Ivan Nourdin and Giovanni Peccati. *Normal approximations with Malliavin calculus: from Stein's method to universality*, volume 192. Cambridge University Press, 2012.

[149] Mitia Duerinckx and Antoine Gloria. Multiscale functional inequalities in probability: Constructive approach. *arXiv: Probability*, 2017.

[150] Mitia Duerinckx and Antoine Gloria. Multiscale functional inequalities in probability: Concentration properties. *arXiv preprint arXiv:1711.03148*, 2017.

[151] Antoine Gloria and Felix Otto. An optimal variance estimate in stochastic homogenization of discrete elliptic equations. 2011.

[152] Antoine Gloria and Felix Otto. An optimal error estimate in stochastic homogenization of discrete elliptic equations. *The annals of applied probability*, pages 1–28, 2012.

[153] Mitia Duerinckx and Felix Otto. Higher-order pathwise theory of fluctuations in stochastic homogenization. *Stochastics and Partial Differential Equations: Analysis and Computations*, 8(3):625–692, 2020.

[154] Guillaume Bal. Central limits and homogenization in random media. *Multiscale Modeling & Simulation*, 7(2):677–702, 2008.

[155] Guillaume Bal and Wenjia Jing. Fluctuations in the homogenization of semilinear equations with random potentials. *Communications in Partial Differential Equations*, 41(12):1839–1859, 2016.

[156] Mitia Duerinckx, Julian Fischer, and Antoine Gloria. Scaling limit of the homogenization commutator for gaussian coefficient fields. *arXiv preprint arXiv:1910.04088*, 2019.

[157] Marc Josien and Felix Otto. The annealed calderón-zygmund estimate as convenient tool in quantitative stochastic homogenization. *Journal of Functional Analysis*, 283(7):109594, 2022.

[158] Shari Moskow and Michael Vogelius. First-order corrections to the homogenised eigenvalues of a periodic composite medium. a convergence proof. *Proceedings of the Royal Society of Edinburgh: Section A Mathematics*, 127(6):1263–1299, 1997.

[159] Shari Moskow and Michael Vogelius. First order corrections to the homogenized eigenvalues of a periodic composite medium. the case of neumann boundary conditions. *Preprint, Rutgers University*, 1, 1997.

[160] Fadil Santosa and Michael Vogelius. First-order corrections to the homogenized eigenvalues of a periodic composite medium. *SIAM Journal on Applied Mathematics*, 53(6):1636–1668, 1993.

[161] David Gérard-Varet and Nader Masmoudi. Homogenization in polygonal domains. *Journal of the European Mathematical society*, 13(5):1477–1503, 2011.

[162] David Gérard-Varet and Nader Masmoudi. Homogenization and boundary layers. *Acta mathematica*, 209(1):133–178, 2012.

[163] Christophe Prange. Asymptotic analysis of boundary layer correctors in periodic homogenization. *SIAM Journal on Mathematical Analysis*, 45(1):345–387, 2013.

[164] Marc Josien and Claudia Raithel. Quantitative homogenization for the case of an interface between two heterogeneous media. *SIAM Journal on Mathematical Analysis*, 53(1):813–854, 2021.

[165] Peter Bella, Julian Fischer, Marc Josien, and Claudia Raithel. Boundary layer estimates in stochastic homogenization. *arXiv preprint arXiv:2403.12911*, 2024.

[166] Fioralba Cakoni, Bojan B Guzina, and Shari Moskow. On the homogenization of a scalar scattering problem for highly oscillating anisotropic media. *SIAM Journal on Mathematical Analysis*, 48(4):2532–2560, 2016.

[167] Fioralba Cakoni, Bojan B Guzina, Shari Moskow, and Tayler Pangburn. Scattering by a bounded highly oscillating periodic medium and the effect of boundary correctors. *SIAM journal on applied mathematics*, 79(4):1448–1474, 2019.

[168] Fioralba Cakoni, Shari Moskow, and Tayler Pangburn. Limiting boundary correctors for periodic microstructures and inverse homogenization series. *Inverse problems*, 36(6):065009, 2020.

[169] Valentin Vinoles. *Problèmes d'interface en présence de métamatériaux: modélisation, analyse et simulations*. PhD thesis, Université Paris-Saclay (ComUE), 2016.

[170] K Kirk Shung and Gary A Thieme. *Ultrasonic scattering in biological tissues*. CRC press, 1992.

[171] Mitsuhiro Ueda and Yasuhiko Ozawa. Spectral analysis of echoes for backscattering coefficient measurement. *The Journal of the Acoustical Society of America*, 77(1):38–47, 1985.

[172] Simon N Chandler-Wilde and Peter Monk. Wave-number-explicit bounds in time-harmonic scattering. *SIAM Journal on Mathematical Analysis*, 39(5):1428–1455, 2008.

[173] Jean-Claude Nédélec. *Acoustic and electromagnetic equations: integral representations for harmonic problems*, volume 144. Springer, 2001.

[174] J Melenk and Stefan Sauter. Convergence analysis for finite element discretizations of the helmholtz equation with dirichlet-to-neumann boundary conditions. *Mathematics of Computation*, 79(272):1871–1914, 2010.

[175] John M Ball, Yves Capdeboscq, and Basang Tsering-Xiao. On uniqueness for time harmonic anisotropic maxwell's equations with piecewise regular coefficients. *Mathematical Models and Methods in Applied Sciences*, 22(11):1250036, 2012.

[176] Théophile Chaumont-Frelet and Euan A Spence. Scattering by finely-layered obstacles: frequency-explicit bounds and homogenization. *arXiv preprint arXiv:2109.11267*, 2021.

[177] Guy Bouchitté and Didier Felbacq. Homogenization near resonances and artificial magnetism from dielectrics. *Comptes Rendus Mathematique*, 339(5):377–382, 2004.

[178] F Murat. H-convergence, séminaire d'analyse fonctionnelle et numérique de l'université d'alger, mimeographed notes. english translation: Murat and l. tartar, h-convergence. *F. Topics in the Mathematical Modelling of Composite Materials, edited by A. Cherkaev and R. Kohn. Birkhäuser Verlag, Boston. Series Progress in Nonlinear Differential Equations and their Applications*, 31, 1977.

[179] Haim Brézis. *Functional analysis, Sobolev spaces and partial differential equations*, volume 2. Springer, 2011.

[180] Robert A Adams and John JF Fournier. *Sobolev spaces*. Elsevier, 2003.

[181] Peter Monk. *Finite element methods for Maxwell's equations*. Oxford University Press, 2003.

[182] Xlife++ : extended library of finite elements in c++. accessed 2023 Feb. 09.

[183] Théophile Chaumont-Frelet and Euan A Spence. Scattering by finely layered obstacles: Frequency-explicit bounds and homogenization. *SIAM Journal on Mathematical Analysis*, 55(2):1319–1363, 2023.

[184] Martin Costabel, Monique Dauge, and Serge Nicaise. Corner singularities and analytic regularity for linear elliptic systems. part i: Smooth domains. 2010.

[185] Giovanni Alessandrini. Strong unique continuation for general elliptic equations in 2d. *arXiv preprint arXiv:1004.4527*, 2010.

[186] I. G. Graham and S. A. Sauter. Stability and error analysis for the helmholtz equation with variable coefficients, 2019.

[187] I.G. Graham, O.R. Pembery, and E.A. Spence. The helmholtz equation in heterogeneous media: A priori bounds, well-posedness, and resonances. *Journal of Differential Equations*, 266(6):2869–2923, 2019.

[188] Giovanni S. Alberti, Habib Ammari, Francisco Romero, and Timothée Wintz. Mathematical analysis of ultrafast ultrasound imaging. *SIAM Journal on Applied Mathematics*, 77(1):1–25, 2017.

[189] P. A. Martin. *Multiple Scattering: Interaction of Time-Harmonic Waves with N Obstacles*. Encyclopedia of Mathematics and its Applications. Cambridge University Press, 2006.

[190] Jordan Bell. The singular value decomposition of compact operators on hilbert spaces, 2014.

[191] Bradley E Treeby and Benjamin T Cox. k-wave: Matlab toolbox for the simulation and reconstruction of photoacoustic wave fields. *Journal of biomedical optics*, 15(2):021314–021314, 2010.

ECOLE
DOCTORALE
DE MATHEMATIQUES
HADAMARD

Titre : Propagation des ultrasons dans des milieux aléatoires multi-échelles et estimation de vitesses effectives.

Mots clés : problèmes inverses, imagerie à ultrasons quantitative, équations aux dérivées partielles, homogénéisation stochastique quantitative

Résumé : L'échographie est une méthode d'imagerie médicale très répandue. Son objectif principal est de fournir des images structurelles précises des tissus biologiques. Ces dernières années, un changement de paradigme s'est opéré, et le but de l'imagerie par ultrasons est maintenant aussi d'obtenir des informations quantitatives sur les paramètres physiques des tissus, qui peuvent ensuite être utilisées pour le diagnostic.
La vitesse de propagation des ondes acoustiques dans les tissus mous joue un double rôle, puisque sa bonne estimation peut être utilisée pour le diagnostic de cancer du sein ou de la stéatose hépatique, mais elle détermine aussi la qualité de la reconstruction structurelle. En effet, l'image est traditionnellement produite en repropageant numériquement les échos mesurés, à la vitesse du son dans l'eau. Cependant, lorsque la vitesse du son à l'intérieur des tissus n'est pas exactement celle dans l'eau, des artéfacts non physiques apparaissent sur les images.
Afin d'établir un estimateur quantitatif de cette vitesse de propagation, il est important de comprendre théoriquement la propagation des ondes acoustiques dans les tissus. Il est admis que les échos sont générés par les petites et nombreuses hétérogénéités à l'intérieur des tissus (noyaux de cellules, mitochondries...). Bien que le modèle de Born soit couramment utilisé, il ne prend pas en compte les effets des variations de vitesses effectives dues à la présence d'hétérogénéités sous-résolues. L'objectif de cette thèse est donc d'établir un modèle de propagation d'onde plus sophistiqué, capable de représenter les variations de vitesses effectives dans les différents tissus. Dans un second temps, on s'attachera à étudier des estimateurs de la vitesse du son introduits précédemment par Alexandre Aubry dans ses travaux.
Nous considérons donc un milieu homogène dans lequel se trouvent de nombreuses hétérogénéités microscopiques. Les hétérogénéités étant sous-résolues et leur distribution inconnue et inaccessible, on modélisera leur nombre et leur position de manière aléatoire. Afin d'obtenir une représentation simple du champ diffusé par le milieu, le formalisme et les techniques d'homogénéisation stochastique quantitative sont employés. En particulier, une asymptotique d'ordre élevé est obtenue.
Nous poursuivons ensuite une analyse asymptotique de la fonctionnelle d'imagerie à partir du modèle d'ordre élevé précédemment obtenu. De plus, l'étude théorique des estimateurs introduits par Alexandre Aubry et de son équipe permet de confirmer et de retrouver une partie des résultats expérimentaux. En particulier, il est possible de retrouver la vitesse effective des tissus à partir d'une moyenne spatiale locale de la fonctionnelle d'imagerie. Des simulations numériques attestent de chacun des résultats théoriques majeurs prouvés dans cette thèse.

Title : Propagation of ultrasounds in random multi-scale media and effective speed of sound estimation

Keywords : inverse problem, quantitative ultrasound imaging, partial differential equation, quantitative stochastic homogenization

Abstract : Ultrasounds are widely used in medical imaging modalities. Originally, the ultrasound devices were built to image the internal structure of the tissues. In recent years, a change of paradigm operated and the goal is now also to assess physical parameters that can be used for medical diagnosis.
The speed of acoustic waves inside soft tissues can be used for diagnosis of breast cancers or hepatic steatosis. Moreover, it determines the quality of the tomographic reconstruction of the tissues. Indeed, the images are usually computed by backpropagating the measured echoes at the speed of sound in water. However, the discrepancy between the speed of sound in water and the actual speed of sound inside the tissues results in nonphysical artifacts on the image.
In order to establish a quantitative estimator of the propagation speed of sound inside the soft tissues, it is necessary to deeply understand the scattering of the medium. It is commonly admitted that the backscattered echoes are produced by numerous unresolved scatterers inside the medium (cell nuclei, mitochondria...). The scattered field is then written using the Born approximation. However, this model does not capture the variation of the effective speed of sound inside the tissue due to the unresolved scatterers. The goal of this thesis is thus to establish a propagation model that takes into account the variations of the effective speed of sound inside the tissues. Then, we will theoretically study the estimators previously introduced by Alexandre Aubry in his work.
The tissue is here modeled as a bounded homogeneous medium in which lie unresolved scatterers. As their distribution is unknown and inaccessible, their number and position is modeled as a random process. To obtain a simple form of the backscattered field, the techniques and tools developed for the quantitative stochastic homogenization theory will be used and a high-order asymptotic expansion will be proven. An asymptotic analysis of the imaging functional is carried out by using the high-order asymptotic expansion. Furthermore, the theoretical study of the estimators introduced by Alexandre Aubry and his team confirms and justifies some of the experimental results. In particular, it is possible to recover the effective speed of sound by a local spatial average of the imaging function. Numerical simulation supports each and every major result proven in this thesis.

Institut Polytechnique de Paris
91120 Palaiseau, France